Three dimensional Cellular Automaton – Finite Element (CAFE) modeling for the grain structures development in Gas Tungsten / Metal Arc Welding processes

Shijia Chen

ParisTech
INSTITUT DES SCIENCES ET TECHNOLOGIES
PARIS INSTITUTE OF TECHNOLOGY

MINES ParisTech

École doctorale n° 364 : Sciences Fondamentales et Appliquées

Doctorat ParisTech

T H È S E

pour obtenir le grade de docteur délivré par

l'École nationale supérieure des mines de Paris

Spécialité " Science des Matériaux "

présentée et soutenue publiquement par

Shijia CHEN

04/07/2014

Three dimensional Cellular Automaton-Finite Element (CAFE) modeling for the grain structures development in Gas Tungsten / Metal Arc Welding processes

Modélisation tridimensionnelle Automate Cellulaire - Éléments Finis (CAFE) pour la simulation du développement des structures de grains dans les procédés de soudage GTAW / GMAW

Directeur de thèse : **Charles-André GANDIN**
Co-encadrement de la thèse : **Gildas GUILLEMOT**

Jury

M. Philippe LE MASSON, Professeur, Université de Bretagne-Sud	Président
M. Cyril BORDREUIL, Maître de Conférences, Université Montpellier 2	Rapporteur
M. Damien FABREGUE, Maître de Conférences, INSA de Lyon	Rapporteur
M. Henri NGUYEN THI, Professeur, Université d'Aix-Marseille	Examinateur
M. Charles-André GANDIN, Directeur de recherche CNRS, MINES ParisTech	Examinateur
M. Gildas GUILLEMOT, Maître Assistant, MINES ParisTech	Examinateur

T H È S E

MINES ParisTech
Centre de mise en forme des matériaux – UMR CNRS 7635
1 Rue Claude Daunesse CS 10207, 06904 Sophia Antipolis Cedex, France

Acknowledgment

This work is supported by ARMINES and China Scholarship Council (CSC) (grant 2010623175). I want to thank all the academic and industrial partners of this project. It has been a great honor for me to work with them. I am very grateful to the Center for Material Forming (CEMEF), Mines ParisTech, for providing me the perfect environment to complete this thesis work. I would also like to thank Shanghai Jiao Tong University for recommending me to enter CEMEF. This work would not have been possible though, without the different kinds of contributions of a lot of people.

First of all, I would like to express my deepest sense of gratitude to my Ph.D thesis advisors, Dr. Charles-André Gandin and Dr. Gildas Guillemot, for providing me the opportunity to achieve this work. They give me many invaluable advices and encouragements so that I could find a way to overcome the difficulties.

I would like to thank the members of the jury of this thesis. Many thanks to Dr. Cyril Bordreuil, Dr. Damien Fabrègue, Prof. Philippe Le Masson, and Prof. Henri Nguyen Thi for their great work on my thesis committee.

I would express great thanks to Dr. Tommy Carozzani, Dr. Olivier Desmaison, and Ali Saad. I could never complete my Ph.D work without their valuable research work. Thanks for what they have done, and for all the advices they gave me.

I would like to thank all the members of the SP2 group. Each of them is very nice to provide helps to me. Many thanks are sent to Haithem, Alexis, Tommy, Ali, Takao, Valentine, Carole, Thi-Thuy-My, *etc*. Thanks them for teaching me everything about the research and the life in France.

I would like to thank all the CEMEF staff. Special thanks to Patrick Coels, who provide countless helps to me during my Ph.D period, without one of them I could not continue my Ph.D. Thanks also go to Suzanne and Cyrille, who provided me many helps on the experimental observations. Special mentions are sent to the Chinese friends in CEMEF, without whom I could not have so much pleasure to the research work and sport activities.

Acknowledgment

Most importantly, I would like to express my sincere thanks to my family. My parents, my girlfriend Xuan Zhou, and the rest of my family, always provide love and support to me. I say I would never finish PhD without their love.

Table of contents

List of symbols:

Roman alphabets

a_d	acceleration of the droplet	m s^{-2}
a_g	gravitational acceleration	m s^{-2}
C_p	volumetric heat capacity	J m^{-3} K^{-1}
c_p	specific heat capacity	J kg^{-1} K^{-1}
D	solute diffusion coefficient	m^2 s^{-1}
d	distance	m
E	total free energy	J
e	free energy density	J m^{-3}
F	representation of a variable in surface condition	-
f	mass fraction	-
f_d	frequency of detachment of the droplets	s^{-1}
G_C	solute concentration gradient	(wt%) m^{-1}
G_T	temperature gradient	K m^{-1}
g	volume fraction	-
g^m	volume fraction of the mushy structure (mushy fraction)	-
H	local volume enthalpy	J m^{-3}
h	local mass enthalpy	J kg^{-1}
I	current intensity	A
I_v	index of the cell state	-
Iv	Ivantsov function	-
K	mean interface curvature	m^{-1}
k	partition coefficient of the solute at the interface	-
L	volumetric latent heat	J m^{-3}
L_a	length of the arc plasma	m
L_c	height of the cavity	m
Le	Lewis number	-
m^l	slope of the liquidus line in phase diagram	K $(wt\%)^{-1}$
$\dot{m}_w$	mass flow rate of the filler metal in GMAW	kg s^{-1}
N	density of grains	m^{-3}
Pe_C	solutal Peclet number	-
p	pressure	Pa

$\dot{Q}$	volumetric contribution of heat	W m^{-3}
R_c	radius of the cavity in the fusion zone	m
R	radius	m
T	temperature	K
T_{ext}	environmental temperature	K
T_f	melting temperature of the pure metal	K
T_L	liquidus temperature with the nominal composition	K
T_{liq}	liquidus temperature	K
T_{sol}	solidus temperature	K
t	time	s
U	voltage	V
V_c	volume of the cavity	m^{-3}
v	velocity	m s^{-1}
v^H	velocity of heat source in welding	m s^{-1}
w	mass composition	wt%

Greek alphabets

Γ	Gibbs-Thomson coefficient	K m
γ	interfacial energy	J m^{-2}
ΔG_n	nucleation barrier	J
ΔG_V	free energy changed per unit volume	J m^{-3}
Δs_f	specific entropy of fusion	J K^{-1} kg^{-1}
ΔT	undercooling	K
ΔT_0	nominal freezing range of the alloy	K
ΔT_T	thermal undercooling	K
ΔT_C	solutal undercooling	K
ΔT_R	curvature undercooling	K
ΔT_K	kinetic undercooling	K
Δt	time step in FE model	s
δt	micro time step in CA model	s
δ	derivative of the Heaviside function wrt Level Set function	m^{-1}
ε_R	fixed value for the residual of iterations	-
ε_r	emissivity	-
ϵ	half thickness of the transition zone in LS approach	m
η	efficiency	-
θ	angle	degree
κ	local thermal conductivity	W m^{-1} K^{-1}
κ_c	local mean curvature of the liquid/air interface	m^{-1}

λ_1	primary arm space of dendrites	m
λ_2	secondary arm space of dendrites	m
λ_s	critical wavelength of the solid/liquid interface	m
μ	index of the neighboring cell (cell number)	-
μ_d	dynamic viscosity	Pa s
μ_0	coefficient of kinetic undercooling	m K^{-1} s^{-1}
ν	index of the current cell (cell number)	-
ρ	local mass density	kg m^{-3}
σ_B	Stefan-Boltzmann constant	W m^{-2} K^{-4}
ϕ	phase field variable	-
φ	angle	degree
χ	representation of any material property	-
ψ	Level Set function	m
Ω	supersaturation	-

Others

$\mathcal{H}$	Heaviside function	-

Indices

x_0	initial value
x_{capt}	capture value
x_d	value of the droplets in GMAW
x_n	value in the normal direction
x_{tip}	value at the dendrite tip
x_w	value of the filler wire (consumable electrode) in GMAW
x_μ	value of the cell μ
x_ν	value of the cell ν

Exponents

x^0	initial value
x^{CA}	value in CA model
x^{en}	value of the envelope of the CA cells
x^{FE}	value in FE model
x^α	value in α
$x^{\alpha/\beta}$	value at interface of α/β

x^{∞}	far-field value
$x^{\mathbb{A}}$	intrinsic property of the air
$x^{\mathbb{M}}$	intrinsic property of the metal

Operators

$\langle x \rangle$	average value in the representative volume element
$\langle x^{\alpha} \rangle^{\alpha}$	intrinsic value in α
x^{T}	transposition
$\nabla \cdot$	divergence
∇	gradient

General introduction

Khan [Kha07] defines welding as a process of permanent joining of two materials (usually metals) through localized coalescence resulting from a suitable combination of temperature, pressure and metallurgical conditions. Welding is an essential process for industries. Various welding products exist in many types of manufacturing industries such as aerospace, marine, automotive and oil. Besides the structure design and production planning of components, the performance of these industries also depends on the welding technology. Therefore, the study of welding processes is of great importance to improve the final performance of welded components in these industries.

The welding processes can be classified considering the combination of temperature and pressure endured in the processes. Based on the source of energy, welding processes can be classified in several categories, such as Gas Welding, Arc Welding, Resistance Welding, Solid State Welding, *etc*. [Kha07]. In order to join two components or parts together, either plastic deformation (in solid-state-welding) or melting (in fusion welding) of their two surfaces could be implemented. The present study is focused on the fusion welding process in which the solidification step is of primary importance in the final properties of the welded parts. The welded parts in fusion welding process, usually called workpieces, are melted by the heat source with an adding filler metal (or not) to form a pool of molten material (called weld puddle or weld pool). The molten material then becomes a strong joint after cooling. Finally, the two parts are combined by the joints.

The qualities of the welds are significantly dependent on the grain structures, such as the grain size and grain orientation. The grain structures formed in welding process are not only determined by the material properties and the environmental conditions, but also the process conditions, such as the input power, the velocity of the torch, or the amount of the filler metal. Therefore, suitable welding conditions to get the satisfied weld quality and to avoid the formation of the defects (*e.g.* porosity, cavities and hot cracking) are required. Thanks to the development of the welding theory and the computation ability, the welding

process can be numerically simulated before the real industrial implementation in order to predict the grain structure development.

However, the numerical simulation of this grain structure development during the welding process requires tackling the different scales. Indeed the methods to solve the conservation equations at the macro scale of the process are different from the methods required to treat the microstructure evolutions. The dimension of the workpiece in welding is usually of the order of m, while the typical magnitude of the grain structure (meso scale) is of the order of 10 μm to 100 μm. Moreover, the dendrites that develop to form the grains have a lower scale (micro scale). It is not realistic to solve this problem with a single methodology. The objective of the present research work is to establish a 3D numerical model to simulate the grain structure formed during welding.

3D Cellular Automaton (CA) – Finite Element (FE) modeling is an efficient way to simulate the nucleation and growth of solidification grain structures in the context of casting processes [Gan99]. This approach is usually known as CAFE modeling and has been widely used for the simulations of solid structures formed from the melt during casting processes. The CAFE model solves and couples the problems at different scales. Although the recent progresses of the CAFE model were significant [Gui04, Car12], they did not permit to handle simulations of the grain structure during welding. Indeed, in welding process, the preexisting grain structure has a main influence on the development of the new grain structure. The initial structure is remelted and the grains develop at the liquid / solid boundary onto the partially remelted grains. For a multipass welding process, the structures formed in previous passes act as the initial structure for the new pass. Therefore, multiple pass welding that requires the possibility of several successive simulations and large domain computation has not been studied. Moreover, the development of the grain structure with the addition of the filler metal which increases the domain of the weld and thus the grain structure has not been modeled. These are the general objectives of the present work.

The thesis will be organized as:

Chapter I will present the fundamental theory related to the solidification of welding process in micro scale and grain scale.

Chapter II will present the simulation methods for the modeling of grain structure development in solidification in micro scale (dendrites) and in meso scale (grains), respectively.

Chapter III will present the CAFE model, which is developed to simulate the grain structure evolution in welding. Since progresses of CAFE model on the simulation of solidification in casting process is significant, the contribution of the present work is the extension for the welding process.

Chapter IV will present the application of the 3D CAFE model on the simulation of the grain structure development in different welding processes. The influences of the numerical and process parameters will be shown. And the predicted grain structures will be discussed.

Chapter I Fundamental theory of welding

1.1. Welding process

During welding process, as the heat source interacts with the material, the severity of thermal histories experienced by the material varies from region to region, resulting in three distinct regions for the material [Dav03]. As schematically shown in **Fig. I-1**, a fusion line is circling the heat source which is laid on the middle of this figure at a given time. This fusion line can be considered as the interface between the fully liquid-state and other parts of the material (usually a mushy state with the mixture of solid and liquid phases). A fusion zone (FZ) is formed aligned with the path of the heat source. In addition, a heat affected zone (HAZ) is adjacent to the fusion zone. Only solid state phase transformation takes place in this zone due to the medium thermal influence of the heat source. Finally, base metal (BM) is the material whose structure is not affected by the heat source.

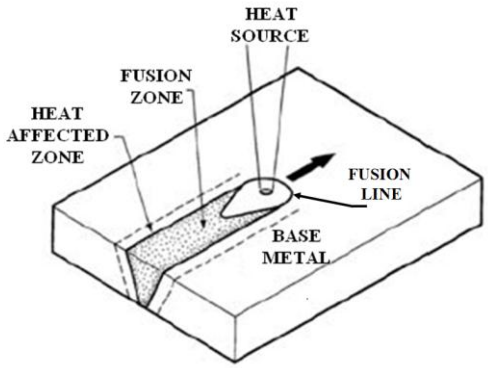

Fig. I-1 Schematic illustration of the three distinct regions in fusion welding [Dav03]

The structure of the workpiece will evolve based on the thermal history during the welding process. Besides the base metal which is not affected by the heat source and keeps unchanged, the characteristic structure of the fusion zone and heat affected zone can be summarized as follows:

Fusion zone: the FZ experiences melting and then solidifies as the heat source moves away. It thus undergoes a very rapid solid-to-liquid-to-solid transformation. It is sometimes available to be considered as a mini-casting depending on the movement of the heat source. Grains grow from the partially melted base metal to form the columnar structure after solidification. As the heat source is continuously moving, its speed is an important factor to control the final structure. **Fig. I-2** shows the different structure formed in the FZ for two speeds of the heat source. The grains formed for a low speed heat source in **Fig. I-2** (a) are

trying to align to the moving direction, but the grains formed for a high speed heat source in **Fig. I-2** (b) are close to perpendicular to the moving direction due to the elongated weld pool.

A specific region might experience several cycles of these transformations due to complicated trajectories of the heat source in some welding processes (*e.g.* in case of multiple passes welding process). As a consequence of repeated temperature increase and decrease, significant spatial changes of the structure can be observed, which depart from the simple schematic given in **Fig. I-2**.

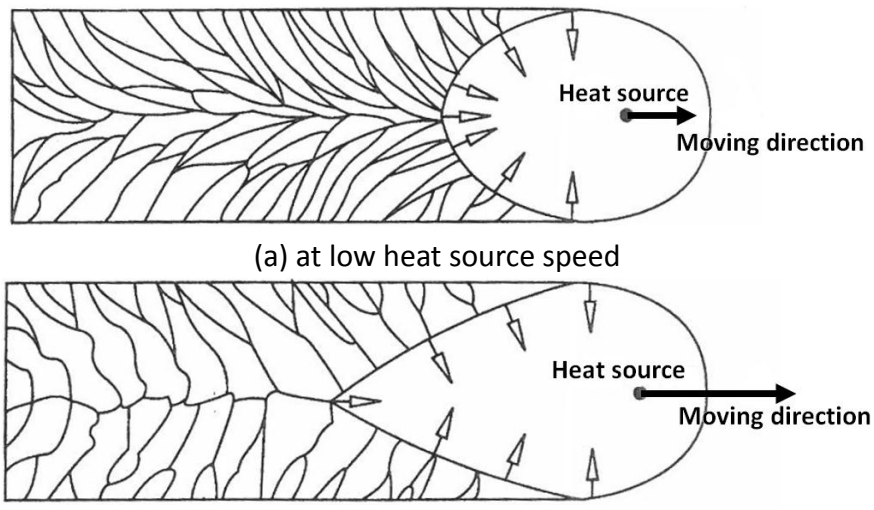

(a) at low heat source speed

(b) at high heat source speed

Fig. I-2 Schematic illustration of the grain structure formed in the fusion zone, (a): at low heat source speed and (b): at high heat source speed [Por92, Gro94]. The black arrows represent the moving direction of heat source. The white arrows represent the growth direction of the columnar grains.

Heat affected zone: the HAZ is located beside the FZ. Different from FZ, the HAZ is not melted by the heat source. However, the thermal cycles and temperature gradients induced by welds cause the microstructure to evolve by solid state transformation, such as grain growth, recrystallization, phase change, annealing and tempering [Gro94]. These transformations result in the formation of different sub-regions in the HAZ referred to as coarse-grain region, fine-grain region and partially-transformed region [Elm01, Elm03].

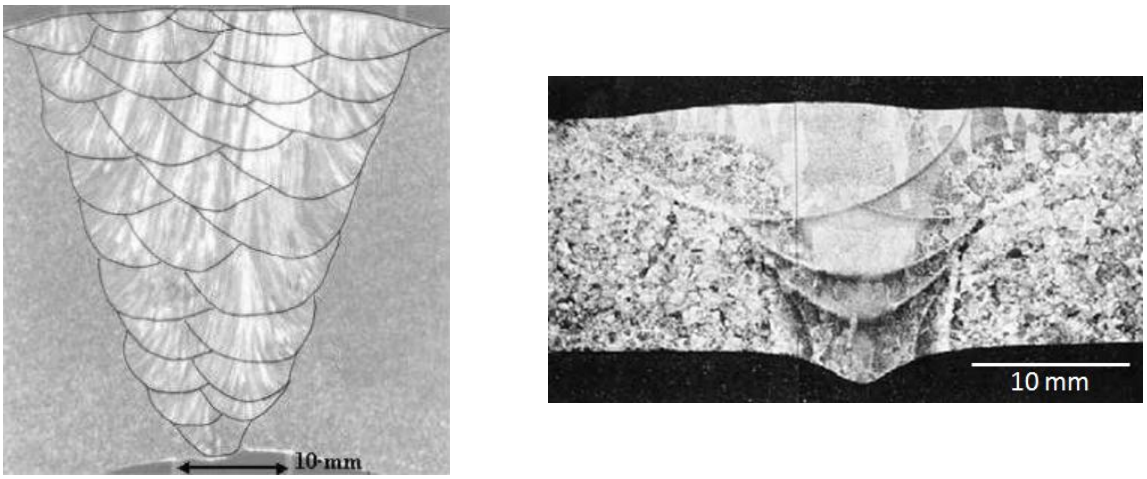

(a) (b)

Fig. I-3 Final structure of transverse section after multiple passes of (a): shielded Metal Arc Welding process in a stainless steel laminated metal sheet of the 316-L type with the shielded electrode of the OK 63-25 type [Moy03], and (b): Gas Tungsten Arc Welding process in 14 mm thick Grade 23 titanium pipe [Smi99]

However, when the thickness/width of the weld to be achieved between the two components exceeds the limitation of the single pass technology used, the multiple passes welding processing should be implemented. It is frequently found as a joint process between large components. The final structure of the fusion zone becomes much more complicated than that observed in single pass welding. **Fig. I-3** shows the final structure in a transverse cross section for multi-pass welding processes. It is seen that the new grains can grow into different passes to form long columnar grains.

Among the various techniques used in welding processes, “the term arc welding applies to a large and varied group of processes that use an electric arc as the source of heat to melt and join metals” [USA93]. The Gas Tungsten Arc Welding and Gas Metal Arc Welding are of the common techniques among the Arc Welding. The present work is focused on the grain structures formation during these welding processes.

1.1.1. Gas Tungsten Arc Welding

Gas Tungsten Arc Welding (GTAW) is a process that melts and joins metals by heating them with an arc established between a non-consumable tungsten electrode and the workpiece [Kou02], as schematically shown in **Fig. I-4**. It was developed in the late 1930s in order to weld magnesium alloys [All11]. Because inert gas is usually used as the shielding gas (in special cases a non-inert gas can be added in a small quantity to the shielding gas), it is also referred to as the Tungsten Inert Gas (TIG) process.

In GTAW process, the workpiece melts due to the heat transfer from the arc, leading to the formation of a weld pool. The arc zone is full of an inert gas (usually helium, argon or a mixture of these two) to protect the tungsten electrode and the molten metal from oxidation, and to provide a conducting path for the arc current. GTAW is usually implemented without adding metal. In this case, the metals are joined by the fusion alone. Moreover, it is sometimes possible to add the filler metal supplied from filler rods. The composition of the filler rods should be suitable to the parent metals being welded. Generally, the thickness/width of the part to be welded determines the need for filler rod or not.

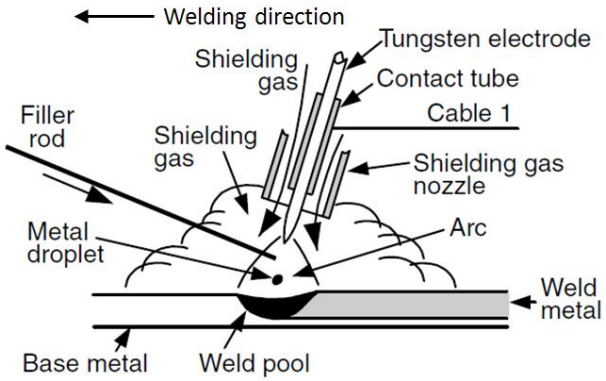

Fig. I-4 Schematic illustration of welding area in Gas Tungsten Arc Welding [Kou02]

In the GTAW process, the heat produced by the arc is the multiplication of the arc current and the arc voltage. About 70% of the heat is generated at the positive terminal (anode) of the arc. Therefore, GTAW process is normally operated with the tungsten electrode or cathode negative (negative polarity) and the workpiece or anode positive [All11]. This is used to put the heat to the workpiece to form the weld pool.

GTAW can be used to join stainless steels (austenitic, ferritic and martensitic types) and many nickel-base super-alloys where high-quality welds are required. It is well suited for welding thin sheet and foil of all weldable metals because it can be controlled at very low amperages (2 to 5 A) required for these thicknesses. In addition, the feeding rate of the filler metal is independent of the welding current, thus allowing a variation in the relative amount of the fusion of the base metal and the fusion of the filler metal. So the control of dilution and energy input to weld can be achieved without changing the size of the weld [Kou02].

However, it is not suitable to weld the metals and alloys with very low melting points due to the high temperature caused by the arc, which makes it difficult to control the weld pool.

1.1.2. Gas Metal Arc Welding

Gas Metal Arc Welding (GMAW) is a process that melts and joins metals by heating them with an arc established between a consumable electrode and the workpiece [Kou02], as schematically shown in **Fig. I-5**. It was introduced to industry in the late 1940s, originally developed with the use of a continuously fed aluminum wire electrode [Lin13]. Nowadays, it is also referred to as the Metal Inert Gas (MIG) process due to the use of inert gas as the shielding gas. Like in GTAW process, the non-inert gas is used in some special cases of GMAW process with a small quantity. Therefore, GMAW is a more appropriate name than MIG.

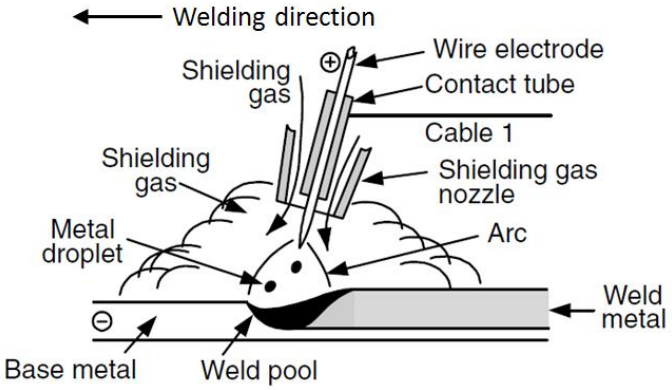

Fig. I-5 Schematic illustration of welding area in Gas Metal Arc Welding [Kou02]

Compared to GTAW, the electrode wire which is the positive anode in GMAW is continuously fed into the arc and deposited as weld metal. Because the electrode wire used for GMAW is thinner than that used for other types of welding, the melting rates of the electrodes in GMAW are very high. The mode of metal transfer affects the weldability. Four modes can be described in the GMAW process [Lin13]:

Short-Circuit Metal Transfer: the Short-Circuit Metal Transfer mode is operated at low voltages and welding current. Therefore, it is a low heat input mode in the GMAW process, referring to **Fig. I-6** (a). All the metal transferred from the electrode to the base material (or the puddle) is electrically shorted by physical contact between them. The shielding gas is usually carbon dioxide or a mixture of 75-80% argon, plus 25-20% carbon dioxide. This kind of mode is suitable for welding thin sections.

Globular Transfer: the Globular Transfer mode occurs when the welding current and wire speed are increased above the maximum for Short-Circuit transfer mode. The continuously fed metal is a combination of short-circuits and gravity-assisted large drops, referring to **Fig. I-6** (b). Because the irregularly shaped molten droplets do not follow the axial detachment from the electrode, the spatter of droplets in this mode is severe. The shielding gas is used with carbon dioxide or a mixture of argon and carbon dioxide.

Axial Spray Transfer: the Axial Spray Transfer mode is a higher energy mode than Globular Transfer. The continuously fed metal is in such a high energy level to result in a steam of small molten droplets, which are propelled axially to detach from the electrode across the arc, shown in **Fig. I-6** (c). The shielding gas is a mixture of argon plus 1-5% oxygen or the mixture of argon plus less than 18% carbon dioxide. This mode can be applied to the material with large thickness due to its excellent weld fusion.

Pulsed Spray Transfer: the Pulsed Spray Transfer is developed in order to control the weld spatter and eliminate the incomplete fusion defects which are usual in Globular and Short-Circuit Transfer modes. In this mode, the welding current is cycled between a high peak level to a low background level. The droplet is sprayed into the puddle during the high peak level like the Axial Spray Transfer mode (see **Fig. I-6** (c)). The shielding gas is selected to be argon with a maximum of 18% carbon dioxide. This mode can be used for a wide range of welding.

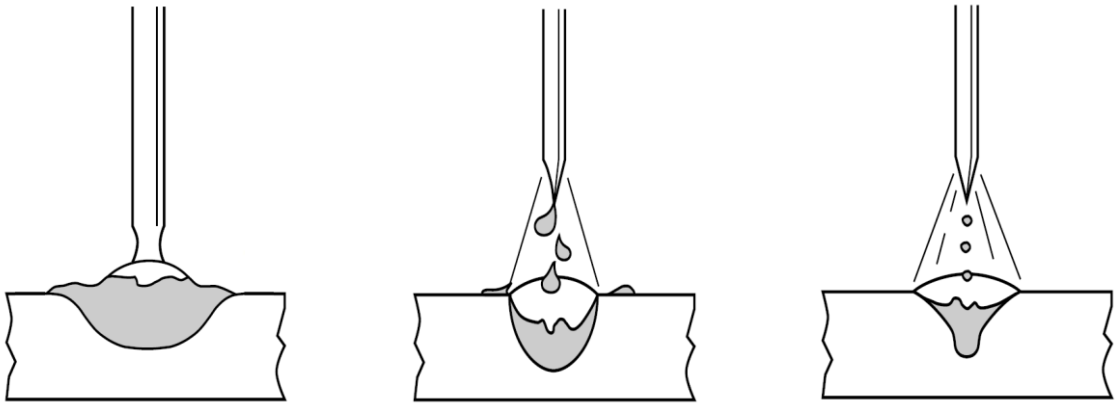

Fig. I-6 Schematically illustrations of (a): Short-Circuit Metal Transfer, (b): Globular Transfer and (c): Axial Spray Transfer/ Pulsed Spray Transfer [Lin13]

GMAW can be used for a wide range of material such as carbon steel, stainless steel, aluminum, magnesium, copper, nickel, silicon, bronze and tubular metal-cored surfacing

alloys [Lin13]. Compared to GTAW, GMAW is allowed to weld thicker workpieces at higher speeds due to the much higher deposition rate. However, it is hard to control the GMAW guns in small areas or corners.

1.2. Microstructure of solidification

Most of the current knowledge of solidification in fusion zone is derived from an extrapolation of the knowledge of solidification during castings, and single crystals growth at lower temperature gradients and growth rates [Dav75]. Although solidification in weld pool is not exactly the same in casting, it is consistent to apply the classical solidification theory to welding. Then the differences between welding and casting will be discussed.

1.2.1. Nucleation

In the classical solidification theory, nucleation is considered as the creation of a cluster of atoms with a crystalline structure [Dan09]. The clusters which are too small to survive are called embryos, whereas those that are large enough to remain stable in the liquid are called nuclei. The nuclei can form in two separate categories, namely homogeneous and heterogeneous nucleation. The nuclei which form from the melt spontaneously without any aids of impurities, is called to nucleate homogeneously. In the opposite, it is heterogeneous nucleation when the nuclei form on the foreign particles in the melt or at the interfaces of melt container.

Considering the homogeneous nucleation, it requires a large driving force (or a large undercooling below the equilibrium liquidus temperature) to stabilize the clusters of atoms (or nuclei). The free energy to form a critical sized cluster (or called homogeneous nucleation barrier), ΔG_n^{homo}, is given by [Dan09]:

$$\Delta G_n^{homo} = \frac{16\pi}{3}\frac{\left(\gamma^{s/l}\right)^3}{\Delta G_V^2} \qquad \textbf{(I-1)}$$

where $\gamma^{s/l}$ is the solid/liquid (s/l) interfacial energy, ΔG_V is the free energy changed per unit volume for solidification, which depends on the undercooling:

$$\Delta G_V = \rho \Delta s_f \Delta T \quad \textbf{(I-2)}$$

where ρ is the density, Δs_f is the specific entropy of fusion, ΔT is the undercooling for nucleation.

The stable nuclei form homogeneously when the driving force of undercooling can compensate the nucleation barrier ΔG_n^{homo}. However in some cases, nucleation can take place in another different way, namely heterogeneous nucleation. In this nucleation method, the nucleation is initiated on a foreign surface (foreign substrate f). In such case, the free energy to form a critical sized cluster (or called heterogeneous nucleation barrier), ΔG_n^{heter}, is given by:

$$\Delta G_n^{heter} = \Delta G_n^{homo} \cdot f(\theta) \quad \textbf{(I-3)}$$

$$\text{with} \quad f(\theta) = \frac{1}{4}(2 + cos\theta)(1 - cos\theta)^2 \quad \textbf{(I-4)}$$

where $f(\theta) \in [0,1]$ is a geometric factor that depends on the wetting angle θ defined as **Fig. I-7** (a).

Eq. (I-3) shows that the ΔG_n^{heter} only differs from ΔG_n^{homo} by a geometric factor $f(\theta)$ which is less than one (or equal one in the extreme condition). Therefore, the nucleation in heterogeneous way is easier than in homogeneous way. **Fig. I-7** (b) shows the variation of $f(\theta)$ depending upon θ.

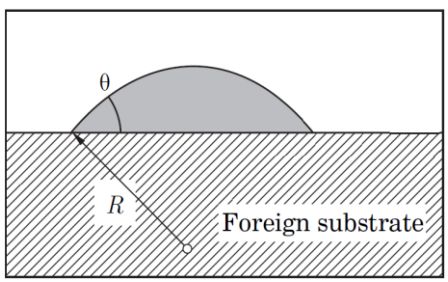

(a)

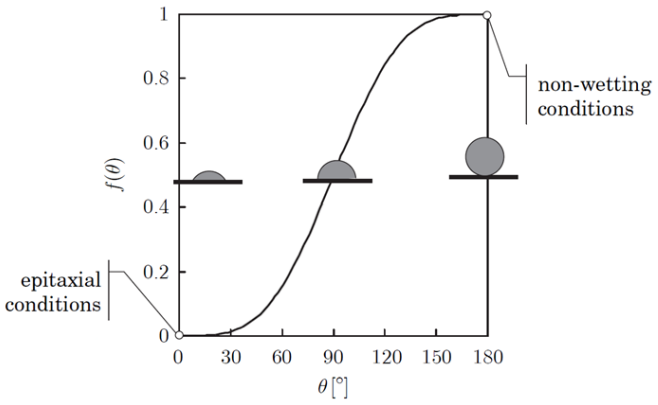

(b)

Fig. I-7 (a): the heterogeneous nucleation at a liquid/substrate interface with the radius, R, and (b): the function of $f(\theta)$ with respect to the wetting angle θ in heterogeneous nucleation [Dan09].

According to **Fig. I-7** (b), three typical equilibrium shapes of nucleus depending on θ can be summarized:

When $\theta = 180°$, $f(\theta) = 1$. It corresponds to non-wetting conditions of the formed nucleus on the foreign substrate (or particle). This case is equivalent to the homogeneous nucleation, namely $\Delta G_n^{heter} = \Delta G_n^{homo}$.

When $\theta = 90°$, $f(\theta) = 0.5$. This condition occurs when the surface energy between foreign substrate and liquid $\gamma^{f/l}$ is the same as that between foreign substrate and solid $\gamma^{f/s}$. In this case, the nucleus is in the shape of hemisphere, thus reduce the energy barrier by the requirement of half atoms than that in homogeneous nucleation. So, $\Delta G_n^{heter} = 0.5\Delta G_n^{homo}$.

When $\theta = 0°$, $f(\theta) = 0$. This case occurs when the foreign substrate is exactly the same as the nucleation phase. There is no energy barrier for the nucleation, and the solidification is only limited to grain growth. Therefore, $\Delta G_n^{heter} = 0$.

In the weld pool during welding process, the solidification starts from the partially melted grains, which could be considered as the foreign substrates with respect to the liquid in the weld pool. According to the third case above, the substrates (partially melted grains) are the same as the solid phase, $\Delta G_n^{heter} = 0$. Thus the nucleation barrier vanishes in weld pool. The solidification reduces to the epitaxial grain growth, which will be explained in **Section 1.3.1**.

1.2.2. Interface between solid and liquid

As mentioned in **Section 1.2.1**, there is not nucleation barrier since growth proceed from already existing solid phases. In the absence of nucleation events, the solidification reduces to the growth from partially melted grains. The stability of the solid/liquid interface is critical to determine the final microstructure of the fusion zone.

In the classical theory of solidification [Dan09], the interface between solid and liquid in pure metal during a directional solidification can be considered as planar. The propagation of the solid is mainly controlled by the temperature gradient in the liquid at the interface, $G_T^{l\,s/l}$. If it is positive, which is verified during directional solidification for pure metal, the interface can keep a planar morphology. If $G_T^{l\,s/l}$ is negative, encountered during equiaxed solidification in an undercooled melt for pure metal, the interface is not stable and thus turn to dendritic morphology.

However, the analysis is more complicated for alloys because it is necessary to take into account solute diffusion in the liquid. Flemings shows several solidification structures that can be obtained in directionally solidified binary alloys [Fle74]. As initially shown by Rutter *et al.* [Rut53], the variation of these different morphologies of structure depends upon the relationship between the temperature gradient in the liquid at the interface, $G_T^{l\,s/l}$, and the velocity of the solid/liquid interface, $v^{s/l}$ [Fle74, Liu95]. Although the temperature gradient $G_T^{l\,s/l}$ is positive in directional solidification condition, the solute concentration gradient in the liquid at the interface, $G_C^{l\,s/l}$, is negative due to the smaller solubility in the solid than that in the liquid. Consequently, the interface is defined to be under conditionally stable condition [Fle74, Deb95]. Examined by the concept of constitutional undercooling (or called constitutional supercooling), the criterion for plane front stability of alloys is:

$$\frac{G_T^{l\,s/l}}{v^{s/l}} \geq \frac{\Delta T_0}{D^l} \qquad \textbf{(I-5)}$$

where ΔT_0 is the nominal freezing range of the alloy, and D^l is the solute diffusion coefficient in the liquid. If **Eq. (I-5)** is satisfied, the front will remain planar. In the opposite, if **Eq. (I-5)** is not satisfied, namely $\frac{G_T^{l\,s/l}}{v^{s/l}} < \frac{\Delta T_0}{D^l}$, which is the usual situation during solidification of alloys, the planar front will be unstable. As a consequence of geometrical unstability, a microstructure, *e.g.* dendrite, will form.

Considering the directional solidification of a binary alloy with a planar front initially, the constitutional undercooling criterion is graphically illustrated in **Fig. I-8**. Due to the solute enrichment in the liquid at the solid/liquid interface shown in **Fig. I-8** (a), the liquidus temperature corresponding to the composition and the actual temperature in the liquid are shown in **Fig. I-8** (b) and (c) for different conditions. The solid/liquid interface is thermodynamically stable if the actual temperature ahead of it is above the local liquidus temperature, which corresponds to the case of **Fig. I-8** (b). If the actual temperature is below the local liquidus temperature, as shown in the case of **Fig. I-8** (c), the interface is unstable and break down to a cellular or dendritic boundary.

Tiller *et al*. [Til53, Dan09] explained that in the case of **Fig. I-8** (b), any perturbation to the interface will be remelted. Consequently, the planar interface will be stable during growth. In

the opposite in the case of **Fig. I-8** (c), a perturbation will continue to grow, thus the planar interface will become unstable. The growing condition departs from the planar stability. The interface morphology will change from planar to cellular or dendritic. Solid cellular or dendrites can coexist with the intercellular or interdendritic liquid, respectively.

According to **Eq. (I-5)**, the higher the actual temperature gradient $G_T^{l\,s/l}$ and the lower the planar growth rate $v^{s/l}$, the easier for the planar solid/liquid interface to keep stable. On the other hand, the higher the freezing range ΔT_0 and the lower the diffusion coefficient D^l, the more difficult for the planer solid/liquid interface to be stable. **Fig. I-9** shows the two structure morphologies of cellular and dendrites during directional solidifications.

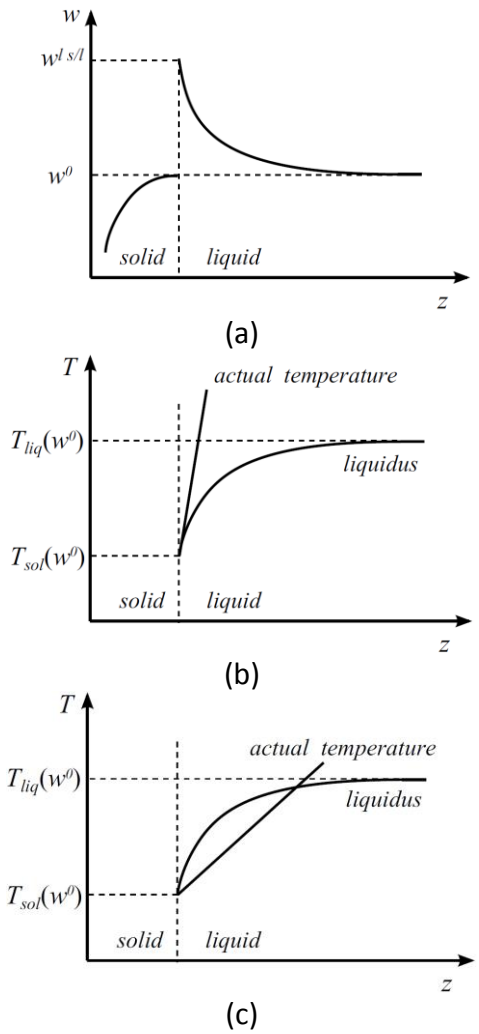

Fig. I-8 Illustration of constitutional undercooling criterion during the directional solidification of a binary alloy with a planar front initially, (a): composition profile and solute enrichment layer ahead of steady-state planar solidification front, (b): stable condition for planar growth, and (c): unstable condition for planar growth [Deb95]. Note w^0 is the nominal solute mass composition of the melt, $w^{l\,s/l}$ is the solute equilibrium mass composition at the interface in liquid.

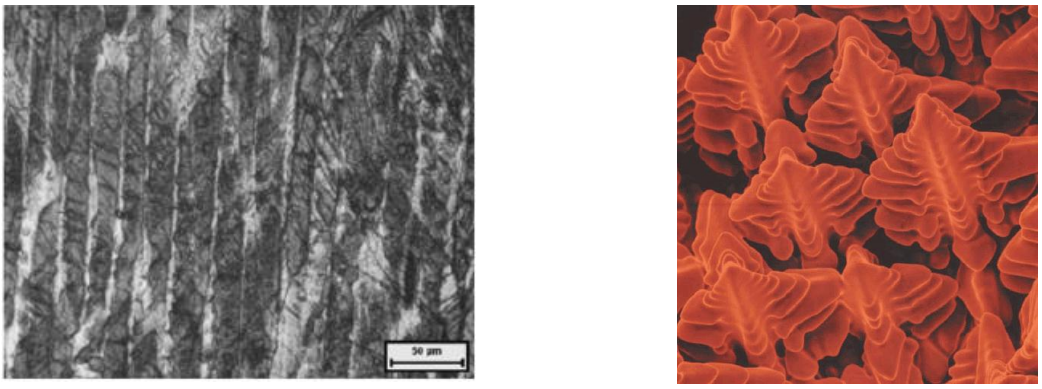

(a) (b)

Fig. I-9 Different structural morphologies during solidification, (a): cellular of Zn-2.2wt% Cu alloy [Bri12], and (b): columnar dendrite of a Ni-base superalloy [Deb95].

1.2.3. Dendritic grain growth

The solution for the dendritic growth of a pure substance in an undercooled melt was first studied by Ivantsov [Iva47]. The analysis was later generalized by Horvay and Cahn [Hor61]. The growth of a dendrite tip with a paraboloid shape (a parabolic shape in 2D and paraboloid in 3D) in an infinite undercooled melt with far-field temperature, $T^{l\infty}$, is assumed to grow at a constant velocity, v_{tip}, along its axis in a shape-preserving way. The geometry of this paraboloid is characterized by its radius of curvature at the tip, R_{tip}. Therefore, the problem reduces to the solution of the relationship among the given undercooling ΔT ($\Delta T = T_{liq}(w^{l\infty}) - T^{l\infty}$), the velocity v_{tip} and the radius R_{tip}, which is called later as Ivantsov solution.

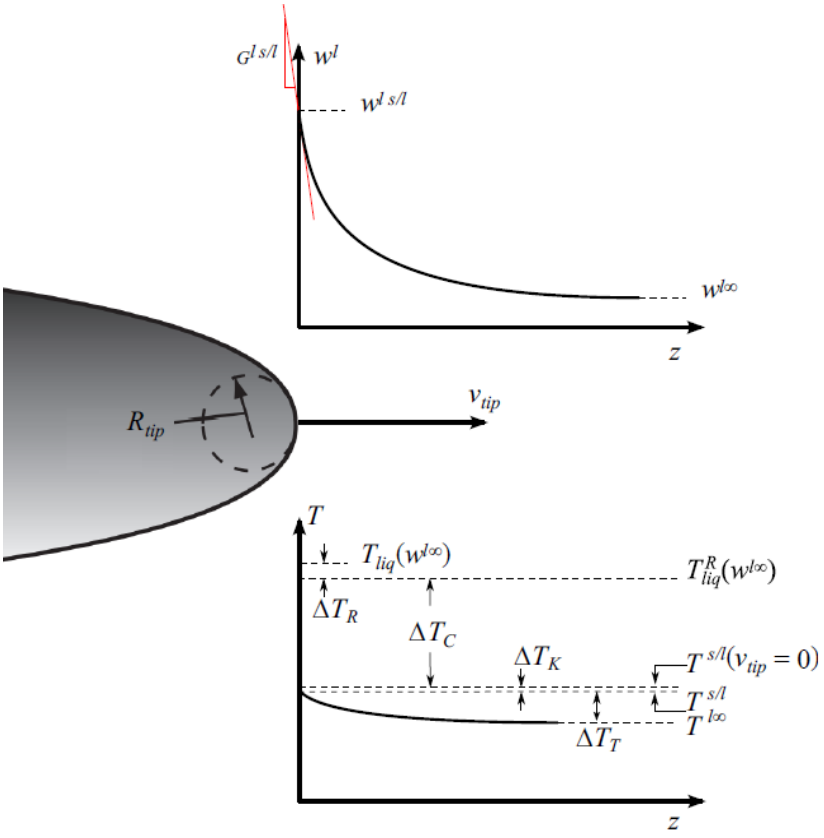

Fig. I-10 Schematic illustration of the dendrite tip growth with undercooling [Dan09]

It is convenient to analyze the dendrite tip kinetic law in binary alloys first, and then extend it to the multicomponent alloys.

1.2.3.1. Dendrite tip kinetic law in binary alloys

In binary material systems, the total undercooling ΔT can be split to four contributions: the thermal undercooling, ΔT_T, the solutal undercooling, ΔT_C, the curvature undercooling, ΔT_R and the kinetic undercooling, ΔT_K.

$$\Delta T = \Delta T_T + \Delta T_C + \Delta T_R + \Delta T_K \quad \textbf{(I-6)}$$

On the right hand side of **Eq. (I-6)**, the thermal undercooling ΔT_T is defined as:

$$\Delta T_T = T^{s/l} - T^{l\infty} \quad \textbf{(I-7)}$$

where $T^{s/l}$ is the temperature of the interface between solid and liquid. Note that in metals the thermal diffusion is much faster than the solutal diffusion by a factor 10^2 ~ 10^4 ($Le = \alpha/D$ with $\alpha = \kappa/\rho c_p$ where Le is the Lewis number, D is the solutal diffusion coefficient, and α is the thermal diffusion coefficient corresponding to the ratio of thermal conductivity, κ, and the multiplication of density, ρ, and specific heat capacity, c_p.) [Kur86]. ΔT_T is much smaller than ΔT_C and thus can be neglected. Therefore, in the following, it is considered that there is no temperature gradient around the dendrite generally.

At the interface, the deviation from the equilibrium temperature corresponding to a zero speed of the advance of the interface is considered to be the driving force for the solute attachment of the liquid phase into the solid crystal [Les86]. This kinetic undercooling ΔT_K can be defined as:

$$\Delta T_K = \frac{v_{tip}}{\mu_0} \quad \textbf{(I-8)}$$

where μ_0 is the coefficient of kinetic undercooling. Generally, μ_0 is the order of 0.01 m K^{-1} s^{-1} [Les86]. Considering that the growth velocity v_{tip} is usually small in solidification with the order of 10^{-4} m s^{-1}, the magnitude of ΔT_K is 0.01 K. Even in the welding case with the grain growth velocity no more than 0.01 m s^{-1}, the magnitude of ΔT_K is not more than 1 K, whereas the total undercooling is much larger for the alloys studied in the present work. ΔT_K can thus be neglected.

The curvature undercooling ΔT_R can be estimated by the Gibbs-Thomson expression:

$$\Delta T_R = \frac{2\Gamma^{s/l}}{R_{tip}} \quad \textbf{(I-9)}$$

where $\Gamma^{s/l}$ is the Gibbs-Thomson coefficient, defined as the ratio of the specific solid/liquid interface energy to the melting entropy. As the radius of the dendrite tip is usually in the scale of microns, the curvature effect could give an important contribution to the total undercooling for small value of R_{tip}.

The solutal undercooling, ΔT_C, can be estimated by:

$$\Delta T_C = m^l\left(w^{l\infty} - w^{l\,s/l}\right) \quad \textbf{(I-10)}$$

where m^l is the approximation of the constant slope of the liquidus line in the phase diagram, $w^{l\infty}$ is the far-field solute mass composition in the melt, which can also be considered as the nominal solute mass composition of the melt w^0, $w^{l\,s/l}$ is the solute equilibrium mass composition at the interface in liquid. Generally, ΔT_C accounts for most amount of the total undercooling for alloys.

Therefore, the total undercooling ΔT can be split to **Eq. (I-11)**, neglecting the contributions ΔT_T and ΔT_K :

$$\Delta T = \Delta T_C + \Delta T_R = m^l\left(w^{l\infty} - w^{l\,s/l}\right) + \frac{2\Gamma^{s/l}}{R_{tip}} \quad \textbf{(I-11)}$$

According to Ivantsov, the supersaturation can be calculated by a so-called Ivantsov function around a paraboloid of revolution:

$$\Omega = \frac{w^{l\,s/l} - w^{l\infty}}{w^{l\,s/l} - w^{s\,s/l}} = \frac{w^{l\,s/l} - w^{l\infty}}{w^{l\,s/l}(1-k)} = \mathrm{Iv}(Pe_C) \quad \textbf{(I-12)}$$

where Ω is the supersaturation around the paraboloid, $w^{s\,s/l}$ is the solute equilibrium mass composition at the interface in the solid, k is the partition coefficient of the solute between the liquid and solid phases at the interface, namely $w^{s\,s/l} = kw^{l\,s/l}$, Iv is the Ivantsov function, Pe_C is the solutal Peclet number.

The Ivantsov function is defined as:

$$\mathrm{Iv}(x) = x\,\exp(x)\,\mathrm{E}_1(x) \quad \textbf{(I-13)}$$

where E_1 is the exponential integral function, defined as:

$$\mathrm{E}_1(x) = \int_x^{\infty} \frac{e^{-t}}{t} dt \qquad \textbf{(I-14)}$$

The solutal Peclet number Pe_C is defined as:

$$Pe_C = \frac{R_{tip} v_{tip}}{2D^l} \qquad \textbf{(I-15)}$$

where D^l is the solutal diffusion coefficient in liquid. **Eq. (I-12)**, **(I-13)**, **(I-14)**, **(I-15)** can give the relationship between the solutal undercooling ΔT_C and the dendrite growth which is characterized by solutal Peclet number Pe_C.

It is worth noting that the set of **Eq. (I-11)**, **(I-12)**, **(I-13)**, **(I-14)**, **(I-15)** do not yield unique values for R_{tip} and v_{tip}. Rather, a solution is obtained only in terms of their product, expressed in the solutal Peclet number Pe_C. Therefore, for any given undercooling ΔT, there is an entire family of solutions. However, experiments [Gli84] showed that, for a given undercooling, the dendrites always select a particular growth velocity and tip radius.

Langer *et al*. [Lan78] provided another relationship for the unknowns R_{tip} and v_{tip}. They showed that the dendrite tips do grow closely to a state which can be called marginally stable. Kurz *et al.* [Kur86] later adopted this approximate relationship in the KGT model:

$$R_{tip} = \lambda_s \qquad \textbf{(I-16)}$$

where λ_s is the minimal critical wavelength of the solid/liquid interface at the limit of stability. As the instability wavelength of a sphere and of a planar interface differ only by a numerical factor which is close to unity, λ_s of the planar interface was used by Kurz [Kur86]. In small solutal Peclet number Pe_C and neglecting the temperature gradient around the dendrite, λ_s can be calculated by (Note that the thermal gradient in the liquid at the dendrite tip, $G_T^{l\,s/l}$, is ignored):

$$\lambda_s = 2\pi \sqrt{\frac{\Gamma^{s/l}}{m^l G_C^{l\,s/l}}} \qquad \textbf{(I-17)}$$

where $G_C^{l\,s/l}$ is the solutal gradient in the liquid at the dendrite tip. It can be calculated using a flux balance at the dendrite tip:

$$G_C^{l\,s/l} = -\frac{(1-k)w^{l\,s/l}v_{tip}}{D^l} \quad \textbf{(I-18)}$$

Substitute **Eq. (I-17)**, **(I-18)** into **Eq. (I-16)**, and rearrange it to get:

$$R_{tip}^2 v_{tip} = \frac{4\pi^2 D^l \Gamma^{s/l}}{m^l(k-1)w^{l\,s/l}} \quad \textbf{(I-19)}$$

Finally, joining **Eq. (I-19)** into the set of **Eq. (I-11)**, **(I-12)**, **(I-13)**, **(I-14)**, **(I-15)** could yield unique values for R_{tip} and v_{tip} under a given undercooling ΔT for a binary material.

1.2.3.2. Dendrite tip kinetic law in multicomponent alloy

Bobadilla *et al*. [Bob88] proposed to extend the KGT model for the growth kinetics of a multicomponent dendrite tip, hereafter referred to as BLL model. Rappaz *et al*. [Rap99] later summarized this model briefly. In BLL model, the following assumptions are made:

- no thermal gradient at the scale of the grain;
- neglect the thermal and kinetic undercooling;
- low growth rate at the marginal stability limit;
- independent solute fields given by the Ivantsov solution;
- neglect off-diagonal diffusion terms.

Under these assumptions, the growth of the dendrite tip is governed by the following equations. Based on the assumptions above, considering the solute element $j = [1, n]$ in the phase diagram with linear simplification of each curves, the total undercooling is given by:

$$\Delta T = \Delta T_C + \Delta T_R = \sum_{j=1}^{n} m_j^l \left(w_j^{l\,\infty} - w_j^{l\,s/l}\right) + \frac{2\Gamma^{s/l}}{R_{tip}} \quad \textbf{(I-20)}$$

where $w_j^{l\,s/l}$ and $w_j^{l\,\infty}$ are the equilibrium mass composition of j at the interface in the liquid and the far-field mass composition of j in the liquid, respectively. For each solute element j, the corresponding supersaturation is given by:

$$\Omega_j = \frac{w_j^{l\,s/l} - w_j^{l\,\infty}}{w_j^{l\,s/l}\left(1 - k_j\right)} = \mathrm{Iv}\left(Pe_{C,j}\right) \quad \textbf{(I-21)}$$

where k_j is the partition coefficient of element j. The solutal Peclet number $Pe_{C,j}$ associated with element j is defined by:

$$Pe_{C,j} = \frac{R_{tip} v_{tip}}{2D_j^l} \quad \textbf{(I-22)}$$

where D_j^l is the diffusion coefficient of element j in the liquid.

Accordingly, R_{tip} is given by the marginal stability condition:

$$R_{tip} = 2\pi \sqrt{\frac{\Gamma^{s/l}}{\sum_{j=1}^{n} m_j^l G_j^{l\,s/l}}} \quad \textbf{(I-23)}$$

where m_j^l is the slope of the liquidus line corresponding to element j, $G_j^{l\,s/l}$ is the gradient of element j in the liquid at the dendrite tip, which can be calculated by:

$$G_j^{l\,s/l} = -\frac{\left(1 - k_j\right) w_j^{l\,s/l} v_{tip}}{D_j^l} \quad \textbf{(I-24)}$$

Finally, the set of **Eq. (I-20)**, **(I-21)**, **(I-22)**, **(I-23)**, **(I-24)** can yield the unique values for R_{tip} and v_{tip} under a given undercooling ΔT for a multicomponent material.

1.2.4. Microsegregation

During solidification in casting as well as in welding, the solute redistribution is an important phenomenon because the segregation of solute components can significantly affect the microstructure and properties, and even the cracks at macro scale. Segregation of solute components at scales larger than several hundred micrometers is called macrosegregation. It is mainly due to solute transport by the effect of convection in the liquid. On the other hand, the segregation depending on solute diffusion in the liquid and solid between dendrite arms within the range of 10 to 100 μm is called microsegregation [Deb95]. Microsegregation mainly defines the solidification path, which supplies the relationship between the temperature, the solute concentrations and the fraction of each phase.

For dendrite growth during welding, the solute redistribution at micro scale is considered at both the dendrite tip and in the interdendritic region, which are schematically shown in **Fig. I-11**. The solute redistribution at dendrite tip (marked by a red circle) is mainly determined by the solutal undercooling, ΔT_C, which is described in **Section 1.2.3**. Considering the solute redistribution in the interdendritic region, the growth of dendrite (secondary arms) can be approximately considered as a planar growth in a small and closed volume element with the width equal to $\lambda_2/2$ (marked by a red rectangle).

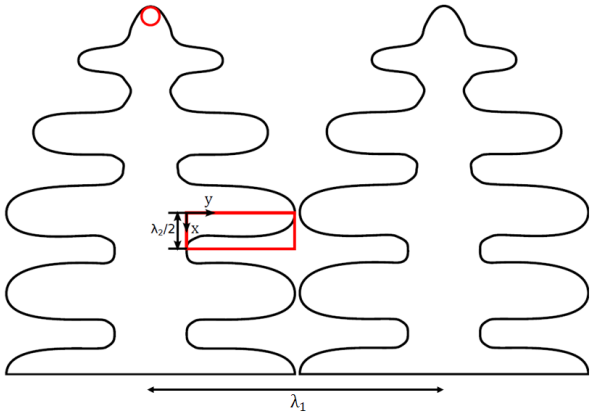

Fig. I-11 Schematic illustration of the two regions controlling microsegregation. Note λ_1 and λ_2 represent the primary and secondary arm spaces, respectively.

Several models of microsegregation could be applied in the regions mentioned above. The first one is the Lever Rule model. It assumes equilibrium solidification with complete diffusion of solute components in both liquid and solid and no tip undercooling. The second model is proposed by Gulliver [Gul13] and Scheil [Sch42]. It assumes no diffusion of solute components in solid phases, but complete diffusion in the liquid, still with no tip undercooling.

Lever Rule: The Lever Rule adopts the simplest way to model solute redistribution. Based on the assumption of complete diffusion in solid and liquid, and interface equilibrium, the concentration of solute can be read from phase diagram or computed thermodynamically.

Lever Rule model can easily give the relationship between the temperature, solute concentration of element B and the fraction of each phase. **Fig. I-12** illustrates a part of a linear phase diagram for a binary alloy system. Above the liquidus temperature, T_{liq}, it is fully liquid. When the temperature decrease to T, the liquid and solid phase coexist for this

alloy. Based on the phase diagram and the hypothesis of the model, the mass concentrations of liquid and solid change to w_B^l and w_B^s, respectively.

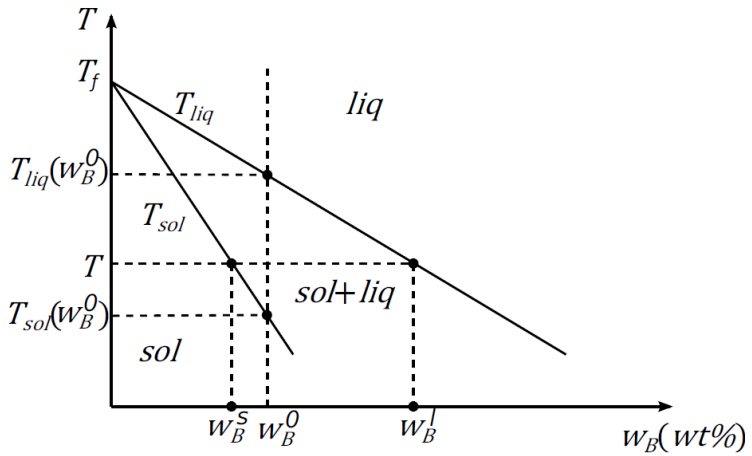

Fig. I-12 Schematic illustration of a linear phase diagram for an alloy with weight concentration $\boldsymbol{w_B^0}$, using straight lines to represent the liquidus and solidus curves.

A global mass balance can be write to deduce the mass fraction of each phase:

$$f^l = \frac{w_B^0 - w_B^s}{w_B^l - w_B^s} \quad \textbf{(I-25)}$$

$$f^s = \frac{w_B^l - w_B^0}{w_B^l - w_B^s} \quad \textbf{(I-26)}$$

In addition, because the liquidus and solidus curves are assumed to be linear, it is convenient to deduce the liquidus and solidus temperatures as:

$$T_{liq}(w_B^0) = T_f + m^l w_B^0 \quad \textbf{(I-27)}$$

$$T_{liq}(w_B^l) = T = T_f + m^l w_B^l \quad \textbf{(I-28)}$$

$$T_{sol}(w_B^s) = T = T_f + m^s w_B^s \quad \textbf{(I-29)}$$

where T_f is the melting temperature of the pure component, m^l and m^s are the slopes of the liquidus and solidus lines, respectively. In order to simplify the expressions, we can consider the constant partition coefficient k to represent the ratio for solute partitioning between solid and liquid:

$$k = \frac{w_B^s}{w_B^l} \quad \textbf{(I-30)}$$

Eq. (I-30) implies that $k < 1$ according to the phase diagram in **Fig. I-12**.

Finally, substituting **Eq. (I-27)**, **(I-28)**, **(I-29)** and **(I-30)** into **Eq. (I-25)** and **(I-26)**, the mass fraction of liquid and solid yield:

$$f^l = 1 - f^s \quad \textbf{(I-31)}$$

$$f^s = \frac{1}{1-k}\frac{T - T_{liq}(w_B^0)}{T - T_f} \quad \textbf{(I-32)}$$

According to **Eq. (I-31)** and **(I-32)**, the fraction of each phase is dependent on the temperature T. If the temperature evolution is known, the mass fraction of each phase can be explicitly computed. It provides the possibility to link the heat transfer at macro scale to the structure evolutions at micro scale.

If the density of each phase is assumed to be the same and keeps constant, the volume fraction of liquid and solid by Lever Rule model can be deduced with the same relations:

$$g^l = 1 - g^s \quad \textbf{(I-33)}$$

$$g^s = \frac{1}{1-k}\frac{T - T_{liq}(w_B^0)}{T - T_f} \quad \textbf{(I-34)}$$

Gulliver-Scheil: the Gulliver-Scheil model assumes that there is no solute diffusion in the solid phases but complete diffusion in the liquid phase. However, at the solid/liquid interface, it is still assumed that partitioning of solute obeys the phase diagram in equilibrium condition.

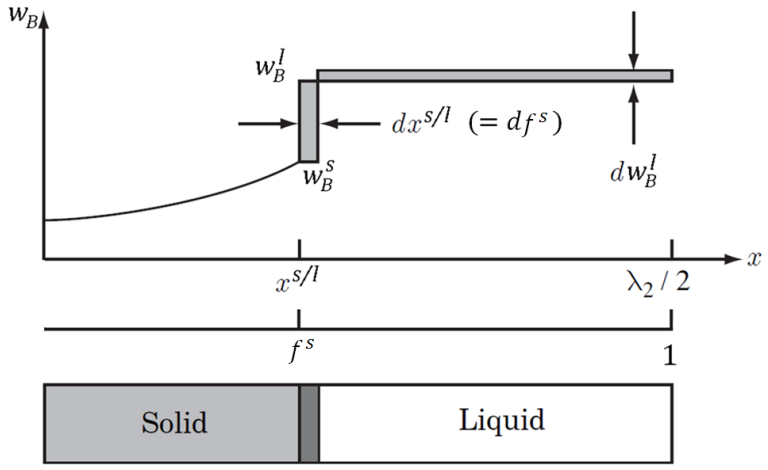

Fig. I-13 Schematic illustration of solute partitioning according to the Gulliver-Scheil microsegregation model [Dan09]

If the density of each phase is assumed to be the same and keeps constant, consider the equilibrium condition at the interface in **Fig. I-13**, and take the partition coefficient k into account to obtain

$$(1-k)w_B^l df^s = (1-f^s)dw_B^l \quad \textbf{(I-35)}$$

According to **Eq. (I-35)**, the solute rejected by the moving interface is balanced by the increase of the solute concentration in the liquid. In the absence of undercooling, the initial condition is $w_B^l = w_B^0$ and $f^l = 1$. Assuming the partition coefficient is constant, **Eq. (I-35)** rearranges to:

$$\int_1^{f^l} \frac{df^l}{f^l} = -\frac{1}{1-k}\int_{w_B^0}^{w_B^l} \frac{dw_B^l}{w_B^l} \quad \textbf{(I-36)}$$

Finally, it yields the Gulliver-Scheil equation:

$$w_B^l = w_B^0 (f^l)^{k-1} \quad \textbf{(I-37)}$$

Consider that the liquidus curve is linear with the slope m^l. Combine **Eq. (I-27)**, **(I-28)** and **(I-37)** to yield

$$f^l = \left(\frac{T-T_f}{T_{liq}(w_B^0)-T_f}\right)^{1/(k-1)} \quad \textbf{(I-38)}$$

$$f^s = 1 - f^l = 1 - \left(\frac{T-T_f}{T_{liq}(w_B^0)-T_f}\right)^{1/(k-1)} \quad \textbf{(I-39)}$$

As the density of each phase is assumed to be the same and keeps constant, the volume fraction of liquid and solid phases by Gulliver-Scheil model can be computed with the same relations:

$$g^l = \left(\frac{T-T_f}{T_{liq}(w_B^0)-T_f}\right)^{1/(k-1)} \quad \textbf{(I-40)}$$

$$g^s = 1 - g^l \quad \textbf{(I-41)}$$

1.2.5. Microstructure evolution during welding

As shown in **Fig. I-1**, the workpiece of welding is divided into three distinct regions, *i.e.* the fusion zone, the heat affected zone and the base metal. The final properties of the welded

joints significantly depend on the microstructures and properties of the fusion zone and the heat affected zone [Smi70, Dav75, Sve90, Hus96]. The structure evolution in the fusion zone is discussed hereafter.

The knowledge of solidification behavior in fusion zone during welding process can be extrapolated from that of casting process. According to the introduction of **Section 1.2.1** to **Section 1.2.4**, the structure in the fusion zone depends on the following factors during welding process [Deb95]:

- The local undercooling, ΔT
- The growth rate of the solid/liquid interface in the weld pool, $\boldsymbol{v}^{s/l}$
- The temperature gradient in the liquid at the solid/liquid interface, $G_T^{l\,s/l}$
- The alloy composition of the welding metal.

Local undercooling: local undercooling, ΔT, means how far a liquid alloy of a given composition is cooled down below its equilibrium liquidus temperature before it starts solidifying [Deb95]. Different from casting, solidification of weld pool does not face the nucleation barrier because all the grains grow from the partially melted grains from the base metal, *i.e.* epitaxial growth. Therefore, upon directional solidification, the local undercooling ΔT only adjusts to the local isotherm's velocity.

Growth rate: $\boldsymbol{v}^{s/l}$ is the rate of the solid/liquid interface. It can be used to represent the rate of solidification. In welding process, it varies considerably with the locations in the weld pool due to the different local thermal conditions. Considering a steady-state welding, in which the shape of weld pool keeps unchanged, the interface growth rate is related to the velocity and direction of the moving heat source.

As a first approximation, the growth direction in which the solidification front propagates following that of temperature gradient, the solid/liquid interface being normal to it. The growth rate is therefore related to the velocity of the moving heat source $\boldsymbol{v}^H$.

$$\left|\boldsymbol{v}^{s/l}\right| = \boldsymbol{v}^H \cdot \boldsymbol{n} = |\boldsymbol{v}^H| cos\theta \qquad \textbf{(I-42)}$$

where $\boldsymbol{n}$ is the unit direction normal to the solid/liquid interface, parallel to $\boldsymbol{v}^{s/l}$, θ is the angle between the interface normal $\boldsymbol{n}$ and the welding direction. Note this relationship is

only available in the rear part of the weld pool where solidification occurs, *i.e.* $cos\theta > 0$. It is schematically illustrated in **Fig. I-14** (a) and (b).

Eq. (I-42) shows that the velocity of the moving interface is determined by the angle θ if its position is known. Therefore, the location where the temperature gradient is along the direction of the heat source adopts the largest solidification rate. However, this relationship does not reflect the morphological anisotropy of the solid/liquid interface movement during welding process. In welding, the solid/liquid interface usually takes the morphology of dendrites due to the constitutional undercooling criterion [Fle74]. This criterion is explained in **Section 1.2.2**. During the growth with dendritic morphology, dendrites always grow along the so-called preferred growth directions (or called "easy growth" direction by Fleming [Fle74]). These preferred growth directions of different crystal structures are listed in **Tab. I-1**. For cubic metals particularly, the preferred growth direction is <100> [Dav75, Dan09, Cha10]. Consequently, for a specific dendritic growth along a general crystallographic direction $[hkl]$, its dendritic growth rate $\boldsymbol{v}^{hkl}$ is related to the growth rate of interface $\boldsymbol{v}^{s/l}$ by:

$$\left|\boldsymbol{v}^{s/l}\right| = \boldsymbol{v}^{hkl} \cdot \boldsymbol{n} = |\boldsymbol{v}^{hkl}| cos\varphi \qquad \textbf{(I-43)}$$

where φ is the angle between the interface normal $\boldsymbol{n}$ and $[hkl]$. This relationship is schematically illustrated in **Fig. I-14** (c).

Finally, combining **Eq. (I-42)** and **Eq. (I-43)**, the dendritic growth rate in steady-state is given by:

$$|\boldsymbol{v}^{hkl}| = |\boldsymbol{v}^{H}| \frac{cos\theta}{cos\varphi} \qquad \textbf{(I-44)}$$

Eq. (I-44) reveals that in the case of steady state welding process, the actual rate of grain growth $\boldsymbol{v}^{hkl}$ is related to the velocity of the moving heat source. However, in different location of the weld pool, the growth rate is different with respect to the angle θ and φ. Accordingly, the grain growth rate is high when the normal of interface is close to the direction of the moving heat source due to the small value of θ. In addition, in the steady-state case, the grain with the preferred growth direction close to the temperature gradient ($\varphi = 0$) will have smaller undercooling, resulting from its more advanced distance than

other grains [Rap93]. This relationship leads to the selection of the grains during the welding process, together with their crystallographic directions.

Tab. I-1 Preferred growth directions for dendritic growth [Kur98, Dan09, Cha10]

Crystal structure	Preferred growth direction	Examples
face-centered cubic (FCC)	<100>	Al, Cu, Ni, γ-Fe
body-centered cubic (BCC)	<100>	δ-Fe, Succinonitrile (SCN)
body-centered tetragonal (BCT)	<110>	Sn
hexagonal close-packed (HCP)	<10$\bar{1}$0>	Zn, H_2O (snow)
	<0001>	$Co_{17}Sm_2$

Temperature gradient: the temperature gradient in the liquid at the interface, $G_T^{l\,s/l}$, plays an important role on determining the morphology of the solid/liquid interface based on the constitutional undercooling criterion [Fle74]. It is difficult to evaluate $G_T^{l\,s/l}$ due to the fact that it is strongly affected by convection in the weld pool. However, it can be estimated based on computational modeling.

Alloy composition: besides the cooling conditions, the alloy composition also determines the final solidification microstructure after welding. Two basic growth morphologies of grains exist with respect to the alloy composition. These are dendritic and eutectic morphologies (Generally, a mixture of both can exist) [Kur98].

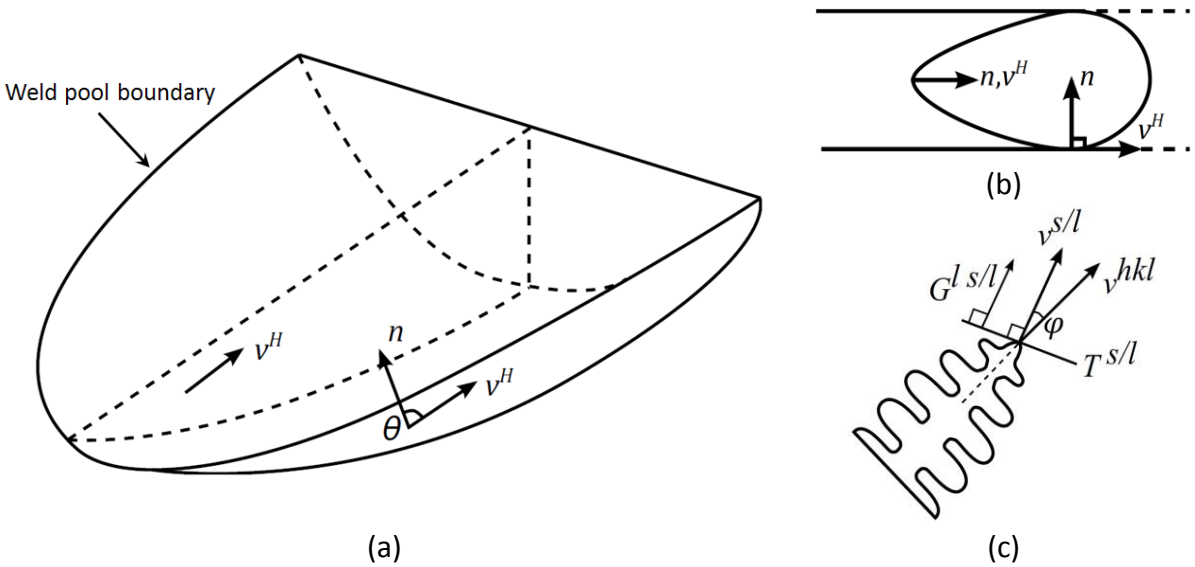

Fig. I-14 Schematic illustrations of the relationships among the heat source velocity, $\boldsymbol{v}^H$, the interface growth rate, $\boldsymbol{v}^{s/l}$, and the dendritic growth rate, $\boldsymbol{v}^{hkl}$. (a): the velocity in weld pool in 3D, (b): top view of weld pool, and (c): the relationship between $\boldsymbol{v}^{s/l}$ and $\boldsymbol{v}^{hkl}$ [Deb95].

1.3. Grain structure of welding

In this section, the solidification grain structure evolution during welding is presented. The solidification occurs in the fusion zone when the heat source moves away. Firstly, the grains grow epitaxially from the partially melted base metal. Then, the epitaxial grains compete to grow. That is to say the grains whose preferred growing directions are perpendicular to the weld pool boundary overgrow the grains whose preferred growing directions are not. Note that the heterogeneous nucleation may occur by fragmentation or intentional inoculant.

1.3.1. Epitaxial grain growth

As explained in **Section 1.2.1** during the welding process, the existing base metal at the fusion line acts as the substrate. Nucleation does not take place in this configuration. The liquid metal of the weld pool is in contact with the substrate grains. The crystals can epitaxially grow from the existing grains into the liquid. This is schematically shown in **Fig. I-15** (a). It can be seen that the crystals grow into the liquid, thus propagating in the original grain orientations.

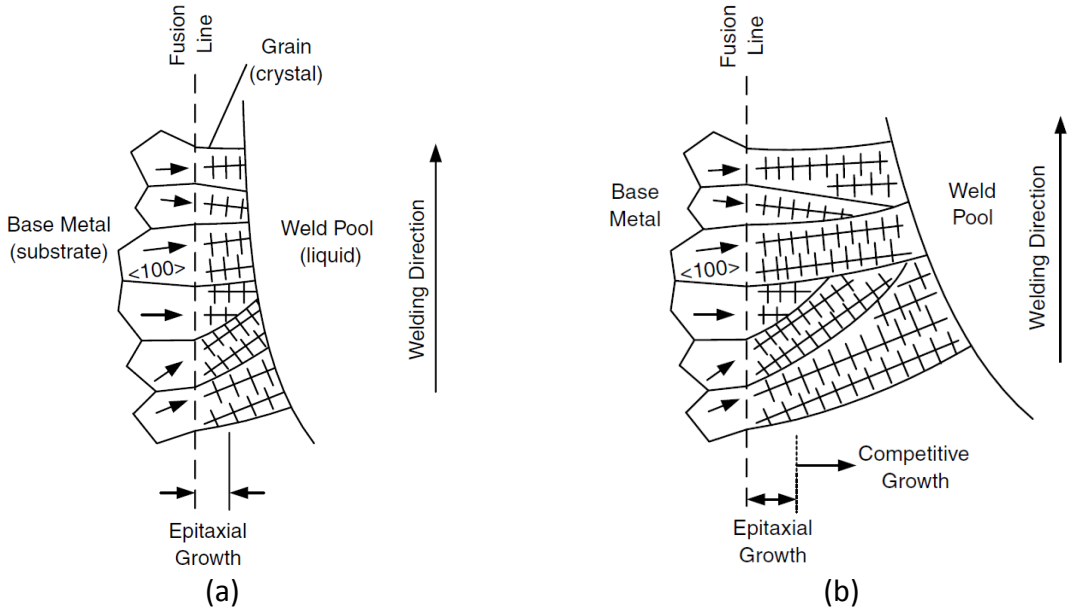

Fig. I-15 Schematic illustration of (a): epitaxial grain growth near the fusion line, and (b): grain competition in the fusion zone [Kou02].

1.3.2. Grain growth competition

The grain growth competition takes place in the fusion zone. It is schematically shown in **Fig. I-15** (b). The grains whose preferred <100> growth directions are aligned with the

temperature gradient overgrow those that are not. This mechanism was explained by Rappaz and Gandin for solidification during casting process [Rap93] as shown in **Fig. I-16**.

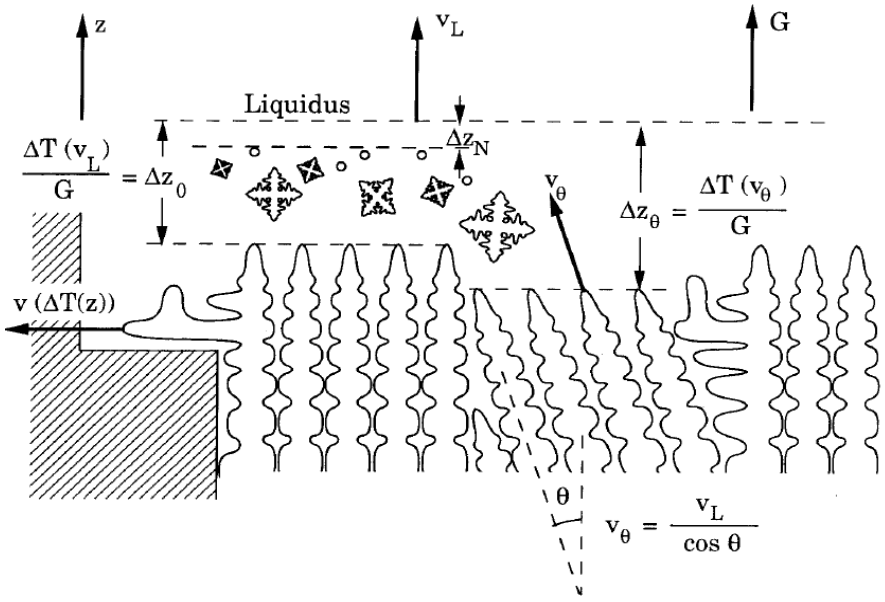

Fig. I-16 Schematic illustration of the grain growth mechanisms occurring in a dendritic alloy with a non-uniform temperature [Rap93]

The grain growth competition mechanism can be summarized as "the 'best alignment' selection criterion for dendrite grains corresponds to a minimum undercooling criterion". In the quasi-stationary situation shown in **Fig. I-16**, the left and right grains contain dendrites with <100> aligned with the temperature gradient, namely perpendicular to the liquidus isotherm (dashed line). Therefore, the two grains grow with the same velocity as that of the movement of the liquidus isotherm, v_L. For the middle grain with preferred growth direction misoriented from the temperature gradient with an angle θ, the growth velocity, v_θ, is larger than that of the liquidus isotherm to keep the projection term, $v_\theta cos\theta$, the same so as the liquidus isotherm velocity, v_L. Based on the grain growth kinetics, the undercooling at the dendrite tip of the middle grain is thus larger than that of side grains. Therefore, the middle grain is out-grown by the side grains. This out-grown situation can be achieved by two ways:

- The middle grain hit the left grain and finally cannot grow any more.
- The right grain extends to the free liquid due to the diverging between the two grain directions.

Finally, the middle grain stop growing while the other grains, which contain the more favorable growth direction, keep growing. In the columnar zone, grains compete with respect to the orientations to form the final columnar structures.

1.3.3. Nucleation inside the weld pool

Nucleation can take place inside the weld pool to form equiaxed grains. Intentional addition of particles of inoculant to the melt can enhance the heterogeneous nucleation in the weld pool. Inoculant powders (foreign particles) added in the weld pool will promote the nucleation inside the weld pool. **Fig. I-17** shows that the inoculation increases the nucleation in the welds and prevents the growth of the columnar grains in the fusion zone. This kind of refined grain structure is reported to have a significant increase for the ductility of the welds [Pet73].

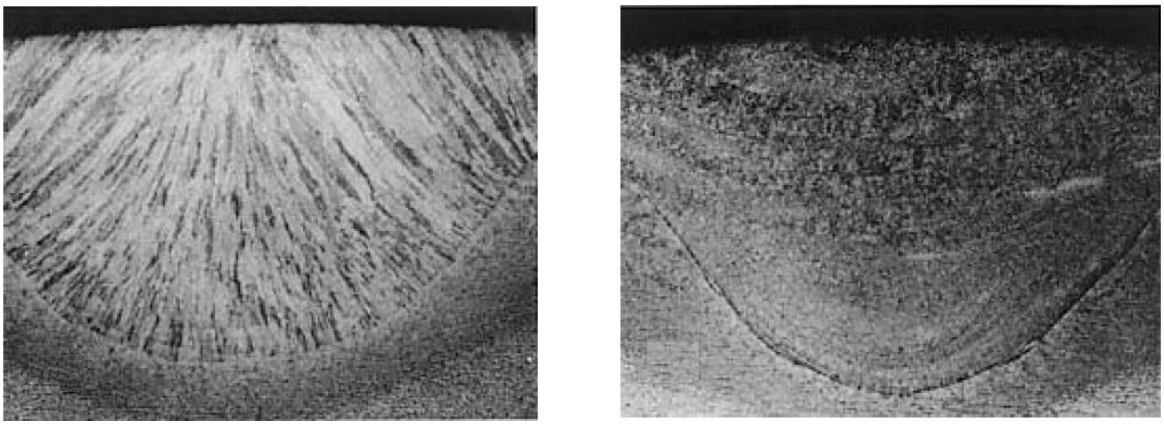

(a) (b)

Fig. I-17 Effect of inoculation on grain structure in submerged arc welding of C-Mn steel (magnification 6×), (a): without inoculation, (b): inoculation with titanium [Hei86, Kou02].

The convection in weld pool can cause the detachment of the existing dendrite arms in the weld pool (*i.e.* dendrite fragmentation). **Fig. I-18** shows the beginning of dendrite fragmentation occurring in solidification during casting. The authors pointed out that it will continue growing dendritically while it is transported away from the front of the columnar region. It could safely be conjectured that this fragment can form a new grain inside the undercooled melt. Similarly in the weld pool, if the dendrite fragments can survive the weld pool temperature, they will act as nuclei for the formation of new equiaxed grains in the weld.

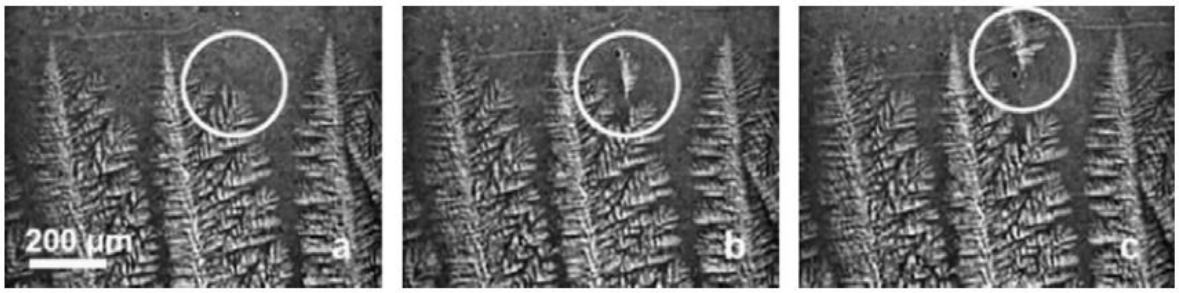

(a) (b) (c)

Fig. I-18 In situ observation of localized fragmentation during solidification of an Al-20wt.%Cu alloy at (a): t=0s, (b): t=2.25s, and (c): t=4.50s [Ruv07].

1.3.4. Grain structure during welding process

As shown in **Fig. I-2**, the final grain structure of the weld is affected by the welding speed because the columnar grains tend to grow aligned with the temperature gradient. **Fig. I-19** schematically illustrates more details of the conditions encountered in welding. It can be seen that the weld pool is approximately elliptical shape at low welding speed (**Fig. I-19** (a)) but adopt teardrop shape at high welding speed (**Fig. I-19** (c)). Since the trailing pool boundary of an elliptical weld pool in low welding speed is curved, the columnar grains therefore curve to grow perpendicular to the pool boundary, shown in **Fig. I-20** (a). On the other hand, in the case of high welding speed with a teardrop shape weld pool, the columnar grains grow perpendicular to the straight pool boundary, shown in **Fig. I-20** (b).

In addition, axial grains can also exist in the fusion zone. The axial grains grow in the direction of the welding (axial direction) and thus block the growth of the columnar grains inward the center of the fusion zone. However, the thickness of the axial grain layer differs with the welding speed. In the case of welding with elliptical weld pool in **Fig. I-19** (b), a long section of the trailing pool boundary can be perpendicular to the axial direction and induce a thick layer of axial grains. Oppositely, in the case with teardrop weld pool in **Fig. I-19** (d), a relatively small section of the trailing pool boundary has the possibility to be perpendicular to the axial direction. Consequently, a thin layer of axial grains can be seen in this case. The corresponding grain structures are shown in **Fig. I-20** (b) and (d), respectively.

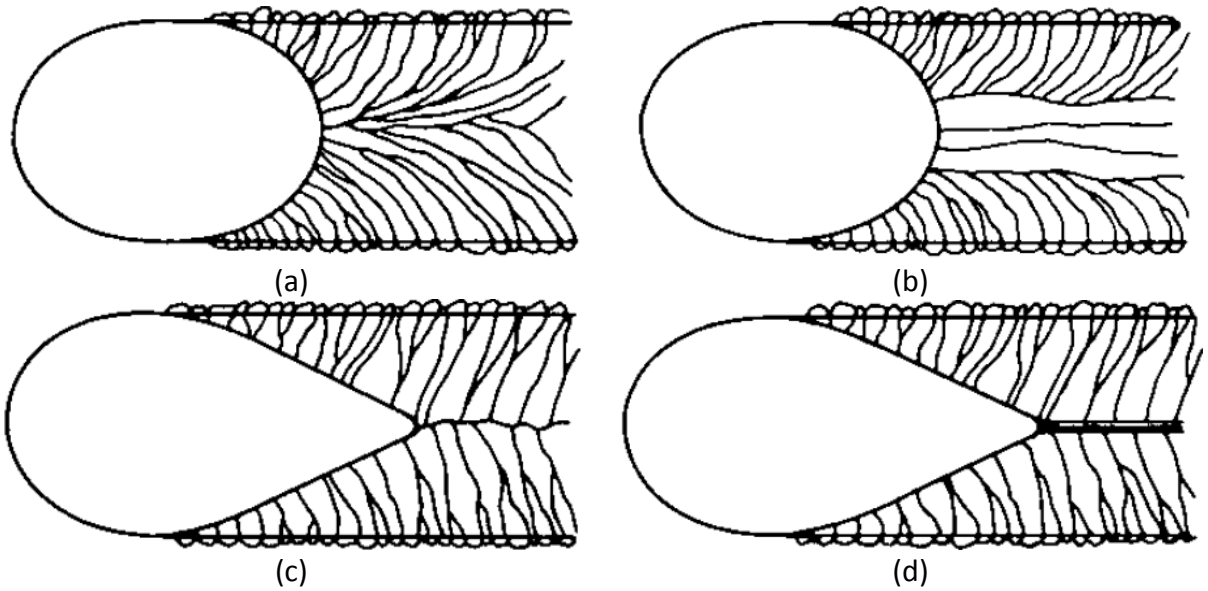

Fig. I-19 Schematic illustration of the grain structure formed in the fusion zone with the effect of welding speed. (a): regular structure at low welding speed, (b): structure with axial grains at low welding speed, (c): regular structure at high welding speed, and (d): structure with axial grains at high welding speed [Kou02]

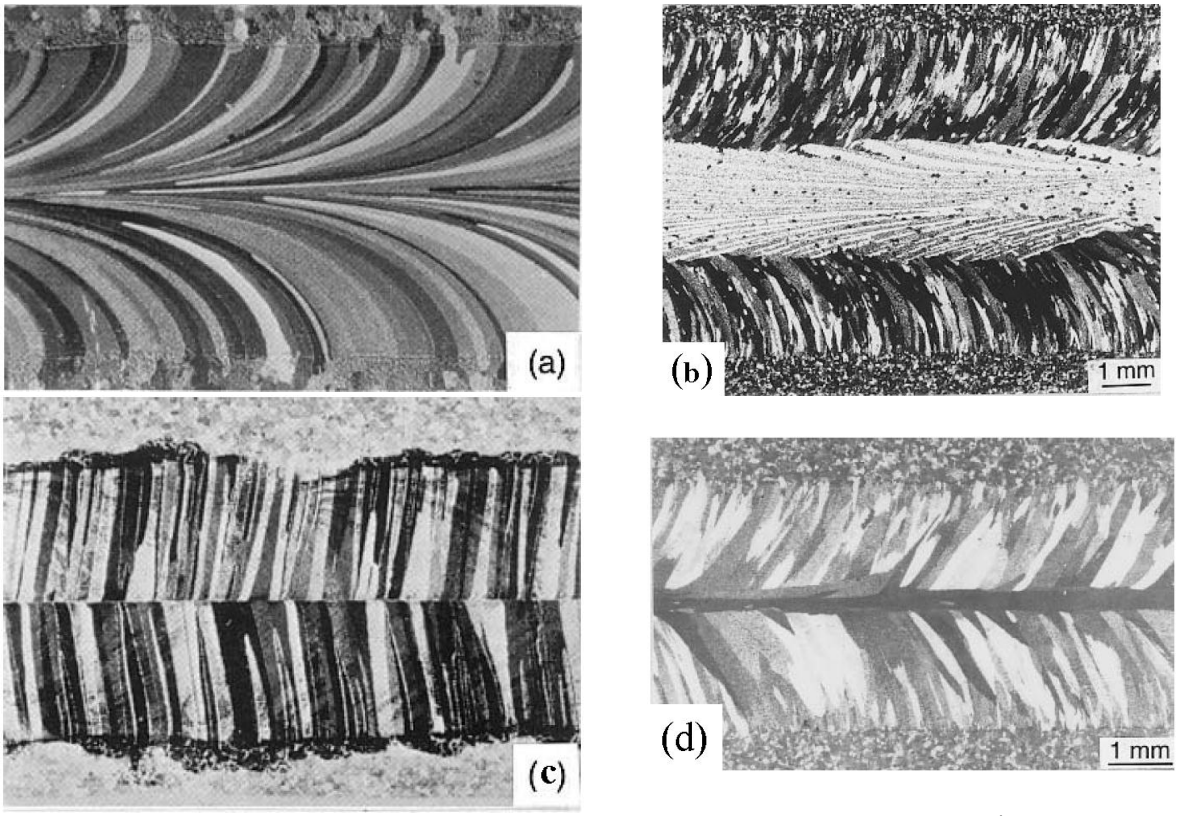

Fig. I-20 Grain structures in GTAW for (a): 99.96% aluminum at 4.17 mm s^{-1} welding speed [Ara73], (b): 5052 aluminum at 4.2 mm s^{-1} welding speed [Kou85a, Kou85b], (c): 99.96% aluminum at 16.67 mm s^{-1} welding speed [Ara73], and (d): 1100 aluminum at 12.7 mm s^{-1} welding speed [Kou02].

1.3.5. Hot cracking during welding process

Hot cracking is a defect manifesting itself as a crack during the solidification of a metallic alloy [Cic05]. It takes place during the final stage of solidification at a high solid fraction (85-99%) when the alloy is mushy. The formation of hot cracking during welding process is affected by many factors, such as the chemical composition, external tensions, welding speed, laser power, *etc* [Cic05]. It is difficult to establish a generic quantitative criterion to predict hot cracking under various conditions [Esk04]. However, detailed analysis of hot cracking in welding or casting indicates that the cracks usually do not appear within grains but along grain boundaries [Wan04], as shown in **Fig. I-21**.

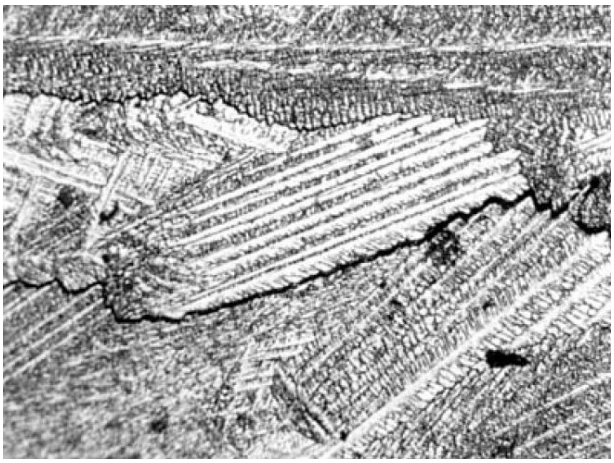

Fig. I-21 Hot cracking in an autogenous bead-on-plate weld of 7075 aluminum (magnification 140×) [Kou02]

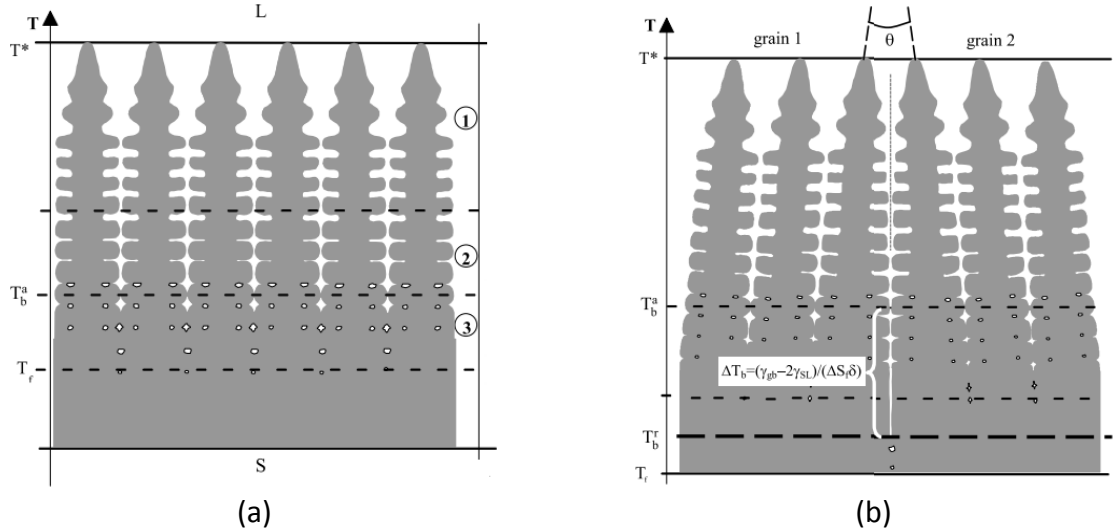

(a) (b)

Fig. I-22 Schematic illustration of the hot cracking sensitive region within the mushy zone during columnar dendritic solidification. T^*, T_b^a, T_b^r, and T_f are tip temperature, coalescence temperature of attractive grain boundary, coalescence temperature of dendritic arms at the grain boundary, and the temperature at which the solid fraction is 1, respectively. (a): single crystal, (b): bi-crystal with repulsive grain boundary. [Wan04]

Wang *et al*. [Wan04] explained this phenomenon from two aspects. The first one is based on the theoretical model proposed by Rappaz *et al*. [Rap03b], due to the different coalescence behavior of dendrites belonging to the same grain (intragranular coalescence) and of dendrites located on both sides of a grain boundary (intergranular coalescence), schematically illustrated in **Fig. I-22**. The stability of the liquid film among the grain boundaries depends on a critical coalescence undercooling, ΔT_b, which is defined for a pure material as:

$$\Delta T_b = \frac{\gamma^{gb} - \gamma^{s/l}}{\Delta S_f} \frac{1}{\delta} \quad \textbf{(I-45)}$$

where γ^{gb} is the grain boundary energy, $\gamma^{s/l}$ is the solid/liquid interfacial energy, ΔS_f is the entropy of fusion per unit volume, δ is the thickness of the diffuse interface for pure material. When ΔT_b is 0 or negative (*e.g.* the case of dendrites belonging to the same grain), the liquid film is morphologically unstable and dendrites join as soon as their interfaces reach the distance of δ, shown in **Fig. I-22** (a). In the opposite, when ΔT_b is positive, the liquid film remains stable to T_b^r, shown in **Fig. I-22** (b).

The second aspect to explain the grain boundary cracking is strain localization. As the solid is stressed during welding process, the accompanying strain is transmitted by the solid and accumulated at the regions where the liquid films exist. According to Wang *et al*., the strain localization factor at wet grain boundaries for columnar grains is 100 times higher than that inside the grain.

The experimental results show that no hot cracking happens in the single crystal case (**Fig. I-23** (a)) as well as the bi-crystal cases with $\theta \leq 12°$ (**Fig. I-23** (b) and (c)), but well developed macroscopic crack is visible in the cases of **Fig. I-23** (d) and (e) with a high value of θ ($\theta \geq 20°$) [Wan04]. The results indicate that even for alloys that are hot cracking sensitive, solidification cracks can be avoided if the grain boundary misorientation angle is small or zero. Therefore, in order to avoid hot cracking, suitable welding conditions should be chosen. The prediction of the final grain structure of the welds is significant to avoid hot cracking.

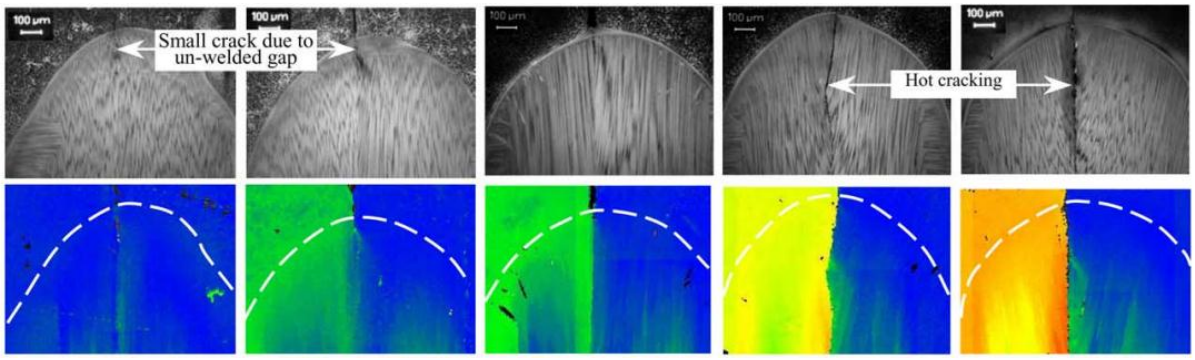

$\alpha = 0°$	$\alpha = 4°$	$\alpha = 6°$	$\alpha = 10°$	$\alpha = 12°$
$\theta = 0°$	$\theta = 8°$	$\theta = 12°$	$\theta = 20°$	$\theta = 24°$
(a)	(b)	(c)	(d)	(e)

Fig. I-23 Microstructures and corresponding EBSD maps of welded (a): single crystal, (b)-(e): bi-crystals. α is the angle between the [001] crystallographic orientation of the crystal and welding direction. $\theta = \alpha + \alpha$, representing the grain boundary misorientation angle for bi-crystals [Wan04].

Bordreuil *et al.* [Bor14] proposed a methodology to investigate hot cracking by coupling the Finite Element (FE) method and Cellular Automaton (CA) method. The thermal and mechanical fields are computed by the FE model at the process scale, while the grain structures are predicted by the CA model at a meso scale. By comparing the pressure computed on the grain boundaries to the cavitation pressure in RDG criterion [Rap99b], the crack susceptibility can be determined. This new approach successfully coupled the process simulation, microstructure generation, and fluid flow along the grain boundaries to investigate the critical location for crack onset. However, due to the limitation of the modeling on the grain structures, it was only implemented in two dimensions. Further improvements on the grain structure modeling in three dimensions can enrich this approach.

1.4. Conclusion

GTAW and GMAW are two of the most common welding techniques in the industry due to the high weld quality and high application range, respectively. The study of the weld metallurgy is important to control and optimize the welding process technique.

Based on the different thermal histories, the workpiece can be divide into three distinct regions, *i.e.* fusion zone, heat affected zone and base metal. Melting and solidification takes place in the fusion zone, while solid phase transformation happens in heat affected zone. The knowledge of solidification during the casting process can be extrapolated to apply for the solidification behavior in the fusion zone during welding process.

Different from the solidification during casting process, the solidification of the fusion zone does not face the barrier for nucleation. The grain growth mainly takes place from the partially melted grains. The grains grow along their preferred growth directions and thus result grain competition. As shown in **Fig. I-2**, **Fig. I-19**, and **Fig. I-20** the final grain structure is significantly affected by the temperature gradient caused by the moving heat source.

Hot cracking is one of the common defects in welding. Its formation is affected by many factors. Experimental results show that it happens along the grain boundary, depending on the misorientation angle. Consequently, it is important to control the final grain structure by adopting the appropriate welding process conditions to avoid the hot cracking. Therefore, numerical prediction of the final grain structure of welds becomes significant for the welding industry.

1.5. French summary

Le **chapitre I** présente les théories fondamentales relatives aux processus de soudage par fusion. Dans un premier temps, le soudage TIG et le soudage MIG, les plus utilisées dans l'industrie, sont décrits, à travers leurs caractéristiques propres. Le procédé TIG présentent des qualités de soudage plus élevés, mais est restreint à certaines utilisations spécifiques, pour un coût de revient plus important. Le procédé MIG, sans égaler les qualités du soudage TIG, et ses possibilités de contrôle, présente une rentabilité plus importante, et un vaste domaine d'application. L'étude de l'évolution métallurgique au sein du cordon de soudure est nécessaire afin de contrôler et d'optimiser les techniques de soudage. Ainsi, et dans un second temps, les théories concernant l'évolution microstructurale des alliages métalliques au cours de la solidification sont présentées. Une attention particulière est portée à la croissance dendritique, et aux processus de microségrégation. Enfin, un état de l'art des structures granulaires observées dans les zones soudées est proposé. permettant une discussion de la formation des structures des grains au cours du soudage, et de l'influence des paramètres procédés. La fissuration à chaud est un des défauts les plus courants observés lors du soudage. Pour cette raison, l'influence de la structure des grains sur l'apparition de ce phénomène est discutée en dernier point, en lien avec l'évolution des structures de grains formées.

Chapter II Simulation models for structure

The simulation of the structure evolution in the fusion zone can be extrapolated from that of solidification in casting. Over recent years, models of solidification in two different interested scales have emerged [Boe00]: (1) modeling of microstructure formation, such as front tracking method and phase field method, *etc*.; (2) modeling of grain structure formation, such as finite element - cellular automaton (CAFE) method.

This chapter will present some numerical methods for the simulation of the structure evolution of solidification at the two scales. It will be found the models corresponding to the microstructure development in **Section 2.1** before the presentation of the grain structure modeling in **Section 2.2**.

2.1. Microstructure modeling

2.1.1. Front tracking method

Developed by Juric and Tryggvason and their coworkers [Jur96, Try01], the front tracking method can easily handle discontinuous material properties between the liquid and solid phases, topology changes and anisotropy of interfacial energy and kinetics. It explicitly provides the location of the solid/liquid interface at all times. The Gibbs-Thomson condition on the interface temperature is also explicitly satisfied. In this method, the interface solution is directly controlled by the undercooling, surface tension, kinetic mobility, thermal conductivity and volumetric heat capacity of the liquid and solid phase. It is not necessary to define any nonphysical simulation parameters. According to Juric *et al.* [Jur96], ignoring volume contraction and expansion as well as fluid convection, the energy conservation equation can be written as:

$$\frac{\partial(C_p T)}{\partial t} = \nabla \cdot (\kappa \nabla T) + Q \qquad \textbf{(II-1)}$$

where C_p is the volumetric heat capacity, κ is the thermal conductivity, Q is an energy source term which accounts for the liberation or absorption of latent heat at the solid/liquid interface with the expression:

$$Q = \int_f q\delta(\boldsymbol{x} - \boldsymbol{x_f})dS \qquad \textbf{(II-2)}$$

where $\delta(\boldsymbol{x} - \boldsymbol{x_f})$ is a three-dimensional delta function that is non-zero only at the solid/liquid interface where $\boldsymbol{x} = \boldsymbol{x_f}$. Therefore, the heat source Q localizes at the solid/liquid

interface. q is the interface heat source related to the latent heat liberation/absorption (assuming that the heat capacity is equal in both liquid and solid):

$$q = Lv(\boldsymbol{n}) \tag{II-3}$$

where L is the volumetric latent heat, $v(\boldsymbol{n})$ is the component of the velocity normal to the interface. In addition, the Gibbs-Thomson temperature condition should be satisfied at the interface for the pure metal:

$$T^{s/l} = T_f - \frac{\gamma(\boldsymbol{n})T_f}{L}K - \frac{v(\boldsymbol{n})}{\mu(\boldsymbol{n})} \tag{II-4}$$

where $T^{s/l}$ is the temperature at the interface, T_f is the equilibrium melting temperature, $\gamma(\boldsymbol{n})$ is the anisotropy surface tension as a function of the local surface normal orientation, K is twice the mean interface curvature and $\mu(\boldsymbol{n})$ accounts for the effect of the anisotropy kinetic mobility. The set of **Eq. (II-1)**, **(II-2)**, **(II-3)**, and **(II-4)** compose the mathematical formation of the solidification problem which the authors solved [Jur96]. **Fig. II-1** presents the result of dendritic solidification. The time evolving interfaces from an initial perturbed circle with four lobes are plotted at non-dimensional time increments of 0.03. It shows that the four initial protrusions grow and become wider and then split, which reflects the growth of a dendrite.

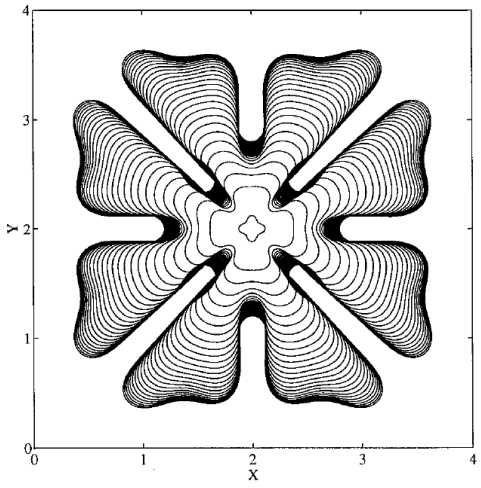

Fig. II-1 Simulated result of dendritic solidification in an insulated cavity by front tracking method in 2D. The final interface plotted for the 400×400 mesh contains 2542 points at time 0.81. All the parameters used in this simulation are presented in [Jur96].

In order to enrich this method with more physical consideration, N. Al-Rawahi *et al.*[Al-R02, Al-R04] improved it to predict the dendrite geometry with the presence of liquid convection

in 2D and later in 3D. The simulated results show that the fluid flow increases the rate of arm growth into the flow and promote more side branching on the upstream side. Because of the physical description of this method, it can be used to provide the results for comparisons with other models, such as the phase field and cellular automaton method [Zhu07].

2.1.2. Phase field method

Phase field method is one of the widely used numerical methods to simulate the evolution of microstructure [Cag86, Cag89, Whe93, War95, Che02, Gra04]. In order to calculate the diffusion and convection process in both the liquid and solid phases considering the complex shapes of the solid/liquid interface, a scalar variable, *i.e.* phase field variable, ϕ, is employed. This variable, ϕ, which is a function of position and time with the range [0,1], is used to describe whether a specific location of the material belongs to the liquid or solid. For instance, the location of material belongs to liquid when $\phi = 0$ while it belongs to solid when $\phi = 1$. It belongs to the solid/liquid interface if $\phi \in (0,1)$. Note that the value of ϕ for each phase depends on the definition of the authors [Boe02, Che02]. Finally, the material can be described by ϕ continuously. Compared to the front tracking method, this continuous description avoids the mathematical difficulties of applying the boundary condition at the interface which is part of the unknown solution.

The principal of the phase field method is to reduce the total free energy, E, over the system, Ω, with respect to time. E is defined as [Boe02]:

$$E = \int_{\Omega} \left[e(\phi, c, T) + \frac{\varepsilon_c^2}{2} |\nabla c|^2 + \frac{\varepsilon_\phi^2}{2} |\nabla \phi|^2 \right] d\Omega \qquad \textbf{(II-5)}$$

where $e(\phi, c, T)$ is the free energy density which depends on the temperature, T, the concentration, c, and the phase field variable, ϕ. ε_ϕ and ε_c are the gradient energy coefficient related to phase field and concentration, respectively.

The behavior of ϕ is governed by an equation which is coupled to equations for heat and solute transport. It is proposed by Allen-Cahn and Cahn-Hilliard [Boe02, Che02]:

$$\frac{\partial \phi}{\partial t} = -M_\phi \left[\frac{\partial e}{\partial \phi} - \varepsilon_\phi^2 \nabla^2 \phi \right] \qquad \textbf{(II-6)}$$

$$\frac{\partial c}{\partial t} = \nabla \cdot \left[M_c c(1-c) \nabla \left(\frac{\partial e}{\partial c} - \varepsilon_c^2 \nabla^2 c \right) \right] \qquad \textbf{(II-7)}$$

where M_ϕ and M_c are the positive mobilities related to the interface kinetic coefficient and solute diffusion coefficient, respectively. **Eq. (II-6)** and **(II-7)** are coupled through the free energy density function $e(\phi, c, T)$. The definition of this function determines the final solution of the phase field. In the simple case for a pure material with two phases, the solution of **Eq. (II-6)** is consistent with the Gibbs-Thomson effect. **Fig. II-2** presents a phase field simulation of free dendritic growth in 3D at low undercooling condition.

Fig. II-2 Snapshot of a simulated result of dendritic solidification by phase field method in 3D. The dimensionless undercooling is 0.1, and the surface tension anisotropy is 0.025. This simulation is performed on regular lattices of size 240×240×800. All the parameters used in this simulation are presented in [Kar00].

Moreover, Beckermann *et al.* [Bec99, Lu05] proposed a new phase field model to simulate the microstructure evolution in solidification processes involving convection in the liquid phase. Some other researchers [Ste96, Eik06] extended the phase field method to simulate the multiphase problems.

2.1.3. Modified cellular automaton model

In the 1990s, the cellular automaton models were firstly used by Rappaz and Gandin [Rap93] to simulate the grain structure evolution of solidification process at meso scale to track the boundary of the mushy zone (*i.e.* the mixture of the liquid and solid phases). This model is traditionally called CAFE model, which will be introduced in **Section 2.2.3**. However, in order to describe more detailed feature such as the side branching of the dendrites, Dilthey and Pavlyk [Dil97, Dil98] proposed a modified cellular automaton (MCA) model in which the local velocity of the cell depends on the local temperature and composition. This model was successfully applied to simulate the dendritic feature formed in fusion zone during welding.

Therefore, the CA method was extended from meso scale to micro scale. In order to distinguish from the CAFE model in **Section 2.2.3**, this modified CA model can be considered as the CA model in microscale to describe the dendritic structure evolution.

Nastac *et al*. [Nas97, Nas99] then further extended this model to include the time-dependent calculation for temperature and solute distribution in the liquid and solid phases, curvature and growth anisotropy. According to the authors, this model is able to simulate not only morphological evolution (including the coarsening and growth/branching of both the secondary and tertiary dendrite arms), segregation patterns at micro scale but also the columnar-to-equiaxed transition (CET) at macro scale for casting alloys. Nevertheless, this model does not identify the influence of crystallographic orientation on the selection of grain growth since it does not consider the preferred growth direction of the grains.

To solve the above problem, Zhu *et al.* [Zhu01a, Zhu01b, Zhu02, Zhu07] proposed a new modified CA model first in 2D and then in 3D. This model adopts the same schemes which have been used in the CAFE model (see **Section 2.2.3**), such as heterogeneous nucleation, preferred growth direction of the grain and growth kinetics of dendrite tip. The main difference from the classical CAFE model is that it considers the solute diffusion locally in both liquid and solid domain:

$$\frac{\partial w^l}{\partial t} = D^l \cdot \nabla^2 w^l + w^l(1-k)\frac{\partial f_{sol}}{\partial t} \quad \textbf{(II-8)}$$

$$\frac{\partial w^s}{\partial t} = D^s \cdot \nabla^2 w^s \quad \textbf{(II-9)}$$

where w^l and w^s are the solute composition in the liquid and solid phases, respectively, D^l and D^s are the solute diffusion coefficient in the liquid and solid phases, respectively, k is the solute partition coefficient, and f_{sol} is the solid fraction, which is computed by the CA model based on the KGT model [Kur86].

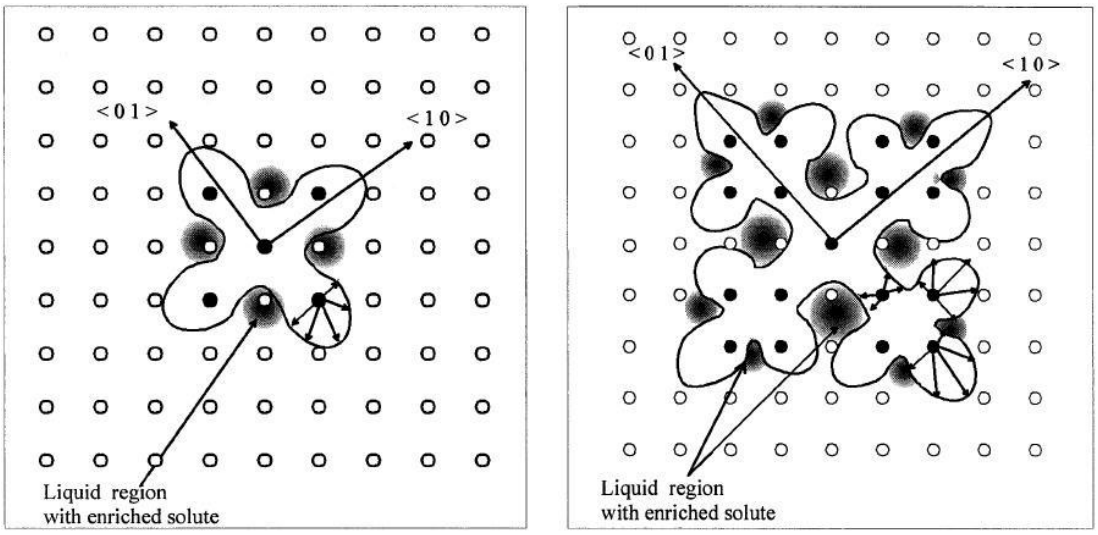

(a) (b)

Fig. II-3 Schematic 2D illustration of (a): the growth and coarsening of primary trunk , and (b): the side branching [Zhu01a]

According to Zhu *et al*. [Zhu01a] illustrated in **Fig. II-3** (a), when the cell with the initial state of liquid solidifies, the solute is rejected to the liquid near the solid/liquid interface due to the solute distribution. Therefore, the interface instability occurs and side branching leads to the formation of the secondary arms, as shown in **Fig. II-3** (b).

Many other researchers such as Wang *et al*. [Wan03], Krane *et al*. [Kra09], Yin *et al*. [Yin11] and Choudhury *et al*. [Cho12] improved this model to simulate the dendritic growth in either equiaxed or columnar morphologies. The latter two authors compared the results by CA with that by phase field to reach quantitative conclusions. **Fig. II-4** (a) shows the 2D dendritic structure for a nickel-based alloy in directional solidification under a temperature of 12 K/mm and a solidification rate of 150 μm/s predicted by Wang *et al*. with a modified CAFD model. **Fig. II-4** (b) is the 3D equiaxed dendrite for an Al-4wt%Cu alloy with the undercooling of 3.81 K predicted by Choudhury *et al*. with modified CA model.

Moreover, some researchers extended this model to directly predict the dendritic growth of grains during welding process. Pavlyk *et al.* [Pav04] simulated the dendritic grain growth under constrained solidification conditions typical for weld pool solidification. The temperature gradient and the solidification velocity in the weld pool were provided by a solution of the heat flow using the Finite Difference Method (FDM). Zhan *et al.* [Zha08, Zha09] developed the morphological evolution of columnar dendrites in the weld pool. The constitutional and curvature undercooling were considered in the computation of the solid-

liquid interface velocity and provided by the FDM. Tan *et al.*[Tan12] proposed a novel model that coupled CA and phase field to simulate the dendritic grain growth. The epitaxial growth was identified by defining both the grain density and dendrite arm density at the fusion line.

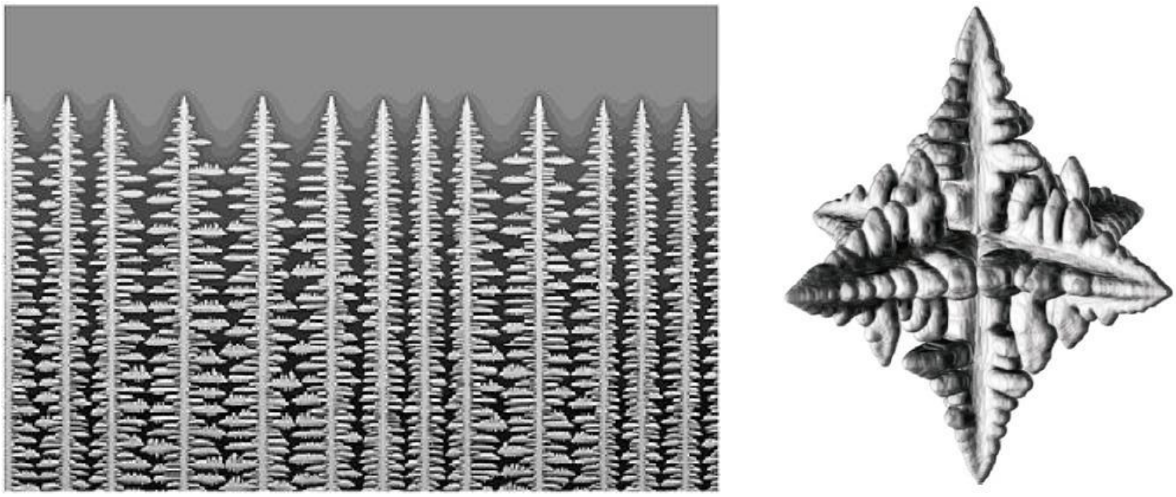

(a) (b)

Fig. II-4 Prediction of (a): dendritic structure in directional solidification process by modified CA model for a nickel-based alloy in 2D [Wan03], and (b): equiaxed dendrites by modified CA model for an Al-4wt%Cu alloy in 3D [Cho12]

2.2. Grain structure modeling

2.2.1. Mushy zone tracking method

A new 2D front tracking method is initially proposed by Browne and Hunt to model the structure evolution at engineering length scales for pure metal [Bro04]. Unlike the traditional front tracking method (see **Section 2.1.1**) which tracks the solid/liquid interface, this method tracks the boundaries between the liquid and a zone of partial solid (*i.e.* mushy zone) which is expanding across the fixed grid domain, schematically shown in **Fig. II-5** (b). In order to distinguish from the traditional front tracking method described in **Section 2.1.1**, this new front tracking method is named mushy zone tracking method in the present work.

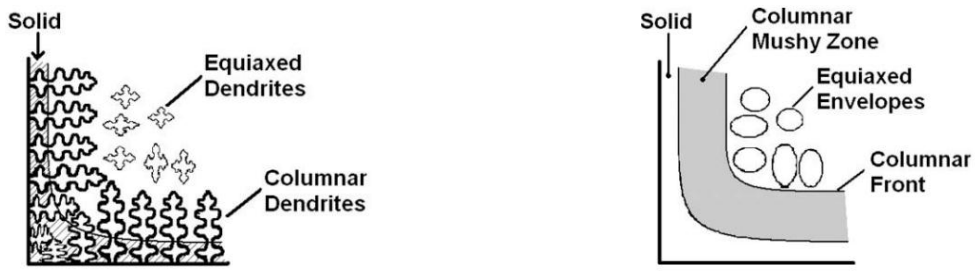

(a) (b)

Fig. II-5 Schematic illustration of (a): dendritic growth and (b): mushy zone tracking representation [McF09].

If the predefined nucleation takes place in the simulated domain, this model then treats the advance of the interface of the mushy structure and liquid. Note that the mushy structure of the columnar zone consists of an array of elongated grains, but the mushy structure of the equiaxed grains are individual crystals. The increase of the mushy area accounts for latent heat release, which corresponds to the energy source term in the energy conservation equation. The interface is defined at discrete points by massless marker particles (*i.e.* markers). The advance of the markers into the liquid, based on the kinetics of dendrite tip, updates the interface between mushy structure and liquid, schematically illustrated in **Fig. II-6**. According to Browne and Hunt, this method is available to track the appearance and progress of a front of columnar dendrites, or an equiaxed grain separately in a freezing liquid, in 2D.

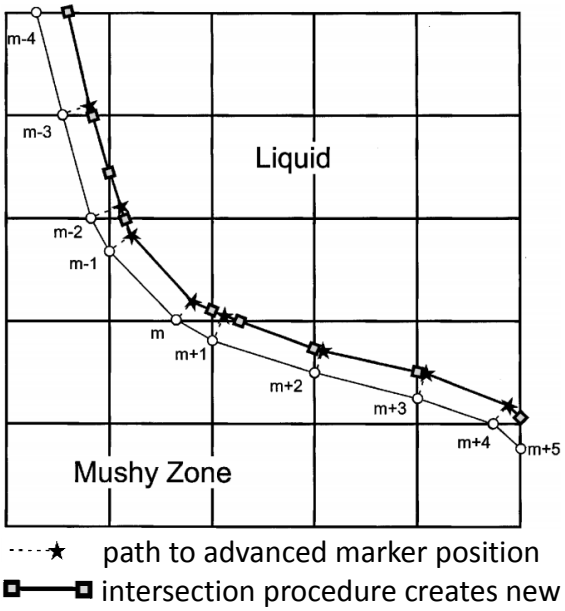

Fig. II-6 Schematic illustration of the intersection procedure to find updated marker positions, which represents the interface of the mushy structure and liquid for the columnar grains zone [Bro04].

McFadden *et al.* [McF09] later extended this method to reflect the CET during the casting for alloys. The impingements between the grains (precisely, between two envelopes of the equiaxed grains, and between the envelope of the equiaxed grain and the boundary of the columnar zone) are modeled. Finally, this method has the capability to predict the as-cast macrostructure, shown in **Fig. II-7**. However, it can be seen that no grain growth competition mechanism is reflected in this method, because all the crystallographic details for the individual dendrites are ignored.

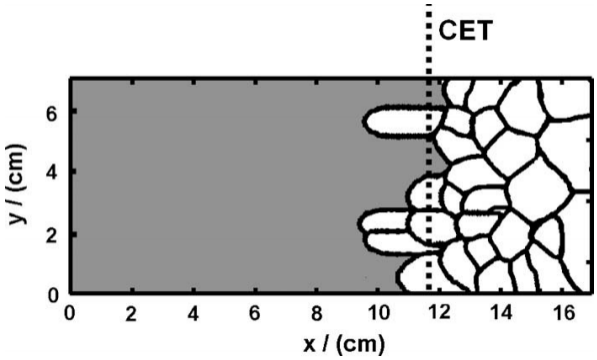

Fig. II-7 Predicted macrostructure for Al-7 wt%Si of directional solidification by mushy zone front tracking method. The columnar zone is represented in grey color, and the equiaxed envelopes are represented in white color. The dashed line indicates the CET position [McF09].

2.2.2. Envelope phase field model

In order to model the equiaxed dendritic solidification on a mesoscopic scale for the pure metal, a new method, *i.e.* envelope phase field model (note that this name is used to distinguish the traditional phase field method in **Section 2.1.2**) is initially proposed by Steinbach *et al.* [Ste99, Ste05]. In this model, a grain envelope is defined as a smooth surface connecting the dendrite tips and the growing branches, shown in **Fig. II-8**. The micro-temperature field on the scale of the tip radius and the macro-temperature field outside the envelope are matched over the stagnant film, which is bounded by a confocal envelope. The thickness of the stagnant film is δ_f. A phase field variable, $\phi \in [0,1]$, is used to describe whether a specific location belongs to the melt ($\phi = 0$) or the grain ($\phi = 1$). The authors take the stagnant film as the transition zone. Finally, the growth of the grain envelope reduces to be the propagation of ϕ.

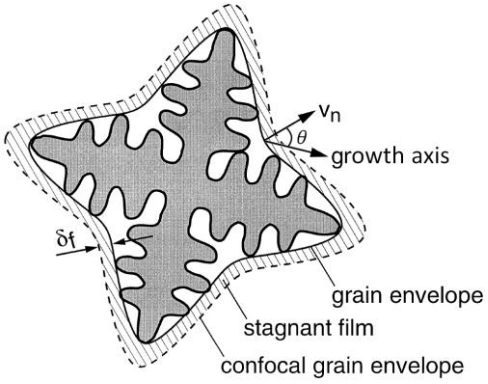

Fig. II-8 Schematic illustration of the grain envelope, the stagnant film, and the confocal envelope, defined in the envelope phase field model [Ste99].

The evolution of the phase field variable, ϕ, is determined by the normal velocity of the envelop, $\boldsymbol{v_n}$, which is defined as:

$$\boldsymbol{v_n} = v_{tip}\boldsymbol{n} \cdot cos\theta \qquad \textbf{(II-10)}$$

where v_{tip} is the dendrite tip velocity, which is a function of the confocal envelope temperature and the film thickness, $\boldsymbol{n}$ is the exterior normal vector to the envelop, and θ is the angle between the normal and the growth axis of the nearest dendrite tip, shown in **Fig. II-8**.

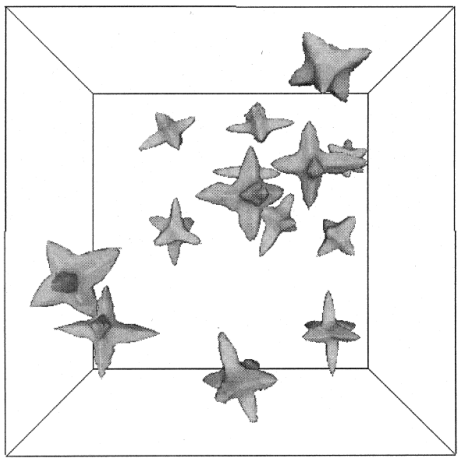

Fig. II-9 Predicted envelop shapes of 14 equiaxed dendritic grains. All thermophysical properties are those of succinonitrile (SCN) [Ste99].

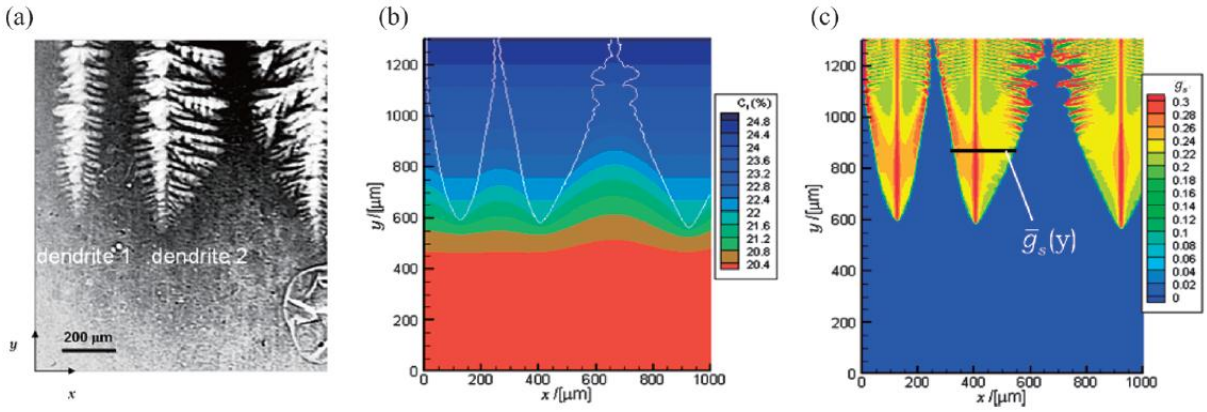

Fig. II-10 Results for directional solidification of an Al-20 wt% Cu alloy with G = -18 K mm^{-1}, and $\boldsymbol{v_n}$= 10.5 μm s^{-1}. (a): radiographic image from the experiment, (b): predicted grain envelopes and liquid solute concentration field, and (c): predicted solid fraction field [Del10].

This model is used to simulate the growth of equiaxed dendrites for pure substance, shown in **Fig. II-9**. Delaleau *et al.* [Del10] later extended it for the simulations of directional solidification of binary alloys in 2D. Good agreements between the measured and predicted

results are found, shown in **Fig. II-10**. However, the simulated domain is limited in 1 mm^2. Therefore, it is difficult to predict the grain structure in as-casting scale.

2.2.3. CAFE model

Initially proposed by Rappaz and Gandin [Rap93], the CAFE model is used to track the boundary of the growing grains with the liquid phase during casting. The internal structure of the dendritic grains is not modeled. This model is able to simulate the grain structure evolution of solidification at the industrial scale.

Based on the work of Hesselbarth and Göbel [Hes91], who modeled recrystallization, Rappaz and Gandin [Rap93] pointed out that a cellular automaton method for solidification obeys the following rules:

First, the space is divided into cells of equal size, usually squares or hexagons in two dimensions, cubes in three dimensions, arranged on a regular lattice. The regular lattice of cells is laid into the space referred to the simulation domain. Each cell is denoted by a unique index ν to identify itself.

Second, the neighborhood of each cell is defined. For a given cell ν, its neighborhood is predefined linked to the connection relationship. The definition of the neighborhood is adapted to the model of different kinds of behaviors. The neighborhood of the first nearest cells (4 cells in 2D, 6 cells in 3D) is called "Von Neumann neighborhood", referred to **Fig. II-11** (a). On the other hand, the neighborhood of first and second nearest cells in 2D (8 cells), and first, second and third nearest cells in 3D (26 cells) is called the "Moore neighborhood", referred to **Fig. II-11** (b) [Mit98].

(a) (b)

Fig. II-11 Schematic illustration in 2D for (a): the Von Neumann neighborhood, and (b): the Moore neighborhood. In both case, the cell ν itself is shaded by red color [Mit98]

Third, each cell is characterized by different variables (*e.g.* temperature, crystallographic orientation) and states (*e.g.* liquid, solid). Depending on the simulation behavior, different variables and states could be imposed to the cell.

Finally, the rules of transition (*e.g.* transformation from liquid cell to solid cell) are defined. The rules of transition determine the evolution of the state of a given cell during one time step. Two kinds of rules can be adopted. The first is based on the variables of the cell itself, such as the temperature, fraction of phase, *etc*. The second is based on the states of the neighboring cells. The CA model can adopt one or the both rules, depending on the physical behavior that it simulates.

The CA model for solidification can be established based on the four rules above. Schematically shown in **Fig. II-12** (a), two equiaxed grains and one columnar grain (composed of two dendrites) exist in the melt at a given time during solidification. The objective of the CAFE model is to change the cell states to represent the existing grains and to simulate grain growth. This is shown in **Fig. II-12** (b). Each grain is represented by a set of cells with the same states, that is to say the three grains are represented by green, blue and red colors, respectively. The cells with white color represent the remaining melt.

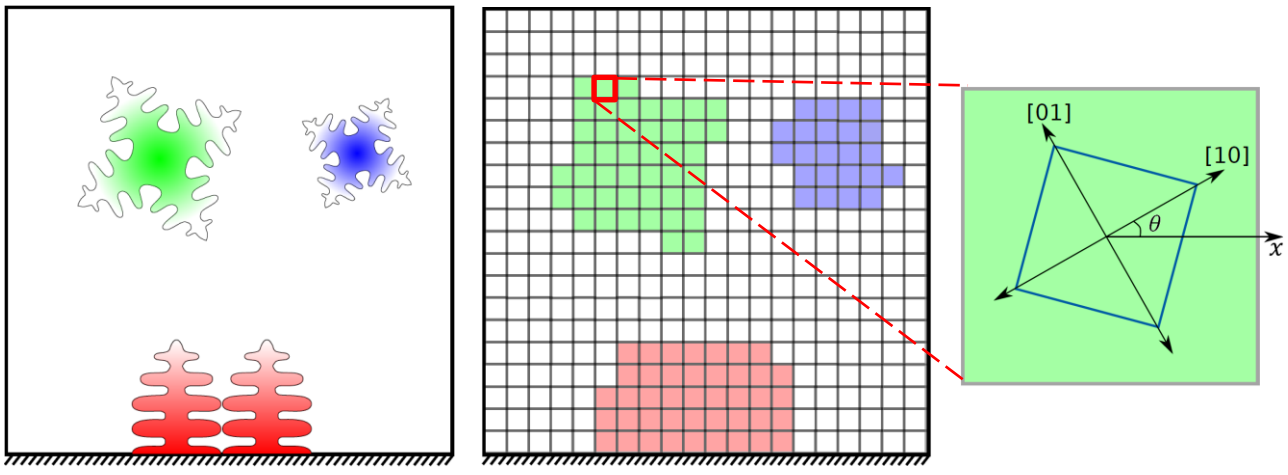

Fig. II-12 Schematic 2D illustration of (a): the dendritic grains in the melt, (b): the CA representation, and (c): the square envelop inside a cell.

Consider the set of cells colored in green which represent the grain in the top left of **Fig. II-12** (b). Each cell contains the crystallographic information of this grain, *i.e.* the angle, θ, defined in **Fig. II-12** (c), between the [10] preferred growth direction and the x axis of reference. The overall grain information is simplified to a square (in 2D) or octahedron (in

3D) with the main diagonals corresponding to the crystallographic directions of the grains (<10> in 2D, <100> in 3D) linked to the cell, shown in **Fig. II-12** (c). This square (or octahedron) can grow based on the dendrite tip growth kinetics (*e.g.* KGT model [Kur86]) to capture its neighborhood. If the neighboring cell is captured, *i.e.* the square shape in **Fig. II-12** (c) encompass a liquid cell, the state of this liquid cell is changed to correspond to the capturing cell.

In the CAFE model for solidification during casting process, the nucleation and grain growth are considered. However, there is no difference for the growth process between grains nucleated close to a mold wall or those nucleated in the bulk liquid. Since the growth of each cell is independent from each other, the grains becoming columnar or equiaxed only depend on the local temperature gradient, dendrite growth velocity and material properties.

Heterogeneous nucleation: as presented in **Section 1.2.1**, heterogeneous nucleation takes place when the liquid material is undercooled to a specific degree. The surface nucleation and bulk nucleation are included in the CAFE model for the casting process. A continuous nucleation distribution is used to describe the grain density increase:

$$N(\Delta T) = \int_0^{\Delta T} \frac{dN}{d(\Delta T')} d(\Delta T') \qquad \textbf{(II-11)}$$

Rappaz and Gandin [Rap93, Gan94] adopted a Gaussian function to describe both of the nucleation types. The characteristics of these two distributions are mean undercooling, ΔT_{max} , standard deviation, ΔT_{σ} , and the total density of grains, N.

In the CAFE model, the locations of the nucleation events are randomly chosen among all the CA cells. In addition, the crystallographic direction of each nucleus is also randomly selected based on a set of orientation classes.

Grain growth: the grain starts to grow after nucleation either on the surface or in the bulk of melt. Note that here the grain growth process refers to the formation of grains from the undercooled liquid, thus it contains phase transformation. Compared to the generation of random nucleation sites locations and crystallographic directions, the treatment of grain growth is much more difficult. This is because the configuration of the CA lattice has a direct influence upon the simulated results of the microstructure [Rap93]. In the CAFE model, the

final structure should maintain the crystallographic information from the nucleated grain. Therefore, the problem to eliminate the anisotropy influence of the CA lattice reduces to the algorithms of capture of neighborhood by a specific cell.

In order to solve this problem, Gandin and Rappaz proposed three methods for the capturing algorithms, namely “dendrite tip correction” [Rap93], “rectangle growth” [Gan94, Gan96], and “decentered square” [Gan97, Gan99]. However, the first algorithm cannot be extended to non-uniform temperature situations, whereas the second one is difficult to extend to 3D. In the third algorithm, a new envelop is created for the captured cell, making sure that one of the apices coincide to the closest apex of the capturing envelope. So the new envelop is decentered from its “cell center” so as to overcome the influence of anisotropy of the CA lattice.

The cellular automaton model is then coupled with the finite element method (CAFE model) in both weak scheme and full scheme [Gan99].

For the weak coupling scheme [Gan99]:

- The temperature of the FE nodes is computed by the energy conservation equation in the FE domain;
- The temperature of a cell is linearly interpolated from the nodes of FE element to which it belongs at each time step. The undercooling of each cell can be calculated.
- The structure evolution is therefore computed based on the dendrite tip growth kinetics which is a function of the local undercooling of each cell, *e.g.* KGT model [Kur86].

This weak coupling scheme between FE and CA does compute the solidification path at each FE node using a given microsegregation model. No undercooling of the growth front is used to release the latent heat. Therefore, a fully coupling scheme is proposed by authors, later improved and validated by Guillemot *et al.* [Gui04]:

- The enthalpy of the FE nodes is computed by the energy conservation equation in the FE domain;
- The enthalpy of each cell is interpolated from the nodes of the corresponding FE element;

- The cell enthalpy is converted to a local temperature and internal volume fraction of solid, considering the fraction of the envelop computed by the CA method;
- The computed temperature and fraction of solid (the multiplication of internal volume fraction of solid and the fraction of envelop) are interpolated to the FE nodes.

This full coupling scheme takes into account the influence of the microstructure evolution on the heat flow due to the latent heat release. However, some limitations of this scheme exist:

- The conversion of enthalpy to temperature and solid fraction is performed at each cell, requiring huge memory resources if the computation domain is large;
- As mentioned by the author, this scheme does not ensure the heat balance at each FE node because of the summation over CA cells for redistribution at FE nodes for the temperature and solid fraction. However, this scheme ensures heat balance at the CA scale.

Therefore, Carozzani *et al.* [Car12, Car14] proposed a new model to remove the limitations above:

- The enthalpy at FE nodes is computed by the energy conservation equation in the FE domain based on a given microsegregation model;
- A second FE mesh referred to as CA mesh is used to generate the CA grid of cells. Fields can be transported between the two meshes;
- The temperature of a cell is linearly interpolated from the last known nodes of CA element at each step. The undercooling of each cell can be calculated;
- The fraction of envelop is computed based on the dendrite tip growth kinetics in CA model;
- Summation of the fraction of envelop over the cells is interpolated to FE nodes and used for the conversion of the FE node enthalpy to FE node temperature based on the microsegregation model.

For this full coupling scheme, all the conversions of enthalpy to temperature are performed in the FE node. This implementation reduces the cost for computation compared with previous scheme [Gan99, Gui04]. In addition, because the energy conservation equation is

solved at the FE nodes based on the microsegregation model and the fraction of structure (envelop) computed by CA, the incoherency of enthalpy in FE nodes is removed.

As mentioned before, the CAFE model does not consider the internal structure of the grains. The main idea of this model is to track the growing dendrite envelop on the grid of cell lattice. It is available to simulate the grain structures in the scale of an industrial process. However, the morphological evolution of grains is ignored.

2.3. Conclusion

Simulation models for the structure evolution of the solidification at two different scales are presented in this Chapter.

In the micro scale, the front tracking method, the phase field method, and the modified cellular automaton model focus on the solid/liquid interface evolution for the dendrites in the melts, namely the formation of the microstructure. However, it is difficult for these models to predict the whole as-casting macrostructure due to the sharply increased computation costs.

In the scale of grains (meso scale), the mushy zone tracking method, the envelope phase field method, and the CAFE method simulate the evolution of the envelope which contain the dendrites and the around mushy zone. These methods have the capacity to predict the grain structure of the macro domain. However, the morphological evolution of the grains is ignored.

Due to the advantages of the CAFE method to predict the grain structure development in large scale casting, as presented by Carozzani *et al.* [Car12, Car14], it provides the possibility to use it on the simulation of other processes. Consequently, this method is developed to model the grain structure formation during welding process, which is presented in the next chapter.

2.4. French summary

Le **chapitre II** présente les différents modèles numériques utilisés pour la modélisation de l'évolution des structures de grains lors de la solidification. Les approches détaillées sont développées par rapport à une échelle microscopique ou à une échelle mésoscopique. Dans

une première partie, les méthodes de suivi de front, du champ de phase et de l'automate cellulaire modifié sont décrites. Elles permettent le suivi, à l'échelle microscopique, de l'évolution de l'interface solide/liquide lors de la formation de dendrites au cours de la solidification. Dans ce cas, la croissance des dendrites ainsi que leurs morphologies ramifiées peuvent être directement simulées. Cependant, ces modèles rencontrent des difficultés pour prédire l'intégralité de la macrostructure à l'échelle du procédé. Celles-ci sont principalement dues aux temps de calcul associés qui deviennent très élevés lorsque ces modèles sont appliqués à ces échelles spatiales supérieures. Ils ne sont donc pas adaptés à l'étude du développement des structures aux échelles macroscopiques. D'autres modèles s'intéressent à la formation des grains à l'échelle mésoscopique et font l'objet d'une seconde partie. La méthode de suivi de la zone pâteuse, la méthode du champ de phase appliquée à une enveloppe définie par rapport à une dendrite et la méthode CAFE simulent l'évolution d'un domaine plus large, incluant la structure dendritique, et le liquide voisin, définissant ainsi une 'enveloppe de grains' dont on réalise le suivi. Ces méthodes, intermédiaires en échelle spatiale, permettent la prédiction de la structure dans le domaine macroscopique mais ne prennent pas en compte l'évolution morphologique des grains. Elles présentent alors un compromis intéressant entre les approches micro et macro, en donnant la possibilité de prédire le développement des structures de grains à l'échelle de pièces de fonderie, ou, dans la situation présente, à celle du cordon de soudure, en des temps de calcul raisonnables.

Chapter III CAFE model

3.1. Presentation of CAFE model

The CAFE model initially proposed by Rappaz and Gandin [Rap93, Gan94] and later extended by Guillemot and Carozzani [Gui04, Car12] is used to solve the solidification problem and to simulate the grain structure evolution during casting process. The present work aims to extend it to simulate the grain structure evolution during melting and solidification in welding process, particularly for GTAW and GMAW. Accordingly, the CAFE model established in the present work is based on the coupling of several models which are implemented at different scales:

Macro scale: the mass, energy and momentum conservation equations for the whole system are resolved on a finite element mesh, referred to as FE mesh, which is schematically shown in **Fig. III-1** (a). This FE mesh is usually adapted to the temperature field. Accordingly, this macro model is referred to as FE model in the following.

Meso scale: the development of the envelopes of the grains in the fusion zone is resolved on a second finite element mesh, referred to as CA mesh, which is schematically shown in **Fig. III-1** (b1). This CA mesh is always fixed during the computations, and its domain is usually smaller than that defined by FE mesh. The fields such as the temperature can be communicated between the adaptive FE mesh and the fixed CA mesh. A CA grid made of a regular lattice of square cells in 2D or cubic cells in 3D is predefined and superimposed on the CA mesh, shown in **Fig. III-1** (b2). Each cell is therefore linked to the CA element to which it belongs. A single grain is represented by a set of cells which contain the same information such as grain number, grain orientation, *etc*. This meso model is referred to as CA model.

Micro scale: the kinetic models of dendritic growth (*e.g.* KGT model [Kur86] in the present work) are implemented in the cells to compute the growth of the dendrite (its overall shape is represented by the dashed blue square shown in **Fig. III-1** (c)) to reflect the microstructure evolution indirectly. This micro model is implicitly established in the cells.

Fig. III-1 (d) schematically illustrates the composition of phases for cells. Consider that the cell represents a zone composed by a dendrite and extradendritic liquid. The liquid phase l_0 in **Fig. III-1** (d) represents the extradendritic liquid. The other liquid phase l_1 is the interdendritic liquid. The solid phase s is the solid in the dendrite. The fraction of l_1 and s corresponds to the fraction of the dendrite envelope. Note that in fact these phases are only

related to the microsegregation model which is only considered on the nodes of the FE mesh. These detailed structures are not used on the cells.

In order to clarify the concepts used in the present CAFE model, they are summarized here:

- FE mesh: the adaptive mesh for the Finite Element resolution of average conservation equations;
- FE element: element in the FE mesh;
- FE node: node in the FE element;
- CA mesh: the fixed mesh for Cellular Automaton resolution;
- CA element: element in the CA mesh;
- CA node: node in the CA element;
- CA grid: grid made of the regular lattice of cells;
- CA cell: cell in the CA grid.

As presented above, in the CAFE model, there are two meshes on which the FE and CA models are implemented. The advantages for the use of two meshes are:

The very first and immediate improvement for CAFE model is that it permits a reduction of the size of the CA problem. Because the actual welding domain is usually smaller than the domain of workpiece, it is convenient to consider a volume of the domain smaller for the CA model than that for the FE model. This is done by considering FE and CA meshes with different sizes of dimensions. That is to say the FE model to solve the heat flow problem on the domain corresponds to the workpiece and the CA model to generate the CA grid and compute the grain structure on a reduced domain corresponds to the actual welding dimension. Comparing **Fig. III-1** (a) and (b1), the dimension of the CA mesh is thus smaller than that of the FE mesh.

The use of two meshes permits to perform optimizations of the FE mesh for the heat flow computation, *i.e.* mesh adaptation, while the CA mesh can be kept fixed. The CA mesh is used to establish the belonging of a CA cell to a CA element. It becomes unique since the CA mesh is fixed. This establishment of relationship will be presented in **Section 3.5**.

Finally, the use of two meshes permits the possibility to handle independent partitioning in parallel computation as explained by Carozzani *et al.* [Car14]. It is generally supposed that

the complexity of the problem directly depends on the number of nodes and elements partitioned in the memory of computing units (Note that the CA cells are always linked to the CA elements). In order to maximize parallel efficiency of the CAFE resolution, a good way is to balance the number of elements in computing units and communications among them. The two independent partitions give the advantages to treat the FE problem and CA problem differently by remeshing for FE mesh, *i.e.* the FE problem needs finer elements at high temperature, but the CA problem does not. The algorithm of partitioning is detailed in [Car14].

The FE and CA models used in the present work will be detailed in **Section 3.2** and **Section 3.3**, respectively. Moreover, communications between the two models then needs to be organized: following the CAFE coupling scheme [Car12], the temperature field computed on the FE mesh must be projected onto the CA mesh for performing the algorithms of melting and grain growth on the CA grid. On the other hand, the fraction of growing structure associated to the elements defined for a given node of the CA mesh should be made available on the FE mesh to solve the heat flow problem. This handling will be presented in detail in **Section 3.4**. In addition, the advantage of CA model is that, unlike for the resolution of the FE Model, the CPU time is almost linear in the number of cells which are in the computer memory [Rap96, Car14]. Therefore, it decreases the CPU time if only the cells related to the weld are allocated into the computation memory. That is to say the cells which are not affected by the welding are not necessary to be taken into account. Therefore, a specific numerical treatment, namely a dynamic strategy for the allocation/deallocation of the CA cells into the computer memory, is implemented in the CA model. This strategy will be presented in **Section 3.5**.

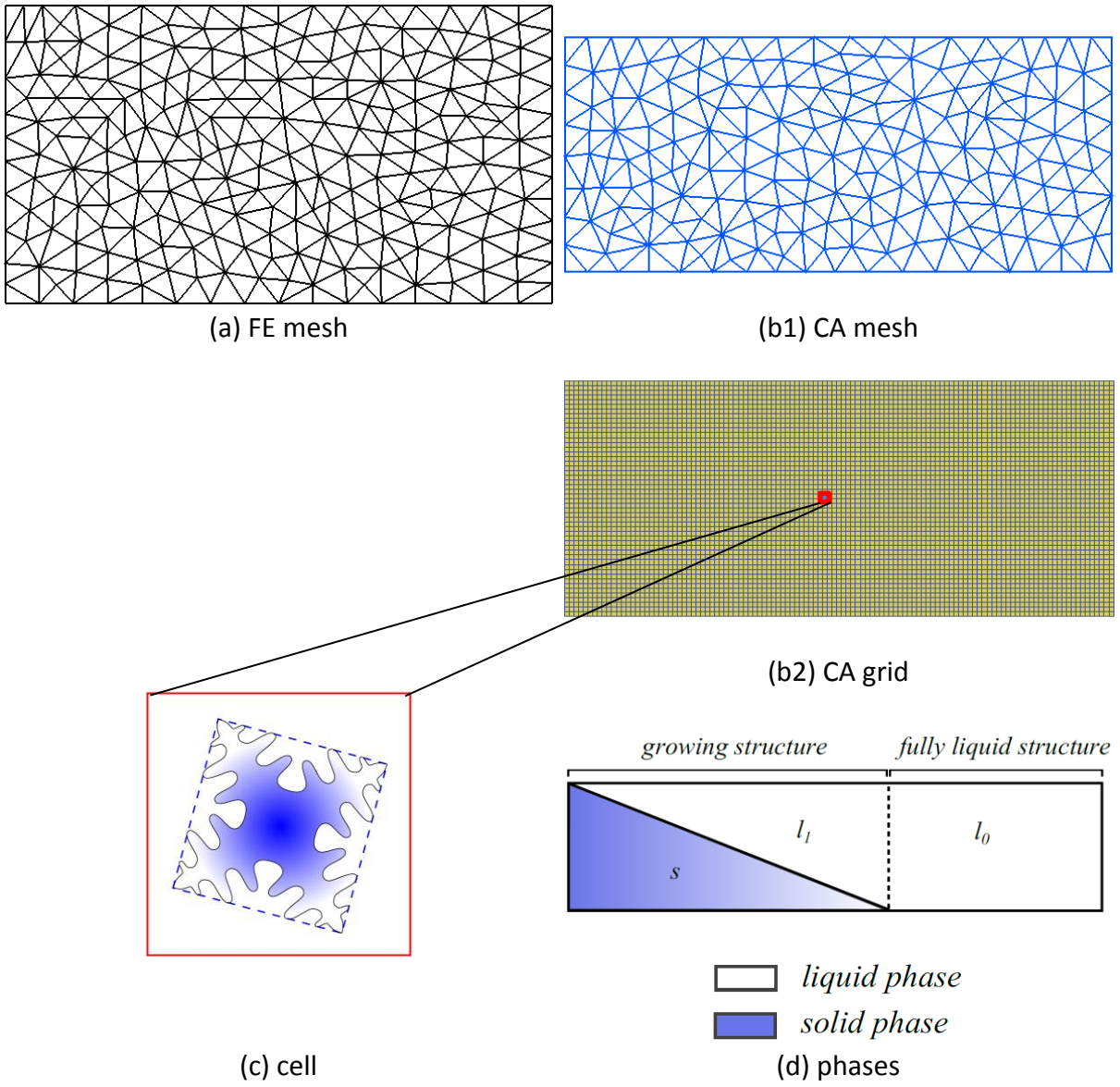

Fig. III-1 Schematic illustration of the different scale models in 2D. (a): the FE mesh on which the FE model is resolved, (b1): the CA mesh on which the CA model is resolved, (b2): the CA grid is generated and superimposed on the CA mesh, (c): the dendrite tip kinetics is applied for the growth of envelope in the cell, and (d): the phases, considered in the solidification process and computed at the FE nodes.

3.2. FE model

As mentioned in **Chapter I**, the solid/liquid interface of solidification during welding process is rarely smooth and regular. The dendritic grains grow into the fusion zone from the partially melted base metal. In such situation with complex morphology of phases, averaged continuity equations are used to resolve the heat flow in the whole domain of the workpiece. The average values of variables in representative volume elements (RVE) are solved with the finite element method. In the present work, the types of elements are triangle in 2D and tetrahedron in 3D.

Before presenting the FE model, some hypothesis in the present work for welding processes are listed:

- Constant and equal phase densities;
- Transport contributions due to solid deformation and liquid flow are neglected;
- No macrosegregation takes place for the welding domain.

In the present CAFE model, the structure evolutions for GTAW and GMAW processes are modeled, whereas the domains of the FE models are different. Differences of the FE mesh for GTAW and GMAW processes are summarized:

- For GTAW, in which no material is added into the system, the FE domain represents that of the workpiece. The heat transfer with the environment is applied as boundary conditions.
- For GMAW, in which the filler metal is added into the system due to the consumable electrode, the FE domain contains both the workpiece and the surrounding air where the weld bead forms. In this model, the heat transfer between metal and air is modeled.

Note that the GTAW process can be also simulated by the FE model containing the workpiece and the surrounding air. It will be verified in **Section 4.2.1**. The idea of the first FE model is to decrease the computation time without considering the surrounding air domain.

The FE models corresponding to GTAW and GMAW processes are present in **Section 3.2.1** and **Section 3.2.2**, respectively.

3.2.1. FE model for GTAW

3.2.1.1. Energy conservation equation

In the present work, it is supposed that no filler metal is added in the GTAW process. Therefore, the domain of the workpiece is fixed. Ignoring the mechanical contributions and the transport contributions due to liquid flow in a parallelepipedic domain that represents the workpiece in a welding process, the energy conservation average over all phases can be established [Rap03]:

$$\frac{\partial\langle\rho h\rangle}{\partial t} - \nabla\cdot\langle\kappa\boldsymbol{\nabla}T\rangle = \dot{Q} \qquad \textbf{(III-1)}$$

where ρ is the local mass density assumed uniform and constant for all phases, h is the local mass enthalpy, κ is the local thermal conductivity, and $\dot{Q}$ is a volumetric contribution of heat due to the heat source during welding process. The angle brackets $\langle\cdot\rangle$ represent the average value for the variables which are inside it. $\langle\rho h\rangle$ can be considered to be the average volume enthalpy in RVE, notated by $\langle H\rangle$. The local average temperature of the RVE is assumed to be the same in all phases. Consequently, it is possible to write the diffusive term as:

$$\langle\kappa\boldsymbol{\nabla}T\rangle = \langle\kappa\rangle\boldsymbol{\nabla}T \qquad \textbf{(III-2)}$$

where $\langle\kappa\rangle$ is the average thermal conductivity. Substituting **Eq. (III-2)** into **Eq. (III-1)**, using the notation of the average volume enthalpy, **Eq. (III-1)** is changed to be:

$$\frac{\partial\langle H\rangle}{\partial t} - \nabla\cdot(\langle\kappa\rangle\boldsymbol{\nabla}T) = \dot{Q} \qquad \textbf{(III-3)}$$

where $\langle H\rangle$ is the average volume enthalpy of all phases in the RVE.

A Fourier flux condition and the Stefan-Boltzmann law can be applied at the boundary of the domain, with a heat flux given by:

$$j_{T,n} = h_T(T - T_{ext}) + \sigma_B\varepsilon_r(T^4 - T_{ext}^4) \qquad \textbf{(III-4)}$$

where $j_{T,n}$ is the heat flux in the normal direction of the metal surface due to the heat conduction, convection and radiation. Usually negative value of $j_{T,n}$ is imposed at the boundary to reflect the heat extraction from the metal to environment. h_T is the heat transfer coefficient, σ_B is the Stefan-Boltzmann constant (σ_B = 5.67×10^{-8} W m^{-2} K^{-4}), ε_r is the

emissivity of the metal surface, and T_{ext} is the environmental temperature. It should be noticed that an adiabatic condition can be imposed by this condition considering $h_T = 0$ and $\varepsilon_r = 0$.

3.2.1.2. Volumetric heat source in GTAW

The volumetric heat source used in the present work for GTAW process is based on the double ellipsoidal model proposed by Goldak *et al.* [Gol84]. This model is available to simulate the high digging action of the arc which transports the heat below the surface in GTAW process. The power density distribution is illustrated in **Fig. III-2**.

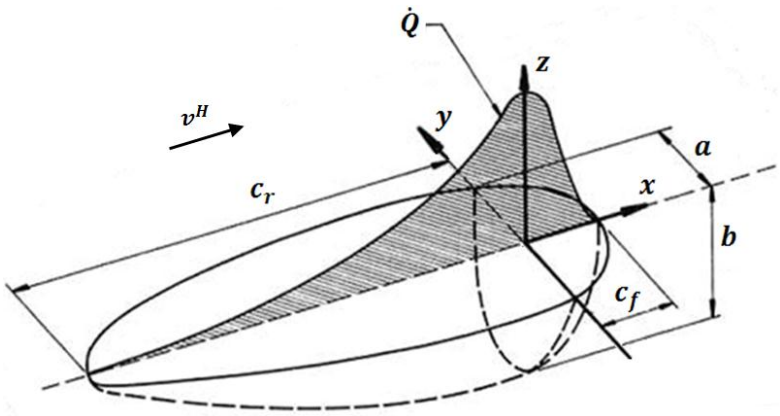

Fig. III-2 Schematic illustration of the double ellipsoid heat source (Goldak heat source) configuration in 3D [Gol84]

Assuming that the center of this heat source configuration is originally located at point (X_S, Y_S, Z_S) and moves with the velocity v^H in the x-axis direction, this volumetric heat source, $\dot{Q}$, considering the configuration in **Fig. III-2** at time t, can be expressed mathematically as below:

$$\begin{cases} \dot{Q}(x,y,z,t) \\ \quad = \dfrac{6\sqrt{3} f_i \dot{Q}_{input}}{abc_i \pi\sqrt{\pi}} exp\left\{-3\left[\dfrac{\left(x-(X_S+v^H t)\right)^2}{{c_i}^2} + \dfrac{(y-Y_S)^2}{a^2} + \dfrac{(z-Z_S)^2}{b^2}\right]\right\} \\ f_f + f_r = 2 \\ \dot{Q}_{input} = UI\eta \end{cases} \quad \textbf{(III-5)}$$

where (x, y, z) is the coordinates of the point in the defined domain. $\dot{Q}_{input}$ is the input power which is computed by the multiplication of the input voltage, U, the input current, I, and the heat source efficiency, η. f_i is the fraction of the heat deposited in the front or rear quadrants. a, b and c_i are the semi-axes of the ellipsoidal heat source in the y, z and x

direction, respectively. For the subscript of f_i and c_i, $i = f$ if $x \geq X_S + v^H t$ (*i.e.* the front quadrants), and $i = r$ if $x < X_S + v^H t$ (*i.e.* the rear quadrants).

It should be noted that due to the continuity of the volumetric heat source, the values of $\dot{Q}$ at the plane ($x = X_S + v^H t$) computed by **Eq. (III-5)** must be equal for both the front and rear quadrants. Therefore, the constraint for f_f and f_r is obtained as $f_f/c_f = f_r/c_r$. Consequently, the values for these two coefficients are determined as $f_f = 2c_f/(c_f + c_r)$ and $f_r = 2c_r/(c_f + c_r)$. It is also worth noting that the expression of $\dot{Q}$ is under the assumption that the moving direction of the heat source is along x axis. If the moving direction is changed, it is necessary to change its expression correspondingly.

In the present work, the parameters $c_f = c_r = c$ are adopted. That is to say, the shapes are the same for the front and rear parts. Accordingly, $f_f = f_r = 1$. $\dot{Q}_{input}$ is chosen to be the input parameter for the heat source directly. Finally, the input parameters of the Goldak heat source are $\dot{Q}_{input}$, v^H, a, b, c, and (X_S, Y_S, Z_S).

3.2.2. FE model for GMAW

Different from the GTAW process, filler metal is added into the fusion zone due to the consumable electrode in the GMAW process to form the weld bead. Schematically illustrated in **Fig. III-3** (a), the formation of the weld bead changes the interface between the metal and the environment. Accordingly, based on the work of Desmaison *et al.* [Des13], the FE model for GMAW is established in a Level Set (LS) approach containing both the metal (workpiece) and its surrounding air, shown in **Fig. III-3** (b). The LS approach is used to overcome the numerical and modeling difficulties due to the metal/chamfer contacts or/and the contacts between the weld joints (weld bead) after the successive passes in the multi-pass GMAW process. The FE model in the Level Set approach is presented briefly hereafter.

3.2.2.1. Level Set approach

As illustrated in **Fig. III-3** (b), the FE domain contains the metal domain (workpiece) and the surrounding air domain where the weld bead is expected to form due to the consumable electrode in GMAW process. The interface between the metal and the surrounding air domain is defined by a distance function, namely the Level Set (LS) function, ψ, with the value of 0 (the yellow curve in **Fig. III-3** (b)). The formation of the weld bead on the

workpiece results to the change of the interface between the two domains. At any time of the process, the value of ψ for any point, *M*, corresponds to the signed distance between *M* itself and the metal/air interface. Following the work of Desmaison *et al.* [Des13], in the present work, negative values of ψ are proposed to determine the points in the metal domain while positive values of ψ correspond to those in the air domain, which mathematically corresponds to:

$$\begin{cases} \psi < 0 & \text{if } M \in \text{metal domain} \\ \psi = 0 & \text{if } M \in \text{metal/air interface} \\ \psi > 0 & \text{if } M \in \text{air domain} \end{cases} \quad \textbf{(III-6)}$$

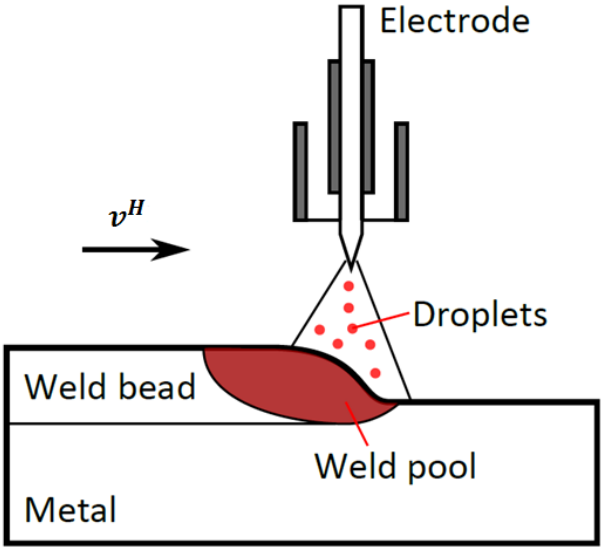

(a)

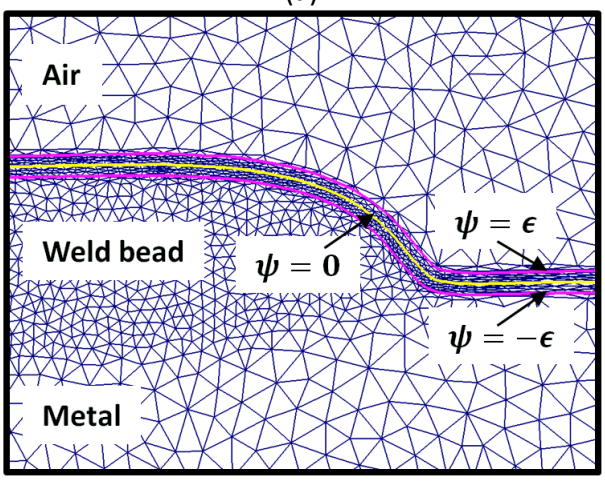

(b)

Fig. III-3 (a): schematic illustration of the GMAW process. The electrode moves with the velocity of v^H. The liquid droplets are added into the weld pool to form the weld bead after solidification. The boundary of the weld bead updates the interface between the metal and the environment. (b): definition of the FE mesh in LS approach. The FE domain is divided into metal and air domain, separated by the interface with $\psi = 0$. A transition zone is defined between the range $[-\epsilon, \epsilon]$. The properties of metal and air are averaged in this zone.

In order to ensure the resolution in the FE domain, all the material properties are averaged using the local value of the Heaviside function, $\mathcal{H}(\psi)$, which is defined as follows:

$$\begin{cases} \mathcal{H}(\psi) = 0 & \text{if } \psi < -\epsilon \\ \mathcal{H}(\psi) = \frac{1}{2}\left[1 + \frac{\psi}{\epsilon} + \frac{1}{\pi} sin\left(\frac{\pi\psi}{\epsilon}\right)\right] & \text{if } |\psi| \leq \epsilon \\ \mathcal{H}(\psi) = 1 & \text{if } \psi > \epsilon \end{cases} \quad \textbf{(III-7)}$$

where ϵ is the half thickness of the transition zone between the metal domain and air domain. The boundaries of this transition zone are represented by the two purple curves in **Fig. III-3** (b). Note that ϵ is a parameter of the present LS approach, taken as a small positive value. **Eq. (III-7)** reveals that $\mathcal{H}(\psi)$ continuously evolves from 0 to 1 in the transition zone $[-\epsilon, \epsilon]$, shown in **Fig. III-4**.

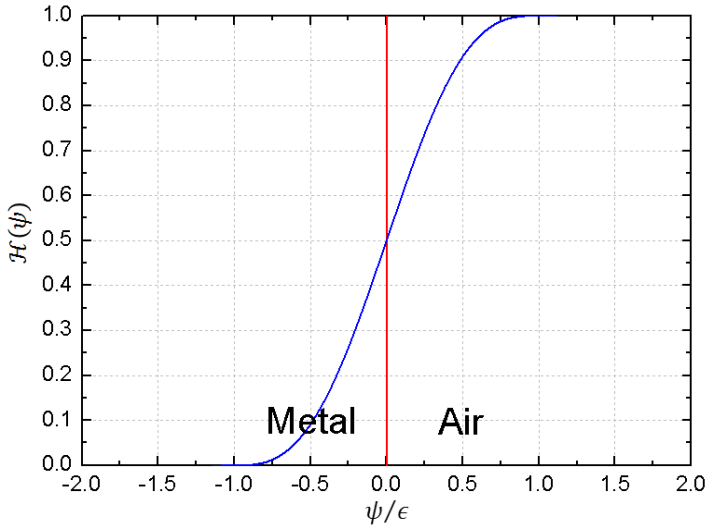

Fig. III-4 Heaviside function $\mathcal{H}(\psi)$ with respect to ψ/ϵ

Any material property, χ, is defined as an average value of the metal and air properties in the local position based on the Heaviside function:

$$\langle\chi\rangle = \big(1 - \mathcal{H}(\psi)\big)\langle\chi\rangle^{\mathbb{M}} + \mathcal{H}(\psi)\langle\chi\rangle^{\mathbb{A}} \quad \textbf{(III-8)}$$

where $\langle\chi\rangle^{\mathbb{M}}$ and $\langle\chi\rangle^{\mathbb{A}}$ are the local intrinsic value of the property of the metal and air, respectively, and ψ is the value of the distance function at the local position. Note that $\langle\chi\rangle^{\mathbb{M}}$ is also the average value of the intrinsic properties of each phase in the metal. This mixing law (which can be considered as a mixing law over space), **Eq. (III-8)**, reveals that the volume fraction of air at a specific point is defined by $\mathcal{H}(\psi)$. Accordingly, the fraction of metal is

explicitly defined by $1-\mathcal{H}(\psi)$. In order to simplify the expression, the Heaviside function is only expressed by $\mathcal{H}$ to represent the fraction of air in the following contents.

According to **Eq. (III-7)** and **Eq. (III-8)**, the material properties of a specific point locating outside the transition zone correspond to either the properties of metal or that of the air. If the point locates inside the transition zone, its material properties correspond to the summation of the value of the metal and air properties weighted by their corresponding space fractions ($\mathcal{H}(\psi)$ corresponds to the space fraction of air, $1-\mathcal{H}(\psi)$ corresponds to the space fraction of metal).

In addition, it should be noticed that in the Level Set approach, no explicit interface is defined (the interface is defined by $\psi=0$ implicitly). That is to say it is impossible to impose the surface conditions directly at the metal/air interface. However, thanks to the Continuum Surface Force (CSF) method proposed by Brackbill *et al.* [Bra92], it is available to transform these surface conditions into volumetric conditions. The general form of the CSF method can be represented by:

$$\int_S F dS = \int_V F\,\delta(\psi) dV \qquad \textbf{(III-9)}$$

where F is an interfacial value imposed at the metal/air interface, S. $\delta(\psi)$ is the derivative of the Heaviside function, $\mathcal{H}(\psi)$, with respect to the Level Set function, ψ, namely: $\delta(\psi)=\frac{\partial \mathcal{H}(\psi)}{\partial \psi}$. Consequently, the term $F\delta(\psi)$ can be considered as a volumetric term imposed in the volume, V, at the transition zone. It should be emphasized that this CSF method can be applied for both scalar and vector fields.

3.2.2.2. Cavity model for droplets

In GMAW, the molten metal from the consumable electrode, namely the droplets, impinge in the fusion zone to form the weld bead. In order to model the formation of the weld beads (in other words, the formation of the new interface between the metal and air), it is necessary to define the volume where these droplets impinge in the fusion zone.

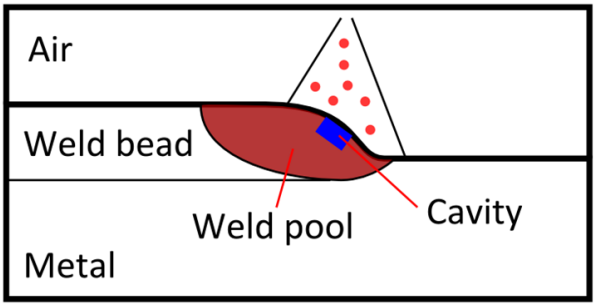

Fig. III-5 Schematic illustration of the cavity (the blue rectangle (2D) below the metal/air interface inside the weld pool) in which the droplets impinge. Note that the shape of cavity is actually defined by ψ. Therefore, it follows the curvature of the interface.

Following the work of Desmaison *et al.* [Des13, Bel13], the molten droplets fall in a limited cylindrical region (also called cavity) of the fusion zone, which is schematically shown in the **Fig. III-5** as a blue rectangle (in the view of the transverse section of the workpiece). Its radius, R_c, is considered to be twice bigger than that of the droplets, R_d [Des13, Bel13]. R_d is defined as:

$$R_d = \left(\frac{3\rho_w(T_{0,w})R_w^2 v_w}{4 f_d \rho_w(T_d)}\right)^{\frac{1}{3}} \quad \textbf{(III-10)}$$

where $\rho_w(T_{0,w})$ is the density of the filler wire (*i.e.* the consumable electrode) at its initial temperature $T_{0,w}$. $\rho_w(T_d)$ corresponds to the density of the filler wire at the temperature of droplets, T_d. In the present work, the density of the filler wire is considered to be the same at different temperatures due to the fact that the shrinkage of the material is not modeled. R_w is the radius of the filler wire (the electrode), and v_w is the velocity of the adding filler wire which is vertically inward the metal/air interface. f_d is the frequency of detachment of the droplets defined by [Kim03]:

$$f_d = \frac{-243.44}{1 + exp\left(\frac{I - 291.086}{6.06437}\right)} + 323.506 - 0.8741I + 0.0025I^2 \quad \textbf{(III-11)}$$

where I is the current intensity. Combining **Eq. (III-10)** and **Eq. (III-11)**, R_c is thus determined by the relationship $R_c = 2R_d$.

The height of the cavity, L_c, is modeled as [Kum94] and later corrected by [Des13]:

$$L_c = -\frac{2\gamma^{l/a}}{R_c \rho a_g} + 2\sqrt{\left(\frac{\gamma^{l/a}}{R_c \rho a_g}\right)^2 + \frac{R_c v_d^2}{24 a_g}} \quad \textbf{(III-12)}$$

where $\gamma^{l/a}$ is the liquid/air surface tension, ρ is the local density of the liquid metal in the fusion zone, a_g is the gravitational acceleration and v_d is the velocity of the droplets falling into the weld pool. v_d is defined by:

$$v_d = \sqrt{v_{0,d}^2 + 2a_d L_a} \quad \textbf{(III-13)}$$

where $v_{0,d}$ is the initial droplet velocity. a_d is the acceleration of the droplet, which is assumed to be constant through the arc plasma. L_a is the length of the arc plasma. $v_{0,d}$ is computed by [Lin01, Des13]:

$$v_{0,d} = \sqrt{-0.33692 + 0.00854(I/2R_d)} \quad \textbf{(III-14)}$$

where I is the current intensity applied to the electrode.

Substituting **Eq. (III-13)** and **Eq. (III-14)** into **Eq. (III-12)**, the value of L_c is determined. The volume of the cavity is computed by the relationship:

$$V_c = \pi R_c^2 L_c \quad \textbf{(III-15)}$$

3.2.2.3. Mass conservation equation in the cavity

In the cavity where the droplets impinge, the adding metal rate should be added on the right hand side of the mass conservation equation:

$$\frac{\partial \langle \rho \rangle}{\partial t} + \nabla \cdot \langle \rho \boldsymbol{v} \rangle = \frac{\dot{m}_w}{V_c} = \frac{\rho_w(T_{0,w}) R_w^2 v_w}{R_c^2 L_c} \quad \textbf{(III-16)}$$

where the right hand side term is the ratio of the mass flow rate of the filler metal, $\dot{m}_w$, by the volume of the cavity, V_c. Note that the right hand term is time and space averaged for the droplets in the delivery region (*i.e.* the plasma) and the cavity. Neglecting the variation of the density in the liquid of the cavity (ρ is constant in the cavity), **Eq. (III-16)** can be simplified:

$$\nabla \cdot \langle \boldsymbol{v} \rangle = \frac{\dot{m}_w}{\rho V_c} = \frac{\rho_w(T_{0,w})}{\rho} \frac{R_w^2 v_w}{R_c^2 L_c} \quad \textbf{(III-17)}$$

It should be mentioned again that no shrinkage is considered in the present work. Thus, $\dot{m}_w$ is calculated considering the same density for the filler wire at different temperatures. In addition, the ratio of density, $\rho_w(T_{0,w})/\rho$, has to be considered equal to 1. Moreover,

Eq. (III-17) is considered in the whole FE domain, the local expansion rate (*i.e.* the right hand term) is simplified:

$$\begin{cases} \dfrac{\dot{m}_w}{\rho V_c} = \dfrac{R_w^2 v_w}{R_c^2 L_c} & \text{in the cavity} \\ \dfrac{\dot{m}_w}{\rho V_c} = 0 & \text{outside the cavity} \end{cases} \quad \textbf{(III-18)}$$

3.2.2.4. Weld bead development

Following the work of Desmaison *et al.* [Des13], for the development of weld bead, the driving forces are considered to be the normal component of the surface tension and the gravity volume force. The arc pressure is ignored. Marangoni forces are supposed to have little impact on the weld bead shape and are thus ignored. Indeed, their impact is mainly discussed in fluid flow into the weld pool.

The normal component of the surface tension force, $\boldsymbol{F}_\gamma$, and the gravity volume force, $\boldsymbol{F}_g$, are defined by:

$$\boldsymbol{F}_\gamma = K_c \gamma^{l/a} \boldsymbol{n} \quad \textbf{(III-19)}$$

$$\boldsymbol{F}_g = \rho \boldsymbol{a_g} \quad \textbf{(III-20)}$$

with $K_c = -\nabla \cdot \boldsymbol{n}$ **(III-21)**

$$\boldsymbol{n} = \frac{\boldsymbol{\nabla}\psi}{\|\boldsymbol{\nabla}\psi\|} \quad \textbf{(III-22)}$$

where K_c is the local mean curvature of the liquid/air interface, $\boldsymbol{n}$ is the unit outward normal vector of this interface, $\boldsymbol{a_g}$ is the vector of the gravitational acceleration.

As explained previously, no surface conditions are applied at the metal/air interface in the Level Set approach. The normal component of the surface tension force $\boldsymbol{F}_\gamma$ is thus transformed to a volume force, using the CSF method as presented previously in **Eq. (III-9)**. Consequently, the whole volumetric driving force is:

$$\boldsymbol{F} = \delta(\psi)\boldsymbol{F}_\gamma + \boldsymbol{F}_g \quad \textbf{(III-23)}$$

The momentum conservation equation is established as:

$$\langle\rho\rangle\left(\frac{\partial\langle\boldsymbol{v}\rangle}{\partial t} + \langle\boldsymbol{v}\rangle \cdot \boldsymbol{\nabla}\langle\boldsymbol{v}\rangle\right) - \nabla \cdot \left(\langle\mu_d\rangle(\boldsymbol{\nabla}\langle\boldsymbol{v}\rangle + \boldsymbol{\nabla}\langle\boldsymbol{v}\rangle^T)\right) + \boldsymbol{\nabla}p = \boldsymbol{F} \quad \textbf{(III-24)}$$

where p is the pressure in the weld pool, and μ_d is the dynamic viscosity. Coupling **Eq. (III-24)** and **Eq. (III-17)**, the velocity field can be solved. It should be emphasized that the velocity solved by the momentum conservation equation only results from the added droplets. No fluid flow is considered in the weld pool.

Finally, the level set function is updated due to the movement of the interface:

$$\frac{\partial \psi}{\partial t} + \langle \boldsymbol{v} \rangle \cdot \boldsymbol{\nabla} \psi = 0 \qquad \textbf{(III-25)}$$

Solved by **Eq. (III-25)**, the value of the Level Set function, ψ, is updated and thus the interface of the metal and air is updated with the definition of $\psi = 0$. Note that a reinitialization operation is used in order to keep the Eikonal property, *i.e.* $\|\boldsymbol{\nabla}\psi\| = 1$. It is thus obtained by solving the Hamilton-Jacobi equation:

$$\frac{\partial \psi}{\partial \tau} = S(\psi)(1 - \|\boldsymbol{\nabla}\psi\|) \qquad \textbf{(III-26)}$$

where $S(\psi)$ is the function sign. More details about this operation are available in [Des13, Bas06].

3.2.2.5. Energy conservation equation

In the case of the GMAW process, the movement of the interface between the metal and the air will lead the heat transport in the whole system. As mentioned in **Section 3.2.2.1**, the properties of a specific point *M* in the system are the averaged values of air and metal properties by the space mixing law. So the intrinsic energy conservation equation for the air and the metal enthalpies could be established, respectively:

$$\frac{\partial \langle H \rangle^{\mathbb{A}}}{\partial t} + \nabla \cdot \langle H\boldsymbol{v} \rangle^{\mathbb{A}} - \nabla \cdot (\langle \kappa \rangle^{\mathbb{A}} \boldsymbol{\nabla} T) = \dot{Q}^{\mathbb{A}} \qquad \textbf{(III-27)}$$

$$\frac{\partial \langle H \rangle^{\mathbb{M}}}{\partial t} + \nabla \cdot \langle H\boldsymbol{v} \rangle^{\mathbb{M}} - \nabla \cdot (\langle \kappa \rangle^{\mathbb{M}} \boldsymbol{\nabla} T) = \dot{Q}^{\mathbb{M}} \qquad \textbf{(III-28)}$$

Before applying the space mixing law which corresponds to **Eq. (III-8)**, **Eq. (III-27)** and **Eq. (III-28)** are weighted by their corresponding space fractions to get:

$$\mathcal{H}\left[\frac{\partial \langle H \rangle^{\mathbb{A}}}{\partial t} + \nabla \cdot \langle H\boldsymbol{v} \rangle^{\mathbb{A}} - \nabla \cdot (\langle \kappa \rangle^{\mathbb{A}} \boldsymbol{\nabla} T)\right] = \mathcal{H}\dot{Q}^{\mathbb{A}} \qquad \textbf{(III-29)}$$

$$(1 - \mathcal{H})\left[\frac{\partial \langle H \rangle^{\mathbb{M}}}{\partial t} + \nabla \cdot \langle H\boldsymbol{v} \rangle^{\mathbb{M}} - \nabla \cdot (\langle \kappa \rangle^{\mathbb{M}} \boldsymbol{\nabla} T)\right] = (1 - \mathcal{H})\dot{Q}^{\mathbb{M}} \qquad \textbf{(III-30)}$$

The three left hand terms in **Eq. (III-29)** can be transformed to:

$$\mathcal{H}\,\frac{\partial\langle H\rangle^{\mathbb{A}}}{\partial t}=\frac{\partial(\mathcal{H}\langle H\rangle^{\mathbb{A}})}{\partial t}-\langle H\rangle^{\mathbb{A}}\frac{\partial\mathcal{H}}{\partial t} \quad \textbf{(III-31)}$$

$$\mathcal{H}\,\nabla\cdot\langle H\boldsymbol{v}\rangle^{\mathbb{A}}=\nabla\cdot(\mathcal{H}\langle H\boldsymbol{v}\rangle^{\mathbb{A}})-\langle H\boldsymbol{v}\rangle^{\mathbb{A}}\cdot\boldsymbol{\nabla}\mathcal{H} \quad \textbf{(III-32)}$$

$$-\mathcal{H}\,\nabla\cdot(\langle\kappa\rangle^{\mathbb{A}}\boldsymbol{\nabla}T)=-\nabla\cdot(\mathcal{H}\langle\kappa\rangle^{\mathbb{A}}\boldsymbol{\nabla}T)+(\langle\kappa\rangle^{\mathbb{A}}\boldsymbol{\nabla}T)\cdot\boldsymbol{\nabla}\mathcal{H} \quad \textbf{(III-33)}$$

Similarly, the three left hand terms in **Eq. (III-30)** can be transformed to:

$$(1-\mathcal{H})\,\frac{\partial\langle H\rangle^{\mathbb{M}}}{\partial t}=\frac{\partial\Big((1-\mathcal{H})\langle H\rangle^{\mathbb{M}}\Big)}{\partial t}+\langle H\rangle^{\mathbb{M}}\frac{\partial\mathcal{H}}{\partial t} \quad \textbf{(III-34)}$$

$$(1-\mathcal{H})\,\nabla\cdot\langle H\boldsymbol{v}\rangle^{\mathbb{M}}=\nabla\cdot\Big((1-\mathcal{H})\langle H\boldsymbol{v}\rangle^{\mathbb{M}}\Big)+\langle H\boldsymbol{v}\rangle^{\mathbb{M}}\cdot\boldsymbol{\nabla}\mathcal{H} \quad \textbf{(III-35)}$$

$$-(1-\mathcal{H})\,\nabla\cdot(\langle\kappa\rangle^{\mathbb{M}}\boldsymbol{\nabla}T)=-\nabla\cdot\Big((1-\mathcal{H})\langle\kappa\rangle^{\mathbb{M}}\boldsymbol{\nabla}T\Big)-(\langle\kappa\rangle^{\mathbb{M}}\boldsymbol{\nabla}T)\cdot\boldsymbol{\nabla}\mathcal{H} \quad \textbf{(III-36)}$$

Finally, applying the space mixing law, **Eq. (III-8)**, summing **Eq. (III-29)** and **Eq. (III-30)**, and rearrange the equation, substituting **Eq. (III-31)** - **Eq. (III-36)** to get the energy conservation equation in LS approach:

$$\begin{aligned}&\frac{\partial\langle H\rangle}{\partial t}+\nabla\cdot\langle H\boldsymbol{v}\rangle-\nabla\cdot(\langle\kappa\rangle\boldsymbol{\nabla}T)\\&=\dot{Q}+\frac{\partial\mathcal{H}}{\partial t}(\langle H\rangle^{\mathbb{A}}-\langle H\rangle^{\mathbb{M}})+\boldsymbol{\nabla}\mathcal{H}\cdot(\langle H\boldsymbol{v}\rangle^{\mathbb{A}}-\langle H\boldsymbol{v}\rangle^{\mathbb{M}})\\&\quad-\boldsymbol{\nabla}\mathcal{H}\cdot(\langle\kappa\rangle^{\mathbb{A}}\boldsymbol{\nabla}T-\langle\kappa\rangle^{\mathbb{M}}\boldsymbol{\nabla}T)\end{aligned} \quad \textbf{(III-37)}$$

where the four terms on the right hand side correspond to the added volumetric heat source, the added terms for temporal variation, heat transport and heat diffusion terms due to the movement of the LS function, respectively. In addition, the three terms on the left hand side are deduced from the space mixing law (**Eq. (III-8)**).

3.2.2.6. Heat source in GMAW

In the present model for the GMAW process, the total input power, $\dot{Q}_{input}$, is divided into two parts: the first part, $\dot{Q}_{plasma}$, corresponds to the arc plasma for heating the workpiece, and the second part, $\dot{Q}_{droplet}$, is used to melt the electrode to form the droplets, namely:

$$\dot{Q}_{input}=\dot{Q}_{plasma}+\dot{Q}_{droplet} \quad \textbf{(III-38)}$$

Therefore, the heat source, $\dot{Q}$, which is included on the right hand side of **Eq. (III-37)**, contains the following two contributions: the first one, $\dot{Q}_P$, which can be considered as a surface heat flux, is provided by the arc plasma, $\dot{Q}_{plasma}$, and the second one, $\dot{Q}_D$, which is a

volumetric heat source, is associated to the molten droplets, $\dot{Q}_{droplet}$, supplied by the consumable electrode. In addition, a third contribution should be considered, which is a surface cooling source, $\dot{Q}_{CR}$, induced by the heat convection and thermal radiation effect at the metal/air interface. The three contributions are schematically shown in **Fig. III-6**.

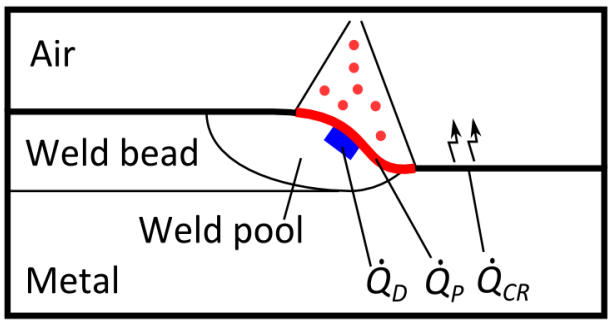

Fig. III-6 Schematic illustration of the heat source considered in GMAW process with $\dot{Q}_P$: surface heat source due to the plasma, $\dot{Q}_D$: volumetric heat source due to the droplets, and $\dot{Q}_{CR}$: surface heat transfer.

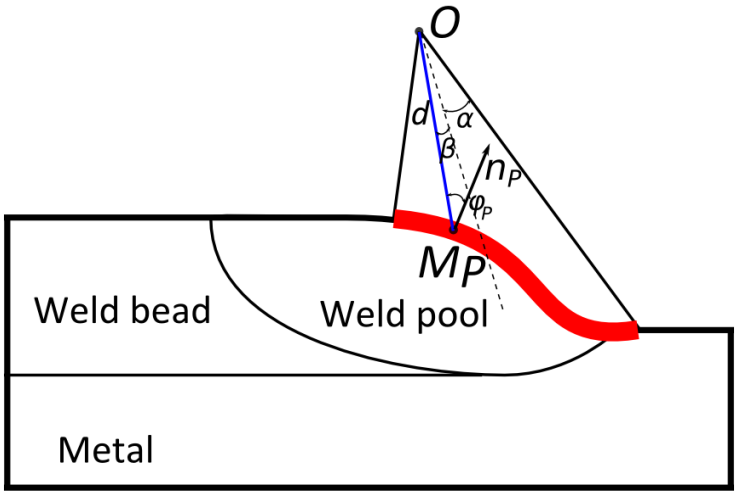

Fig. III-7 Definition of the plasma heat source geometry with the angular Gaussian condition. M_P is a local point locating in the transition zone. d is the distance between M_P and the plasma origin point O. α is the half angle of the plasma heat source. β is the angle of OM_P and the angle bisector line of the plasma (the dashed line). φ_P is the angle of OM_P and the local normal of the surface, n_P.

The surface heat flux due to the plasma, $\dot{Q}_P$, is defined as an angular Gaussian condition with the configuration of **Fig. III-7** [Des13]:

$$\dot{Q}_P = \frac{3\dot{Q}_{Plasma}}{K_P 2\pi d^2(1-cos\alpha)} exp\left(-3\left(\frac{\beta}{\alpha}\right)^2\right) cos\varphi_P \qquad \textbf{(III-39)}$$

where K_P is a normalization factor expressed as:

$$K_P = 0.95 + 0.0347\alpha^2 \quad \textbf{(III-40)}$$

The other parameters in **Eq. (III-39)** are illustrated in **Fig. III-7**.

The volumetric heat source associated with the molten droplets, $\dot{Q}_D$, is modeled by:

$$\dot{Q}_D = \frac{\dot{Q}_{droplet}}{V_c} = \frac{\dot{m}_w}{\rho V_c} H^d = \frac{\rho_w(T_{0,w})}{\rho} \frac{R_w^2 v_w}{R_c^2 L_c} H^d \quad \textbf{(III-41)}$$

where H^d is the volume enthalpy of the droplets.

The surface cooling source, $\dot{Q}_{CR}$, is defined corresponding to the cooling condition applied at the metal/air interface. $\dot{Q}_{CR}$ corresponds to the Fourier flux condition plus the Stefan-Boltzmann law:

$$\dot{Q}_{CR} = h_T(T - T_{ext}) + \sigma_B \varepsilon_r (T^4 - T_{ext}^4) \quad \textbf{(III-42)}$$

Note that **Eq. (III-42)** has the same expression as **Eq. (III-4)**. The difference is that $\dot{Q}_{CR}$ cannot be applied as boundary condition at the metal/air interface in GMAW simulations.

Finally, substituting **Eq. (III-39)**, **Eq. (III-41)** and **Eq. (III-42)** into **Eq. (III-37)**, and applying the CSF method for the surface heat fluxes, the energy conservation equation becomes:

$$\begin{aligned} &\frac{\partial \langle H \rangle}{\partial t} + \nabla \cdot \langle H \boldsymbol{v} \rangle - \nabla \cdot (\langle \kappa \rangle \boldsymbol{\nabla} T) \\ &= \delta(\psi)\left(\dot{Q}_P - \dot{Q}_{CR}\right) + \dot{Q}_D + \frac{\partial \mathcal{H}}{\partial t}(\langle H \rangle^{\mathbb{A}} - \langle H \rangle^{\mathbb{M}}) + \boldsymbol{\nabla}\mathcal{H} \cdot (\langle H \boldsymbol{v} \rangle^{\mathbb{A}} - \langle H \boldsymbol{v} \rangle^{\mathbb{M}}) \\ &\quad -\boldsymbol{\nabla}\mathcal{H} \cdot (\langle \kappa \rangle^{\mathbb{A}} \boldsymbol{\nabla} T - \langle \kappa \rangle^{\mathbb{M}} \boldsymbol{\nabla} T) \end{aligned} \quad \textbf{(III-43)}$$

3.2.3. Temperature solver

There are two unknown variables in both **Eq. (III-3)** (for GTAW process) and **Eq. (III-43)** (for GMAW process), namely the average volume enthalpy, $\langle H \rangle$, and the local temperature, T. During the welding process, the two variables are in a complicated relationship which is far from linear due to the phase transformation. This introduces a non-linearity for the resolution. Therefore, to establish the relationship between them becomes important for the resolution of this problem. In the average continuity theory, the average volume enthalpy is defined to be the summation of the volume enthalpy of each phase multiplying their corresponding volume fractions. However, in the CAFE model, the volume fraction of each

phase is related to the CA model. Consequently, this $\langle H\rangle - T$ relationship will be presented in detail in **Section 3.4.4** after the introduction of the CA model.

Suppose that the $\langle H\rangle - T$ relationship has been established. The non-linear equation **Eq. (III-3)** and **Eq. (III-43)** can be resolved using iterative methods, for example the Newton-Raphson method in the present work. It is available to choose the average volume enthalpy, $\langle H\rangle$, as the primary unknown, and then convert it to temperature, T, based on the $\langle H\rangle - T$ relationship. On the other hand, the second method is to choose T to be the primary unknown, and then convert it to $\langle H\rangle$. The first method is called Enthalpy Solver [Car12], while the second one is the Temperature Solver [Saa14]. In the present work, the Temperature Solver [Saa14] is adopted for the solutions of both **Eq. (III-3)** and **Eq. (III-43)**.

It is considered that **Eq. (III-3)** is a special case of **Eq. (III-43)** with $\mathcal{H} = 0$ and $\boldsymbol{v} = 0$. Therefore, only the method to solve **Eq. (III-43)** is presented hereafter. The first simplification for the resolution is for the transport term in the left hand side of **Eq. (III-43)**:

$$\nabla \cdot \langle H\boldsymbol{v}\rangle = \langle \boldsymbol{v}\rangle \cdot \boldsymbol{\nabla}\langle H\rangle + \langle H\rangle \nabla \cdot \langle \boldsymbol{v}\rangle \tag{III-44}$$

Substitute **Eq. (III-17)**, **(III-41)** and **(III-44)** into **Eq. (III-43)**, and rearrange it to be:

$$\begin{aligned}&\frac{\partial\langle H\rangle}{\partial t} + \langle \boldsymbol{v}\rangle \cdot \boldsymbol{\nabla}\langle H\rangle - \nabla \cdot (\langle \kappa\rangle \boldsymbol{\nabla} T)\\ &= \delta(\psi)\left(\dot{Q}_P - \dot{Q}_{CR}\right) + \frac{\dot{m}_w}{\rho V_c}(H^d - \langle H\rangle) + \frac{\partial \mathcal{H}}{\partial t}(\langle H\rangle^{\mathbb{A}} - \langle H\rangle^{\mathbb{M}})\\ &\quad + \boldsymbol{\nabla}\mathcal{H} \cdot (\langle H\boldsymbol{v}\rangle^{\mathbb{A}} - \langle H\boldsymbol{v}\rangle^{\mathbb{M}}) - \boldsymbol{\nabla}\mathcal{H} \cdot (\langle \kappa\rangle^{\mathbb{A}} \boldsymbol{\nabla} T - \langle \kappa\rangle^{\mathbb{M}} \boldsymbol{\nabla} T)\end{aligned} \tag{III-45}$$

Note that the term $\frac{\dot{m}_w}{\rho V_c}$ is determined by **Eq. (III-18)**. The second simplification for the resolution is to assume that all the right hand side terms in **Eq. (III-45)** are known explicitly, corresponding to the values at the previous time step. Consequently, it is available to use a volumetric term $\dot{Q}'$ to represent the whole right hand side terms:

$$\frac{\partial\langle H\rangle}{\partial t} + \langle \boldsymbol{v}\rangle \cdot \boldsymbol{\nabla}\langle H\rangle - \nabla \cdot (\langle \kappa\rangle \boldsymbol{\nabla} T) = \dot{Q}' \tag{III-46}$$

3.2.3.1. Global residual

Generally, the resolution of the non-linear problem in finite element method is to find the value of the unknown variables which zeros the global residual vectors. In the present work,

the temporal discretized residual for **Eq. (III-46)** after assembly operation at the non-linear iterative step (k) of current time step $t + \Delta t$ can be written:

$$\{\boldsymbol{R}^{(k)}\} = [\boldsymbol{M}]\left(\{\langle \boldsymbol{H}\rangle^{(k)}\} - \{\langle \boldsymbol{H}\rangle^{t}\}\right) + [\boldsymbol{A}]\{\langle \boldsymbol{H}\rangle^{(k)}\} + [\boldsymbol{K}]\{\boldsymbol{T}^{(k)}\} - \{\boldsymbol{B}\} + \{\boldsymbol{Q}\} \quad \textbf{(III-47)}$$

where $\{\langle \boldsymbol{H}\rangle^{t}\}$ is the column vector of average volume enthalpy at time t, which is the beginning of current time step. $\{\langle \boldsymbol{H}\rangle^{(k)}\}$ and $\{\boldsymbol{T}^{(k)}\}$ are the column vector of average volume enthalpy and temperature at the non-linear iteration step (k) in this time step, respectively. $\{\boldsymbol{R}^{(k)}\}$ is the column vector of global residual of this problem at the non-linear iteration step (k) in this time step. The four vectors above have the same dimension of the components with the number of nodes of this problem.

The matrices $[\boldsymbol{M}]$, $[\boldsymbol{A}]$, $[\boldsymbol{K}]$ and the column vector $\{\boldsymbol{B}\}$, $\{\boldsymbol{Q}\}$ are defined as:

$$[\boldsymbol{M}]_{ij} = \int_{\Omega} \frac{1}{\Delta t} N_i N_j d\,\Omega \quad \textbf{(III-48)}$$

$$[\boldsymbol{A}]_{ij} = \int_{\Omega} N_i \langle \boldsymbol{v}\rangle \cdot \boldsymbol{\nabla} N_j d\,\Omega \quad \textbf{(III-49)}$$

$$[\boldsymbol{K}]_{ij} = \int_{\Omega} \langle \kappa\rangle \boldsymbol{\nabla} N_i \cdot \boldsymbol{\nabla} N_j d\Omega + \int_{S_{ext}} h_T N_i N_j dS \quad \textbf{(III-50)}$$

$$\{\boldsymbol{B}\}_i = \int_{S_{ext}} h_T N_i T_{ext} dS \quad \textbf{(III-51)}$$

$$\{\boldsymbol{Q}\}_i = \int_{\Omega} N_i \dot{Q}_{Ti} d\Omega \quad \textbf{(III-52)}$$

where i and j are the global numbers for the nodes, N_i and N_j are the interpolation functions, Δt is the time step. The column vector $\{\boldsymbol{B}\}$ and $\{\boldsymbol{Q}\}$ correspond to the contributions of environmental temperature and input heat.

3.2.3.2. Linearization

The essence of the Temperature Solver is to transform the non-linear resolution to a linear equation using Newton-Raphson iterative scheme. For the iterative step $(k+1)$, the transformed linear equation can be given:

$$\begin{aligned}&\left[([\boldsymbol{M}] + [\boldsymbol{A}])\left(\frac{d\langle H\rangle}{dT}\right)^{(k)} + [\boldsymbol{K}]\right]\{\boldsymbol{dT}\} \\ &= -[\boldsymbol{M}]\left(\{\langle \boldsymbol{H}\rangle^{(k)}\} - \{\langle \boldsymbol{H}\rangle^{t}\}\right) - [\boldsymbol{A}]\{\langle \boldsymbol{H}\rangle^{(k)}\} - [\boldsymbol{K}]\{\boldsymbol{T}^{(k)}\} + \{\boldsymbol{B}\} - \{\boldsymbol{Q}\}\end{aligned} \quad \textbf{(III-53)}$$

with

$$\{\boldsymbol{dT}\} = \left\{\boldsymbol{T}^{(k+1)}\right\} - \left\{\boldsymbol{T}^{(k)}\right\} \quad \textbf{(III-54)}$$

Substitute **Eq. (III-54)** into **Eq. (III-53)** and rearrange it to get the linear equation with respect to $\left\{\boldsymbol{T}^{(k+1)}\right\}$:

$$\begin{aligned}&\left[([\boldsymbol{M}]+[\boldsymbol{A}])\left(\frac{d\langle H\rangle}{dT}\right)^{(k)}+[\boldsymbol{K}]\right]\left\{\boldsymbol{T}^{(k+1)}\right\}\\&=-[\boldsymbol{M}]\left(\left\{\langle\boldsymbol{H}\rangle^{(k)}\right\}-\{\langle\boldsymbol{H}\rangle^{t}\}\right)-[\boldsymbol{A}]\left\{\langle\boldsymbol{H}\rangle^{(k)}\right\}+\left[([\boldsymbol{M}]+[\boldsymbol{A}])\left(\frac{d\langle H\rangle}{dT}\right)^{(k)}\right]\left\{\boldsymbol{T}^{(k)}\right\}\\&\quad+\{\boldsymbol{B}\}-\{\boldsymbol{Q}\}\end{aligned} \quad \textbf{(III-55)}$$

For **Eq. (III-55)**, only $\left\{\boldsymbol{T}^{(k+1)}\right\}$ is unknown, and the values of other variables can be computed by the following, supposing that $\{\boldsymbol{T}^{t}\}$ and $\left\{\boldsymbol{T}^{(k)}\right\}$ are known:

- $\{\langle\boldsymbol{H}\rangle^{t}\}$ is converted from $\{\boldsymbol{T}^{t}\}$ by the $\langle H\rangle - T$ relationship;
- $\left\{\langle\boldsymbol{H}\rangle^{(k)}\right\}$ is converted from $\left\{\boldsymbol{T}^{(k)}\right\}$ by the $\langle H\rangle - T$ relationship;
- $\left(\frac{d\langle H\rangle}{dT}\right)^{(k)} = \frac{\langle H\rangle^{(k)} - \langle H\rangle^{(k-1)}}{T^{(k)} - T^{(k-1)}}$

Note that $\left(\frac{d\langle H\rangle}{dT}\right)^{(k)}$ is calculated using Morgan's approach [Mor78]. $\left\{\boldsymbol{T}^{(k+1)}\right\}$ can be computed by **Eq. (III-55)**. Consequently, the values of the other variables can be updated by:

- $\left\{\langle\boldsymbol{H}\rangle^{(k+1)}\right\}$ is converted from $\left\{\boldsymbol{T}^{(k+1)}\right\}$ by the $\langle H\rangle - T$ relationship;
- $\left(\frac{d\langle H\rangle}{dT}\right)^{(k+1)} = \frac{\langle H\rangle^{(k+1)} - \langle H\rangle^{(k)}}{T^{(k+1)} - T^{(k)}}$

3.2.3.3. Definition of convergence

The residual of **Eq. (III-55)** at the iterative step $(k+1)$ can be given:

$$\begin{aligned}\left\{\boldsymbol{R}_{\boldsymbol{E}}^{(k+1)}\right\} = {}&[\boldsymbol{K}]\left\{\boldsymbol{T}^{(k+1)}\right\}+[\boldsymbol{M}]\left(\left\{\langle\boldsymbol{H}\rangle^{(k+1)}\right\}-\{\langle\boldsymbol{H}\rangle^{t}\}\right)+[\boldsymbol{A}]\left\{\langle\boldsymbol{H}\rangle^{(k+1)}\right\}\\&-\{\boldsymbol{B}\}+\{\boldsymbol{Q}\}\end{aligned} \quad \textbf{(III-56)}$$

The resolution is considered to be converged after $(k+1)$ iterations if the norm of the residual $\left\{\boldsymbol{R}_{\boldsymbol{E}}^{(k+1)}\right\}$ is small enough to reach:

$$\left\|\boldsymbol{R}_{\boldsymbol{E}}^{(k+1)}\right\| < \varepsilon_R \left\|\boldsymbol{R}_{\boldsymbol{E}}^{(1)}\right\| \quad \textbf{(III-57)}$$

where ε_R is a fixed but small value, and $\left\{\boldsymbol{R}_{\boldsymbol{E}}^{(1)}\right\}$ is the residual of first iteration at the current time step given by **Eq. (III-56)** but with the value of variables:

- $\left\{\langle \boldsymbol{H} \rangle^{(1)}\right\}$ is converted from $\{\boldsymbol{T}^t\}$ by the $\langle H \rangle - T$ relationship;
- $\left(\frac{d\langle H \rangle}{dT}\right)^{(1)} = \frac{\langle H \rangle^t - \langle H \rangle^{t-\Delta t}}{T^t - T^{t-\Delta t}}$

As seen in **Eq. (III-55)**, the mass matrix $[\boldsymbol{M}]$ and advection matrix $[\boldsymbol{A}]$ are weighted by the term, $d\langle H \rangle / dT$. Therefore, this term, $d\langle H \rangle / dT$, has a significant influence on the convergence of the final resolution of the Newton – Raphson iterative scheme. In the very beginning of the resolution with $t = 0$, $d\langle H \rangle / dT$ is initialized with a "real" physical value related to the heat capacity of the material. When iteration starts, the initial value of $d\langle H \rangle / dT$ is computed as $\left(\frac{d\langle H \rangle}{dT}\right)^{(1)}$ and then updated by $\left(\frac{d\langle H \rangle}{dT}\right)^{(k+1)}$.

3.2.4. Verification of the FE model for GMAW

The energy conservation equation **Eq. (III-45)** shows that three terms are added on its right hand side, in comparison with the conventional form in [Rap03]. The three terms can be considered as additional with respect to the temporal variation contribution, the transport contribution and diffusion contribution on the right hand side, respectively, due to the change of the LS function, ψ. Therefore, it is necessary to verify them for the energy conservation equation **Eq. (III-45)**.

A 2D case is used to verify the energy conservation equation in Level Set approach. In this 2D case, the FE domain, Ω^{FE}, is composed by two subdomains, Ω^A and Ω^B. Each subdomain is composed by a single phase, namely phase A and B, respectively, shown in **Fig. III-8**. The interface of A subdomain and B subdomain is determined by the Level Set function, ψ, with the value of 0. The numerical parameters for these domain definitions are listed in **Tab. III-1**. It is assumed that no phase transformation takes place between phase A and B. The material properties of phase A and B are tabulated and shown in **Fig. III-9**. In order to simplify this test case, it is supposed that phase A and B have the same density and thermal conductivity listed in **Tab. III-1**. In addition, for the whole FE domain, all the boundaries are adiabatic. That is to say no heat exchange with the outside environment. In this test case, the material is vertically added into A subdomain at the interface of the two subdomains. Therefore,

according to the definition of the axis shown in **Fig. III-8**, the Y component of the velocity of the bottom boundary is set to be 0, and the X components of the velocities of the left and right boundaries are set to be 0, too.

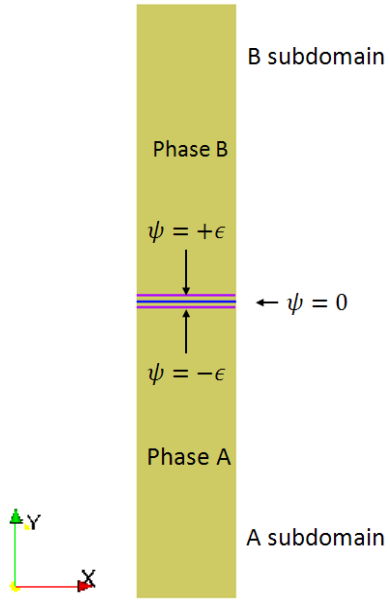

Fig. III-8 Definition of the FE domain with the size of 20×120 mm^2. The FE domain is composed by A subdomain and B subdomain, each of which has the size of 20×60 mm^2. The interface between the two subdomains is represented by the LS function with the value of 0. A transition zone with the half thickness, ϵ, is defined.

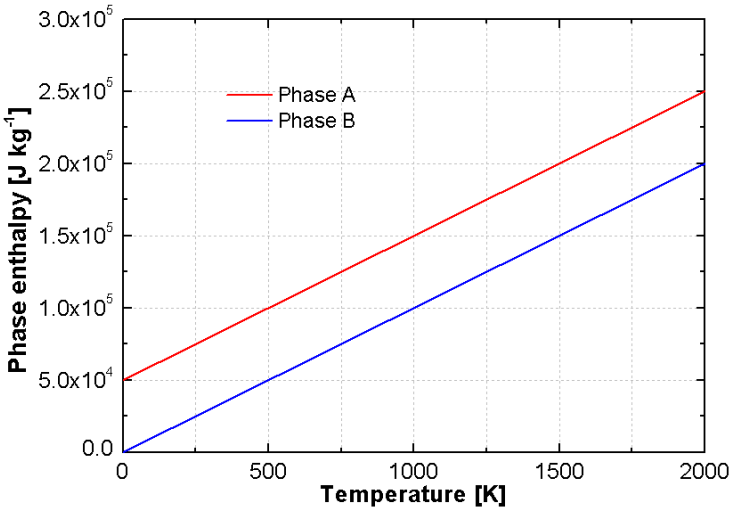

Fig. III-9 Tabulated mass enthalpy with respect to the temperature of phase A and B

Tab. III-1 Parameters of the FE model for the test cases

Parameter	Symbol	Value									Unit
		Test1	Test2	Test3	Test4	Test5	Test6	Test7	Test8	Test9	
FE domain	Ω^{FE}	20×120									mm^2
A subdomain	Ω^{A}	20×60 (bottom part)									mm^2
B subdomain	Ω^{B}	20×60 (upper part)									mm^2
Half thickness of transition zone	ϵ	1.2	1.2	1.2	0.8	1.6	1.2	1.2	1.2	1.2	mm
Time step	Δt	0.025	0.025	0.025	0.025	0.025	0.01	0.05	0.025	0.025	s
FE element size (fixed)	l_{FE}	0.2	0.2	0.2	0.2	0.2	0.2	0.2	0.1	0.3	mm
Density	$\rho^A = \rho^B$	7500									$kg\ m^{-3}$
Initial temperature	$T_0^A = T_0^B$	1000									°C
Thermal conductivity	$\kappa^A = \kappa^B$	0	1	40	0	0	0	0	0	0	$W\ m^{-1}\ K^{-1}$
Temperature of droplets	T_d	1000									°C
Radius of filler wire	R_w	10									mm
Adding velocity of filler wire	v_w	2									$mm\ s^{-1}$
Radius of cavity	R_c	10									mm
Height of cavity	L_c	10									mm

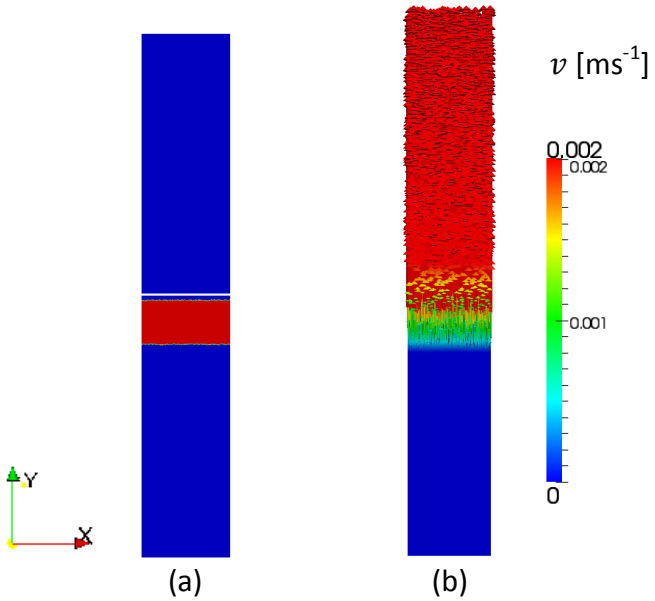

Fig. III-10 (a): location of the cavity for the adding material, and (b): the computed velocity due to the adding material at time t = 0.025 s.

The adding material is supposed to have the same material properties as phase A. The parameters of the adding process are intentionally defined in **Tab. III-1**. The cavity is located below the transition zone. Since $R_w = R_c = R^{FE}$ (R^{FE} represents the half width of the FE domain), the interface between A and B (defined by $\psi = 0$) moves in the Y direction with the value of v_w. The case Test1 is considered to be the reference test, comparing to the other tests in **Tab. III-1**. The location of the cavity and the velocity of the nodes at time t = 0.025 s of Test1 are shown in **Fig. III-10**.

Summarization of this test case:

- No heat flux is put into the FE domain. No heat exchange with outside environment for the FE domain.
- Phase A and B have the same material properties except the $H - T$ relationship. They are initialized to be at the same temperature (1000 °C).
- Filler material has the same properties as phase A and at the same temperature.
- The X dimensions of filler wire, cavity and FE domain are the same.

The objectives of this test case are:

- Verify the energy conservation based on the resolution of **Eq. (III-45)**.
- Verify that the temperature distribution is uniform based on the resolution of **Eq. (III-45)**.

The variation of the energy of the whole system results from two contributions. The first contribution is from the adding material. The second one is from the amount of air pushed out of the system by the adding material. Because of the simplification of this test case, it is available to compute the energy evolution of the whole system analytically. **Fig. III-11** shows the comparison between the analytical and simulated energy evolution of the whole system. It reveals that the simulated energy of the whole system increases linearly and coincides with the analytical result.

However, for the temperature distribution in the system of Test1, it reveals that the temperature varies in the zone where the value of the Heaviside function changes with time and space. This variation from the initial temperature can be reduced by increasing the value of the thermal conductivity of each phase, but cannot be overcome, as shown in **Fig. III-12**, referring to Test1 – Test3. **Fig. III-13** shows the temperature profiles with respect to the Y component of the coordinates of the nodes for Test1 – Test3. The temperature field varies from its initial value at the interface of the two subdomains and its vicinity. The maximum temperature locates at the interface (100 mm of the Y coordinate of the nodes, which corresponds to $\psi = 0$), but the minimum temperature locates beside it. It can be seen that the variation of the temperature decreases as the values of thermal conductivity increases, which indicates that the temperature variation can be reduced by the heat diffusion.

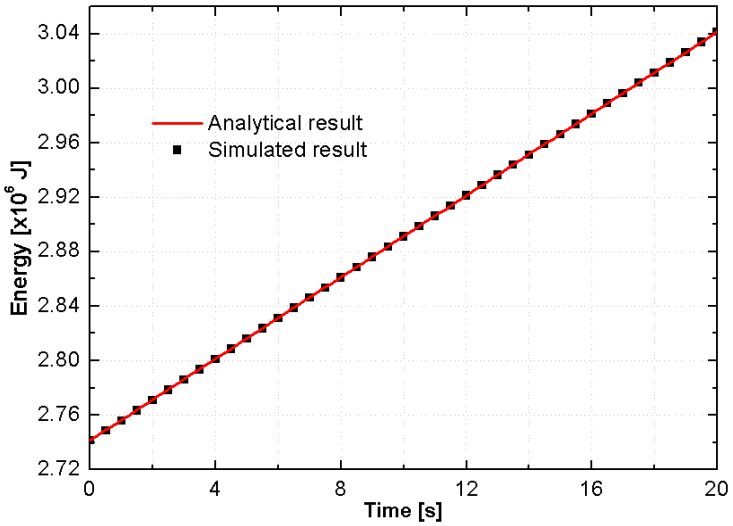

Fig. III-11 Comparison between the analytical and simulated energy of the whole system for Test1.

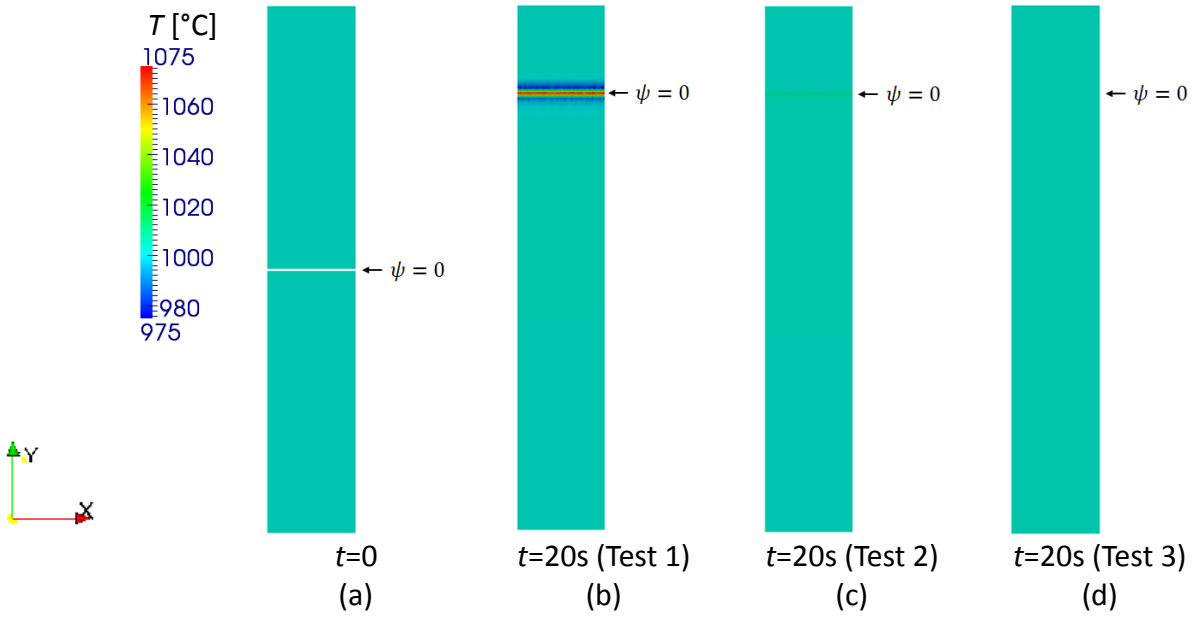

Fig. III-12 Temperature distribution at (a): t=0, (b): t=20 s with $\kappa^A = \kappa^B = 0$ W m^{-1} K^{-1}, (c): t=20 s with $\kappa^A = \kappa^B = 1$ W m^{-1} K^{-1}, and (d): t=20 s with $\kappa^A = \kappa^B = 40$ W m^{-1} K^{-1}.

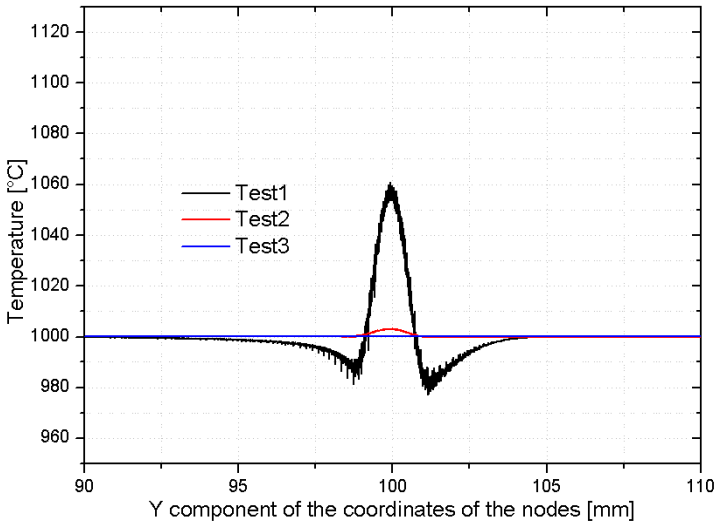

Fig. III-13 Temperature profiles with respect to the Y component of the coordinates of the nodes for Test1, Test2 and Test3.

The values of thermal conductivities are only related to the material properties, which cannot be modified numerically. Reviewing **Eq. (III-45)**, three additional terms are added on the right hand side. It can be seen they are related to the time and space derivatives of the Heaviside function. Therefore, the numerical parameters which affect the change of the Heaviside function are tested:

- half thickness of the transition zone, ϵ, (Test1, Test4, Test5);
- the time step, Δt, (Test1, Test6, Test7);
- the FE element size, l_{FE}, (Test1, Test8, Test9).

Note that the parameters of each test are presented in **Tab. III-1**. **Fig. III-14** shows the temperature profiles with respect to Y coordinates of all the FE nodes at 20 s for Test4 – Test9, comparing with Test1 (reference test).

The influence of ϵ on the temperature distributions is shown in **Fig. III-14** (a). It is seen that the variation of temperature decreases as the value of ϵ increases. This is because the heat exchange is localized in the transition zone. Numerically, the values of $\frac{\partial \mathcal{H}}{\partial t}$ and $\boldsymbol{\nabla}\mathcal{H}$ on the right hand side of **Eq. (III-45)** decrease in the transition zone when ϵ is enlarged. The effects of these additional terms in **Eq. (III-45)** are weakened. Therefore, the temperature differences decrease.

The influence of the time step, Δt, on the temperature distribution is shown in **Fig. III-14** (b). It is seen that the largest variation of temperature happens for the case in which Δt is smallest (*i.e.* Test6). This is mainly due to the increase of the temporal derivatives with respect to the time.

Finally, the influence of FE element size, l_{FE}, on the temperature distribution is shown in **Fig. III-14** (c). Note that the FE mesh is fixed and no mesh adaptation is implemented. The variation of temperature decreases as the value of l_{FE} decreases. Although it is not fully converged in the sense that the two finest meshes give completely identical results, it is believed to obtain converged results with very fine mesh.

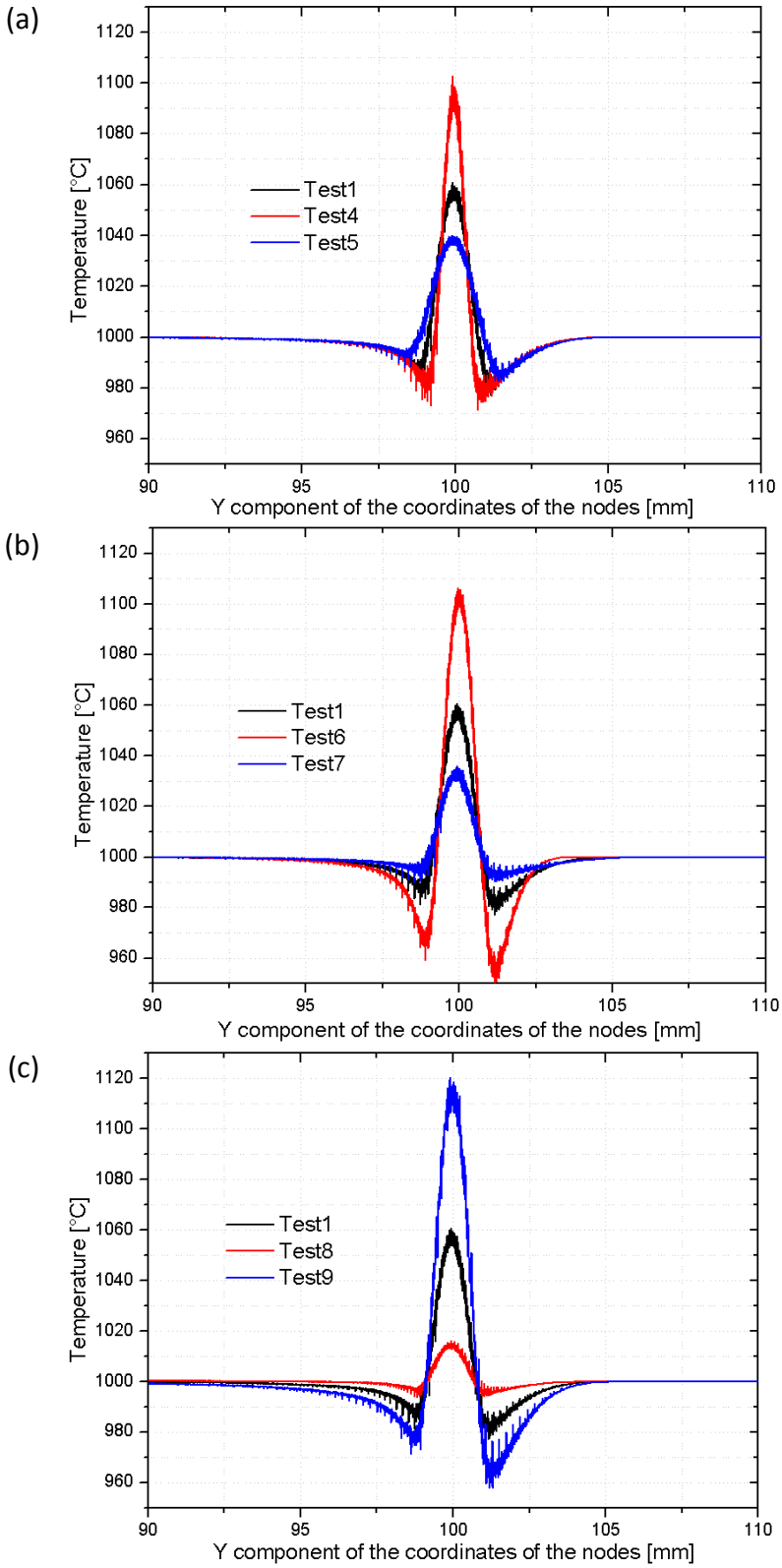

Fig. III-14 Temperature profiles with respect to the Y component of the coordinates of the nodes for (a): Test1, Test4 and Test5, (b): Test1, Test6 and Test7, and (c): Test1, Test8 and Test9. The parameters of each test are presented in **Tab. III-1**.

3.3. CA model

As mentioned in **Chapter II**, the Cellular Automaton model is defined based on four rules: (i) spatial discretization to cells, (ii) neighborhood definition, (iii) cell states definition, and (iv) transition rule. **Section 3.3.1** will present the first three rules. The forth one, *i.e.* transition rule, will be divided into different situations and presented in **Section 3.3.2** – **Section 3.3.5**.

3.3.1. Cell definition

In the present work, the domain of the CA mesh is discretized into a regular lattice of square cells in 2D (shown in **Fig. III-1**) or cubic cells in 3D. All the cells have the same size and keep fixed during the simulation. The required cell size should be small enough to reproduce the branching mechanisms of dendrite arms and thus grain competition. The typical cell size is of the order of 50 to 100 μm [Gan99].

For the neighborhood definition, the Moore type is adopted in the present work. For a specific cell ν, the number of neighboring cells is 8 (1st and 2nd nearest) in 2D, or 26 (1st, 2nd and 3rd nearest) in 3D.

The state of the cell indicates the phases to which it belongs. For the cell ν, its state, I_ν, is defined as:

- $I_\nu = 0$, if this cell locates in the fully liquid zone. It is called liquid cell.
- $I_\nu = 1$, if this cell locates in the growing mushy zone. A decentered growing envelope is created within this cell. It is called growing cell.
- $I_\nu = 2$, if the growing envelope reaches its maximum shape which is predefined depending on its neighborhood. This envelope stops growing. This cell is called fully mushy cell.

In case of the CA model for GMAW process in Level Set approach, a new type is proposed:

- $I_\nu = -10$, if this cell locates in the air domain. This cell is called air cell.

A few notes should be made for the definition of the cell states:

For the liquid cell $(I_\nu = 0)$, it is considered that it is fully liquid (*i.e.* l_0 in **Fig. III-1** (d)).

For the growing cell ($I_\nu = 1$), it is associated with an envelope which locally coincide with the grain shape and crystallographic orientation. The phases of a growing cell can be considered to be the combinations of the extradendritic liquid (l_0), the interdendritic liquid (l_1), and solid (s). Note that the mixture of l_1 and s can be considered as the mushy structure. As explained in **Section 2.2.3**, in order to overcome the influence of the anisotropy of the cell lattice, the envelope is decentered within the site of the corresponding cell. The envelope depends on the nature of the solidifying structure of the material. Taking steel as an example, the preferred dendritic growth directions of δ-Fe (BCC crystal structure) and γ-Fe (FCC crystal structure) are both <100> (see **Tab. I-1**). The trunks and arms of the dendritic grains align along the <100> directions. Therefore, the envelopes associated with the cells are defined as a square in 2D and an octahedron in 3D with the main half diagonals to be the <100> crystallographic directions of the corresponding grains. The apices of the envelopes (4 apices for square cell in 2D and 6 apices for cubic cell in 3D) are considered to be the dendrite tips of the crystal. Dendrite tip growth kinetics can thus be implemented on the apices to control the envelope growth [Gan99, Car12]. The undercooling of the dendrite tip is considered to be the same as that of the cell. The positions of the apices finally determine the shape of the envelope. When the shape of the growing envelope is large enough to reach the maximum shape which is predefined depending on the neighborhood, the envelope stops growing.

For the fully mushy cell ($I_\nu = 2$), it is considered that it corresponds to the interdendritic liquid (l_1), and solid (s). The fraction of the mushy structure in the cell is equal to be 1.

Note that the cells with the states $I_\nu \geq 0$ are used to represent the metal. It is enough to describe the grain structure evolution during GTAW process in which no filler material is added. However, in case of GMAW process, the air domain is contained in the CA model besides the metal domain. Therefore, the air cell is used to occupy the space of air domain. For the air cell ($I_\nu = -10$), it is considered that it is air phase. The negative value of its state is used to distinguish it from the metal cells.

In the present work, it is assumed that no nucleation takes place in the weld pool. The following sections will present the algorithm of transition rules for the cells among different

states: (i) melting, (ii) grain growth and capture, (iii) fraction of envelope and (iv) adding metal (in case of GMAW).

Note that the two parts (ii) and (iii) belong to the work of T. Carozzani *et al.* [Car12]. In order to provide a complete description of the CA model for welding process, the algorithms are yet presented hereafter.

Before the introduction of the transition rules, the basic principle of the CA model should be emphasized: In CA model, each cell is scanned sequentially. When a specific cell v is being scanned, it is considered as the "current cell". It is available to change the state of the current cell by the transition rule, but not accepted to change those of its neighboring cells.

3.3.2. Melting

During the welding process, the workpiece is heated by the heat source. Physically, the initial metal encounters one of the two situations below:

- The metal is fully melted to become liquid and form the weld pool.
- The metal is partially melted and will serve for epitaxial growth following the direction of the temperature gradient when the solidification takes place.

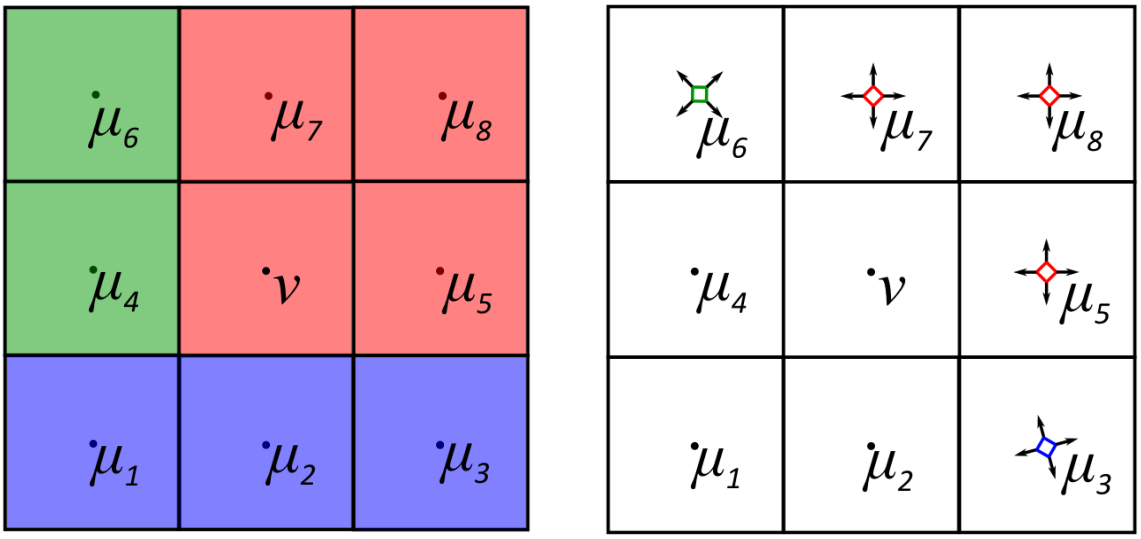

(a) at t before melting (b) at $t + \Delta t$ after melting

Fig. III-15 illustration of the transition of the cell states during melting

In the CA model, the melting algorithm is proposed to reflect both situations above. As shown in **Fig. III-15** (a), a cluster of cells with the initial fully mushy states $(I_v = I_{\mu_i} = 2)$ before melting belongs to three grains which are marked by blue, green and red colors,

respectively. At time t, the temperatures of all the cells are below the liquidus temperature, T_L.

At time $t + \Delta t$, the temperatures of the non-liquid metal cells ν, μ_1, μ_2, and μ_4 become higher than liquidus temperature, *i.e.* $T_\nu \geq T_L$ and $T_{\mu_i} \geq T_L$ with $i = 1, 2\ and\ 4$, the states of the four cells are thus changed to be liquid, *i.e.* $I_\nu = 0$ and $I_{\mu_i} = 0$ with $i = 1, 2\ and\ 4$. In **Fig. III-15** (b), the four cells are thus changed to be white color as liquid cells.

In addition, for the other fully mushy cells μ_i ($i = 3, 5, 6, 7, and\ 8$) which are still below liquidus temperature, they are considered to locate at the solid/liquid interface. Consequently, they are changed to be growing state ($I_{\mu_i} = 1$ with $i = 3, 5, 6, 7, and\ 8$). As shown in **Fig. III-15** (b), new envelopes with the value of half diagonal equal to 0 is created in the center of μ_i ($i = 3, 5, 6, 7,\ and\ 8$), *i.e.* $C_{\mu_i}^{en} = C_{\mu_i}$. The information of crystallographic orientations and the grain numbers is kept as their initial values. Note that the arrows represent the preferred growth direction (<10> in 2D and <100> in 3D).

According to the principle of CA model, only the state of current cell can be changed. So, when the current cell is switched to μ_i during scanning, I_{μ_i} could be changed. In conclusion, the transition rule for melting is listed in **Tab. III-2**, assuming that the current cell is ν:

Tab. III-2 Transition rule for melting

Cell state before transition	Transition condition	Cell state after transition
$I_\nu > 0$	$T_\nu \geq T_L$	$I_\nu = 0$
$I_\nu = 2$	∃ neighboring cell μ, $I_\mu = 0$	$I_\nu = 1$

3.3.3. Grain growth and capture

As the heat source moves away, solidification takes place in the fusion zone. The partially melted grains at the solid/liquid interface grow epitaxially followed by the grain growth competition. This grain growth mechanism is explained in **Section 1.3.1** and **Section 1.3.2**.

The algorithm of grain growth and capture defines the transition rule for a cell which evolves from liquid ($I_\nu = 0$) to growing ($I_\nu = 1$). As shown in **Fig. III-16**, it is locally reflected by the expansion of the envelope of the cell with its half diagonal defined as the preferred growth direction <100>. The apices of the envelope correspond to the leading dendrite tips of the crystal. As the half diagonal of the envelope R_ν^{en} increases, the positions of the apices are

updated. The growth velocity of R_ν^{en}, v_ν^{en}, is a function of the local undercooling, ΔT_ν, taken at the center of cell ν, which itself is a function of time. The relationship between v_ν^{en} and ΔT_ν can be modeled by the dendrite tip kinetics model, such as the KGT model [Kur86].

The envelope of a cell can be created in the following ways:

- The envelope is created in a cell which is at the boundary with a liquid cell (this liquid cell is formed due to the melting).
- The envelope is created in a liquid cell which is captured by neighboring growing cells.

As explained in **Section 3.3.2**, for the cell ν that is located at the boundary with the liquid after remelting, the centers of the cell and the envelope coincide to each other, *i.e.* $C_\nu^{en} = C_\nu$. Therefore, the half diagonal R_ν^{en} is simply given by the integral over time of the growth of the dendrite tip:

$$R_\nu^{en}(t) = \int_{t_{\nu\,M}}^{t} v_\nu^{en}\big(\Delta T(t')\big)dt' \qquad \textbf{(III-58)}$$

where $t_{\nu\,M}$ is the time when ν is changed to be growing cell due to the melting, $\Delta T(t')$ is the local undercooling of the cell, ant t is the current time.

However, for the cell ν which is captured by neighboring growing cells, the centers of the cell and the envelope are not necessarily equal to each other. R_ν^{en} can be computed by:

$$R_\nu^{en}(t) = R_\nu^{en0} + \int_{t_{\nu\,capt}}^{t} v_\nu^{en}\big(\Delta T(t')\big)dt' \qquad \textbf{(III-59)}$$

where $t_{\nu\,capt}$ is the time when ν is captured, R_ν^{en0} is the initial value of half diagonal of this envelope. The determination of R_ν^{en0} is presented hereafter.

As long as the envelope of ν is large enough to encompass the center of a neighboring liquid cell, μ ($I_\mu = 0$), μ is then considered to be "captured". Its state, I_μ, is changed to be 1. At the same time, a new decentered envelope is created to associate to it. The grain number and crystallographic orientation associated to μ are set to be identical with those of ν. Note ν is called capturing cell, and μ is called captured cell in the following.

The capturing cell ν can be the cell which is captured by its neighbors at previous time t as shown in **Fig. III-16** (a). A decentered square envelope is set to associate to cell ν with the

initial value of half diagonal, R_ν^{en0}. The envelope then grows at the velocity of v_ν^{en} in the directions of <10> (*i.e.* $[10]$, $[01]$, $[\bar{1}0]$, $[0\bar{1}]$). Its half diagonal, R_ν^{en}, is then updated based on **Eq. (III-59)**. In the time-stepping calculation of the CA model, suppose that the envelope of ν will encompass the center of cell μ, at time $t + \Delta t$ shown in **Fig. III-16** (b). Cell μ is then considered to be "captured" by ν.

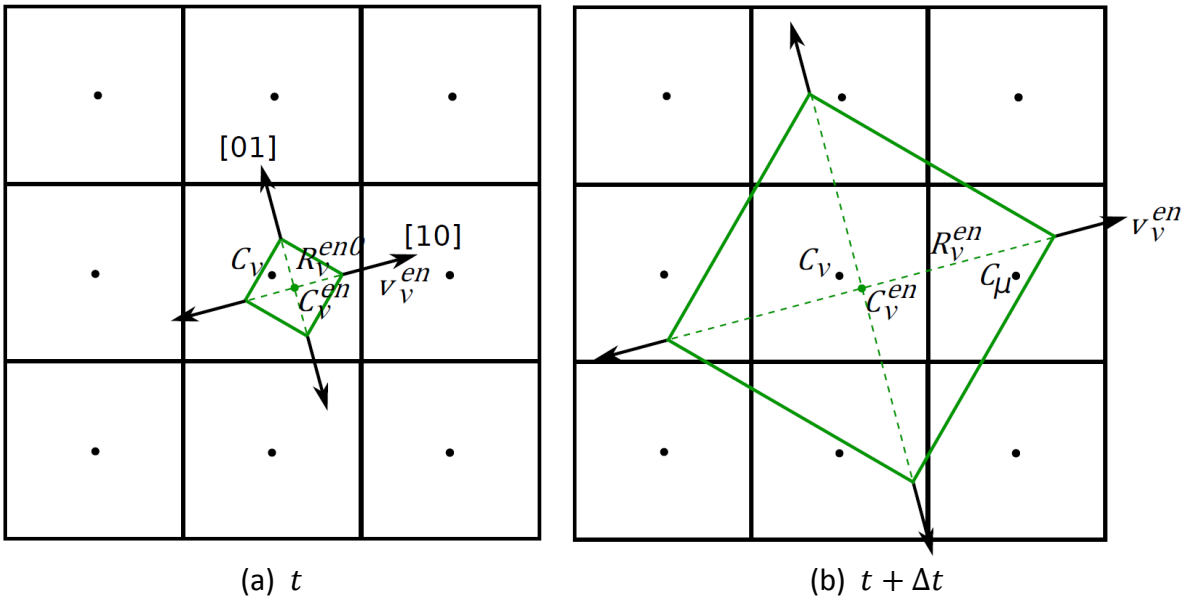

(a) t (b) $t + \Delta t$

Fig. III-16 Illustration of growth of the decentered envelope which is associated to the cell ν from time t to $t + \Delta t$

When μ is captured, a new decentered envelope is created to itself, positioned in such a way that one of its apices coincides with the apex of envelope of ν nearest to μ (*e.g.* $S_{\mu 1}^{en} = S_{\nu 1}^{en}$). This algorithm is shown in **Fig. III-17**. In order to avoid the problem that the envelope becomes too large over time, this envelope is truncated with its half diagonal given by [Gan97]:

$$R_\mu^{en0} = \frac{\sqrt{2}}{2} S_{\mu 1}^{en} S_{\mu 4}^{en} = \frac{\sqrt{2}}{2} \left[Min\left(AS_{\nu 1}^{en}, \sqrt{2} l_{cell}\right) + Min\left(AS_{\nu 4}^{en}, \sqrt{2} l_{cell}\right) \right] \quad \textbf{(III-60)}$$

where A is the point where the center of μ, C_μ, projects on the $(1\bar{1})$ face of the square envelope of ν, defined at the time of capture, $t_{\nu\, capt}$. $(1\bar{1})$ is indeed considered as the capturing face regarding the position of the grain envelope and the cell center, C_μ. $AS_{\nu 1}^{en}$ and $AS_{\nu 4}^{en}$ are equivalent to the distances between C_μ and (11) and $(\bar{1}\bar{1})$ faces, respectively. l_{cell} is the cell size. R_μ^{en0} is the value of initial half diagonal of this envelope.

Once the position and the initial half diagonal of the new envelope are known, the center of the envelope, C_μ^{en}, is defined correspondingly. The envelope of μ then grows based on dendrite tip kinetics model considering the local undercooling of μ itself.

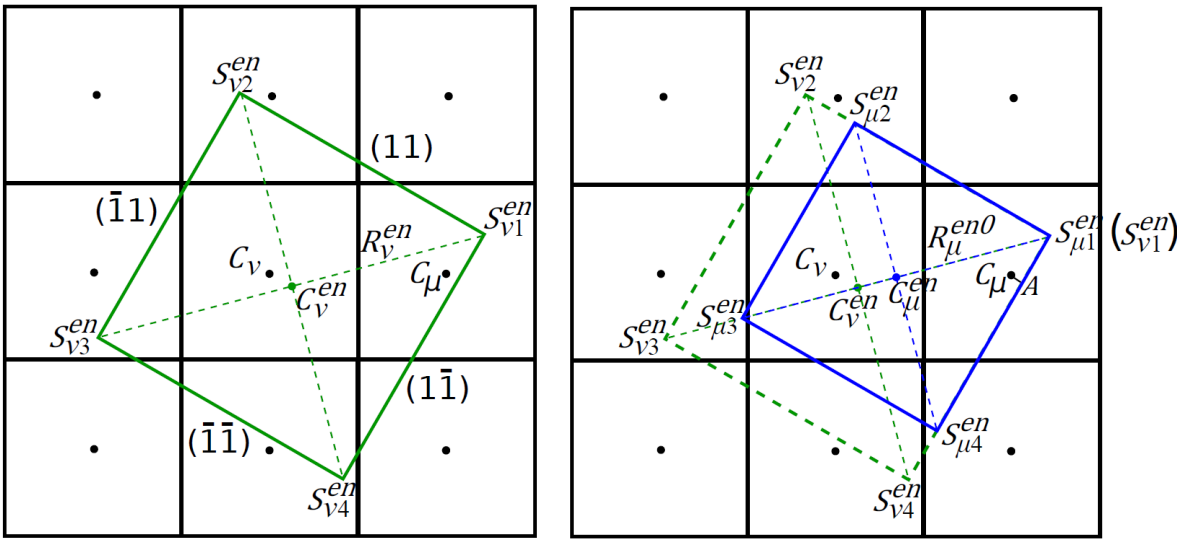

Fig. III-17 illustration of the square envelope of ν (a), and the new created square envelope of μ (b) at the time of capture

The algorithm of grain growth and capture in 3D is similar to that in 2D, and presented in detail in [Gan97, Car12b].

In case the cell μ is captured by several neighboring growing cells during the same time step, the neighboring cell with the most grown envelope is favored. In the other words, μ is only considered to be captured by the neighboring cell which has the largest envelope.

Similarly to the transition rule for melting, it is forbidden to change the states of μ when the current cell is ν. So, when the current cell is switched to μ by the scanning, I_μ could be changed if it is captured by its neighboring cell ν. Assuming that the current cell is ν, the transition rule for capture is thus:

Tab. III-3 Transition rule for capture

Cell state before transition	Transition condition	Cell state after transition
$I_\nu = 0$	Captured by neighboring cell	$I_\nu = 1$

3.3.4. Fraction of envelope

An area fraction in 2D or a volume fraction in 3D of the envelope g_v^{en} is defined for cell v. g_v^{en} is determined by:

$$g_v^{en} = Min\left(\frac{V_v^{en} - V_v^{en0}}{V_v^{en\,max} - V_v^{en0}}, 1\right) \quad \textbf{(III-61)}$$

where V_v^{en0} is the initial volume of the envelope in 3D, $V_v^{en\,max}$ is the maximum volume of the envelope, defined to encompass all the centers of its neighboring cells, and V_v^{en} is the volume of the envelope at current time. These volumetric parameters correspond to the area parameters in 2D.

Note that the initial volume V_v^{en0} can be computed easily when the envelope is created (only equal to 0 in the case of melting). At the same time, the maximum volume $V_v^{en\,max}$ can be estimated due to the position of envelope. The envelope grows until it equals (or exceeds in the time-stepping calculation) $V_v^{en\,max}$. So, there are three cases for g_v^{en}:

- $g_v^{en} = 0$, the envelope does not exist. The cell v is in the state of fully liquid, *i.e.* $I_v = 0$;
- $0 < g_v^{en} < 1$, the envelope is growing, but it does not reach the maximum value. The cell v is in the growing state, *i.e.* $I_v = 1$;
- $g_v^{en} = 1$, the envelope is equal to the maximum value and encompasses all the centers of the neighboring cells. The envelope stops growing, and the cell v is in the fully mushy state, *i.e.* $I_v = 2$.

The value of g_v^{en} can be used to determine the transition of cell from growing state to fully mushy state. When g_v^{en} increases to be 1, the state of the cell changes to be 2, *i.e.* $I_v = 2$. Afterwards, the envelope stops growing. So, the third transition rule is:

Tab. III-4 Transition rule for fraction of envelope

Cell state before transition	Transition condition	Cell state after transition
$I_v = 1$	$g_v^{en} = 1$	$I_v = 2$

3.3.5. Adding metal

In GMAW process, the filler metal detached from the consumable electrode is added into the fusion zone. The interface between the metal domain and air domain thus changes due to the formation of the weld bead. In the CA model, the phenomenon of adding metal is thus reflected by the transformation from the air cell to liquid cell (the adding droplets are assumed to be liquid).

According to the definition of CA cells, if the cell ν is located in the air domain, it is defined as an air cell. That is to say, the value of its LS function ψ_ν is positive. As soon as the value of ψ_ν changes to be negative or zero, ν is considered to be encompassed by the weld bead. Consequently, the state of ν is changed from $I_\nu = -10$ to $I_\nu = 0$. The fourth transition rule is thus:

Tab. III-5 Transition rule for adding metal

Cell state before transition	Transition condition	Cell state after transition
$I_\nu = -10$	$\psi_\nu \leq 0$	$I_\nu = 0$

Note that when the air cell is changed to be liquid cell, it is considered that it belongs to the metal domain. It will affect its neighboring metal cells in the following time steps. Therefore, the transition rules described in **Section 3.3.2** - **3.3.4** will be applied on it.

3.4. Coupling of FE and CA models

CAFE model is the coupling of the resolutions of Finite Element model and Cellular Automaton model. The two models are implemented in an adaptive FE mesh and a fixed CA mesh, respectively. In addition, the CA grid is superimposed on the CA mesh. Therefore, the transportation of the fields among them is essential to the resolution of the CAFE model.

3.4.1. Transport FE mesh→CA mesh→CA cells

The resolution of the energy conservation is implemented on the adaptive FE mesh. Therefore, fields such as the temperature should be transported to CA cells for the resolution of the CA model. The transportation from the FE mesh to the CA cells is linked by the CA mesh. In other words, the fields are transported from FE nodes to CA nodes, and then transported from CA nodes to CA cells.

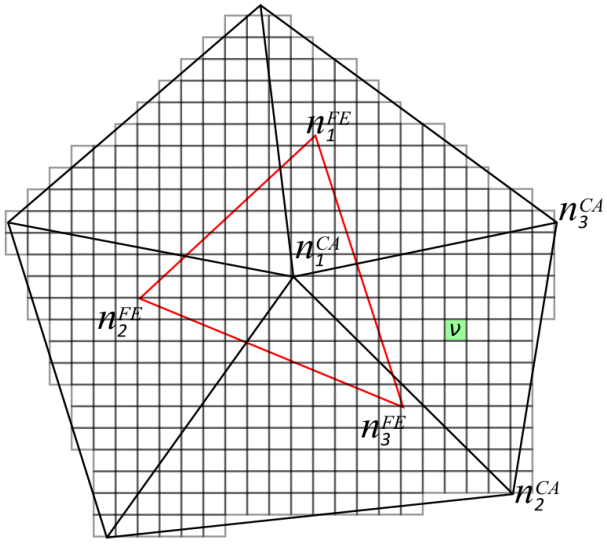

Fig. III-18 Topological links among the triangular FE element, CA element and a square cell.

Superimposing the CA mesh on the FE mesh in the same space, suppose a specific CA node n_j^{CA} (*e.g.* n_1^{CA} shown in **Fig. III-18**) is located inside one FE element E^{FE} composed by FE nodes n_i^{FE} ($n_i^{FE} \in E^{FE}$, *e.g.* n_1^{FE}, n_2^{FE} and n_3^{FE} shown in **Fig. III-18**). The transported value of the variable $x_{n_j^{CA}}^t$ for the CA node n_j^{CA} at time t is interpolated from the variable $x_{n_i^{FE}}^t$ of the FE node n_i^{FE}($n_i^{FE} \in E^{FE}$) by the relation:

$$x_{n_j^{CA}}^t = \sum_{n_i^{FE} \in E^{FE}} \phi_{n_i^{FE}}\left(n_j^{CA}\right) x_{n_i^{FE}}^t \qquad \textbf{(III-62)}$$

where $\phi_{n_i^{FE}}\left(n_j^{CA}\right)$ is the interpolation function of FE node n_i^{FE} estimated for CA node n_j^{CA}.

In addition, for the CA cell v, which is located inside one CA element E^{CA} composed by CA nodes n_j^{CA} ($n_j^{CA} \in E^{CA}$, *e.g.* n_1^{CA}, n_2^{CA}, and n_3^{CA} shown in **Fig. III-18**), the transported value of the variable x_v^t is then interpolated from the variable $x_{n_j^{CA}}^t$ of the CA node n_j^{CA} ($n_j^{CA} \in E^{CA}$) by the relation:

$$x_v^t = \sum_{n_j^{CA} \in E^{CA}} \phi_{n_j^{CA}}(v)\, x_{n_j^{CA}}^t \qquad \textbf{(III-63)}$$

where $\phi_{n_j^{CA}}(v)$ is the interpolation function of CA node n_j^{CA} estimated for cell v.

In the present work, the transported variables from FE mesh to CA cells are the temperature T and LS function ψ (Note T for GTAW, T and ψ for GMAW). It should also be noticed that in

the case of an evolution of this model, any other fields computed on the FE mesh can be transported into any cell. This can help to improve the computation of cell state evolution regarding macro scale evolution.

3.4.2. Transport CA cells→CA mesh→FE mesh

The resolution of the CA model is actually implemented in the CA grid. By scanning the CA cells, the fraction of the envelope, g_v^{en}, is computed. g_v^{en} represents the fraction of the mushy structure (*i.e.* the mixture of the interdendritic liquid (l_1), and solid (s)), which is used to determine the conversion of the enthalpy to temperature based on the solidification path. This conversion is implemented in FE nodes. Therefore, it is necessary to transport g_v^{en} to the FE nodes.

Firstly, compute the mushy fraction of CA node, n_j^{CA}, by scanning the CA cells (rigorously the active cells due to the dynamic allocation algorithm, which will be explained in **Section 3.5**) which are related to n_j^{CA}. Supposing that the CA elements E^{CA} (usually several CA elements) are connected to n_j^{CA} (*e.g.* 5 CA elements are connected to the CA node n_1^{CA} shown in **Fig. III-18**), the fraction of the mushy structure of CA node n_j^{CA} is computed by the relation:

$$g_{n_j^{CA}}^{m} = \frac{\sum_{v \in E^{CA}} \phi_{n_j^{CA}}(v)\, g_v^{en}}{\sum_{v \in E^{CA}} \phi_{n_j^{CA}}(v)} \qquad \textbf{(III-64)}$$

where $g_{n_j^{CA}}^{m}$ is the mushy fraction of the CA node n_j^{CA}.

Secondly, the mushy fraction of CA node is interpolated to FE node. It is similar to the transportation method from FE nodes to CA nodes. Superimposing the FE mesh on the CA mesh, if a specific FE node n_i^{FE} is located inside one CA element E^{CA} composed by CA nodes n_j^{CA} ($n_j^{CA} \in E^{CA}$), the transported value of the mushy fraction $g_{n_i^{FE}}^{m}$ for the FE node n_i^{FE} is interpolated by the relation:

$$g_{n_i^{FE}}^{m} = \sum_{n_j^{CA} \in E^{CA}} \phi_{n_j^{CA}}(n_i^{FE})\, g_{n_j^{CA}}^{m} \qquad \textbf{(III-65)}$$

where $\phi_{n_j^{CA}}(n_i^{FE})$ is the interpolation function of CA node n_j^{CA} estimated for FE node n_i^{FE}.

Two notes for the transportation algorithm above are listed here:

- Calculation of $g_{n_j^{CA}}^m$: in the present work, the CA model is implemented with the algorithm of dynamic allocation of the CA cells. That is to say not all the CA elements connected to n_j^{CA} are activated in the computation memory. In the other words, the CA elements inside which all the CA cells are fully mushy (*i.e.* $g_v^{en} = 1$) are deactivated. This dynamic allocation algorithm will not affect the calculation of $g_{n_j^{CA}}^m$ for the active CA elements. It will be explained in **Section 3.5.2**.
- Calculation of $g_{n_i^{FE}}^m$: in the present work, the size of dimension of the CA mesh is not necessary identical to that of the FE mesh (usually the CA mesh is smaller than the FE mesh in order to reduce the computation cost for the CA resolution). For a specific FE node n_i^{FE} which is located outside the CA mesh, the computation of $g_{n_i^{FE}}^m$ is linearly interpolated from its neighbors. In order to prevent interpolation errors, the dimension of the CA mesh should be chosen large enough to cover the growing structure to ensure that $g_{n_i^{FE}}^m = 1$ for n_i^{FE} which is located beyond the limits of the CA mesh.

3.4.3. Microscopic time step

In the CAFE model, the FE time step, Δt, which is called macroscopic time step, is used to resolve the energy conservation equation. The CA time step, δt, which is called microscopic time step, is used for the resolution of the CA model. δt should be small enough to prevent the propagation of the dendritic growth front (*i.e.* the update of the positions of the apices for the growing envelope) over a distance larger than the cell size. Generally, Δt is too large to fulfill this demand. Thus, δt is re-computed to divide the macroscopic time step by the following equation:

$$\delta t = Min\left(\alpha_{CA}\frac{l_{cell}}{v_{v\,max}^{en}}, \Delta t\right) \quad \textbf{(III-66)}$$

where α_{CA} is a coefficient of the microscopic time step ($\alpha_{CA} \leq 1$), $v_{v\,max}^{en}$ is the maximum dendritic growth velocity, which corresponds to the maximum value of the velocity for the growing cells computed by the KGT model [Kur86]. In the present work, only the growing cells ($I_v = 1$) are scanned for computing the microscopic time step.

The CA model is resolved over the microscopic time step δt from an initial microscopic time $t_m = t$ to the time $t_m = t + \delta t$. This update of t_m stops until $t_m = t + \Delta t$. Note that the final update might use the residual microscopic time step $\delta t' = Min(\delta t, \Delta t - \sum \delta t)$. In addition, the temperature of the cell does not evolve among the micro time steps. That is to say $T_v^{t+\delta t} = T_v^t$. More details about this explicit iterative scheme is presented by Carozzani [Car12b]

3.4.4. Average volume enthalpy-temperature relationship

As explained in **Section 3.2.3**, the energy conservation equation **Eq. (III-3)** and **Eq. (III-43)** can be resolved if the $\langle H \rangle - T$ relationship has been established. **Eq. (III-3)** is a special case of **Eq. (III-43)** with $\mathcal{H} = 0$ and $\boldsymbol{v} = 0$. The computation for $\langle H \rangle$ in LS approach is presented hereafter.

During GMAW, the whole domain is divided into metal and air domains. The metal domain can be considered to be composed by two structures, namely the fully liquid structure and the growing structure (see **Fig. III-1**). The fully liquid structure, which is composed by only the liquid phase (l_0), can be considered to correspond to the structure of the weld pool (*i.e.* $g^m = 0$). However, the growing structure, which is composed by a mixture of the liquid phase (l_1) and solid phase (s), can be considered to correspond to the partially mushy structure where $0 < g^m < 1$ as well as the fully mushy structure $g^m = 1$.

The $\langle H \rangle - T$ relationship can be established by the following relations:

$$\langle H \rangle = \mathcal{H} \langle H \rangle^{\mathbb{A}} + (1 - \mathcal{H}) \langle H \rangle^{\mathbb{M}} \quad \textbf{(III-67)}$$

$$\langle H \rangle^{\mathbb{A}} = \langle H^a \rangle^a \quad \textbf{(III-68)}$$

$$\langle H^a \rangle^a = \langle H^a \rangle^a (T) \quad \textbf{(III-69)}$$

$$\langle H \rangle^{\mathbb{M}} = g^m \langle H^m \rangle^m + (1 - g^m) \langle H^{l_0} \rangle^{l_0} \quad \textbf{(III-70)}$$

$$\langle H^m \rangle^m = \sum_\alpha g^\alpha \langle H^\alpha \rangle^\alpha \quad \textbf{(III-71)}$$

$$g^\alpha = g^\alpha (\langle w_c \rangle, T) \quad \textbf{(III-72)}$$

$$\langle H^\alpha \rangle^\alpha = \langle H^\alpha \rangle^\alpha (\langle w_c^\alpha \rangle^\alpha, T) \quad \textbf{(III-73)}$$

$$\langle w_c^\alpha \rangle^\alpha = \langle w_c^\alpha \rangle^\alpha (\langle w_c \rangle, T) \quad \textbf{(III-74)}$$

$$\langle H^{l_0} \rangle^{l_0} = \langle H^{l_0} \rangle^{l_0} \left(\langle w_c^{l_0} \rangle^{l_0}, T \right) \quad \textbf{(III-75)}$$

$$\langle w_c^{l_0} \rangle^{l_0} = \langle w_c \rangle \quad \textbf{(III-76)}$$

where $\langle H^a \rangle^a$ is the volume enthalpy of air, g^m is the volume fraction of the growing structure, $\langle H^m \rangle^m$ and $\langle H^{l_0} \rangle^{l_0}$ are the intrinsic volume enthalpy of the growing structure and the fully liquid structure (l_0), respectively, g^α and $\langle H^\alpha \rangle^\alpha$ are the volume fraction and the intrinsic volume enthalpy of the phase α, respectively, $\langle w_c \rangle$ is the average composition of the component c, $\langle w_c^\alpha \rangle^\alpha$ and $\langle w_c^{l_0} \rangle^{l_0}$ are the composition of the component c in phase α in the growing structure and in the fully liquid structure, respectively.

It is necessary to explain the set of equations in detail. As the whole domain is composed by metal domain and air domain, the average volume enthalpy is computed by the summation of volume enthalpy ($\langle H \rangle^{\mathbb{A}}$ for air and $\langle H \rangle^{\mathbb{M}}$ for metal) weighted by the space fraction ($\mathcal{H}$ for air and $1 - \mathcal{H}$ for metal) of each domain reflected by **Eq. (III-67)**. Only air phase exist in the air domain. **Eq. (III-68)** shows that the volume enthalpy of air $\langle H \rangle^{\mathbb{A}}$ equals to the intrinsic volume enthalpy of air phase, which is only dependent on the temperature (**Eq. (III-69)**). However, for the metal, the volume enthalpy $\langle H \rangle^{\mathbb{M}}$ is computed by the summation of the intrinsic volume enthalpy ($\langle H^m \rangle^m$ for the growing structure and $\langle H^{l_0} \rangle^{l_0}$ for the fully liquid structure) weighted by corresponding fraction of each structure (g^m for the growing structure and $(1 - g^m)$ for the fully liquid structure), which is reflected by **Eq. (III-70)**. Similarly, **Eq. (III-71)** means that the volume enthalpy of the growing structure $\langle H^m \rangle^m$ is the summation of the intrinsic volume enthalpy of each phase $\langle H^\alpha \rangle^\alpha$ weighted by its corresponding volume fraction g^α (see **Section 4.1** for the definition of the considered phases). For **Eq. (III-72)**, g^α is dependent on the average composition of the material $\langle w_c \rangle$ and the local temperature T. **Eq. (III-73)** and **(III-74)** show that the $\langle H^\alpha \rangle^\alpha$ depends on the local temperature T and intrinsic composition $\langle w_c^\alpha \rangle^\alpha$, which depends on the average composition of the material. Finally for the fully liquid structure which is composed by only the liquid phase l_0, its intrinsic volume enthalpy $\langle H^{l_0} \rangle^{l_0}$ depends on T and intrinsic composition $\langle w_c^{l_0} \rangle^{l_0}$, shown in **Eq. (III-75)**. $\langle w_c^{l_0} \rangle^{l_0}$ is identical to the average composition of the material $\langle w_c \rangle$, shown in **Eq. (III-76)**.

In addition, $\langle H^a \rangle^a(T)$, $g^\alpha(\langle w_c \rangle, T)$, $\langle H^\alpha \rangle^\alpha(\langle w_c^\alpha \rangle^\alpha, T)$, $\langle w_c^\alpha \rangle^\alpha(\langle w_c \rangle, T)$ and $\langle H^{l_0} \rangle^{l_0}\left(\langle w_c^{l_0} \rangle^{l_0}, T\right)$ are tabulated thanks to the software Thermo-Calc [The13] using the TCFE6 thermodynamic database [Shi08]. Each of them depends on the variables in the corresponding parentheses in the tabulation.

3.5. Dynamic allocation

In the present work, the goal of the CA model is to simulate the grain structure in weld pools by changing the state indexes of the cells. According to Gandin *et al.*[Gan94], the branching mechanisms of dendrite arms and thus grain competition can be well reproduced when the cell size is smaller than the critical branching size. This means a typical cell size of the order of 50 to 100 μm is needed. In 3D simulations, it corresponds to 1 to 8 million cubic cells per cm^3. However, the intended resolution scale of the industrial welding model is in the magnitude of meter with a minimum representative domain given by the dimension of a typical coupon, e.g. 350×150×12 mm^3 corresponding to 0.63 to 5.04 billion cells. It would cost a lot of resources to resolve the CA model if all the cells of the coupon are allocated into the memory of the computer. In addition, for modeling of the welding process, the solidification grain structure is usually a small part of the whole domain. In other words, only a small part of the whole domain is taken into account to resolve the CA model, and the rest keeps unchanged (In the present work, the grain structure evolution in the HAZ is neglected). Therefore, a dynamic allocation strategy for the CA cells is included in the CAFE model.

3.5.1. Storage of initial structure

Under welding, the workpiece is at low temperature before being heated and melted by a heat source. Therefore, the initial solid structure is required before calculation. The initial solid structure, usually equiaxed, is deduced from a first CAFE simulation of the structure formed during casting assuming nucleation and growth of grains in a uniform temperature domain [Car12]. The final casting structure is consequently equiaxed. It serves as the initial welding structure and is stored on a hard disk as a set of binary files. In order to satisfy the allocation scheme that will be presented hereafter, each binary file corresponds to a specific CA element. Because the CA mesh is fixed, each binary file can be uniquely linked to the barycentric coordinates of the corresponding CA element. Note that other initial structures could be considered, for instance with an initial texture and elongation that would result from a rolling process of the coupon. Because the present structure is fully equiaxed, grains have an isotropic shape and no preferred crystallographic orientation with respect to the axes of the simulation domain. This strategy of storage is illustrated in **Fig. III-19**. For example, the CA element highlighted in red color in **Fig. III-19** (a) corresponds to the binary

file "a_1_b_1_c_1.bin" in **Fig. III-19** (b) with a_1, b_1 and c_1 linked to its barycentric coordinates. In the same way, each CA element is uniquely linked to a binary file. The number of binary files is thus equal to the number of CA elements.

As each binary file corresponds to a specific CA element, the CA cells which locate inside this CA element are stored in this binary file. In order to retrieve the grain structure by the successive treatment, the stored information for a specific CA cell ν is:

- The index number of the CA cell, ν;
- The index number of the grain which ν belongs to, I_ν^{Grain};
- The crystallographic orientation of the grain which ν belongs to, ψ_ν, θ_ν and ϕ_ν.

In GTAW process, the initial grain structure linked to the CA model is that of the workpiece. Only the fully mushy cells ($I_\nu = 2$) are allowed to be stored in the corresponding files. This is consistent with the strategy of dynamic allocation which will be present hereafter.

In GMAW process, however, the initial grain structure linked to CA model actually contains that of the workpiece as well as that of the air domain. In the present work, it is safe to consider the initial structure of air domain to be the fully mushy structure as well. It is only necessary to change the fully mushy cells to be air states when the value of LS function of these cells are checked to be positive at the time of reading this file from the hard disk. This treatment is used to make compatible the creation of initial grain structures for both GTAW and GMAW processes.

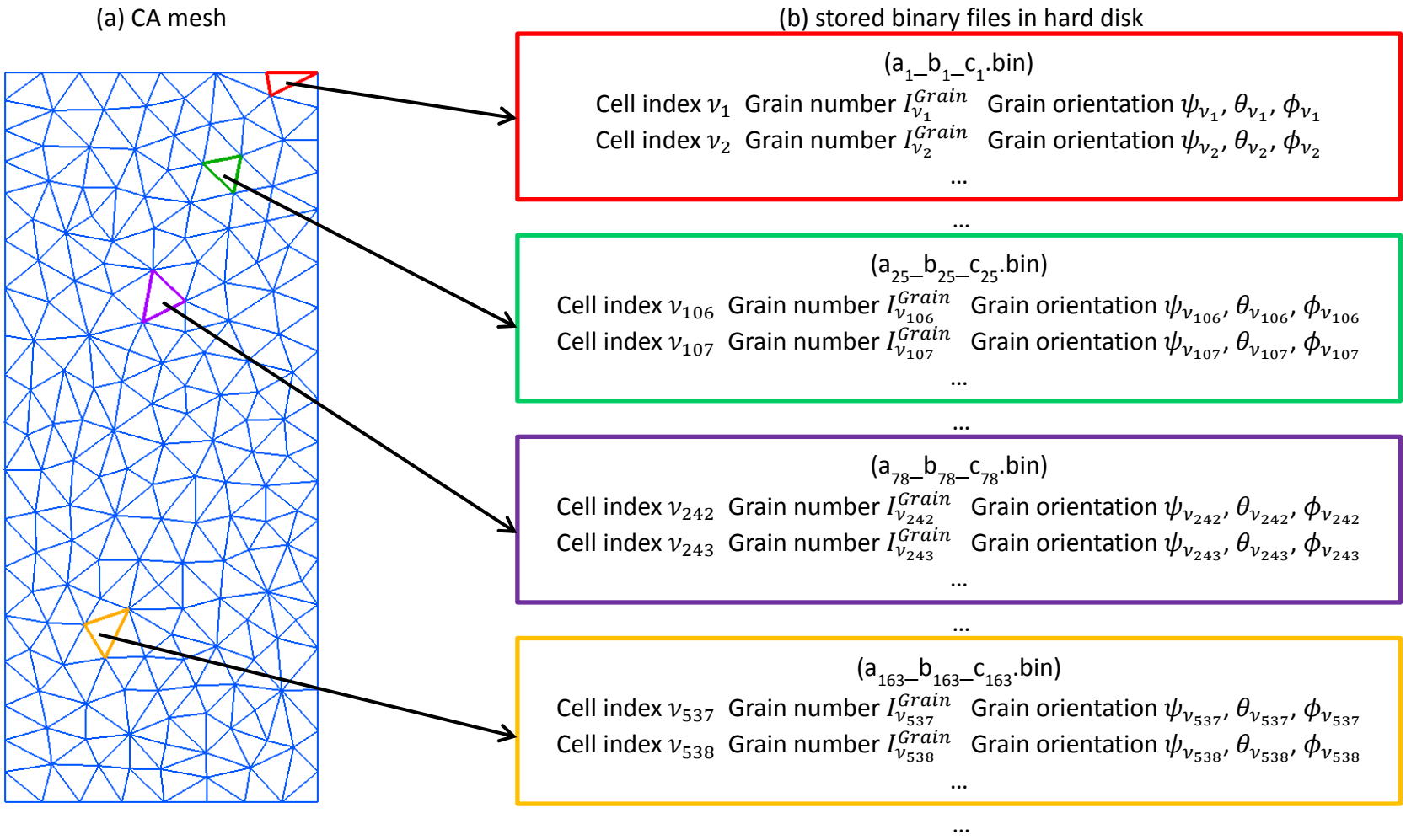

Fig. III-19 Strategy for the storage of the initial structure in the hard disk. (a): the CA mesh used for the creation of initial grain structure. Each CA element is associated to a binary file, shown in (b): the file name a_j_b_j_c_j.bin (a_j_b_j.bin in 2D) is linked to the barycentric coordinates of CA element E_j^{CA}. The information of the cells belonging to E_j^{CA} is stored in the file. Four random chosen binary files linked to four CA elements are listed.

3.5.2. Strategy for dynamic allocation

The objective of the dynamic allocation of the CA cells is to reduce the resolution time and the memory cost for the the CA model.

Fig. III-20 and **Fig. III-21** give illustrations of this optimization in GTAW and GMAW processes, respectively. For the sake of clarity, they are presented in a 2D approximation. Note that all the parameters used in the two simulations are listed in **Appendix A**. The figures present two different domain sizes for the FE and CA meshes as well as a CA grid made of a regular lattice of square cells defined from the CA mesh. The triangular elements in the FE and CA meshes and the square cells in the CA grid are chosen large enough on purpose in order to be able to distinguish them in this illustrative example.

Fig. III-20 shows the top surface of the workpiece in GTAW process. The configuration of the simulation for GTAW process is a traveling heat source at constant velocity from left to right that locally heat and melt the metal, later solidified behind it. The information of the melted zone (weld pool) is provided by the liquidus isotherm drawn as thick dark red contours. Note that, to be conducted, the change of the domain size requires knowing in advanced the size of the weld pool so as to make sure that it is fully included on the domain defined by the reduced CA mesh. As can be seen, the liquidus isotherms computed on the FE mesh, T_L^{FE}, and projected on the CA mesh, T_L^{CA}, differ. This is due to the different sizes of elements used on the FE and CA meshes, *i.e.* FE elements and CA elements. This illustration thus permits to identify the role of the size of the elements on the linear projection from a fine mesh to a coarse mesh. The opposite operation, i.e. projection from the coarse CA mesh to the fine FE mesh, does not lead to such loss of information. One can also see by comparing **Fig. III-20** (t) and (t') that the shape of T_L^{CA} contour changes with time while the shape of T_L^{FE} contour remains stable, i.e. is simply translated due to the heat source move in stationary conditions. This is reached thanks to the mesh adaptation of the FE mesh, not achieved with the fixed CA mesh.

The procedures to activate/deactivate the CA elements and the CA cells are now presented below. The model considers that the initial structure does not evolve if it is not heated to the liquidus temperature. This means that morphological evolution such as solid-state grain

growth is not taken into account. During GTAW process, a specific CA element will be activated when at least one of the conditions below is fulfilled

- at least one node of the element is above the liquidus temperature (Condition A1),
- at least one of its neighboring element fulfills the previous condition (Condition A2).

Condition A2 is necessary in the present dynamic allocation algorithm because the fraction of growing cells of a specific node in the CA mesh is dependent on all the cells in the CA elements connected to this node according to **Eq. (III-64)**. By doing this, the dynamic allocation does not affect the calculation of $g_{n_j^{CA}}^{m}$ for the active CA elements (see **Section 3.4.2**). When a CA element is activated, the corresponding file containing the cell information will be read and then removed from the hard disk. These cells are considered in the CA resolution until the corresponding CA element is deactivated, which occurs when both the conditions below are fulfilled simultaneously:

- all the nodes of the element are below the liquidus temperature (Condition D1),
- the mushy fractions of all the nodes of the element are equal to 1 (Condition D2).

The information associated to the cells belonging to the CA element is then written into a file linked to its barycentric coordinates and stored on the hard disk. It can thus be read again when/if the heat source heats sufficiently the same element, for instance in case of multiple passes.

When time increases from t to t'>t, the liquidus isotherm is moved to the right-hand-side. Consequently, in **Fig. III-20** (CA mesh-t'), the 8 elements highlighted in purple fulfill the activation conditions and are thus activated (Condition A2). The 8 corresponding files with cell information are read and stored into the computer memory prior to be removed from the hard disk, thus allocating the corresponding CA cells defined by these 8 elements, which is shown in **Fig. III-20** (CA grid-t'), *i.e.* the corresponding cells are changed from inactive states (yellow color) to active but not growing states (grey color). During the same period of time, the 8 elements highlighted in black fulfill the deactivation conditions and thus are deactivated (Condition D1 & D2). The cell information of each element is then written into 8 corresponding files and the memory is released of the corresponding CA cells information. Note that the numbers of activated/deactivated elements are independent to each other. In

the CA elements that experience a temperature increase above the liquidus temperature between time t and t', the cells located inside the liquidus isotherm contour are changed to liquid state. This is made visible in **Fig. III-20** (CA grid-t') by considering all cells that have changed color to become light grey between time t and t'. The cells located outside the liquidus isotherm but with liquid neighborhood are changed to growing state, *i.e.* to the black color. The grey cells below the liquidus temperature and far enough from the liquid to have no liquid neighboring cells represent the fully mushy cells.

Fig. III-21 shows the transverse cross section of the workpiece during GMAW process. A traveling surface heat source at constant velocity from left to right is applied on the metal/air interface with droplets falling into the weld pool. The metal/air interface is represented by the blue curve with $\psi = 0$ in FE mesh. The information of weld pool is provided by the liquidus isotherm within the metal domain. Because the two domains are distinguished by the distance function ψ, the value of ψ is thus the added information to determine activation/deactivation of the CA elements and the CA cells.

During GMAW process, a specific CA element will be activated when at least one of the two conditions (Condition A1 and Condition A2) is fulfilled. In the same time, it should fulfill the condition bellow:

- at least one node of the element is located in the metal domain (Condition A3).

Condition A3 is a necessary situation for activation of the CA elements during GMAW process because it clears up the CA elements with high temperature but located in air domain. The CA elements fully located inside the air domain do not affect the grain structure evolution. One active CA element is deactivated as soon as it fulfills both Condition D1 and Condition D2. As explained before, the cell information is written into a binary file linked to the barycentric coordinates. In order to keep compatible with the storage strategy (see **Fig. III-19**), the information of air cells is fixed with $I_v^{Grain} = -10$ and $\psi_v = \theta_v = \phi_v = 181°$.

When time increases from t to t'>t, the metal/air interface is updated and liquidus isotherm is moved to the right-hand-side. Consequently, in **Fig. III-21** (CA mesh-t'), 4 elements highlighted in purple fulfill the activation conditions and are thus activated. The 4 corresponding files are thus read and removed from the hard disk. In the same time, the 8

elements highlighted in black fulfill the deactivation conditions and thus are deactivated. 8 corresponding files with the information of cells are written in the hard disk.

In the CA elements that experience the interface update and temperature increase above the liquidus temperature between time t and t', the cells with positive LS value ($\psi_v > 0$) at time t and located within the metal domain ($\psi_v \leq 0$) at t' are changed to liquid state. It reflects the formation of the weld bead due to the adding metal. The change of cell states in the metal domain is the same as that in GTAW process presented before.

In **Fig. III-20** and **Fig. III-21**, additional information is provided by the FE and CA meshes considering the 3 colors of the elements edges. It corresponds to the partition of the calculation on 3 computing units. As can be seen, partitioning is such that the number of nodes per computing unit is approximately the same. For the CA mesh, partitioning is based on an even distribution of the active CA cells among the 3 computing units [Car14].

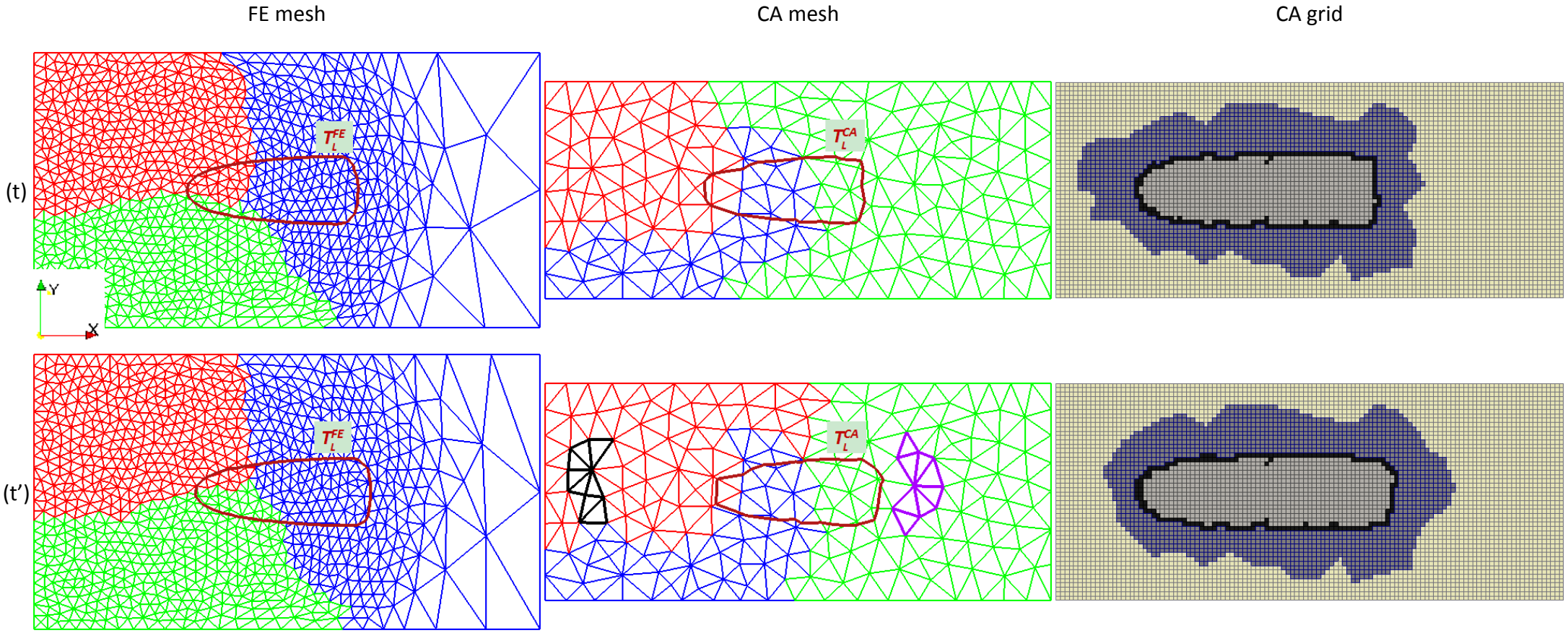

Fig. III-20 2D CAFE illustration of (FE mesh) FE mesh, (CA mesh) CA mesh and (CA grid) CA grid at (t) time t and (t') time t' > t for GTAW process. The domain sizes of FE and CA mesh are 350×190 mm^2 and 350×150 mm^2, respectively. CA grid made of a regular lattice of square cells is superimposed on CA mesh. The heat source moving at constant velocity from left to right between t and t'. The red, green and blue colors of the triangular meshes correspond to the partitions defined for parallel computations on 3 computational units. The square cells in CA grid are (light grey) liquid, (grey) solid and (black) growing (*i.e.* with at least one liquid neighboring cell). They are active and allocated in computer memory. The yellow cells are inactive and out of memory. The thick dark red contours identify (FE mesh) the position of the liquidus isotherm, $\boldsymbol{T_L^{FE}}$, and (CA mesh) its projection onto the CA mesh, $\boldsymbol{T_L^{CA}}$. The size of elements of the FE mesh, CA mesh and cells of CA grid are chosen very coarse on purpose for these illustrations. Triangular contours highlighted in black and purple in (CA-t') correspond to activated and inactivated elements of CA mesh between times t and t', respectively.

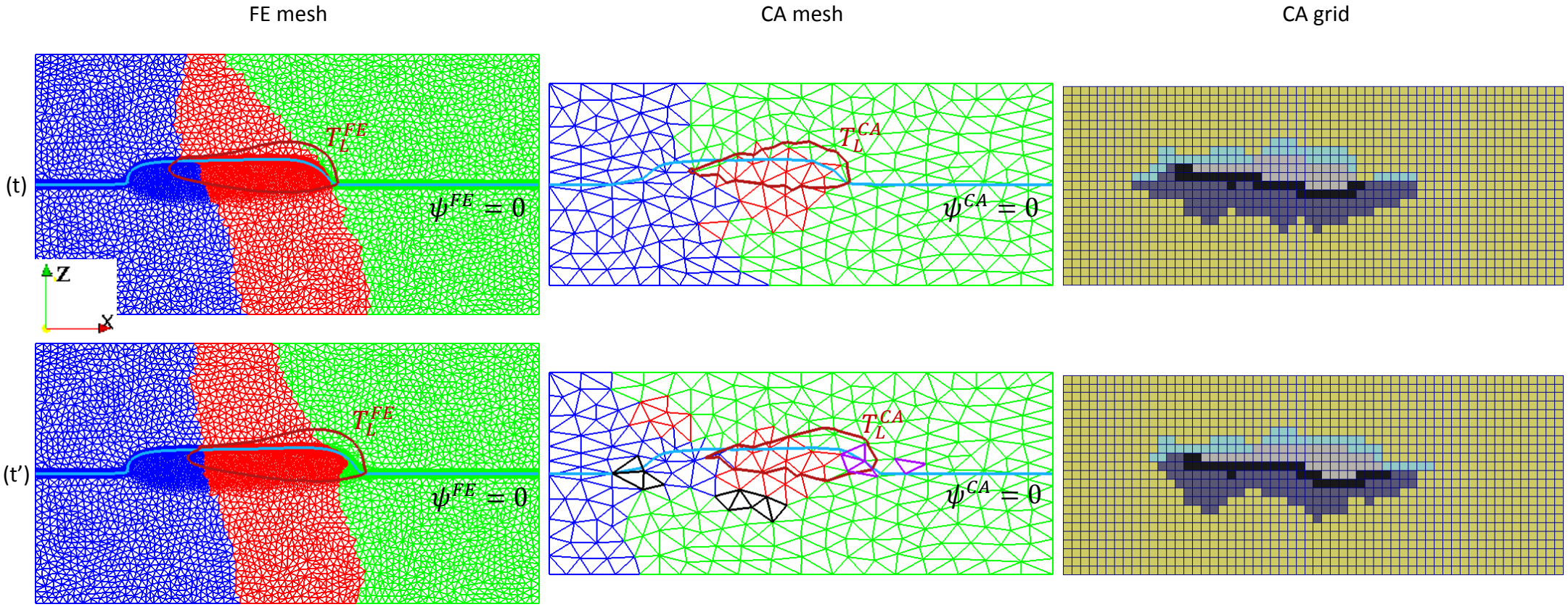

Fig. III-21 2D CAFE illustration of (FE mesh) FE mesh, (CA mesh) CA mesh and (CA grid) CA grid at (t) time t and (t') time t' > t for GMAW process. The domain sizes of FE and CA mesh are 175×90 mm^2 and 175×70 mm^2, respectively. CA grid made of a regular lattice of square cells is superimposed on CA mesh. The heat source moving at constant velocity from left to right between t and t'. The red, green and blue colors of the triangular meshes correspond to the partitions defined for parallel computations on 3 computational units. The square cells in CA grid are (light grey) liquid, (grey) solid, (black) growing (*i.e.* with at least one liquid neighboring cell) and (light blue) air. They are active and allocated in computer memory. The yellow cells are inactive and out of memory. The thick dark red contours identify (FE mesh) the position of the liquidus isotherm, $\boldsymbol{T_L^{FE}}$, and (CA mesh) its projection onto the CA mesh, $\boldsymbol{T_L^{CA}}$. The size of elements of the FE mesh, CA mesh and cells of CA grid are chosen very coarse on purpose for these illustrations. Triangular contours highlighted in black and purple in (CA-t') correspond to activated and inactivated elements of CA mesh between times t and t', respectively.

3.6. Conclusion

The 3D coupled Cellular Automaton – Finite Element (CAFE) model is extended to simulate the grain structure formation during solidification in welding process.

At the macroscopic scale, the FE model solves the mass, energy and momentum conservation equations for the whole system based on an adaptive mesh. For GMAW with metal addition, the FE model is enriched and established in a level set (LS) approach in order to model the evolution of the metal/air interface due to the weld bead development. In the meso scale, the CA model is used to simulate the grain structure evolution. Thus, a second fixed mesh, referred to as CA mesh is used. A CA grid made of a set of cubic cells is superimposed on the CA mesh. By changing the states of the cells, the front of the solidification structure is tracked and simulated. In addition, a new strategy of dynamic activation/deactivation of CA elements and thus allocation/deallocation of CA cells is developed in order to reduce the computation cost.

Finally, this 3D CAFE model can be applied on the simulations of the grain structure formation during single linear pass and multiple linear passes GTAW and GMAW.

3.7. French summary

Le **chapitre III** présente le modèle CAFE développé pour simuler l'évolution structurale des grains lors de la solidification se produisant au cours des procédés de soudage TIG et MIG. La technique des éléments finis est appliquée à la résolution des équations de conservation en masse, énergie et moments pour l'intégralité du système d'étude. Cette méthode repose sur l'utilisation d'un maillage adaptatif et a été enrichie en intégrant une approche Level-Set afin de modéliser l'évolution de l'interface métal/air liée à l'apport de matière réalisé dans le bain de fusion au cours du soudage MIG, le soudage TIG étant considéré sans apport de matière. Le modèle automate cellulaire est utilisé pour simuler l'évolution de la structure de grain en changeant les états des cellules de calcul, selon la nature du domaine qu'ils contiennent. Il permet notamment de modéliser les étapes de fusion et de solidification à l'interface entre la zone pâteuse et la partie liquide au cours du soudage. Cette approche automate cellulaire est couplée à la résolution éléments finis, dans le cadre du modèle CAFE. Afin d'optimiser le temps de résolution et la gestion de la mémoire dans les simulations, un travail d'ajustement des dimensions des mailles pour les éléments finis et les automates

cellulaires a été réalisé. Une taille adaptée des cellules des automates cellulaires est également proposée, à travers la réalisation de différentes simulations. De plus, une nouvelle stratégie d'allocation et de désallocation des Automates Cellulaires a été développée, enrichissant l'approche précédemment développée, et l'adaptant au contexte de la refusion en soudage.

Chapter IV Applications

4.1. Material properties

The application of the present 3D CAFE model for the welding processes is intended to simulate the grain structure evolution for Gas Tungsten Arc Welding and for Gas Metal Arc Welding processes applied to the URANUS 2202 steel. URANUS 2202 steel is a low nickel and low molybdenum duplex stainless steel designed to replace the 304/304L stainless steel grades in most applications, such as liquor tanks for pulp and paper industry, water storage and ducting, architecture and bridge, as well as chemical, oil and gas industries [Arc10]. Its chemical composition is listed in **Tab. IV-1**.

Tab. IV-1 Chemical composition of the URANUS 2202 steel (wt%) [Arc10]

C	Cr	Ni	Mn	Mo	N	Fe
0.02	22	2	<2	<0.45	0.2	balanced

The mass enthalpy and fraction of phases with respect to the temperature for URANUS 2202 steel are established as illustrated in **Fig. IV-1** thanks to the software Thermo-Calc [The13] using the TCFE6 thermodynamic database [Shi08]. The Gulliver-Scheil solidification path [Gul13, Sch42] is adopted in the present work. Consequently, no solute diffusion occurs in the solid phases. Please note that, due to the Gulliver-Scheil approximation, several solid-state transformations are not accounted for, yet experimentally found in this steel. Implementation of such paths can yet be considered using more advanced thermodynamic considerations, such as partial equilibrium and paraequilibrium [Zha13, Kos14]. Moreover, the final state of the phases obtained in the present work is not a balance between the ferrite and austenite (*i.e.* 50% ferrite and 50% austenite) as it is obtained industrially.

In the present work, two solid state phases are taken into account, *i.e.* BCC (ferrite) and FCC (austenite) (see **Fig. IV-1**). Based on the Gulliver-Scheil approximation, the temperature at which the transformation from liquid to BCC takes place is considered to be the liquidus temperature of URANUS 2202, namely $T_L = 1490°C$ as shown in **Fig. IV-1** (b). In addition, the phases considered in the growing structure (mushy zone) are thus liquid, BCC and FCC.

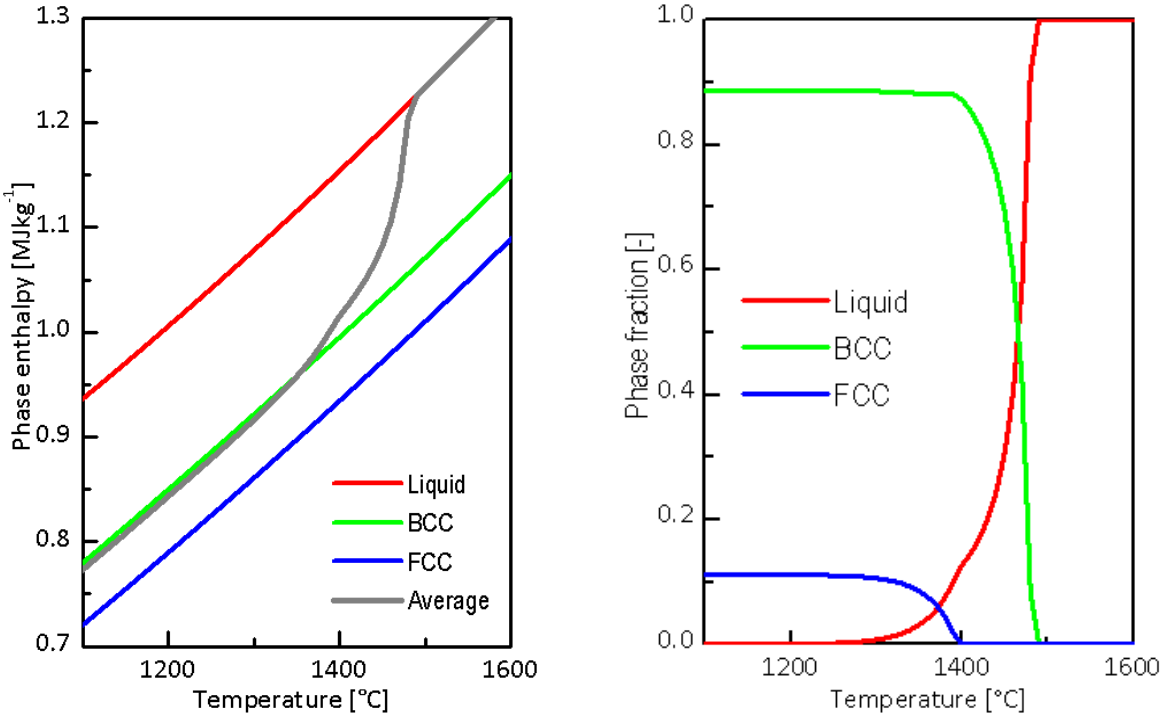

(a) (b)

Fig. IV-1 Properties of liquid, BCC (ferrite), and FCC (austenite) as a function of temperature for the URANUS 2202 steel with (a): mass enthalpy, and (b): mass fraction, assuming the Gulliver-Scheil solidification path [Gul13, Sch42]. Note that the average value in (a) is the sum of the mass enthalpies of each phase weighted by their corresponding phase fractions.

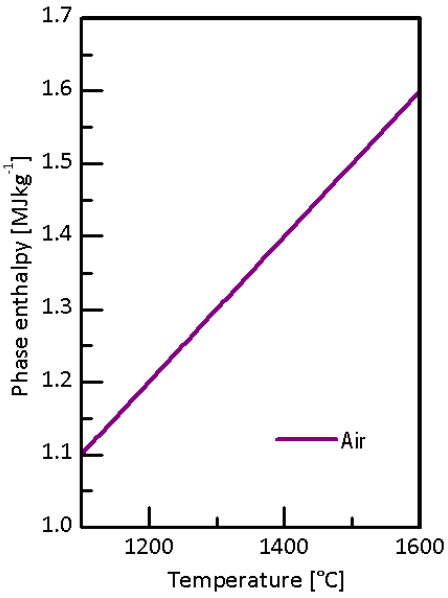

Fig. IV-2 Mass enthalpy with respect to the temperature of the air.

Tab. IV-2 Properties for the metal and air

Parameter	Symbol	URANUS 2202		Air	Unit
		Solid (BCC, FCC)	Liquid		
Density	ρ	7800	7800	1.3	kg m^{-3}
Liquidus temperature	T_L	-	1490	-	°C
Thermal conductivity	κ	40	40	1	W m^{-1} K^{-1}
Dynamic viscosity	μ_d	10^6	5	100	Pa s
Surface tension	$\gamma^{l/a}$	-	1.25	-	N m^{-1}

For simulations of GMAW process, the air domain is considered in the upper part in the FE model (see **Section 3.1.2**). Estimation of its real properties around the weld bead is difficult, especially in the arc plasma. Consequently, the physical properties of the air are taken constant and similar to that of the air in normal condition (*i.e.* at 0 °C and atmospheric pressure). The mass enthalpy with respect to the temperature for the air is thus tabulated and illustrated in **Fig. IV-2**. It should be mentioned that the thermodynamic properties of the air are of few influence on the computation.

Tab. IV-2 lists the material properties for both the metal and the air. Due to the fact that the shrinkage of the metal is not modeled, the density of the metal phases (*i.e.* liquid, BCC and FCC) is assumed to be constant and independent on temperature. However, temperature dependent continuous values are used for thermal conductivity and dynamic viscosity in the present work. The average values are listed here, and the tabulated values are presented in **Appendix B**. In addition, the temperature at which the liquid begins to transform to BCC is considered to be the liquidus temperature (see **Fig. IV-1** (b)).

At last, **Tab. IV-3** lists the grain properties adopted for the simulation with the CAFE model. The initial grain density, N_0, is chosen high in order to generate a fully equiaxed structure with a small size. The dendrite tip kinetic law (L1) is deduced by fitting the computed KGT solution [Kur86] for the steel URANUS 2202 with the polynomial expression. The values of the related parameters are listed in **Tab. IV-4**. In addition, in order to compare the influence of the dendrite tip kinetic law on the final grain structure, another dendrite tip kinetic law (L2) is arbitrarily proposed in the present work with the power law. In the present CAFE model, the undercooling, ΔT, of a specific CA cell, v,is defined as:

$$\Delta T = T_L - T_v \quad \textbf{(IV-1)}$$

where T_L is the liquidus temperature, T_v is the interpolated temperature of cell v.

In **Fig. IV-3**, the red curve represents the relationship between v_{CA} and ΔT for law L1, and the blue curve represents law L2. Large variations are found between L1 and L2. The values of undercooling for a specific value of dendritic growth velocity vary by a huge magnitude when computed by L1 and L2. Such a large variation will cause large changes in the predictions of the grain structure.

Tab. IV-3 Grain structure properties

Parameter	Symbol	Value	Unit
Initial grain density	N_0	10^{11}	m^{-3}
Dendrite tip kinetic law (L1) $v_{CA} = A_1\Delta T^{n_1} + A_2\Delta T^{n_2}$	A_1	8.315×10^{-6}	$m\ K^{-n1}\ s^{-1}$
	n_1	2.49	-
	A_2	9.628×10^{-7}	$m\ K^{-n2}\ s^{-1}$
	n_2	3.622	-
Dendrite tip kinetic law (L2) $v_{CA} = A_3\Delta T^{n_3}$	A_3	1.0×10^{-7}	$m\ K^{-n3}\ s^{-1}$
	n_3	2	-

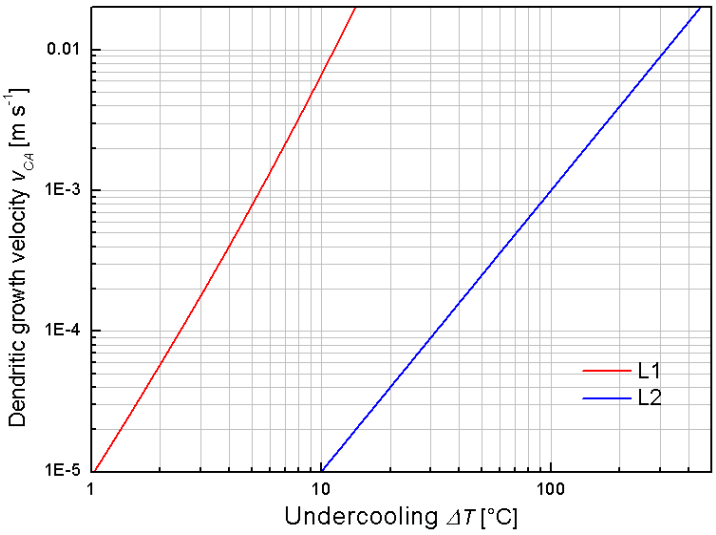

Fig. IV-3 Dendritic growth velocity with respect to the undercooling for L1 and L2, respectively

Tab. IV-4 Parameters of KGT model

Parameter	Symbol	Value	Unit	Reference
Gibbs-Thomson coefficient	$\Gamma^{s/l}$	1.9×10^{-7}	m K	[Kur98]
Diffusion coefficient of solute element in liquid steel	D_C^l	1.1×10^{-8}	$m^2\ s^{-1}$	[Gol74]
	D_{Cr}^l	4.9×10^{-9}	$m^2\ s^{-1}$	[Kub75]
	D_{Ni}^l	5.35×10^{-9}	$m^2\ s^{-1}$	[Cwu12]
	D_{Mn}^l	3.9×10^{-9}	$m^2\ s^{-1}$	[Sai58]
	D_{Mo}^l	5.5×10^{-10}	$m^2\ s^{-1}$	[Gao11]
	D_N^l	4.12×10^{-9}	$m^2\ s^{-1}$	[Vil76]

4.2. Applications

In the present work, two FE models are established for GTAW and GMAW, respectively. In the first FE model for GTAW without adding material (see **Section 3.1.1**), the FE domain corresponds to the domain of the workpiece. In the second FE model in Level Set approach for GMAW with molten droplets adding into the weld pool (see **Section 3.1.2**), the FE domain contains both the workpiece and its surrounding air. The second FE model can also simulate the welding case without adding material. Therefore, the first application of the present 3D CAFE model is to compare the simulated results for a single linear pass upon GTAW process by the two FE models. The results are presented in **Section 4.2.1**.

The second application of the present 3D CAFE model is to simulate single linear pass upon GTAW process for various welding parameters. The influences of the numerical parameters and process parameters are compared for the predictions of grain structure. The results are presented in **Section 4.2.2**.

The third application with the multiple linear passes upon GTAW process is to simulate the propagation of the grain structure among the successive passes. The epitaxial grain growth and grain competition will be shown to affect the final grain structure. This application is presented in **Section** Erreur ! Source du renvoi introuvable..

The fourth application with multiple passes with overlapping depths upon GTAW process is also used to simulate the propagation of the grain structure. It is presented in **Section 4.2.4**.

The fifth application with multiple linear passes upon GMAW process simulates the grain structure evolution with addition of metal. In this case, the Level Set approach is used to

simulate the evolution of the interface between the workpiece metal and the surrounding air. The simulations in 2D and then in 3D are presented in **Section 4.2.5**.

The sixth application with a single linear pass upon GMAW with a V-shaped chamfer is used to simulate the grain structure evolution in more complicated thermal and geometrical conditions. It is presented in **Section 4.2.6**.

Note that in all the following simulations it was assumed no nucleation of equiaxed grains in the weld pool, as is sometime observed in the literature [Kou02]. It would have been possible to handle such nucleation as demonstrated in other 3D CAFE simulations [Car12].

4.2.1. Comparisons of the results simulated by different FE models for a single linear pass upon GTAW

The objective of this section is to compare the results simulated by the different FE models established in the present work for a single linear pass upon GTAW. The case NLS corresponds to the FE model without Level Set approach established in **Section 3.1.1**, while the case YLS corresponds to the FE model in Level Set approach established in **Section 3.1.2**. The parameters of the two cases NLS and YLS are listed in **Tab. IV-5**.

The 3D CAFE model of case NLS is presented in **Fig. IV-4**. The FE domain corresponds to the domain of workpiece (*i.e.* 350×150×12 mm^3). A smaller dimension of CA domain (*i.e.* 180×60×12 mm^3) is adopted in order to reduce the resolution cost of the CA problem. The volumetric heat source proposed by Goldak *et al.* [Gol84] is adopted to model the heat input into the workpiece due to the plasma source. The double ellipsoidal power density distribution of the heat source is given by relationship **Eq. III-5**. The boundary condition modeled by **Eq. III-4** is applied on the entire surfaces of the FE domain.

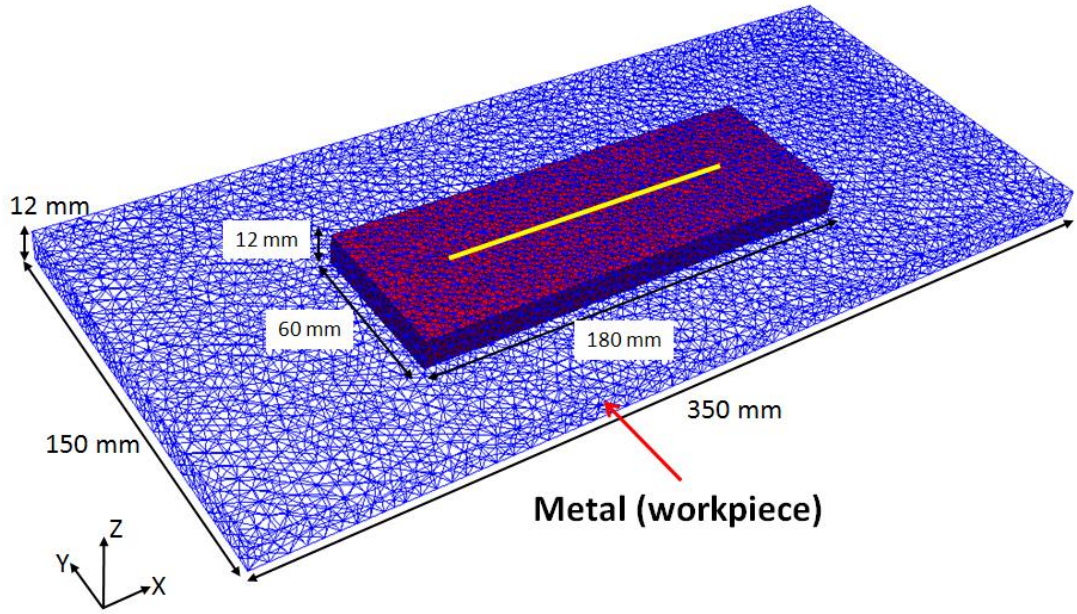

Fig. IV-4 The FE and CA model for the single linear pass upon GTAW process in case NLS. The FE domain is represented by the blue mesh, and the CA domain is represented by the red mesh. The trajectory of the heat source is represented by the yellow line.

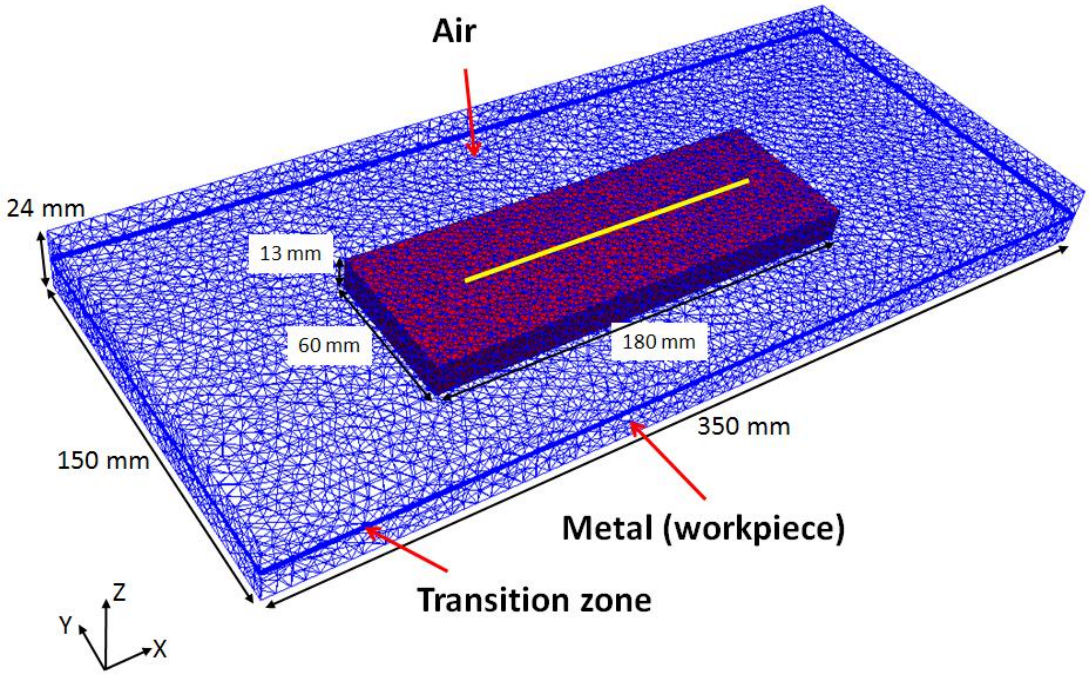

Fig. IV-5 The FE and CA model in Level Set approach for the single linear pass upon GTAW process in case YLS. The FE domain is represented by the blue mesh, and the CA domain is represented by the red mesh. The trajectory of the heat source is represented by the yellow line, which is at the interface between metal domain and air domain.

Tab. IV-5 Parameters for the single linear pass upon GTAW process of cases NLS and YLS (The dendrite tip kinetic law (L1) is presented in **Tab. IV-3**)

Parameter	Symbol	Value		Unit
		NLS	YLS	
FE domain	Ω_{FE}	350×150×12	350×150×24	mm^3
Metal domain in FE mesh	Ω_{FE}^{Metal}	350×150×12	350×150×12	mm^3
Air domain in FE mesh	Ω_{FE}^{Air}	-	350×150×12	mm^3
Half thickness of transition zone	ϵ	-	0.8	mm
CA domain	Ω_{CA}	180×60×12	180×60×13	mm^3
Metal domain in CA mesh	Ω_{CA}^{Metal}	180×60×12	180×60×12	mm^3
Air domain in CA mesh	Ω_{CA}^{Air}	-	180×60×1	mm^3
CA element size (fixed)	l_{CA}	3		mm
Cell size	l_{cell}	80		μm
Time step	Δt	0.05		s
Number of processors	N_{pro}	32		-
Initial temperature	T_0	20		°C
Environmental temperature	T_{ext}	20		°C
Heat transfer coefficient	h_T	5		$W\ m^{-2}\ K^{-1}$
Emissivity	ε_r	0.25		-
Initial grain density	N_0	10^{11}		m^{-3}
Dendrite tip kinetic law	L	L1		-
Velocity of heat source	v^H	2		$mm\ s^{-1}$
Input power of heat source	$\dot{Q}_{input}$	7500		W
Semi-axes in y direction	a	18		mm
Semi-axes in z direction	b	10		mm
Semi-axes in x direction	c	18		mm
Starting point of heat source	X_S, Y_S, Z_S	115, 75, 12		mm
Ending point of heat source	X_E, Y_E, Z_E	225, 75, 12		mm

The 3D CAFE model of case YLS is presented in **Fig. IV-5**. The FE domain (*i.e.* 350×150×24 mm^3) contains the workpiece (*i.e.* 350×150×12 mm^3) and its surrounding air (*i.e.* 350×150×12 mm^3). A transition zone with the thickness, 2ϵ, where the mixing law is applied, is defined. A smaller dimension of CA domain (*i.e.* 180×60×13 mm^3) is adopted in order to reduce the resolution cost of the CA problem. In the CA mesh, the bottom part (*i.e.* 180×60×12 mm^3) is located in the domain of workpiece, and the top part (*i.e.* 180×60×1 mm^3) is located in the air domain. Note that in this case, no material is added into the workpiece and thus the metal/air interface will be kept unchanged. This is why only a very small dimension of air is contained in the CA model. The volumetric heat source proposed by Goldak *et al.* [Gol84] is adopted to model the heat input into the workpiece with the same

values of parameters used in case NLS. The boundary condition modeled by **Eq. III-4** is applied on the bottom and side surfaces of the workpiece. However, due to the fact that there is no explicit definition of the top surface of the workpiece (*i.e.* the interface of metal and air domain) in Level Set approach, a volumetric heat source $-\delta(\psi)\dot{Q}_{CR}$ is applied in the transition zone (see **Section 3.2.2.6**) to model the heat flux at the top surface of the workpiece. In addition, the adiabatic condition is applied on the top surface of the FE domain.

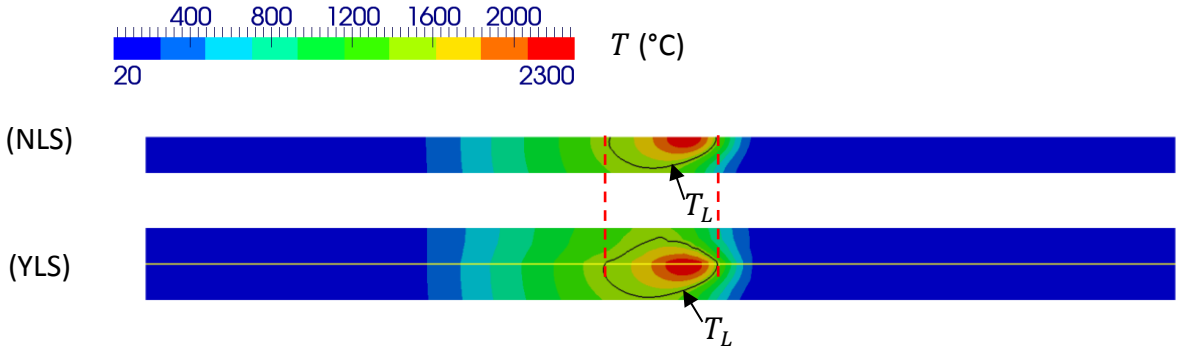

Fig. IV-6 Longitudinal temperature distribution profile of section Y = 75 mm, at t = 37.5 s of (NLS): case NLS, and (YLS): case YLS. The liquidus isotherm computed on the FE mesh is represented by the black contour. In (YLS), the yellow line represents the interface between the workpiece and the surrounding air, defined by LS = 0.

Fig. IV-6 presents the longitudinal temperature distribution profiles of section Y = 75 mm, at t = 37.5 s of the two cases NLS and YLS. Note that the FE domain in case NLS only contains the workpiece, but in case YLS, it contains the workpiece as well as its surrounding air. Therefore, the isotherm with the value of T_L = 1490 °C in (NLS) is an open contour, but is a closed contour in (YLS). Comparing the temperature profiles in the metal domain, they are similar to each other but not identical. The differences of the temperature in the metal domain are affected by the two following parameters which are adopted in case YLS: the first one is the thickness of the transition zone where the material properties are computed by the mixing law in Level Set approach; the second one is the value of thermal conductivity of the air. It can be considered that case NLS corresponds to case YLS with the thickness of transition zone and thermal conductivity of the air are equal to 0 (i.e. ϵ = 0, and κ^{air} = 0).

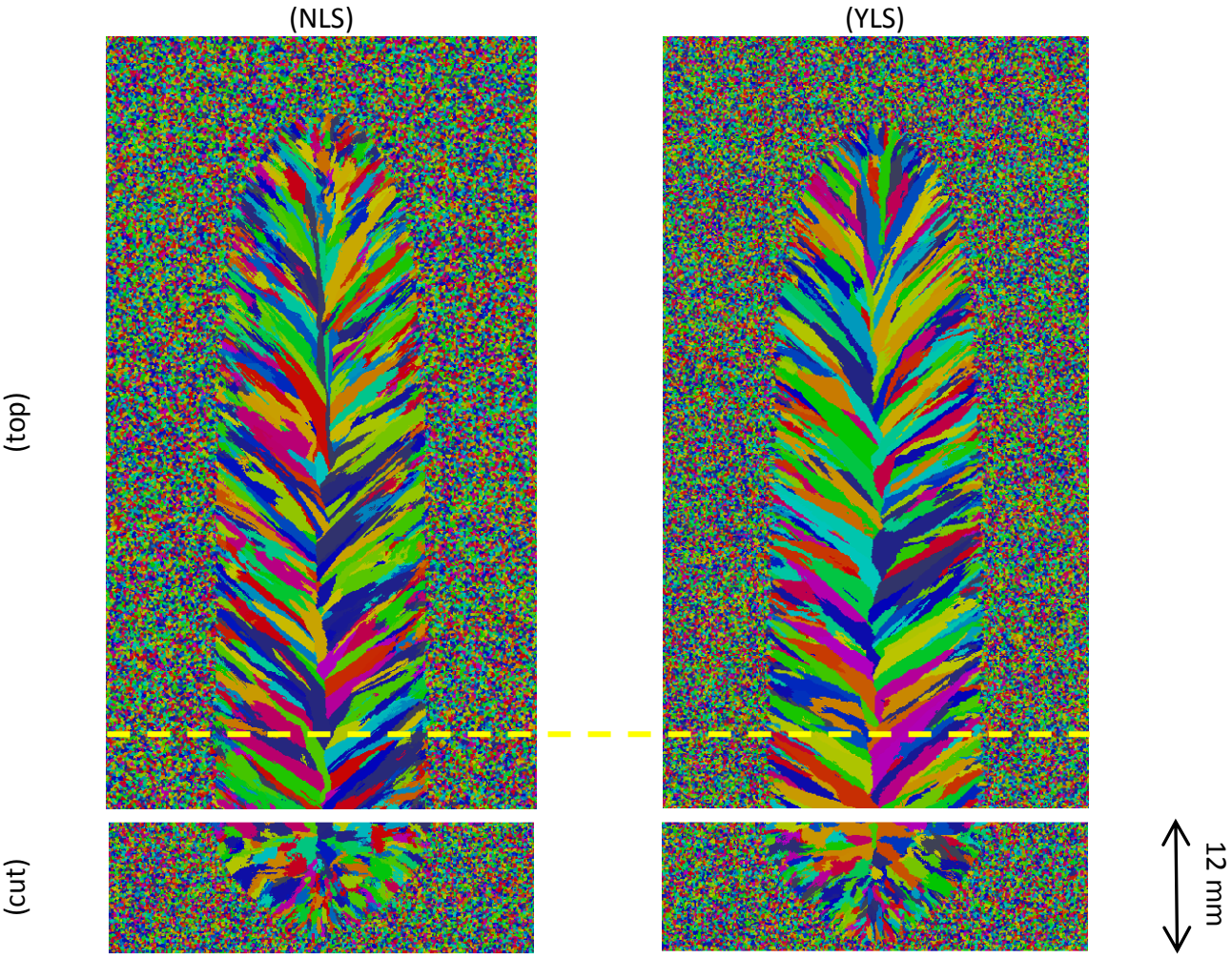

Fig. IV-7 Simulated 3D CAFE grain structure for single linear pass GTAW process with (top) as observed from the top surface of the workpiece in the range 105 mm < X < 195 mm and (cut) in a transverse cross section at X = 175 mm (yellow dashed line). The numerical and process parameters are given in **Tab. IV-5**. Note that the air cells in case YLS are not represented, and thus only the metal cells in (YLS-cut) are presented.

Fig. IV-7 presents the grain structure predicted in cases NLS and YLS, respectively. Note that the X components of grain orientations are represented by the different colors. It is seen that in both cases, columnar grains are formed after solidification of the weld pool. The orientations of columnar grains follow the temperature gradient at the boundary of weld pool. Comparing the grain structures in the two cases, it is clear that they are similar to each other. This is because the temperature distributions are similar in the two cases (see **Fig. IV-6**), although they are modeled in different approaches.

Therefore, the grain structure of the GTAW process without adding material can be simulated by the CAFE model in different approaches (i.e. CAFE model with/without the Level Set approach). Note that the parallel computations for the two simulations make use

of the same number of processors (*i.e.* N_{pro}=32). Comparing the resolution time of case NLS, however, the time for case YLS increases sharply due to the more complicated FE and CA calculation (89 hours for NLS, 170 hours for YLS). Therefore, based on the comparisons of the results shown in **Fig. IV-7** and the computation time, the following cases upon GTAW are simulated by the CAFE model without Level Set approach.

4.2.2. Single linear pass upon GTAW process

The objective of the cases with a single linear pass upon GTAW process (listed in **Tab. IV-6**) is to compare the influences of the numerical parameters (*e.g.* the cell size), process parameters (*e.g.* the input power and velocity of heat source), and the material properties (*e.g.* the dendrite tip kinetic law) on the predictions of the final structures. As explained in **Section 4.2.1**, the CAFE model is applied without Level Set approach.

The CAFE models for all the cases listed in **Tab. IV-6** are identical to that of case NLS, and thus shown in **Fig. IV-4**. The FE domain corresponds to the workpiece. A smaller dimension of CA domain is adopted for each case in order to reduce the resolution cost of the CA problem. The volumetric heat source proposed by Goldak *et al.* [Gol84] is adopted to model the heat input into the workpiece due to the plasma source. The double ellipsoidal power density distribution of the heat source is given by relationship **Eq. III-5**. The boundary condition is applied on the entire surfaces of the FE domain.

As listed in **Tab. IV-6**, all the parameters except the cell size are the same among the cases A1 – A4. The influence of cell size on the prediction of the grain structure during a single pass GTAW is compared. Among the cases B1 – B3, only the values of input power vary. Among the cases C1 – C3, the influence of the velocity of the heat source is compared. Moreover, compared to C1 – C3, different dendrite tip kinetic law is adopted among cases D1 – D3, respectively. Note that the cases A3, B3 and C2 (marked by red color) are in fact the same case.

Influence of cell size l_{cell}

CA cell size, l_{cell}, is a very important numerical parameter of the CAFE model. If the value of l_{cell} is too large, it is hard to reflect the branching mechanisms of dendrite arms and thus the grain competition [Gan94]. Oppositely, if the value of l_{cell} is too small, it increases the

memory cost and time consuming sharply for the simulation. According to Gandin *et al.* [Gan94], a typical cell size of the order of 50 to 100 μm is needed to simulate the grain structure. In order to demonstrate the influence of the cell size, four values, *i.e.* 160 μm, 120 μm, 80 μm and 60 μm are adopted in A1 – A4, respectively.

The final 3D grain structures for cases A1-A4 with respect to the different values of cell size are presented in **Fig. IV-9** (A1)-(A4), respectively. The grain structures on the top surface of the simulated domain and in a transverse cross section are shown in this figure. The initial structure is fully equiaxed with a very small size due to the high initial grain density N_0. Note that the average grain size (about 267μm) is still larger than the largest cell size (160 μm in A1) so that one grain is composed by several cells. However, the smaller the cell size is, the higher the resolution is. It is easy to recognize the region where remelting and resolidification took place because the regrown structure is columnar with an elongated shape factor compared to the initial structure.

Fig. IV-9 (A1) shows a grain structure with many long and wide grains grown toward the centerline of the weld when the cell size is equal to 160 μm. Some giant grains occupy the domain of the weld. However, epitaxial grain growth and grain competition cannot be well reflected after the solidification of the weld pool. During the welding process, the temperature gradient is very high. If the cell size is too large (*e.g.* 160 μm in case A1), the interpolated temperature for the growing cell departs deeply from the expected temperature at the solid/liquid interface. In other words, the computed undercooling for the growing cell is higher than expected value. Consequently, the velocity computed in the growing cell is too large. Neighboring cells with liquid state are captured by the growing cells with augmented growth velocities to form the giant grains. So, the cell size of 160 μm is too large to reflect the correct grain structure evolution during welding process with high temperature gradient.

A smaller cell size is adopted in A2 (120 μm). It permits more grain competition to take place. More columnar grains can be observed in **Fig. IV-9 (**A2). However, it is still shown that huge grains such as the yellow one in the left bottom region appear. That is to say that the cell size, 120 μm, is still too large to reflect the grain competition in welding process.

A large number of columnar grains appear in **Fig. IV-9 (**A3) and **Fig. IV-9 (**A4) with cell size taken equal to 80 μm and 60 μm, respectively. It can be seen that many small columnar grains appear close to the fusion line due to the epitaxial grain growth at the beginning of the solidification of the weld pool. Larger columnar grains locate inside the fusion zone thus reflecting the grain competition. As explained in **Chapter I**, the grains with preferred growth directions aligned to the temperature gradient overgrow those whose preferred growth directions do not align to the temperature gradient. The cell size with value 80 μm and 60 μm can reflect the grain competition appropriately, thus coinciding with literature [Gan94].

However, the resolution time is a very important factor considered in the numerical simulations. Note that for each simulation, parallel computations make use of the same number of processors (*i.e.* N_{pro}=32). However, the time for A4 increases sharply due to the smaller value of the cell size compared with A3 (89 hours for A3, 163 hours for A4). Therefore, based on the comparisons of the results shown in **Fig. IV-9** and the computation time, the cell size, 80 μm, will be adopted in all the following simulations.

Influence of the input power of the heat source $\dot{Q}_{input}$

The input power of the heat source is an important process parameter to affect the grain structure during welding process. As listed in **Tab. IV-6**, three cases (B1 – B3) with increasing input power of the heat source from 4500 W to 7500 W are simulated. The velocities of the heat source are identical to 2 mm s^{-1}.

Fig. IV-10 presents the 3D CAFE grain structure predicted in cases B1 – B3. The dimension of the weld pool is found to decrease when the input power is decreased from 7500 W to 4500 W. In case B1 with input power 4500 W, the weld pool is very small and thus only a tiny part of the domain is remelted. Consequently, small columnar grains are formed after resolidification. It is not easy to determine the grain orientation in this situation. However, in cases B2 and B3, a larger weld pool is formed and thus the number of partially remelted grains which are available for growth in the melt is increased. In addition, the growth competition is also enhanced due to the higher temperature gradient in these situations. In particular, some small grains appear in the centerline of the weld pool in case B2. They are

the columnar grains which grow upward to the top surface from the bottom of the weld pool, shown in **Fig. IV-10** (B2-cut).

Overall, larger input power increases the amount of the partially remelted grains, enhances the grain competition and thus more columnar grains are formed in the fusion zone.

Influence of the velocity of the heat source v^H

In order to predict the influence of the velocity of the heat source on the grain structures, three cases (C1 – C3) with the velocity varying from 1 mm s^{-1} to 5 mm s^{-1} are tested with the parameters listed in **Tab. IV-6**. Note that the different values of input power in C1 – C3 are proposed in order to obtain comparable widths for the weld pool dimensions.

Fig. IV-11 presents the 3D CAFE grain structure of cases C1 – C3. The growth direction of the grains tends to follow the path of the heat source. It can be seen that the grains become more perpendicular to the moving direction of the heat source as the velocity increases from 1 mm s^{-1} to 5 mm s^{-1}. This is due to the change of the weld pool from elliptical shape to teardrop shape in these cases, as shown in **Fig. IV-8** (C1) – (C3). The columnar grains thus tend to grow more perpendicular to the pool boundary.

In addition, some axial grains (*e.g.* in C1 and C2) can indeed even survive columnar competition at the center of the weld and grow over a long distance before they are stopped. The reason is that the temperature gradient remains low in these two simulations so that the grain competition is not highly pronounced according to the grain growth kinetics law. In comparison, competition taking place among the columnar grains predicted for an increased value of the heat source velocity (C3) is such that no axial grains survive.

Overall, these results retrieve common trends expected in solidification structure formed during welding as presented in standard physical metallurgy textbooks [Por92, Gro94, Kou02].

Influence of the dendrite tip kinetic law

The influence of the dendrite tip kinetic law on the final grain structure after welding is presented hereafter. Compared to cases C1 – C3, another set of cases D1 – D3 are tested with the dendrite tip kinetic law (L2).

The trend of the grains formed in the fusion zone in D1 – D3 is similar to that in C1 – C3, comparing **Fig. IV-12** to **Fig. IV-11**. That is to say the grains become more vertical to the moving direction of the heat source with the increase of the moving velocity. Similarly, the axial grains are also found in D1 due to the relatively low temperature gradient.

Compared to C1 – C3, however, something different is found in D1 – D3. Although the velocity and input power of the heat source keep the same for D1 and C1, the columnar grains in D1 are more perpendicular to the moving direction of the heat source. This phenomenon is also found in D2 and D3, compared to C2 and C3, respectively. This is because the undercooling for the growth is sharply increased due to the new grain growth kinetics law adopted by D1 – D3 (see **Fig. IV-3**). The shape of the weld pool in D1 – D3 becomes more elongated than that in C1 – C3, respectively, which is presented in **Fig. IV-8**, comparing C1 and D1, C2 and D2, C3 and D3, respectively. Finally, the columnar grains become perpendicular to the boundary of the elongated weld pool. In addition, the temperature gradient at the end of the weld pool in D1 becomes smaller than that in C1, which results to the increased size of axial grains in D1.

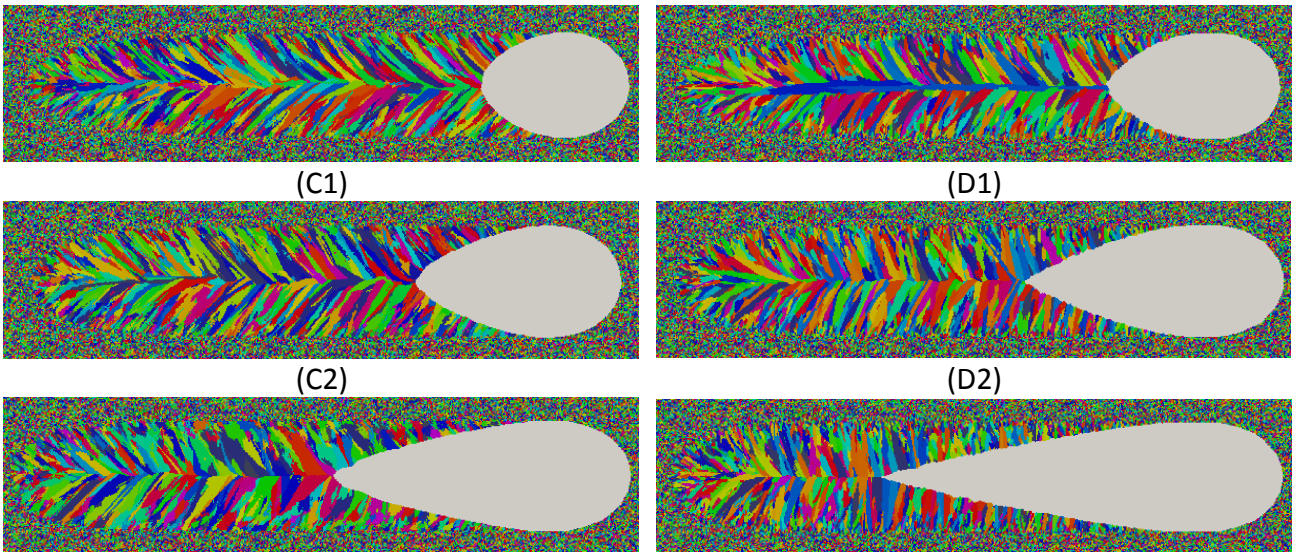

Fig. IV-8 Simulated grain structure for single linear pass GTAW process at a given time, observed from the top surface in the range 110 mm < X < 230 mm. The grey domain represents the weld pool. The liquid cells are not represented. The numerical and process parameters for C1 – C3 and D1 – D3 are given in **Tab. IV-6**.

Tab. IV-6 Parameters for the single linear pass upon GTAW process (The dendrite tip kinetic law (L1) and (L2) are presented in **Tab. IV-3**)

Parameter	Symbol	Value													Unit
		A1	A2	A3	A4	B1	B2	B3	C1	C2	C3	D1	D2	D3	
FE domain	Ω_{FE}	350×150×12													mm^3
Initial FE element size	l_{FE}	5													mm
CA domain	Ω_{CA}	180×60×12													mm^3
CA element size (fixed)	l_{CA}	3													mm
Cell size	l_{cell}	160	120	80	60	80	80	80	80	80	80	80	80	80	µm
Time step	Δt	0.05													s
Number of processors	N_{pro}	32													-
Initial temperature	T_0	20													°C
Environmental temperature	T_{ext}	20													°C
Heat transfer coefficient	h_T	5													$W\ m^{-2}\ K^{-1}$
Emissivity	ε_r	0.25													-
Initial grain density	N_0	10^{11}													m^{-3}
Dendrite tip kinetic law	L	L1	L1	L1	L1	L1	L1	L1	L1	L1	L1	L2	L2	L2	-
Velocity of heat source	v^H	2	2	2	2	2	2	2	1	2	5	1	2	5	mms^{-1}
Input power of heat source	$\dot{Q}_{input}$	7500	7500	7500	7500	4500	6000	7500	4500	7500	15000	4500	7500	15000	W
Semi-axes in y direction	a	18													mm
Semi-axes in z direction	b	10													mm
Semi-axes in x direction	c	18													mm
Starting point of heat source	X_S, Y_S, Z_S	115, 75, 12													mm
Ending point of heat source	X_E, Y_E, Z_E	225, 75, 12													mm

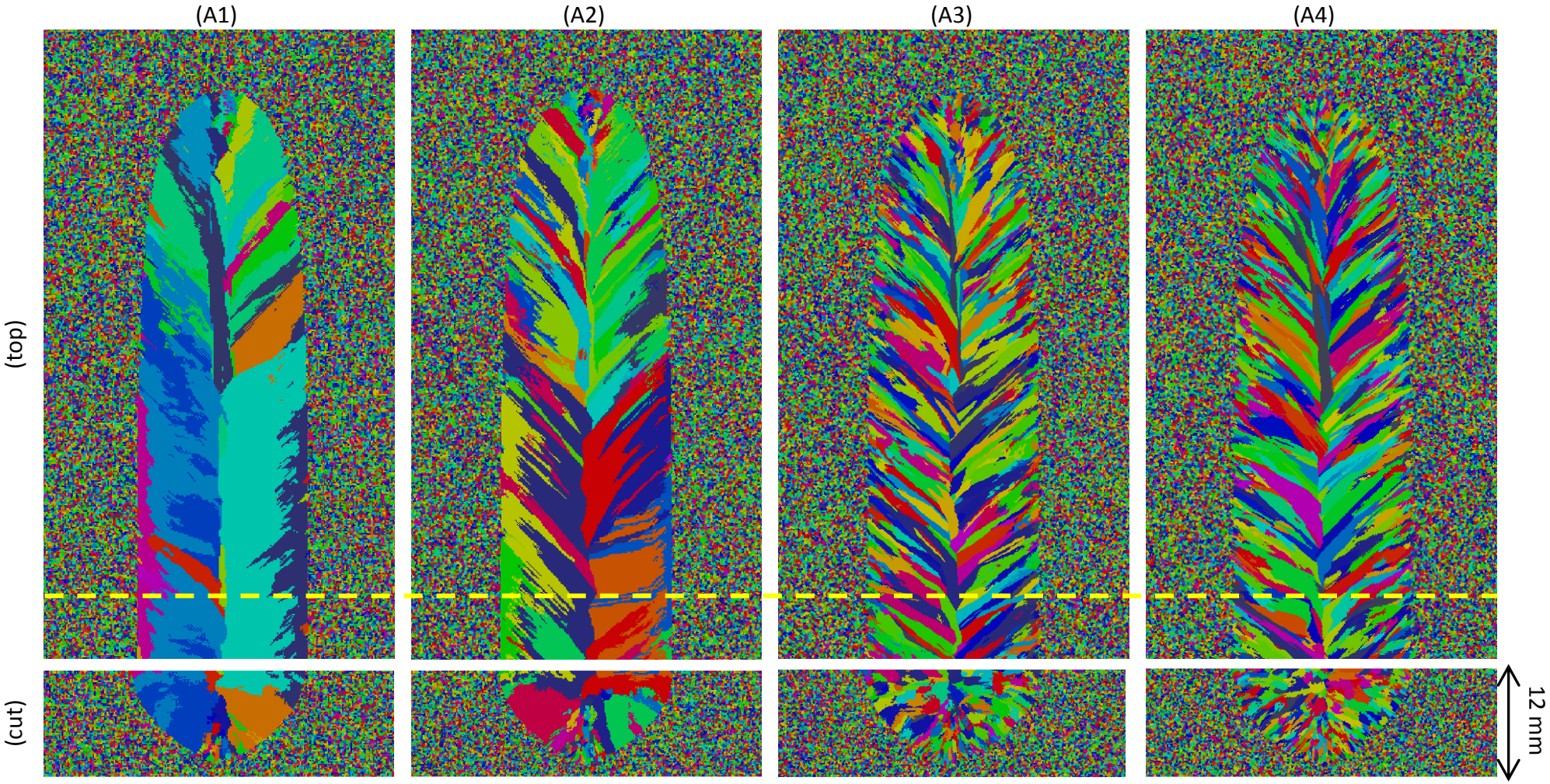

Fig. IV-9 Simulated 3D CAFE grain structure for single linear pass GTAW process with (top) as observed from the top surface of the domain in the range 105 mm < X < 195 mm and (cut) in a transverse cross section at X = 175 mm (yellow dashed line). The numerical and process parameters are given in **Tab. IV-6**. The cell sizes are (A1): 160 μm, (A2): 120 μm, (A3): 80 μm and (A4): 60μm.

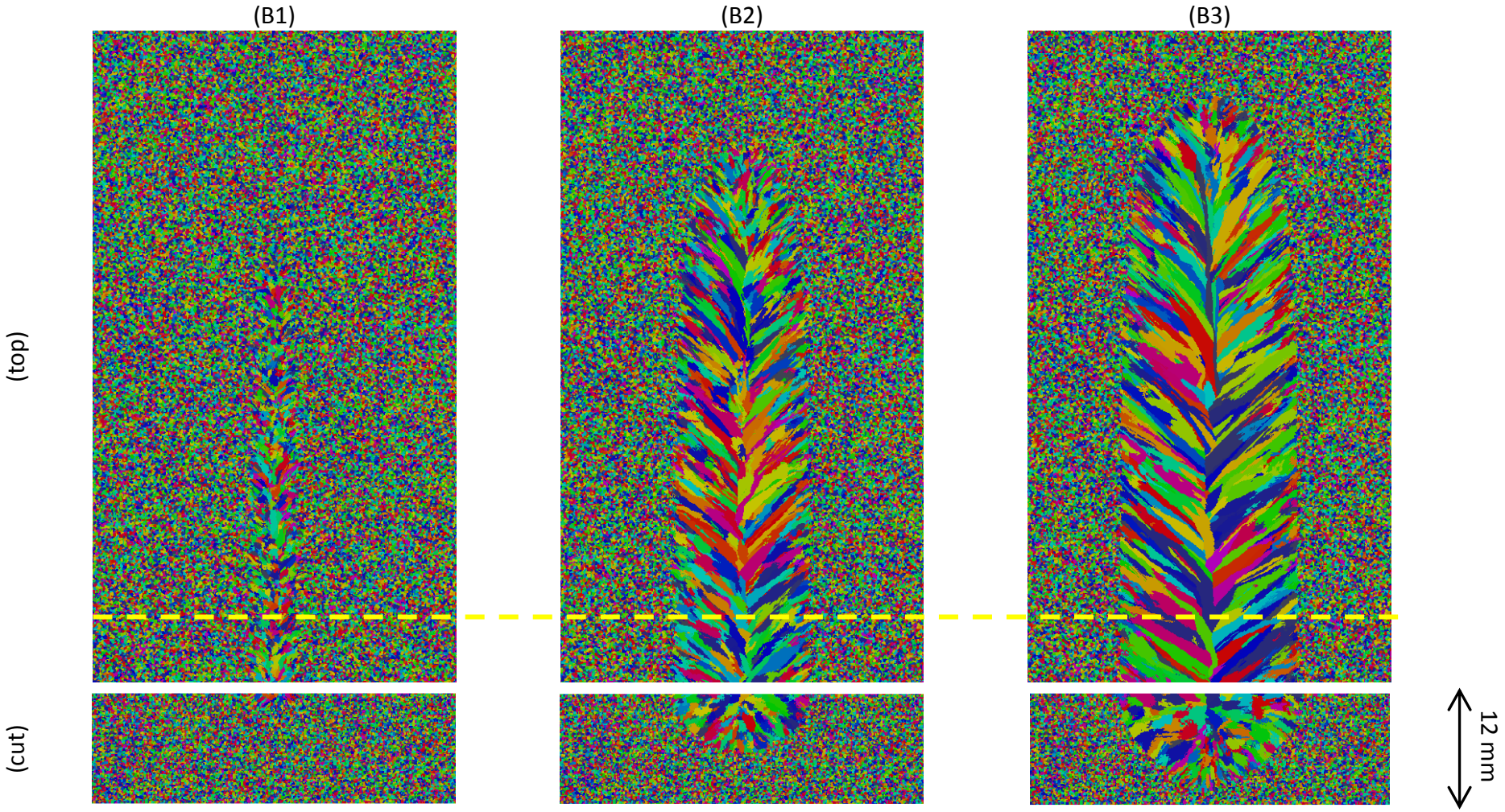

Fig. IV-10 Simulated 3D CAFE grain structure for single linear pass GTAW process with (top) as observed from the top surface of the domain in the range 105 mm < X < 195 mm and (cut) in a transverse cross section at X = 175 mm (yellow dashed line). The numerical and process parameters are given in **Tab. IV-6**. The input powers of heat source are (B1): 4500 W, (B2): 6000 W, and (B3): 7500 W.

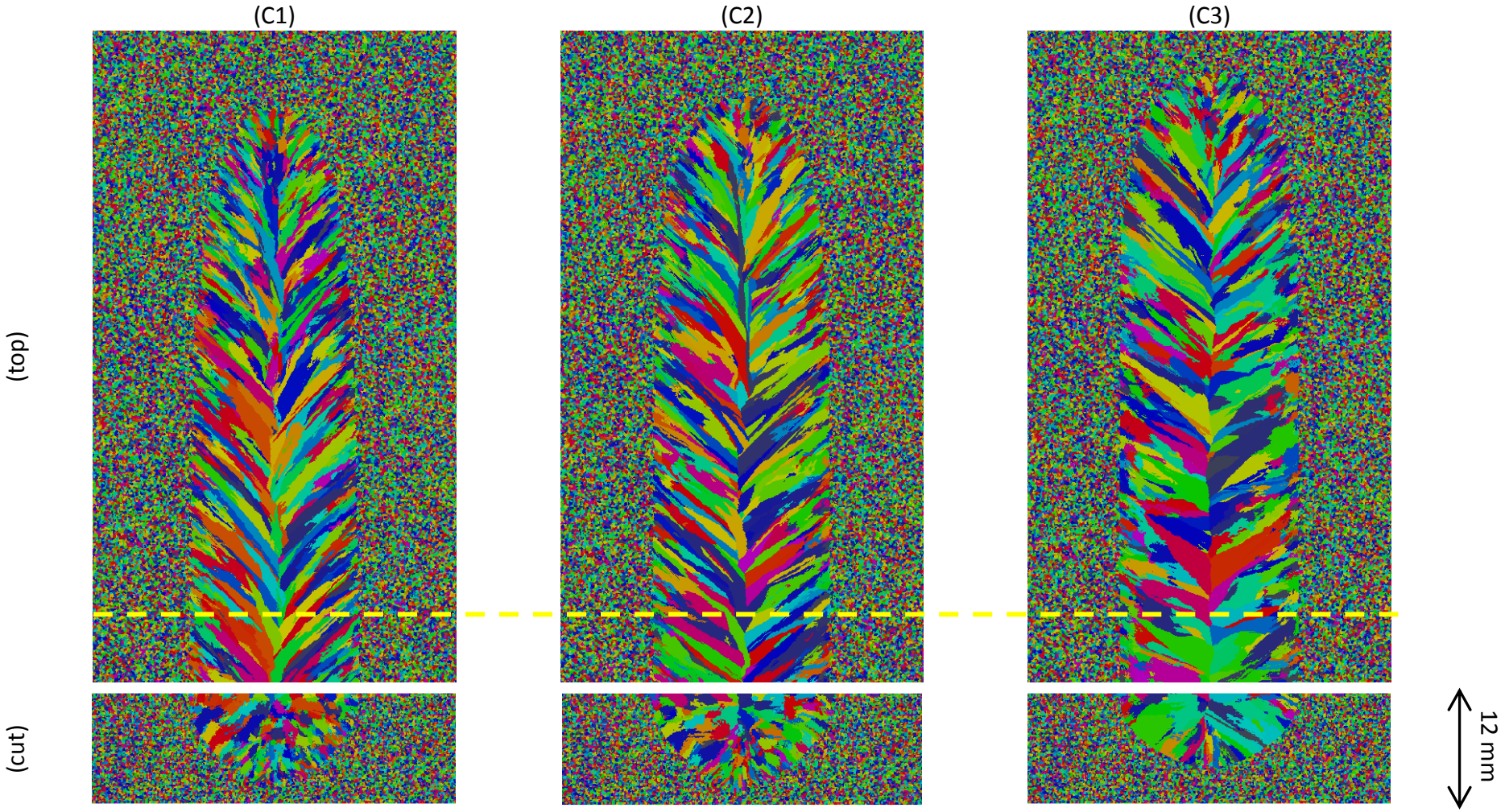

Fig. IV-11 Simulated 3D CAFE grain structure for single linear pass GTAW process with (top) as observed from the top surface of the domain in the range 105 mm < X < 195 mm and (cut) in a transverse cross section at X = 175 mm (yellow dashed line). The numerical and process parameters are given in **Tab. IV-6**. The velocities of heat source are (C1): 1 mm s^{-1}, (C2): 2 mm s^{-1}, and (C3): 5 mm s^{-1}. The dendrite tip kinetic law (L1) are adopted.

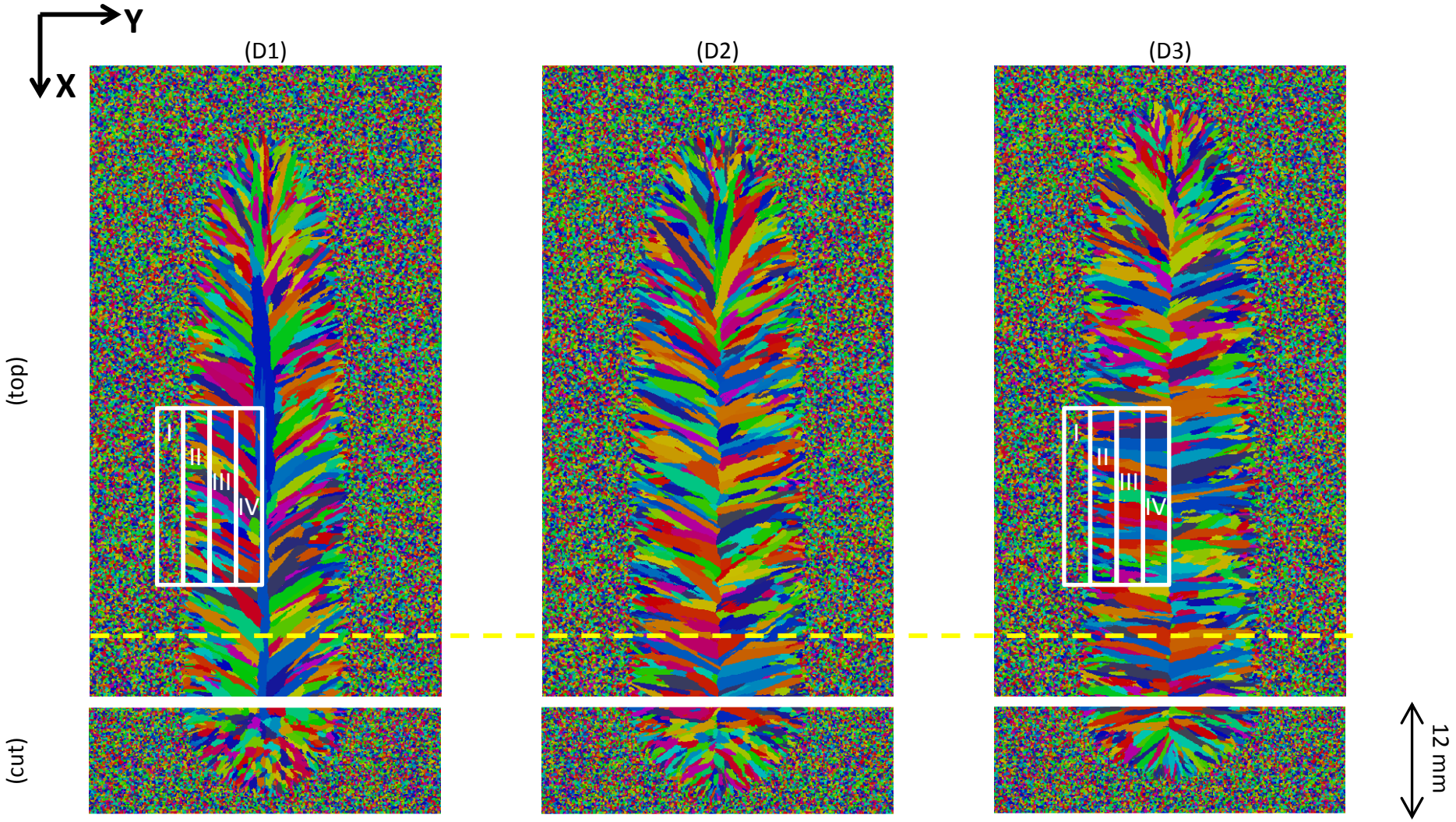

Fig. IV-12 Simulated 3D CAFE grain structure for single linear pass GTAW process with (top) as observed from the top surface of the domain in the range 105 mm < X < 195 mm and (cut) in a transverse cross section at X = 175 mm (yellow dashed line). The numerical and process parameters are given in **Tab. IV-6**. The velocities of heat source are (D1): 1 mm s^{-1}, (D2): 2 mm s^{-1}, and (D3): 5 mm s^{-1}. The dendrite tip kinetic law (L2) are adopted.

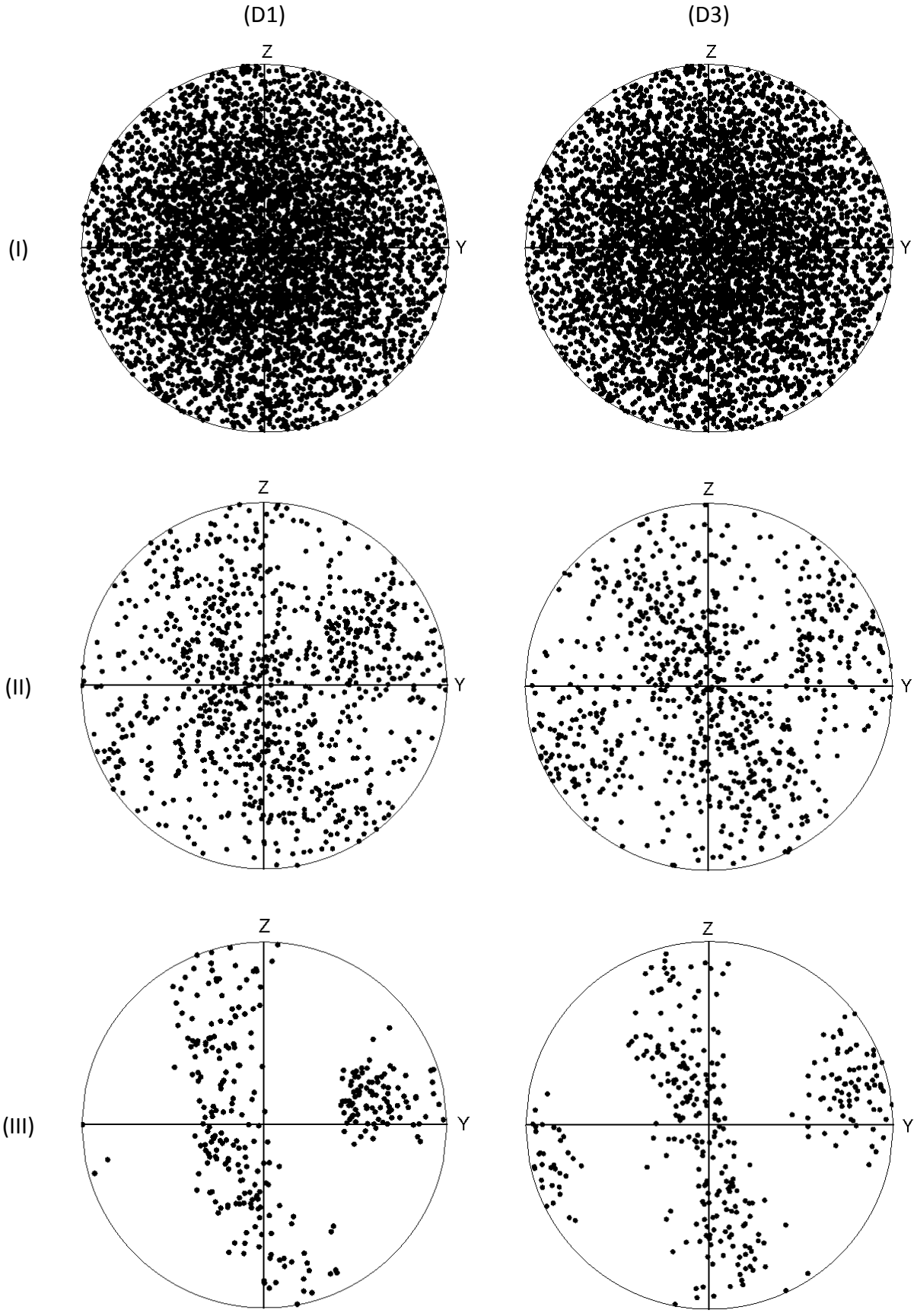
(D1)
(D3)
(I)
(II)
(III)
Z
Y

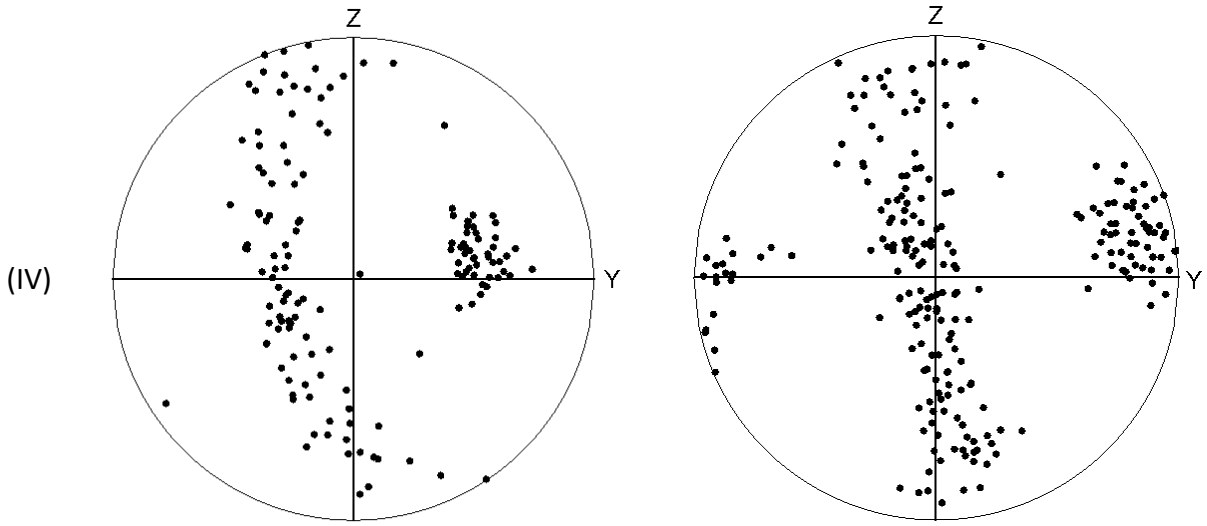

Fig. IV-13 Simulated texture revealed by <100> pole figures for (D1) and (D3), respectively. The pole figures correspond to the zones (I), (II), (III), and (IV) which are marked in **Fig. IV-12**. The normal direction of pole figures corresponds to welding direction (*i.e.* X-axis).

The simulated texture after welding can be revealed by <100> pole figures. **Fig. IV-13** presents the pole figures of the texture for the different zones which are marked by the rectangles in **Fig. IV-12**. The normal direction of these pole figures (*i.e.* the centers of the pole figures) correspond to the welding direction. Taking (D1) as a first example as can be seen in **Fig. IV-12**, zone (I) is located in the region of base metal which is composed by equiaxed grains. Therefore, the cloud of points in **Fig. IV-13** (D1-I) is randomly distributed, revealing the initial homogeneous grain structures. However, the points in **Fig. IV-13** (D1-II) become heterogeneous. This is due to the epitaxial grain growth as well as the beginning of the grain growth competition in zone (II). As the grain growth competition becomes more intense in zone (III), the points are gathered in three regions, shown in **Fig. IV-13** (D1-III). It reveals that the grain selection has already occurred. Moreover, the cloud of points corresponding to zone (IV) becomes more condensed in **Fig. IV-13** (D1-IV) due to the grain growth competition. The remaining grains have their <100> trunk direction within a very small region. In addition, comparing pole figures of (D3), the same trend is found among **Fig. IV-13** (D3-I), (D3-II), (D3-III), and (D3-IV). However, comparing the corresponding pole figures between (D3) and (D1), it shows that the points in (D3) are more aligned with the Y-axis (*i.e.* more perpendicular to X-axis), which is caused by the higher welding velocity in (D3). This phenomenon coincides with the experimental observations shown in **Fig. I-20**.

4.2.3. Multiple linear passes upon GTAW process

The objective of the cases with multiple linear passes upon GTAW process is to simulate the propagation of the grain structure among the passes. It gives better understanding of the improvement achieved by the present 3D CAFE model. The numerical and process parameters of the 3D CAFE calculation of the cases are given in **Tab. IV-7**. The boundary condition is applied on all the surfaces of the workpiece. The 3D CAFE model is presented in **Fig. IV-14**.

Tab. IV-7 Parameters for the multiple linear passes upon GTAW process (The dendrite tip kinetic law (L1) and (L2) are presented in **Tab. IV-3**)

Parameter	Symbol	Value		Unit
		E1	E2	
FE domain	Ω_{FE}	350×150×12		mm^3
Initial FE element size	l_{FE}	5		mm
CA domain	Ω_{CA}	140×90×12		mm^3
CA element size (fixed)	l_{CA}	3		mm
Cell size	l_{cell}	80		μm
Time step	Δt	0.05		s
Number of processors	N_{pro}	64		-
Initial temperature	T_0	20		°C
Environmental temperature	T_{ext}	20		°C
Heat transfer coefficient	h_T	5		$W\ m^{-2}\ K^{-1}$
Emissivity	ε_r	0.25		-
Initial grain density	N_0	10^{11}		m^{-3}
Dendrite tip kinetic law	L	L1	L2	-
Velocity of heat source	v^H	2		$mm\ s^{-1}$
Input power of heat source	$\dot{Q}_{input}$	7500		W
Semi-axes in y direction	a	18		mm
Semi-axes in z direction	b	10		mm
Semi-axes in x direction	c	18		mm
Starting point of heat source (P1)	X_S, Y_S, Z_S	125, 87, 12		mm
Ending point of heat source (P1)	X_E, Y_E, Z_E	215, 87, 12		mm
Starting point of heat source (P2)	X_S, Y_S, Z_S	125, 82, 12		mm
Ending point of heat source (P2)	X_E, Y_E, Z_E	215, 82, 12		mm
Starting point of heat source (P3)	X_S, Y_S, Z_S	125, 77, 12		mm
Ending point of heat source (P3)	X_E, Y_E, Z_E	215, 77, 12		mm
Starting point of heat source (P4)	X_S, Y_S, Z_S	125, 72, 12		mm
Ending point of heat source (P4)	X_E, Y_E, Z_E	215, 72, 12		mm
Starting point of heat source (P5)	X_S, Y_S, Z_S	125, 67, 12		mm
Ending point of heat source (P5)	X_E, Y_E, Z_E	215, 67, 12		mm
Starting point of heat source (P6)	X_S, Y_S, Z_S	125, 62, 12		mm
Ending point of heat source (P6)	X_E, Y_E, Z_E	215, 62, 12		mm

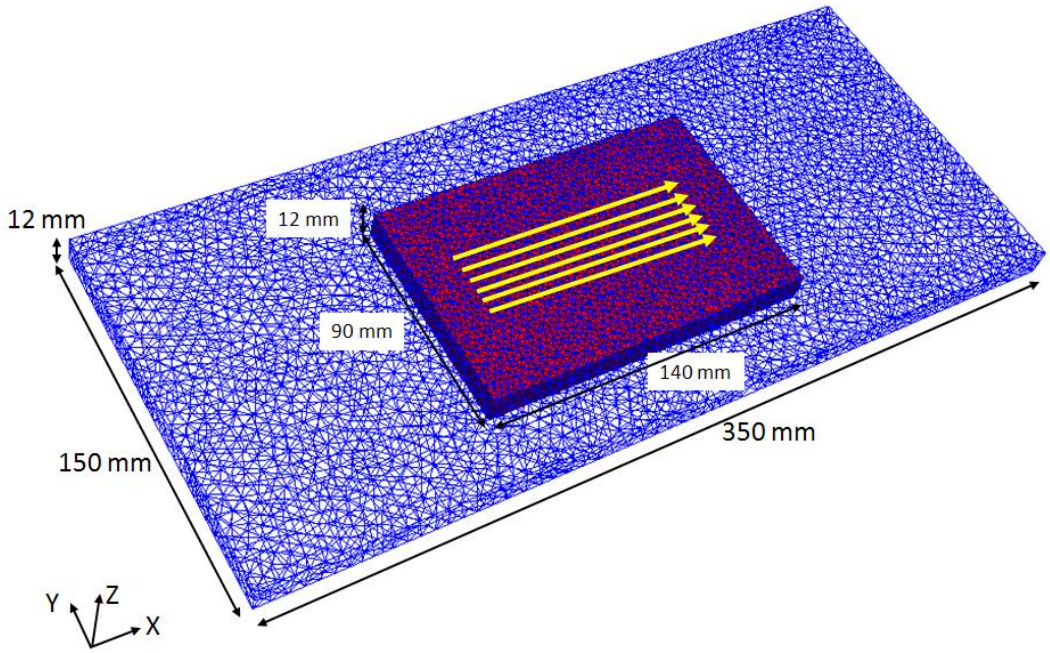

Fig. IV-14 The FE and CA model for the multiple linear passes upon GTAW process. The FE domain is represented by the blue mesh, and the CA domain is represented by the red mesh. The trajectories of the heat source (P1 – P6) are represented by the yellow arrows, respectively.

As represented by the yellow arrows in **Fig. IV-14**, six successive linear passes with parallel direction of the Goldak volumetric heat source are defined by the parameters given in **Tab. IV-7**. The first pass (P1) takes place with the trajectory of heat source from (125, 87, 12) mm to (215, 87, 12) mm. The next passes P2 – P6 are implemented with a -5 mm shift in the Y directions from the previous pass so as to remelt part of the columnar grains formed previously.

Predictions of the final structures are obtained based on different dendritic kinetic laws, *i.e.* (L1) and (L2), respectively. The simulated results of E1 corresponding to (L1) are shown in **Fig. IV-15** and **Fig. IV-16** while the results of E2 corresponding to (L2) are shown in **Fig. IV-17** and **Fig. IV-18**.

Fig. IV-15(FE) gives the FE result at a given time (*i.e.* 36 s after starting the fourth pass) of the multiple linear passes GTAW process. Only part of the FE domain is shown. The hot temperature spot (in red color) at the top surface of the FE domain indicates the position of the heat source. Note that the temperature of the workpiece is reinitialized to be T_0 for each pass which corresponds to a complete cooling condition of the workpiece. The temperature

distribution is thus not affected by the history of previous passes. The mesh size is the finest at the position of the heat source since it is adapted to track the regions of the large temperature gradient. The 3D green contour according to the temperature scale represents the shape of the liquidus isotherm.

Fig. IV-15(CA) gives the corresponding result at the CA mesh. Although the size of CA mesh is smaller than that of the FE mesh (see **Tab. IV-7**) so as to reduce the computation cost, the CA mesh encompasses the whole weld domain. The temperature field of CA mesh is computed from a projection from that of the FE mesh. The shapes of the liquidus isotherm therefore slightly differ due to the different size of the elements in the FE and CA meshes.

The grain structure is shown in **Fig. IV-15**(Grains). Because the liquid cells are not represented, the shape of the weld pool can be directly visualized. It can be seen that the shape of the weld pool closely follows that of the liquidus isotherm where remelting takes place. It is hard to notice the deviation of the shape of the weld pool from the shape of the liquidus isotherm in the CA mesh. This is because the undercooling corresponding to the maximum dendritic growth velocity in this case is about 7 °C (the maximum dendritic growth velocity corresponds to the velocity of the heat source only at steady state in this case), which is small enough in the welding process. In addition, it is found that the columnar grains grow in the direction perpendicular to the boundary of the weld pool, which corresponds to the explanation detailed in **Section 1.3**.

Fig. IV-16 presents the final grain structures after each of the 6 passes, with the same view as in **Fig. IV-15** but also in a transverse cross section. Because the heat source shifts -5 mm at each successive pass (see the trajectories of the heat source in **Tab. IV-7**), the meeting line for the columnar grains thus shifts -5 mm at each successive pass, shown in **Fig. IV-16**(3D). This implies that the heat source has melted the meeting line of the previous pass. It is also noticed that many new columnar grains appear at the top surface on the left side of the meeting line (in other words, the formed columnar grains in **Fig. IV-16**(3D) cannot survive a long distance, and are truncated by new columnar grains). Based on the assumption that no nucleation takes place in the weld pool, it can be explained that these newly appearing columnar grains are the grains which grow upward to the top surface from the bottom of the weld pool and continue growing on the top surface, shown in **Fig. IV-16**(cut). The dendrite

tip kinetic law (L1) implies that more grains have the possibility to take part in the competition due to the very small undercooling for growth. However, this intense grain growth competition does not exist in the next simulation case E2 based on (L2) and thus different grain structure appears. The effects of the dendrite tip kinetic law are presented in **Fig. IV-17** and **Fig. IV-18**.

Compared to the input power of the heat source during welding process, the latent heat released from the solidification has less influence on the temperature distribution. Therefore, the temperature fields in **Fig. IV-15** and **Fig. IV-17** are similar to each other. The shape of the liquidus isotherm in **Fig. IV-17**(FE) and (CA) are thus similar to those in **Fig. IV-15**. However, more attention can be paid in the shape of the weld pool shown in **Fig. IV-17**(Grains). It is seen to significantly depart from the shape of the liquidus isotherm in **Fig. IV-17**(CA). Different from the previous simulation (*i.e.* case E1), the undercooling corresponding to the maximum dendrite tip growth velocity in case E2 is about 140 °C at the steady state of the welding process. That is why a more elongated weld pool appears in **Fig. IV-17**(Grains).

The final grain structures after each of the 6 passes based on the dendrite tip kinetic law (L2) are presented in **Fig. IV-18** (3D) and (cut). It shows very different grain structure from those in **Fig. IV-16** (3D) and (cut), respectively. Due to the more elongated boundary of the weld pool, the orientations of the columnar grains in **Fig. IV-18** (3D) are thus changed to be more perpendicular to the moving direction of the heat source than those in **Fig. IV-16** (3D). In addition, the columnar grains on the left side of the meeting line can survive and grow a very long distance, which is not observed in case E1. The reason is that the temperature gradient remains lower at the solid/liquid interface due to the higher undercooling. Consequently, only the grains with the preferred growth direction highly coinciding the temperature gradient can finally survive. It clearly shows that the meeting line of previous pass is remelted by the heat source of next pass, and thus the new meeting line moves from left to right, shown in **Fig. IV-18** (cut). In addition, due to the smaller temperature gradient at the weld pool boundary, the columnar grains in **Fig. IV-18** (cut) are smoother than those in **Fig. IV-16** (cut), and less columnar grains at top surface are truncated by the new columnar grains formed from the bottom of the weld pool in **Fig. IV-18** (3D).

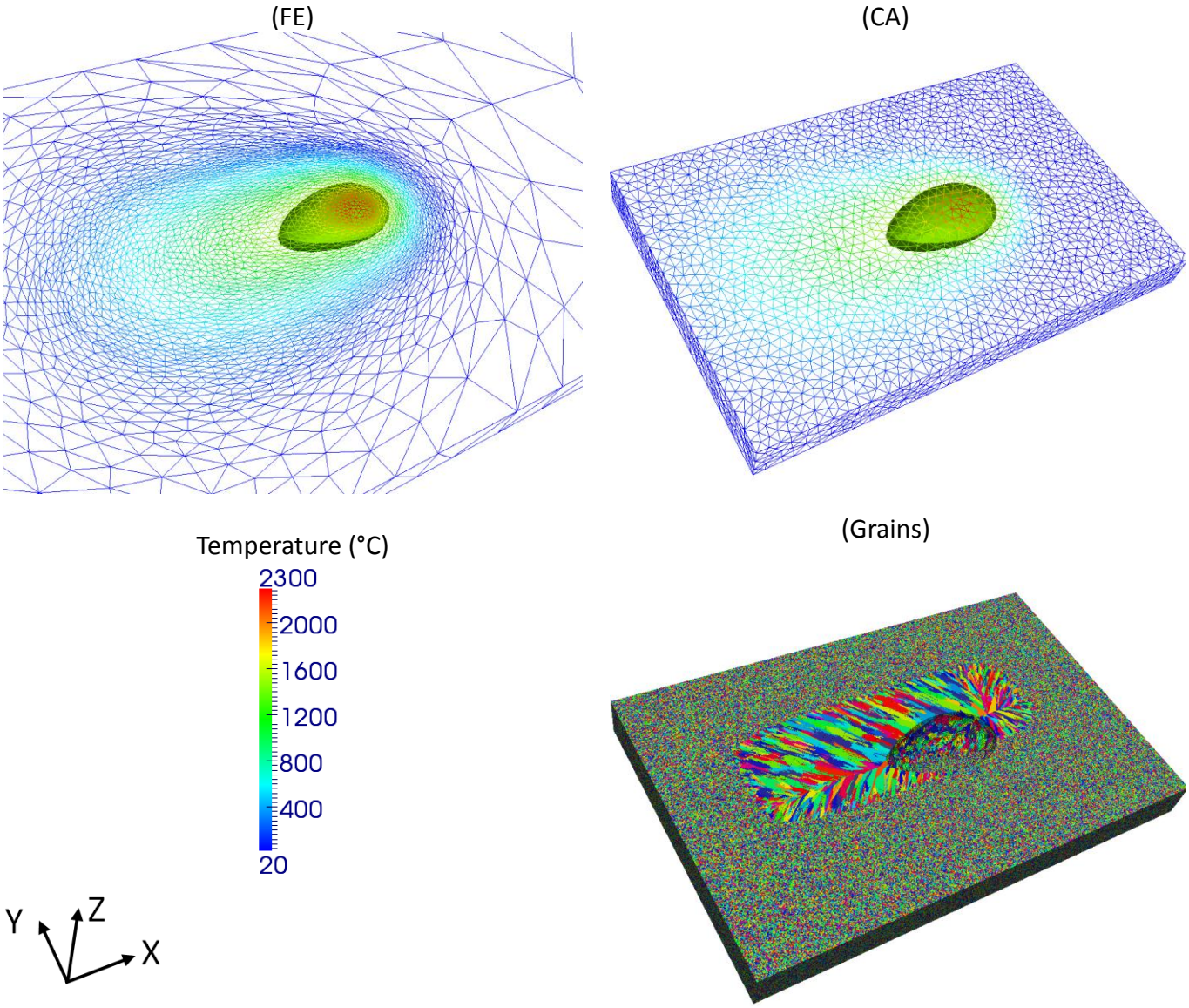

Fig. IV-15 Snapshot at 36 s during the fourth pass (P4) of the 3D CAFE grain structure simulation for the multiple linear passes GTAW (case E1). (FE): part of the refined FE mesh, (CA): fixed CA mesh, and (Grains): grain structure computed based on the dendrite tip kinetic law (L1). The liquidus isotherm computed on the FE mesh is represented by the green contour in (FE). Similarly, the green contour in (CA) represents the liquidus isotherm which is projected from FE mesh. In addition, in (Grains), the liquid structure is transparent so that the solid as well as the mushy zone – liquid boundary is visualized.

(3D) (cut)

(P1)

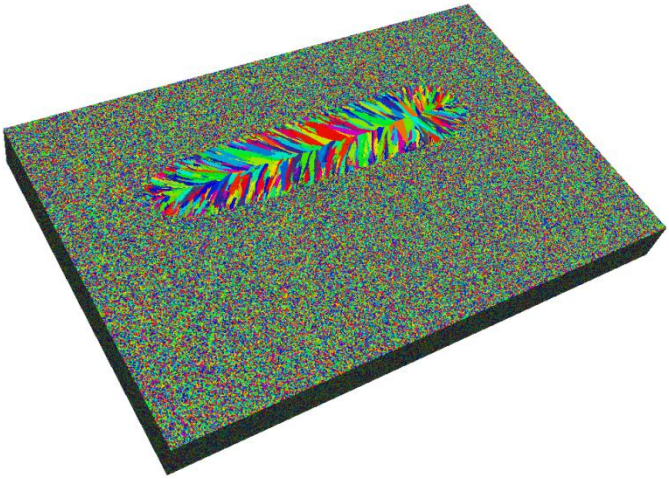

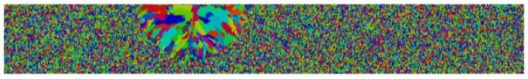

(P2)

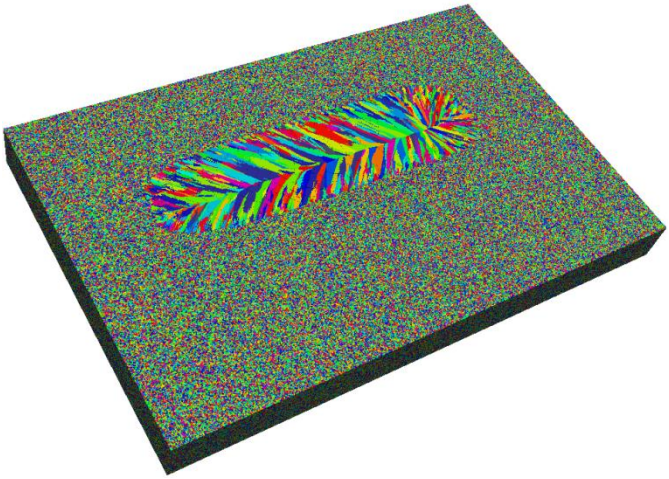

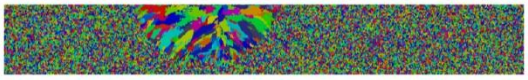

(P3)

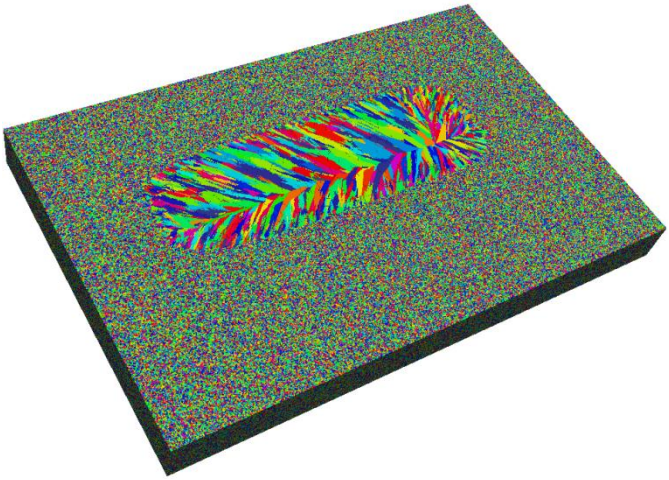

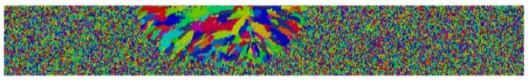

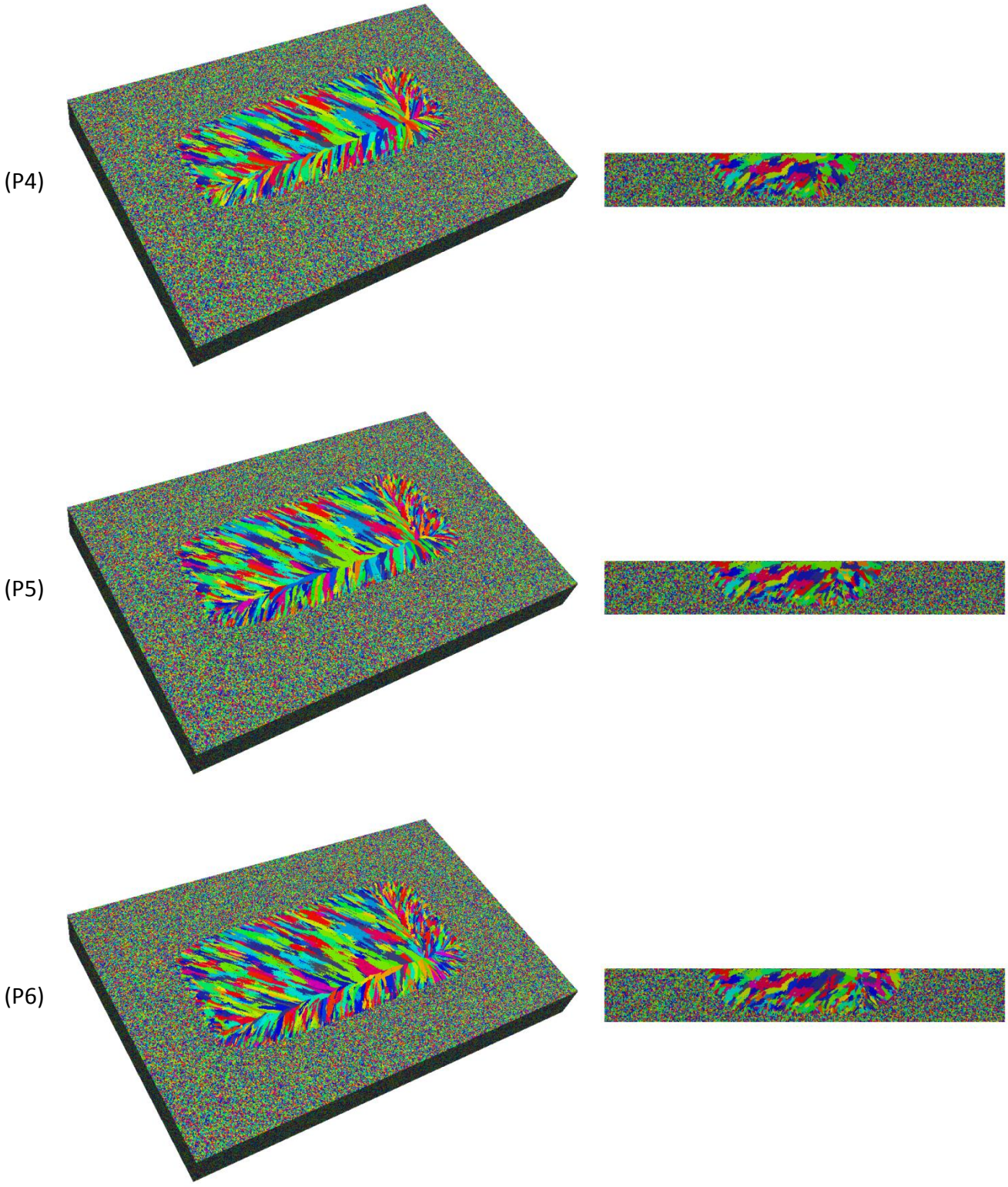

Fig. IV-16 3D CAFE grain structures of the multiple linear passes GTAW simulation (case E1) with the dendrite tip kinetic law (L1), (3D): at the boundary of the CA domain, and (cut): in a transverse cross section at coordinate X = 175 mm at the end of path P1 – P6, respectively.

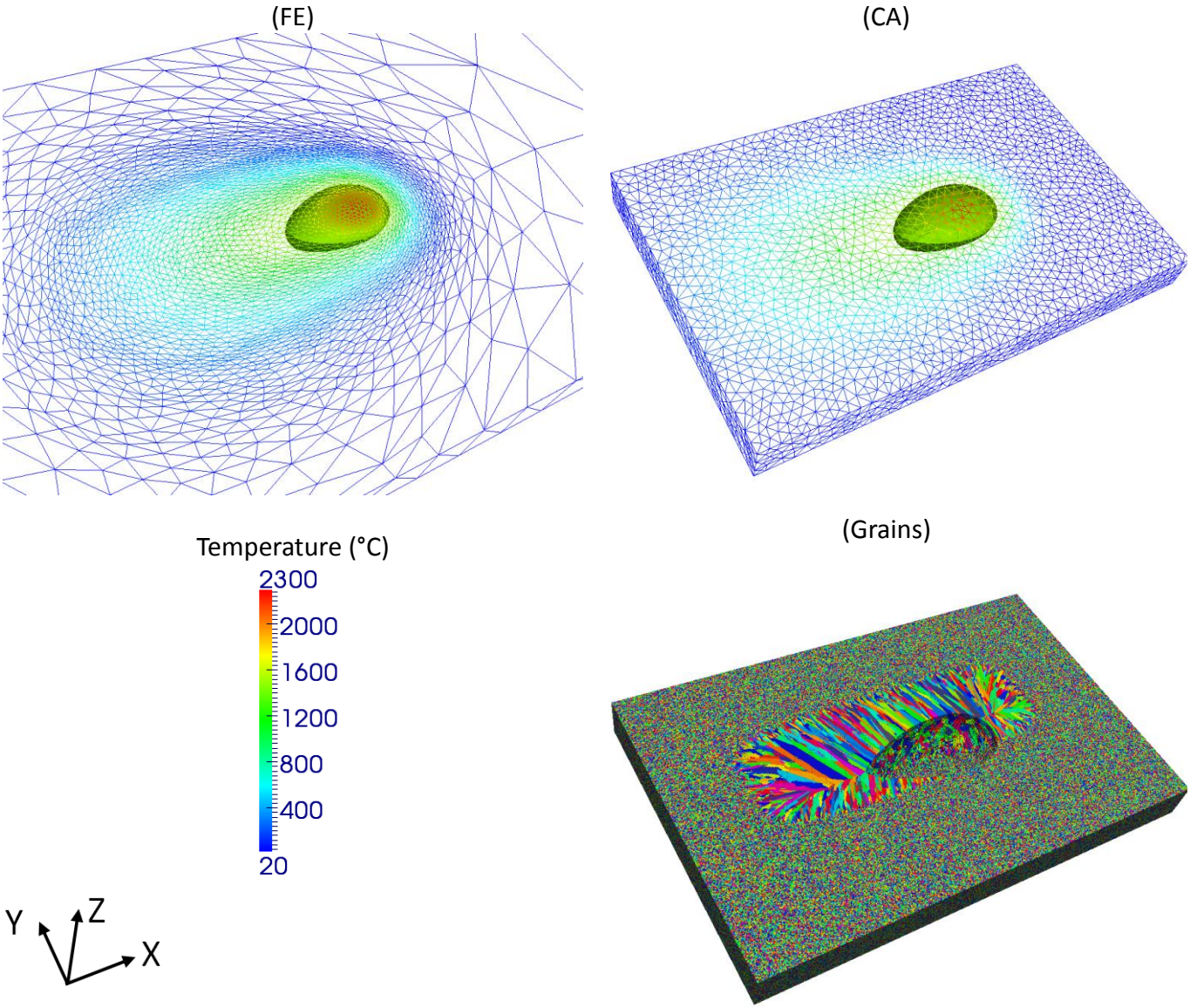

Fig. IV-17 Snapshot at 36 s during the fourth pass (P4) of the 3D CAFE grain structure simulation for the multiple linear passes GTAW (case E2). (FE): part of the refined FE mesh, (CA): fixed CA mesh, and (Grains): grain structure computed based on the dendrite tip kinetic law (L2). The liquidus isotherm computed on the FE mesh is represented by the green contour in (FE). Similarly, the green contour in (CA) represents the liquidus isotherm which is projected from FE mesh. In addition, in (Grains), the liquid structure is transparent so that the solid as well as the mushy zone – liquid boundary is visualized.

(3D) (cut)

(P1)

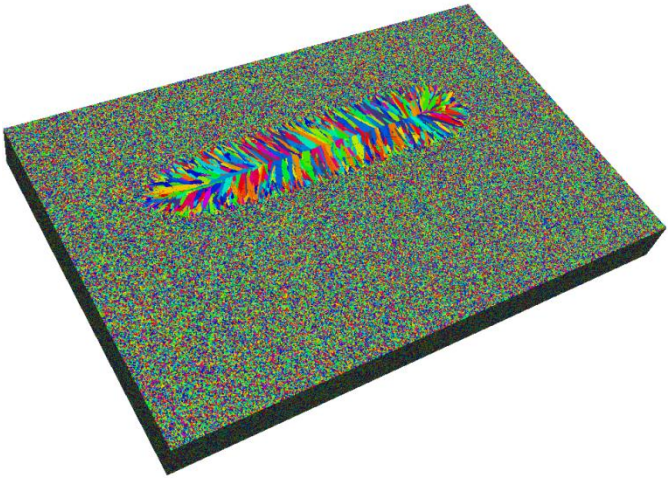

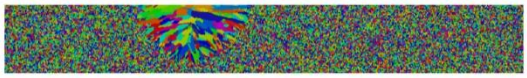

(P2)

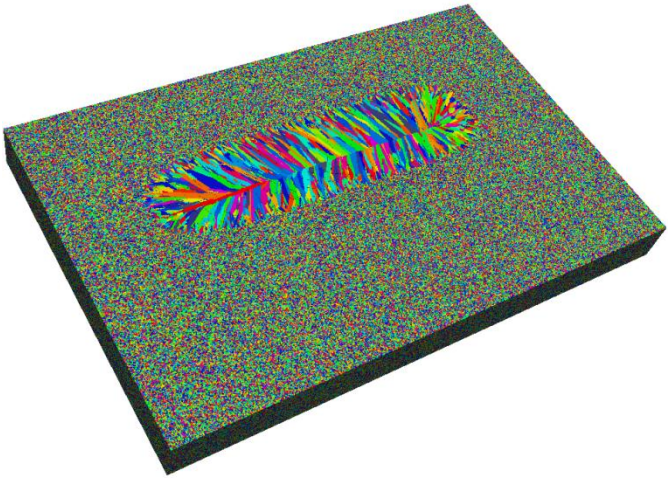

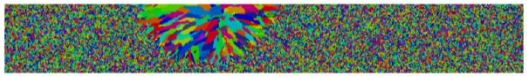

(P3)

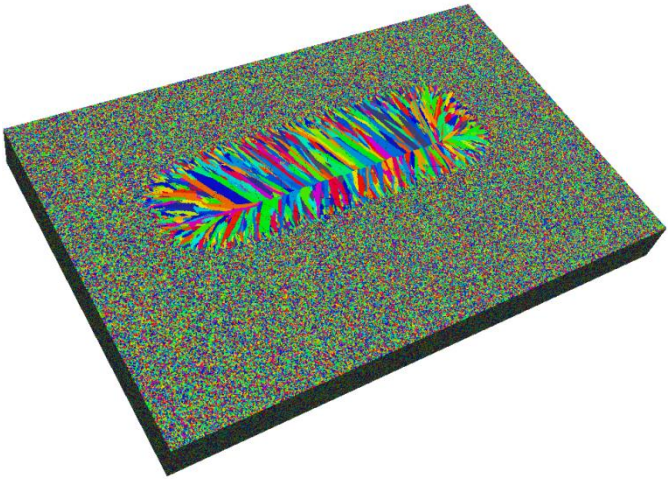

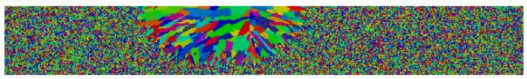

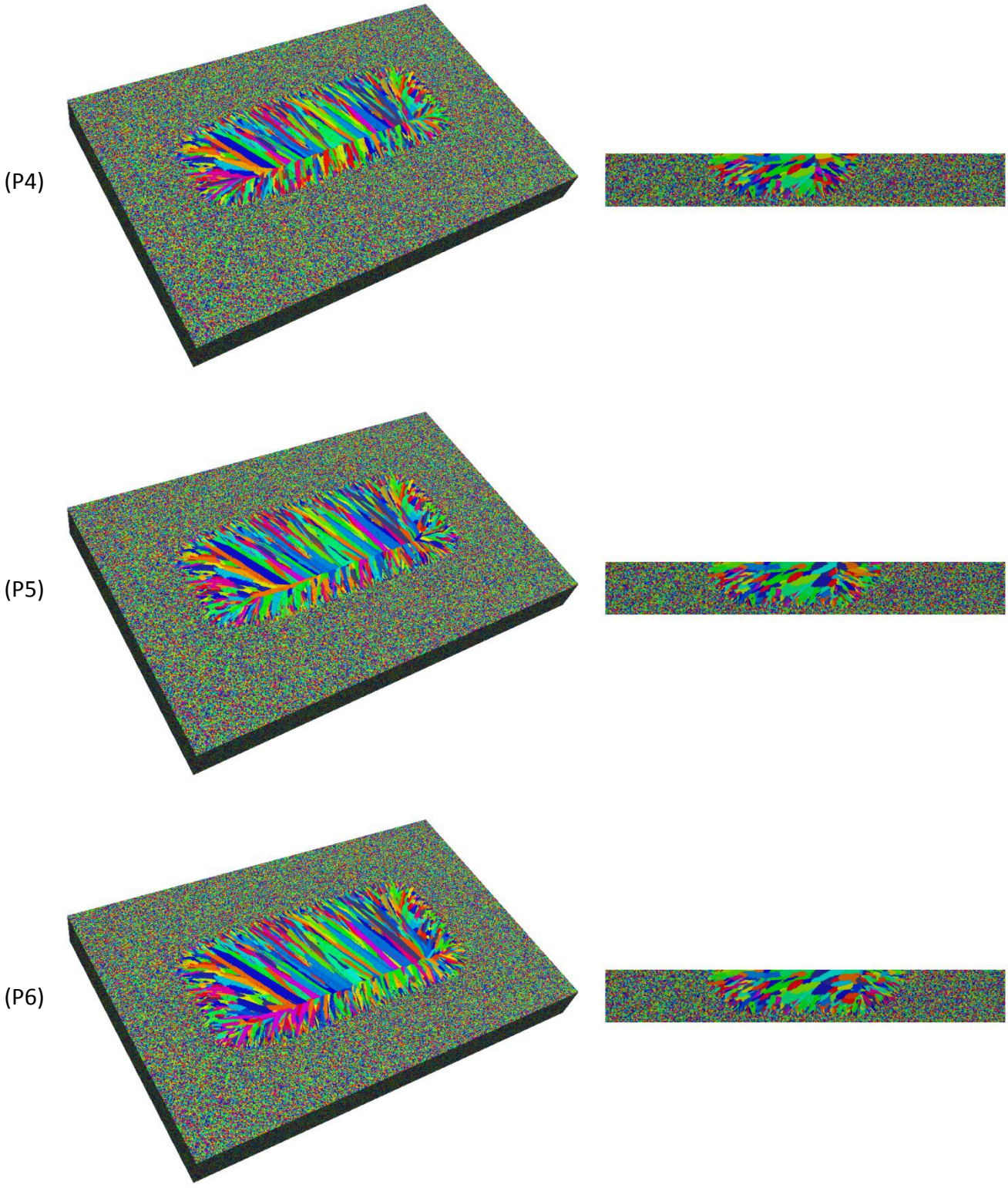

Fig. IV-18 3D CAFE grain structures of the multiple linear passes GTAW simulation (case E2) with the dendrite tip kinetic law (L2), (3D): at the boundary of the CA domain, and (cut): in a transverse cross section at coordinate X= 175 mm at the end of path P1 – P6, respectively.

4.2.4. Multiple passes with overlapping depths upon GTAW process

The predictions upon multiple passes with overlapping depths permit another understanding of grain structure evolution that can be simulated with the present 3D CAFE model. The parameters of the 3D CAFE calculation of this case are given in **Tab. IV-8**. The boundary condition is applied on all the surfaces of the workpiece. The 3D FE model is presented in **Fig. IV-19**. Note that the dimension size of CA domain is identical to that of FE domain, the CA mesh is thus not presented for clarity.

Tab. IV-8 Parameters for the multiple passes with overlapping depths upon GTAW process (The dendrite tip kinetic law (L2) is presented in **Tab. IV-3**)

Parameter	Symbol	Value	Unit
FE domain	Ω_{FE}	120×30×50	mm^3
Initial FE element size	l_{FE}	5	mm
CA domain	Ω_{CA}	120×30×50	mm^3
CA element size	l_{CA}	3	mm
Cell size	l_{cell}	80	μm
Time step	Δt	0.05	s
Number of processors	N_{pro}	64	-
Initial temperature	T_0	20	°C
Environmental temperature	T_{ext}	20	°C
Heat transfer coefficient	h_T	5	$W\ m^{-2}\ K^{-1}$
Emissivity	ε_r	0.25	-
Initial grain density	N_0	10^{11}	m^{-3}
Dendrite tip kinetic law	L	L2	-

Tab. IV-9 Parameters of the Goldak heat source for the multiple passes with overlapping depths upon GTAW process

Parameter	Symbol	Value			Unit
		P1	P2	P3	
Velocity of heat source	v^H	4	4	4	$mm\ s^{-1}$
Input power of heat source	$\dot{Q}_{input}$	25000	18000	15000	W
Semi-axes in y direction	a	3	3	3	mm
Semi-axes in z direction	b	60	50	45	mm
Semi-axes in x direction	c	3	3	3	mm
Starting point of heat source	X_S, Y_S, Z_S	20, 15, 50	20, 17, 50	20, 13, 50	mm
Ending point of heat source	X_E, Y_E, Z_E	100, 15, 50	100, 17, 50	100, 13, 50	mm

As shown in **Fig. IV-19**, three successive linear passes with the Goldak volumetric heat source are defined by the parameters given in **Tab. IV-9**. The starting and ending points of the heat

source are such that overlapping of the weld pools can take place, the first pass taking place at the center of the top XY plane of the domain and the second and third passes taking place on its side with a +2 mm and -2 mm shift in the Y directions, respectively. The values of the input power and semi-axes in z direction vary in order to control the heat source and thus the weld pool with different dimension in each pass.

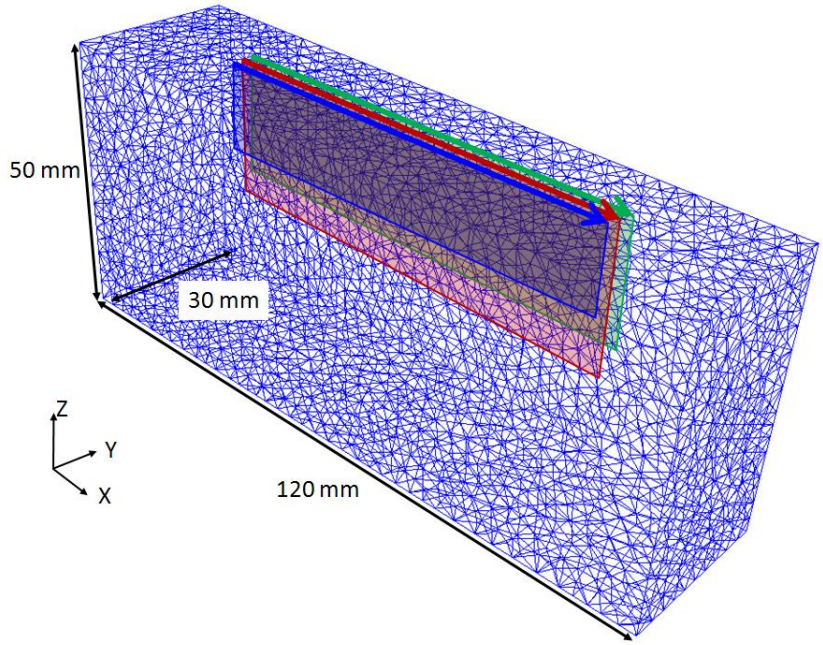

Fig. IV-19 The FE model for the multiple overlapping depths passes upon GTAW process. The FE domain is represented by the blue mesh. The dimension size of CA domain is identical to that of the FE domain, and thus not presented for clarity. The trajectories of the heat source (P1 – P3) are represented by the red, green, and blue arrows, respectively. The rectangles attached to the arrows represent the dimension of the heat source.

Prior to consider the final result of the several passes, the temperature field is given in **Fig. IV-20**(FE) at a given time (*i.e.* 16.25 s) during the first pass. The 3D green contour according to the temperature scale represents the shape of the liquidus isotherm. The temperature field with the liquidus isotherm in CA mesh is projected from FE mesh, shown in **Fig. IV-20**(CA). It is well retrieved in **Fig. IV-20**(Grains) when considering a vertical cross section through the domain at Y = 15 mm (*i.e.* at the center of P1). Half of the shape of the weld pool can be directly visualized due to the use of transparent liquid cells. It follows the shape of the liquidus isotherm in **Fig. IV-20**(CA) but departs from it where growth speed is large. The reason is due to the large undercooling of the growing structure that develops the growth front below the liquidus isotherm. It also reveals the grain growth competition taking

place upon columnar growth and epitaxial growth of the equiaxed grains that are partly melted.

Fig. IV-21 presents the final structure after each of the 3 passes, with the same view as in **Fig. IV-20** but also in a transverse cross section which is vertical to X axis. After the first pass, the columnar grains are found to meet at a symmetrical surface defined by the heat source path. Because the second pass is shifted to the right-hand-side, the columnar grains now form a meeting line also shifted to the right as seen in **Fig. IV-21**(P2-cut). The initial columnar grain structure seen on the right-hand-side of **Fig. IV-21**(P1-cut) was fully remelted up to the lower depth reached by the weld pool. In fact, the weld pool input power was decreased, and Snapshots of temperature distribution as well as the liquidus isotherm of P2 and P3 at 16.25 s are shown in **Fig. IV-22**. But only part of the left-hand-side columnar structure of **Fig. IV-21**(P1-cut) was melted so epitaxial growth could take place on the already existing columnar grains, resulting in the dissymmetry of the structure seen in **Fig. IV-21**(P2-cut). Finally, upon pass 3 operated 2 mm on the left-hand-side of pass 1, namely 4 mm left of pass 2, the structure generated during the second pass is only partially remelted and propagated. A second meeting line appears in the structure. The cross section in **Fig. IV-21**(P3-cut) reveals evidence of the 3 successive passes with a very complicated final grain structure.

Note that the dendrite tip kinetic law in this case presented above is L2. In the present work, the simulation of this case with the dendrite tip kinetic law L1 is not completed. The reason is discussed as follows:

Comparing the kinetic law L1 with L2 in **Fig. IV-3**, the dendritic growth velocity, v_{CA}, computed by L1 is much more sensitive to the undercooling, ΔT, than that computed by L2. That is to say, the same variation of undercooling induces more variations of dendritic growth velocity computed by L1 than by L2.

Due to the large input power and velocity of the heat source (see **Tab. IV-9**), the computed temperature gradient, G_T, at the weld pool is very huge, especially in the front half quadrant of the pool. Consequently, the interpolated temperature into the growing cells (I_v = 1) vary from the expected temperature at solid/liquid interface deeply. This is due to the limitation of the discretization of fields for the CA cells with finite cell size (note that this limitation can be removed only when the cell size equal to 0).

Because v_{CA} computed by L1 is very sensitive to the computed undercooling, a small departure from the expected temperature at solid/liquid interface induces a very giant increase of the computed dendrite growth velocity v_{CA}. Finally, the micro time step δt (computed by **Eq. III-65**) is very small (in this case with L1, δt = 0.000002 s). It will cost a lot of computation resource to complete this simulation due to the tiny value of δt. Therefore, this case with the dendrite tip kinetic law L1 is canceled.

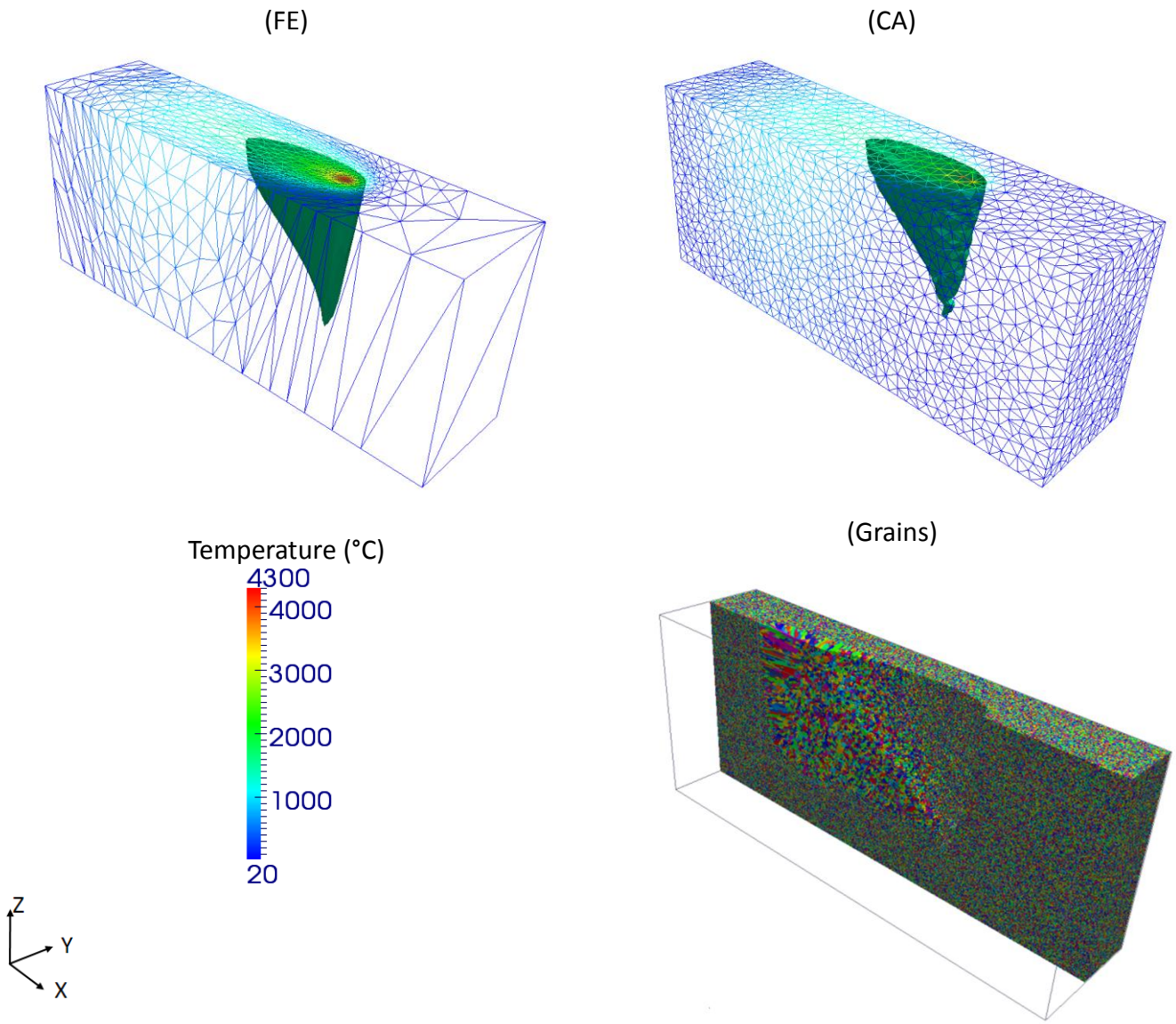

Fig. IV-20 Snapshot at 16.25 s during the first pass (P1) of the 3D CAFE grain structure simulation for the multiple passes GTAW showing (FE): refined FE mesh (colors are proportional to the temperature), (CA): fixed CA mesh, and (Grains): grain structure in half the volume of the domain as well as the mushy zone – liquid boundary where the grain envelops grow into the liquid, computed based on the dendrite tip kinetic law (L2). The liquidus isotherm computed on the refined FE mesh is represented by the green contour in (FE).

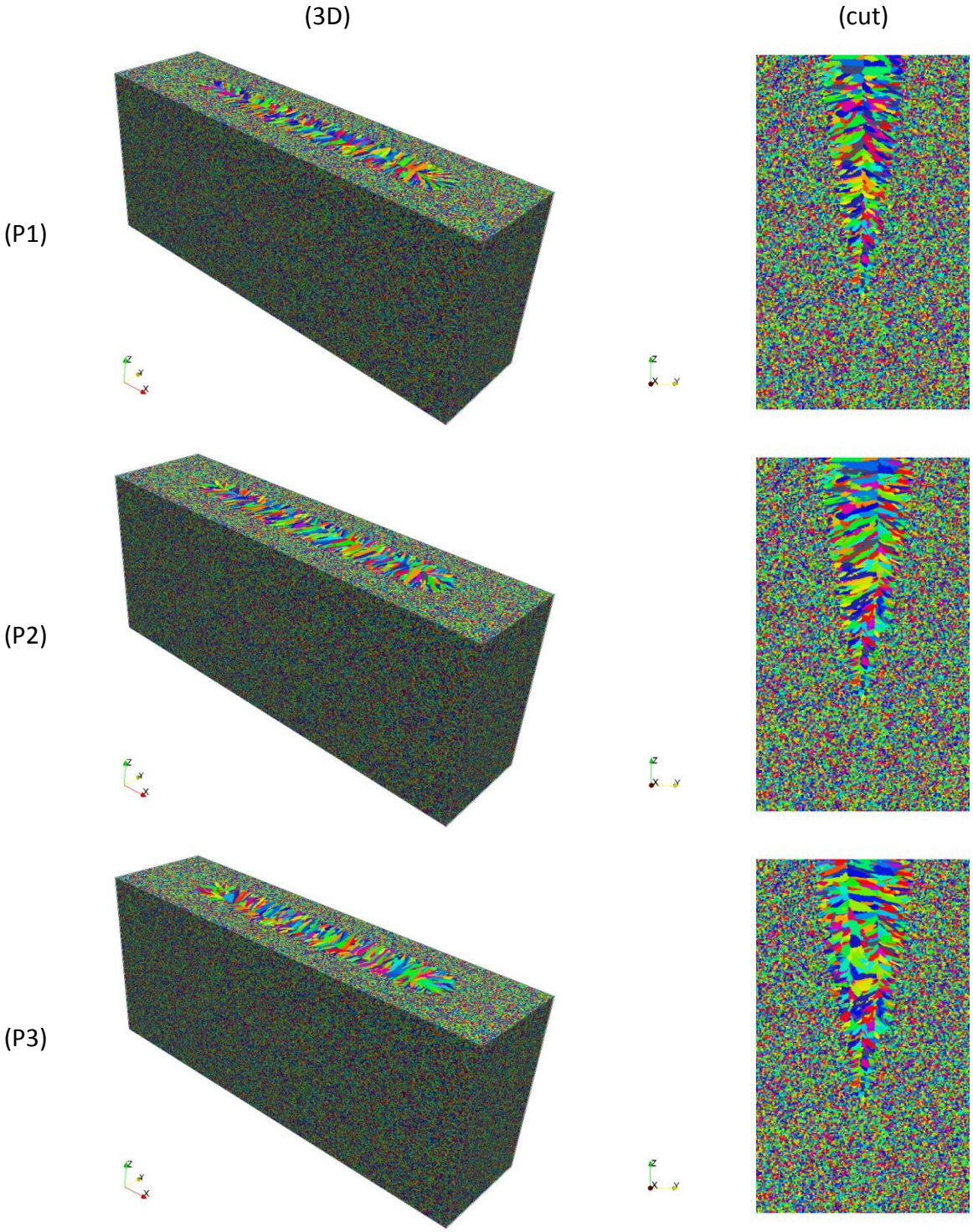

Fig. IV-21 3D CAFE grain structures of the multiple passes GTAW simulation observed (3D): at the boundaries of the domain and (cut) in a transverse cross section at coordinate X = 60 mm at the end of (P1) path 1, (P2) path 2, (P3) path 3.

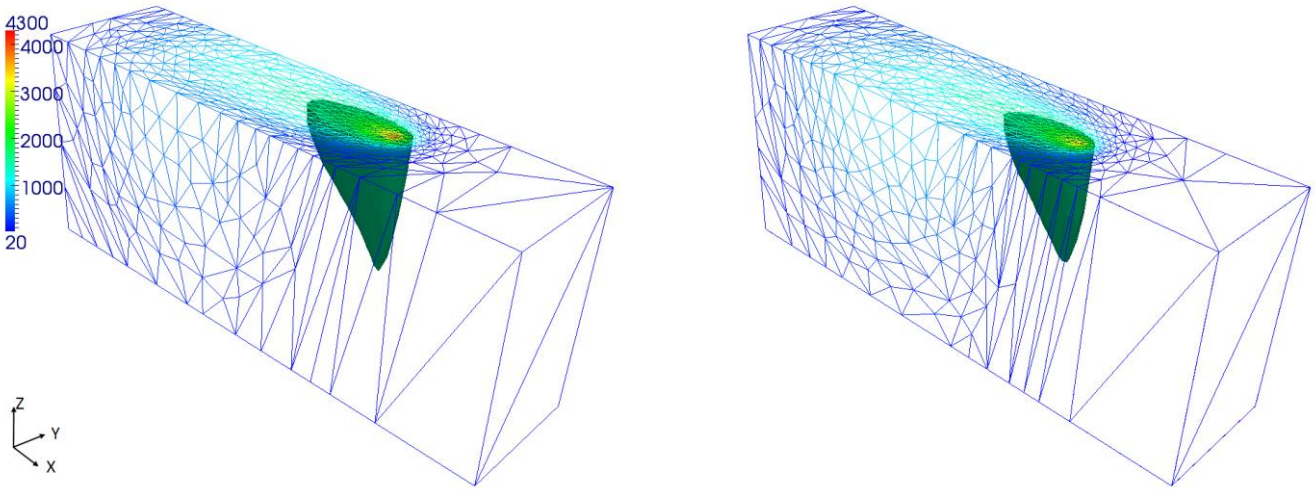

(P2) (P3)

Fig. IV-22 Snapshot at 16.25 s of refined FE mesh (colors are proportional to the temperature), during (P2): the second pass, and (P3): the third pass for the multiple passes GTAW The liquidus isotherm computed on the refined FE mesh is represented by the green contour.

4.2.5. Multiple linear passes upon GMAW process

The objective of the case with multiple linear passes upon GMAW process is to simulate the grain structure evolution among the passes of GMAW process with the adding metal. The numerical model contains the domain of workpieces as well as the domain of surrounding air. The melted filling metal is added on the top surface to form the weld bead. In this case, the filling metal is supposed to be identical to that of workpieces, *i.e.* URANUS 2202.

4.2.5.1. Multiple linear passes upon GMAW process in 2D

A first 2D case in a simple geometry is presented in order to demonstrate the possibility of the present CAFE model on the simulation of the GMAW process.

As illustrated in **Fig. IV-23** (FE), the 2D FE domain contains two parts which represent the metal (*i.e.* workpiece) and surrounding air, respectively. The interface of the two parts is implicitly defined by the Level Set function with the value of 0 (i.e. $\psi = 0$). A transition zone around the interface is defined with the thickness of 2ϵ. The average material properties are computed by the mixing law within the transition zone. A CA mesh is defined and superimposed on the FE mesh. In this case, the dimension of the CA mesh is chosen to be

the same with that of the FE mesh. The values of Level Set function are projected from the FE mesh to the CA mesh. The CA mesh, therefore, is implicitly divided into metal and air. The parameters for the definitions of the FE and CA meshes are listed in **Tab. IV-10**.

Tab. IV-10 Numerical parameters for the multiple linear passes upon GMAW process in 2D (The dendrite tip kinetic law (L2) is presented in **Tab. IV-3**)

Parameter	Symbol	Value	Unit
FE domain	Ω_{FE}	250×30	mm^2
Metal domain in FE mesh	Ω_{FE}^{Metal}	250×12	mm^2
Air domain in FE mesh	Ω_{FE}^{Air}	250×18	mm^2
Half thickness of transition zone	ϵ	0.8	mm
CA domain	Ω_{CA}	250×30	mm^2
Metal domain in CA mesh	Ω_{CA}^{Metal}	250×12	mm^2
Air domain in CA mesh	Ω_{CA}^{Air}	250×18	mm^2
CA element size (fixed)	l_{CA}	3	mm
Cell size	l_{cell}	80	μm
Time step	Δt	0.005	s
Number of processors	N_{pro}	32	-
Initial temperature	T_0	20	°C
Environmental temperature	T_{ext}	20	°C
Imposed temperature (Dirichlet)	T_{impose}	20	°C
Heat transfer coefficient	h_T	5	$W\ m^{-2}\ K^{-1}$
Emissivity	ε_r	0.25	-
Initial grain density	N_0	5×10^7	m^{-2}
Dendrite tip kinetic law	L	L2	-
Velocity of heat source	v^H	13.3	$mm\ s^{-1}$
Input power of heat source	$\dot{Q}_{input}$	4545	W
The power for plasma	$\dot{Q}_{plasma}$	4050	W
The power for droplets	$\dot{Q}_{droplet}$	495	W
Velocity of filling metal (electrode)	v_w	30	$mm\ s^{-1}$
Radius of filling metal (electrode)	R_w	0.6	mm
Temperature of droplets	T_d	2227	°C
Starting point of heat source (P1)	X_S, Y_S	25, 12	mm
Ending point of heat source (P1)	X_E, Y_E	225, 12	mm
Starting point of heat source (P2)	X_S, Y_S	40, 16	mm
Ending point of heat source (P2)	X_E, Y_E	200, 16	mm

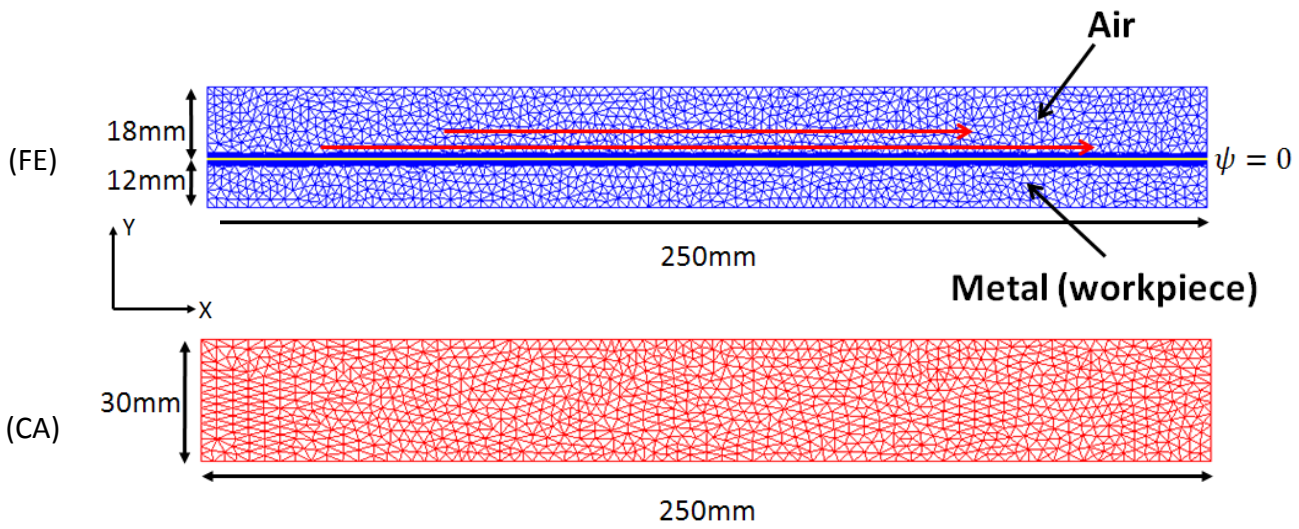

Fig. IV-23 Description of the FE and CA domains of GMAW process in 2D with (FE): the FE mesh (blue color), and (CA): the CA mesh (red color).

Assuming that the environmental temperature, T_{ext}, is 20 °C, the FE domain is initialized with the temperature, T_0, identical to T_{ext}. A Dirichlet condition is imposed on the upper surface of the air domain with the value of $T_{impose} = T_{ext}$. Moreover, adiabatic conditions are imposed for the other surfaces of the FE domain.

Two linear passes of the heat source with metal addition are defined, and represented by the red arrows in **Fig. IV-23** (FE). For GMAW, the FE model is established in a Level Set approach. Therefore, all the surface heat source term should be transformed to a volumetric term using the CSF method. The parameters related to the heat source are listed in **Tab. IV-10**. Three heat sources are defined, corresponding to the plasma, the droplets and the heat lost, respectively (see **Section 3.2.2.6**).

Some notes should be addressed for the parameters of the heat source [Des13]:

- The velocity of the welding, v^H, is 13.3 mm s^{-1} (*i.e.* 0.8 m min^{-1}), which corresponds to the moving velocity of the plasma torch.
- The total power of plasma torch, $\dot{Q}_{input}$, is 4545 W. It is divided into two parts: the first part, $\dot{Q}_{plasma}$, is used to heat the workpiece; the second part, $\dot{Q}_{droplet}$, is to melt the electrode to form the droplets (see **Section 3.2.2.6**). Therefore, $\dot{Q}_{input} = \dot{Q}_{plasma} + \dot{Q}_{droplet}$. The temperature of the droplets is supposed to be constant, and equal to 2227 °C (2500 K).

- The consumable electrode is melted with the velocity, v_w. The radius of the electrode is represented as R_w.

Fig. IV-24 gives the snapshot of simulated results at 12 s of the first pass (P1). The whole FE domain is given in **Fig. IV-24** (FE). The yellow curve represents the interface of metal and air. Comparing to the initial interface in **Fig. IV-23** (FE), the metal/air interface changes due to the formation of the weld bead. The hot temperature spot at the head of weld bead indicates the position of the heat source (the plasma torch precisely). The black contour represents the liquidus isotherm. Note that the FE domain contains the surrounding air, the green contour is thus closed. The corresponding CA result is given by **Fig. IV-24** (CA). The temperature field and Level Set function are projected from the FE mesh. **Fig. IV-24** (Grains) presents the corresponding grain structure. The air cells are not represented and thus unvisualized. The zone in light grey color represents the weld pool which is composed by the liquid cells. The solid as well as the mushy zone – liquid boundary is colored. It shows that columnar grains grow from the base metal and occupy the weld bead, due to the epitaxial growth and grain competition. The metal/air interface is well retrieved by the grain structure (note that the metal/air interface is represented by the yellow curves in **Fig. IV-24** (FE) and (CA), but by the top layer of metal cells in **Fig. IV-24** (Grains)).

Fig. IV-25 gives the snapshot of simulated results at 11.4 s of the second pass (P2). Compared with the results of (P1) in **Fig. IV-24**, the metal/air interface is changed because the second weld bead is formed above the first one, shown in **Fig. IV-25** (FE) and (CA). In addition, due to this change and the definition of the boundary condition, the heat is extracted much faster than that happened in (P1). Consequently, the maximum temperature in (P2) is smaller than that in (P1). The corresponding grain structure is shown in **Fig. IV-25** (Grains). Similarly, the top layer of metal cells coincide with the metal/air interface in **Fig. IV-25** (FE) and (CA). It shows that the columnar grains formed in the first pass epitaxially grow into the second bead. However, a very long grain (in purple color) occupies the top of the second bead. It is due to the shape of the liquidus isotherm and the weld pool, shown in **Fig. IV-25** (CA).

Fig. IV-26 shows the initial and final grain structures after (P1) and (P2), respectively. The initial grain structure in **Fig. IV-26** (Initial) is fully equiaxed with a very small size due to the

high initial grain density N_0. The grains grow epitaxially into the first weld beads, and form the columnar grain structure, shown in **Fig. IV-26** (P1). The orientations of these columnar grains are parallel to the temperature gradient. Afterwards, the columnar grains are first remelted in the second pass, and then continue to grow epitaxially into the second weld bead, shown in **Fig. IV-26** (P2). The grain in purple color can survive for a long distance because its grain orientation coincides with the temperature gradient which is in X direction at the tail of the weld pool. This can be verified by the shape of the weld pool, represented by the grey color in **Fig. IV-25** (Grains).

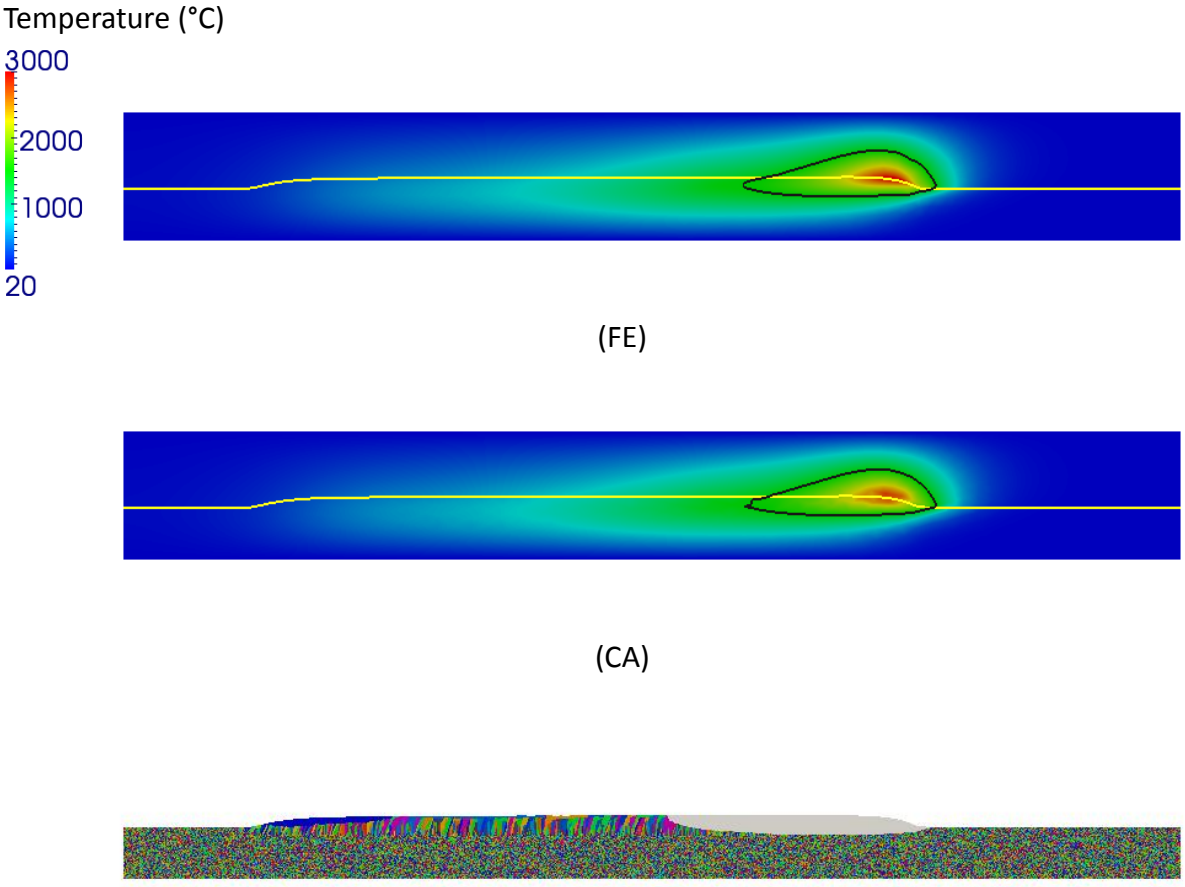

Fig. IV-24 Snapshot at 12 s during the first pass (P1) of the 2D CAFE grain structure simulation for the multiple linear passes GMAW. (FE): the temperature distribution in the FE mesh, (CA): the projected temperature distribution in the CA mesh, and (Grains): the grain structure computed based on the dendrite tip kinetic law (L2). In the (FE) and (CA), the whole domains of the FE mesh and CA mesh are represented. The interface of the metal and air domains is represented by the yellow curves. The black contour represents the liquidus isotherm. In the (Grains), the air cells are not represented, and only the metal cells are visualized. The solid as well as the mushy zone – liquid boundary is colored, and the liquid cells are in light grey.

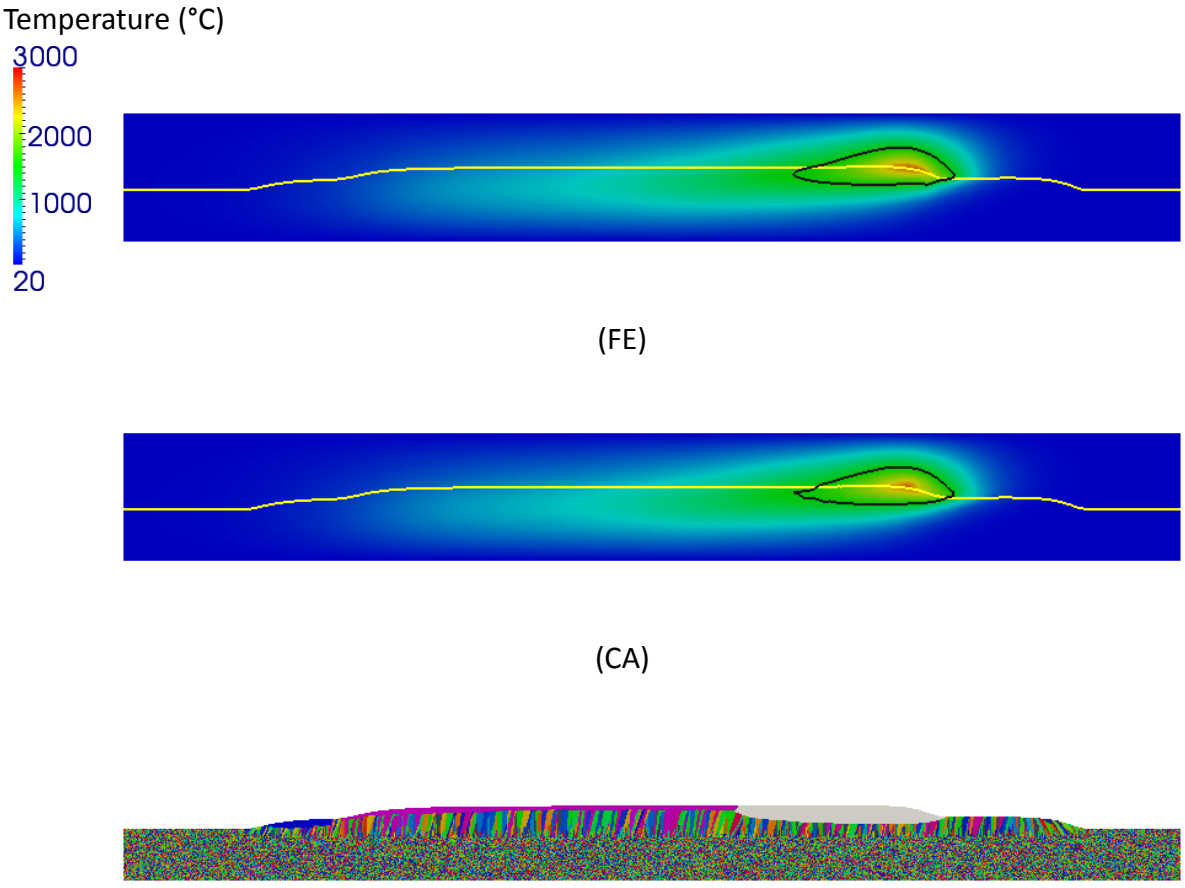

Fig. IV-25 Snapshot at 11.4 s during the second pass (P2) of the 2D CAFE grain structure simulation for the multiple linear passes GMAW. (FE): the temperature distribution in the FE mesh, (CA): the projected temperature distribution in the CA mesh, and (Grains): the grain structure computed based on the dendrite tip kinetic law (L2). In the (FE) and (CA), the whole domains of the FE mesh and CA mesh are represented. The interface of the metal and air domains is represented by the yellow curves. The black contour represents the liquidus isotherm. In the (Grains), the air cells are not represented, and only the metal cells are visualized. The solid as well as the mushy zone – liquid boundary is colored, and the liquid cells are in light grey.

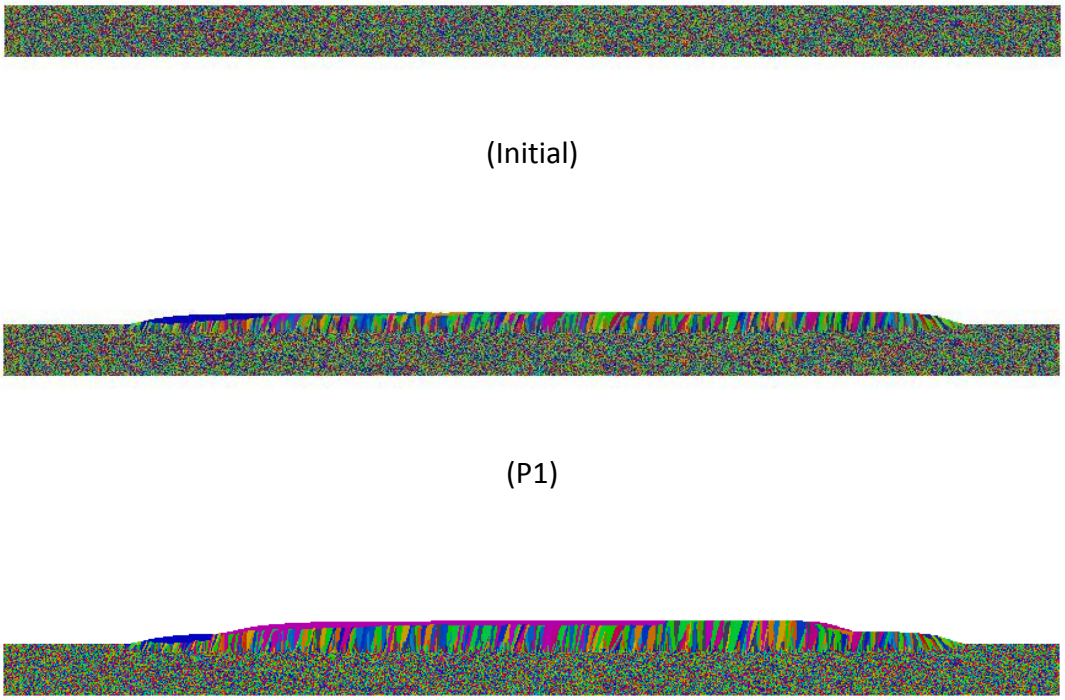

(Initial)

(P1)

(P2)

Fig. IV-26 2D CAFE grain structures of the multiple linear passes GMAW simulation with the dendrite tip kinetic law (L2). (Initial): the initial grain structure, (P1): the final grain structure after the first pass, and (P2): the final grain structure after the second pass. Note that the air cells are not represented, and thus unvisualized.

4.2.5.2. Multiple linear passes upon GMAW process in 3D

The present CAFE model can also be applied to the GMAW process in 3D. As illustrated in **Fig. IV-27**, the FE domain (represented by the blue mesh) is divided into two parts to represent the metal (*i.e.* workpiece) and surrounding air, respectively. The metal is located in the bottom part of the FE domain, while the air is on the top part. A transition zone around the interface is defined with the thickness of 2ϵ. In order to reduce the computation cost, a smaller size of dimension of CA mesh (the red mesh) is defined and superimposed on the FE mesh. Defined by the Level Set function which is projected from the FE mesh, half of the CA mesh belongs to metal domain and the other half belongs to the air domain. Note that the CA domain should encompass the welds. The parameters for the definitions of the FE and CA meshes are listed in **Tab. IV-11**.

Tab. IV-11 Numerical parameters for the multiple linear passes upon GMAW process (The dendrite tip kinetic law (L2) is presented in **Tab. IV-3**)

Parameter	Symbol	Value	Unit
FE domain	Ω_{FE}	250×50×24	mm^3
Metal domain in FE mesh	Ω_{FE}^{Metal}	250×50×12	mm^3
Air domain in FE mesh	Ω_{FE}^{Air}	250×50×12	mm^3
Half thickness of transition zone	ϵ	0.8	mm
CA domain	Ω_{CA}	200×50×12	mm^3
Metal domain in CA mesh	Ω_{CA}^{Metal}	200×50×6	mm^3
Air domain in CA mesh	Ω_{CA}^{Air}	200×50×6	mm^3
CA element size (fixed)	l_{CA}	3	mm
Cell size	l_{cell}	80	μm
Time step	Δt	0.005	s
Number of processors	N_{pro}	64	-
Initial temperature	T_0	20	°C
Environmental temperature	T_{ext}	20	°C
Imposed temperature (Dirichlet)	T_{impose}	20	°C
Heat transfer coefficient	h_T	5	$W\ m^{-2}\ K^{-1}$
Emissivity	ε_r	0.25	-
Initial grain density	N_0	10^{11}	m^{-3}
Dendrite tip kinetic law	L	L2	-
Velocity of welding	v^H	16.7	$mm\ s^{-1}$
Input power of plasma torch	$\dot{Q}_{input}$	9000	W
The power for plasma	$\dot{Q}_{plasma}$	4050	W
The power for droplets	$\dot{Q}_{droplet}$	4950	W
Velocity of filling metal (electrode)	v_w	300	$mm\ s^{-1}$
Radius of filling metal (electrode)	R_w	0.6	mm
Temperature of droplets	T_d	2227	°C
Starting point of heat source (P1)	X_S, Y_S, Z_S	100, 32, 12	mm
Ending point of heat source (P1)	X_E, Y_E, Z_E	225, 32, 12	mm
Starting point of heat source (P2)	X_S, Y_S, Z_S	100, 25, 12	mm
Ending point of heat source (P2)	X_E, Y_E, Z_E	225, 25, 12	mm
Starting point of heat source (P3)	X_S, Y_S, Z_S	100, 18, 12	mm
Ending point of heat source (P3)	X_E, Y_E, Z_E	225, 18, 12	mm

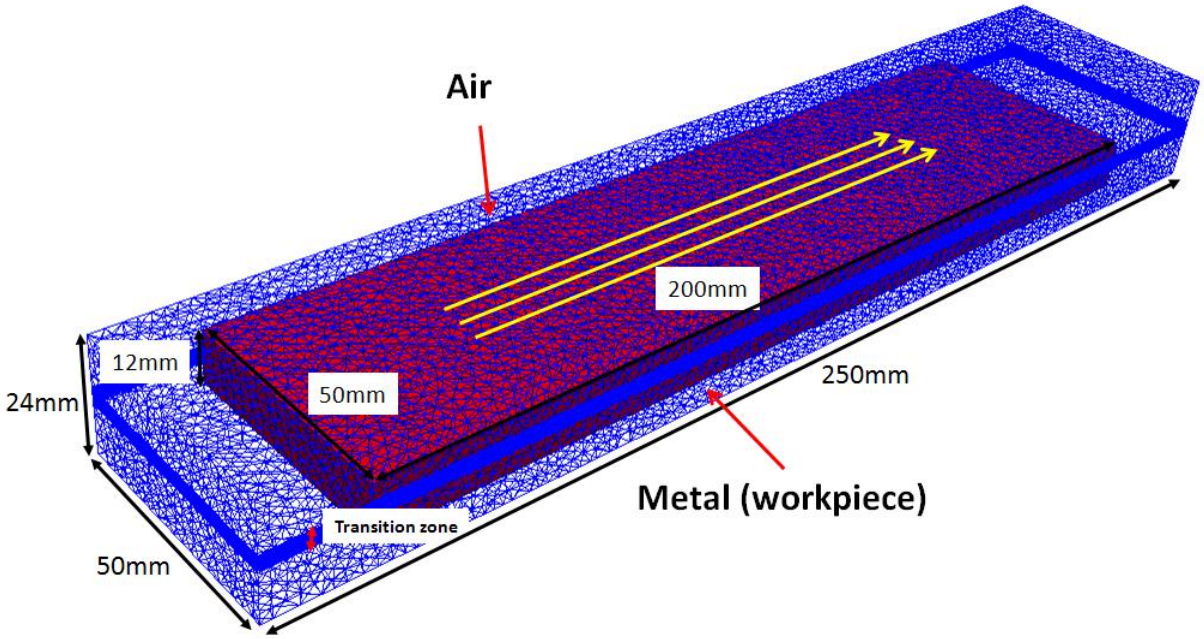

Fig. IV-27 Description of the FE and CA domains of GMAW process. The FE mesh (blue) and CA mesh (red) are divided into two parts, *i.e.* metal and air, respectively. The air is located above the metal. A transition zone with the thickness of 1.6 mm is defined in the middle of the FE domain (half in air domain, half in metal domain). The average material properties are computed by the mixing law within the transition zone. The three yellow arrows represent the successive trajectories of the plasma heat source.

Three successive linear passes of the GMAW are implemented in this simulation. The first pass starts at the point (50, 32, 12) (mm), and the second and third passes starts on its side with -7 mm and -14 mm shifts in the Y direction, respectively. The trajectories of the three passes are represented by the yellow curves in **Fig. IV-27**.

Fig. IV-28 (FE) gives the FE result at a given time (*i.e.* 4 s during the first pass) of the multiple linear passes GMAW process. The whole domain of the FE mesh is represented by the outline with black color, but only the metal domain (workpiece) is visualized. It is seen that a weld bead is formed at the top surface of the workpiece. The hot temperature spot at the surface of the weld bead indicates the position of the heat source (the plasma torch precisely). The corresponding CA result is given by **Fig. IV-28** (CA). The whole domain of the CA mesh is represented by the outline with red color but only the metal domain is shown. In order to compare the different sizes of the FE and CA domains, the FE outline is also superimposed in this figure. It is obvious to notice that the size of CA domain is smaller than that of FE domain. However, the CA domain is large enough to encompass the welds. The values of temperature, T, and the Level Set function, ψ, in CA mesh are projected from the

FE mesh. Because the CA mesh is much coarser than FE mesh, the two fields in CA mesh are not as smooth as those in FE mesh. **Fig. IV-28** (Grains) gives the corresponding grain structure. The liquid and air are not represented in this figure. It is shown that columnar grains occupy the weld bead due to the epitaxial growth and grain competition. The weld pool is located at the head of the weld bead, corresponding to the position of the plasma torch.

Fig. IV-29 presents the final grain structures after each of the 3 passes, with the same view as in **Fig. IV-28** but also in a transverse cross section. It is seen that a weld bead consisting columnar grains is formed after the first pass, shown in **Fig. IV-29** (3D-P1). These columnar grains grow from the base metal, and stopped at the meeting line (symmetrical line) of the weld bead, shown in **Fig. IV-29** (cut-P1). The successive passes are implemented with the shifts of -7 mm from the previous one. The heat source is not large enough to melt half of the previous weld bead, thus the meeting lines are remained, shown in in **Fig. IV-29** (3D-P2) and (3D-P3). Therefore, the columnar grains formed between two neighboring meeting lines are bended to align with the different direction of the temperature gradient at the successive pass. Finally, it is noticed that the dimension of the weld beads are not equal to each other even though the welding parameters are the same for the three passes. In the other words, the size of the weld bead in the Z direction increases, shown in **Fig. IV-29** (cut-P1)-(cut-p3). It can be explained by the movement of the weld pool pushed by the remaining previous weld bead. Note that a few grains with large size occupy the top part of the weld beads, shown in **Fig. IV-29** (cut-P1)-(cut-p3). This phenomenon is also observed in the 2D case (see **Fig. IV-25** (Grains)). The reason is that the computed temperature at the interface is lower than that inside the weld bead at the same coordinates of X component due to the heat extraction. Consequently, a few huge grains occupy the top part of the weld beads.

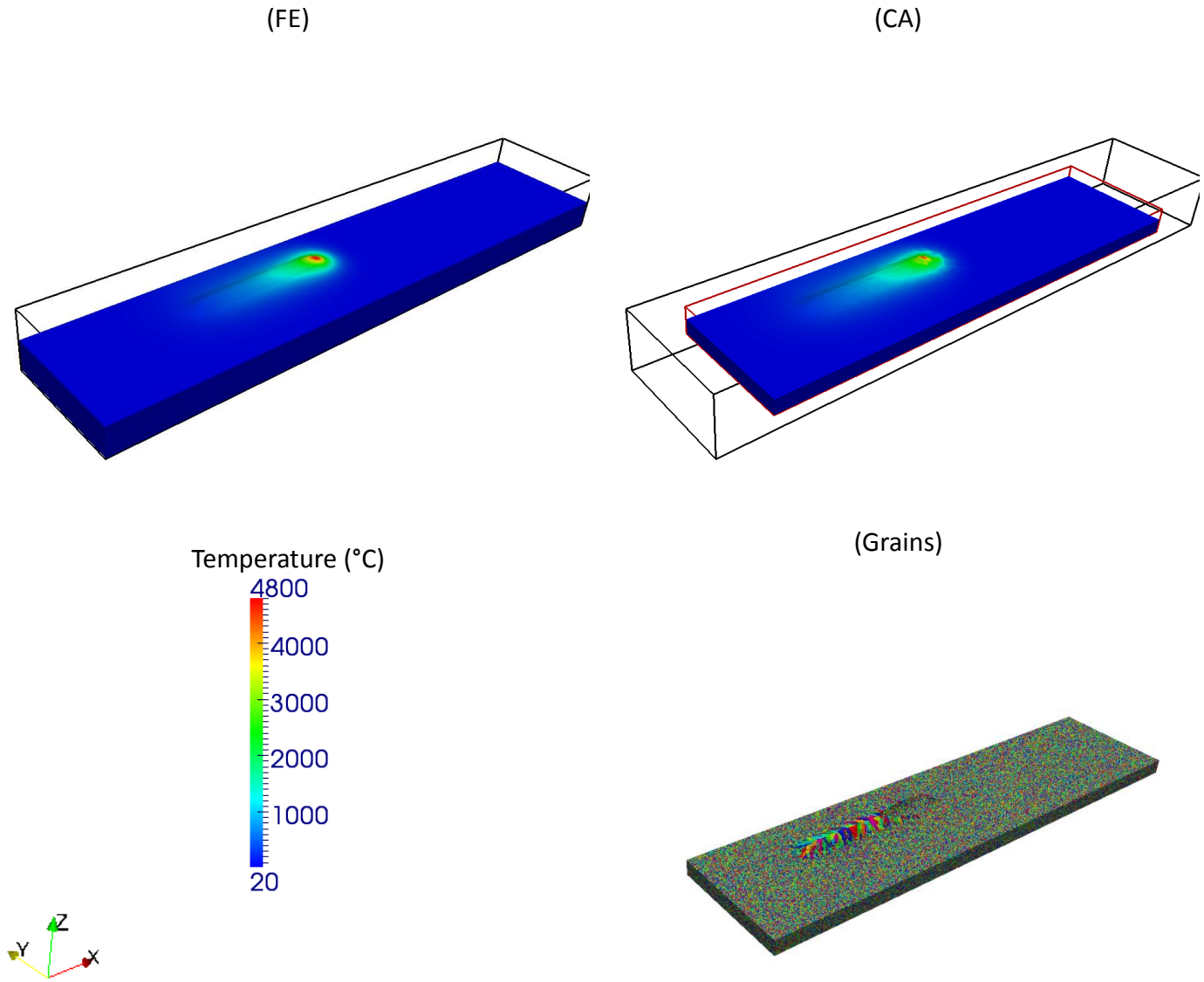

Fig. IV-28 Snapshot at 4 s during the first pass (P1) of the 3D CAFE grain structure simulation for the multiple linear passes GMAW. (FE): the metal domain of the FE mesh, (CA): the metal domain of the CA mesh, and (Grains): the grain structure computed based on the dendrite tip kinetic law (L2). In the (FE) and (CA), the whole domains of the FE mesh and CA mesh are represented by the outlines with black color and red color, respectively. The air domain is not shown. In addition, in (Grains), the liquid structure is not shown, and only the solid as well as the mushy zone – liquid boundary is visualized.

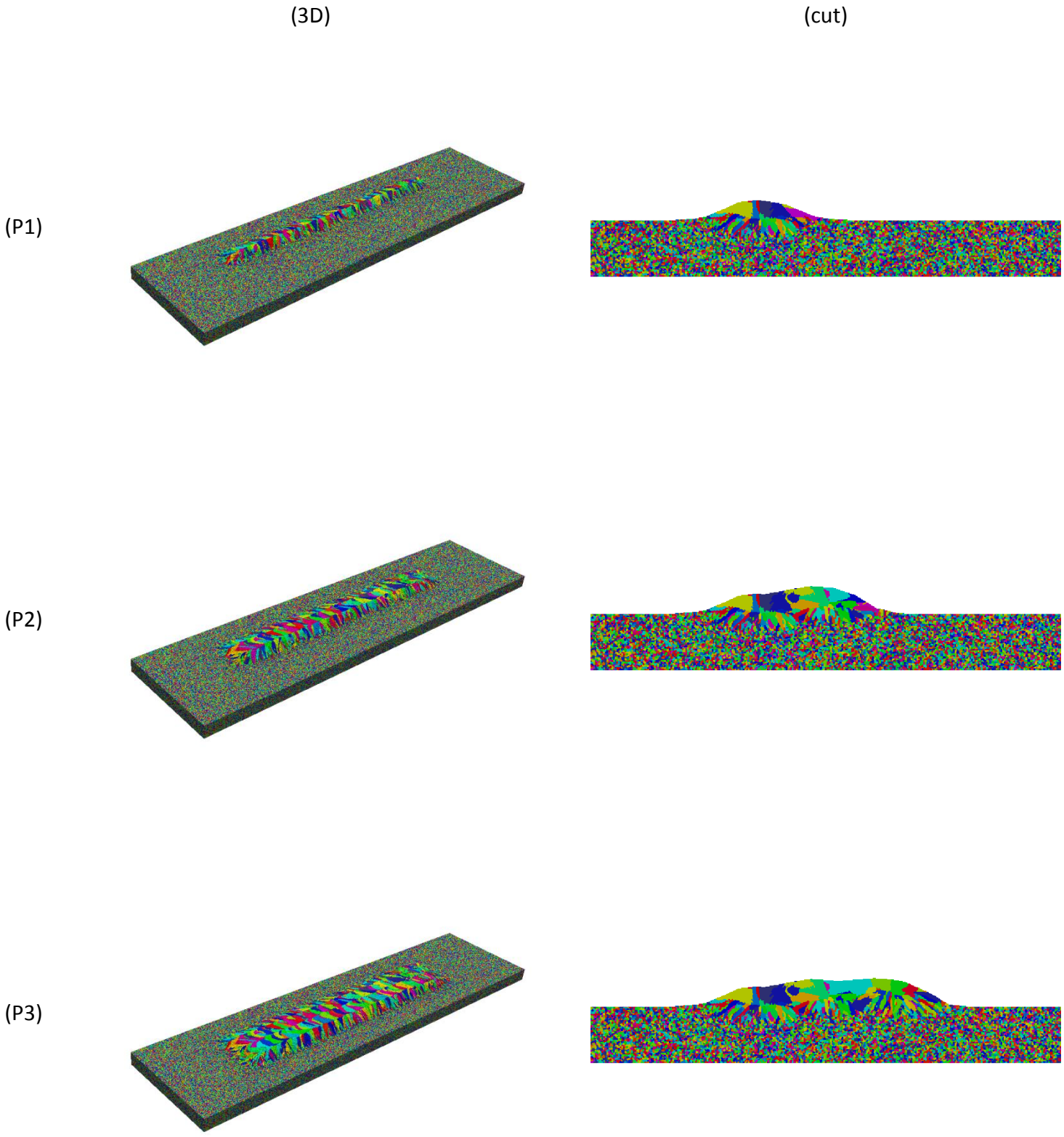

Fig. IV-29 3D CAFE grain structures of the multiple linear passes GMAW simulation with the dendrite tip kinetic law (L2). (3D): the boundary of the metal domain, and (cut): in a transverse cross section at coordinate X = 175 mm at the end of path 1-3, respectively. Note that the air domain is not shown.

4.2.6. Multiple linear passes upon GMAW process with V-shaped chamfer

The objective of the case with multiple linear passes upon GMAW process with V-shaped chamfer is to simulate the grain structure evolution under complicated geometrical and thermal conditions. The numerical FE model contains the domains of the workpieces with a V-shaped chamfer as well as the surrounding air. The melted filling metal is added into the chamfer to form the weld bead. In this case, the filling metal is also supposed to be identical to that of workpieces, *i.e.* URANUS 2202.

The 3D CAFE model is illustrated in **Fig. IV-30** (a) and, the transverse cross sections of X = 0 are illustrated in **Fig. IV-30** (b) and (c) for the FE mesh and CA mesh, respectively. The FE domain (represented by the blue mesh) is divided into two parts to represent the metal (*i.e.* workpiece) and surrounding air, respectively. The workpiece with the V-shaped chamfer is located in the bottom part of the FE domain, while the air is on the top part. The metal/air interface is represented by the Level Set function with the value equal to 0, shown as the yellow curve in **Fig. IV-30** (b). The V-shaped chamfer is thus reflected. The molten droplets are added into the chamfer. A transition zone around the interface between metal and air is defined with the thickness of 2ϵ. In order to reduce the computation cost, a smaller dimension of the CA domain (the red region) is defined as it is usually done for the welding simulations. Similarly, a bottom part of the CA mesh corresponds to metal domain and the top part corresponds to the air domain. In order to reflect the V-shaped chamfer (*i.e.* the metal/air interface) by CA model, a heterogeneous CA mesh is adopted in this case, shown in **Fig. IV-30** (c). The parameters for the definitions of the FE and CA meshes are listed in **Tab. IV-12**.

In this case, the environmental temperature, T_{ext}, is 20 °C, the FE domain is initialized with the temperature, T_0, identical to T_{ext}. A Dirichlet condition is imposed on the upper surface of the air domain with the value of $T_{impose} = T_{ext}$. Moreover, adiabatic conditions are imposed for the other surfaces of the FE domain.

The parameters related to the heat source are also listed in **Tab. IV-12**. Three heat source are proposed corresponding to the plasma, the droplets and the heat lost, respectively (see **Section 3.2.2.6**). The trajectories of the heat source (*e.g.* the plasma) are represented by the yellow arrows in **Fig. IV-31**.

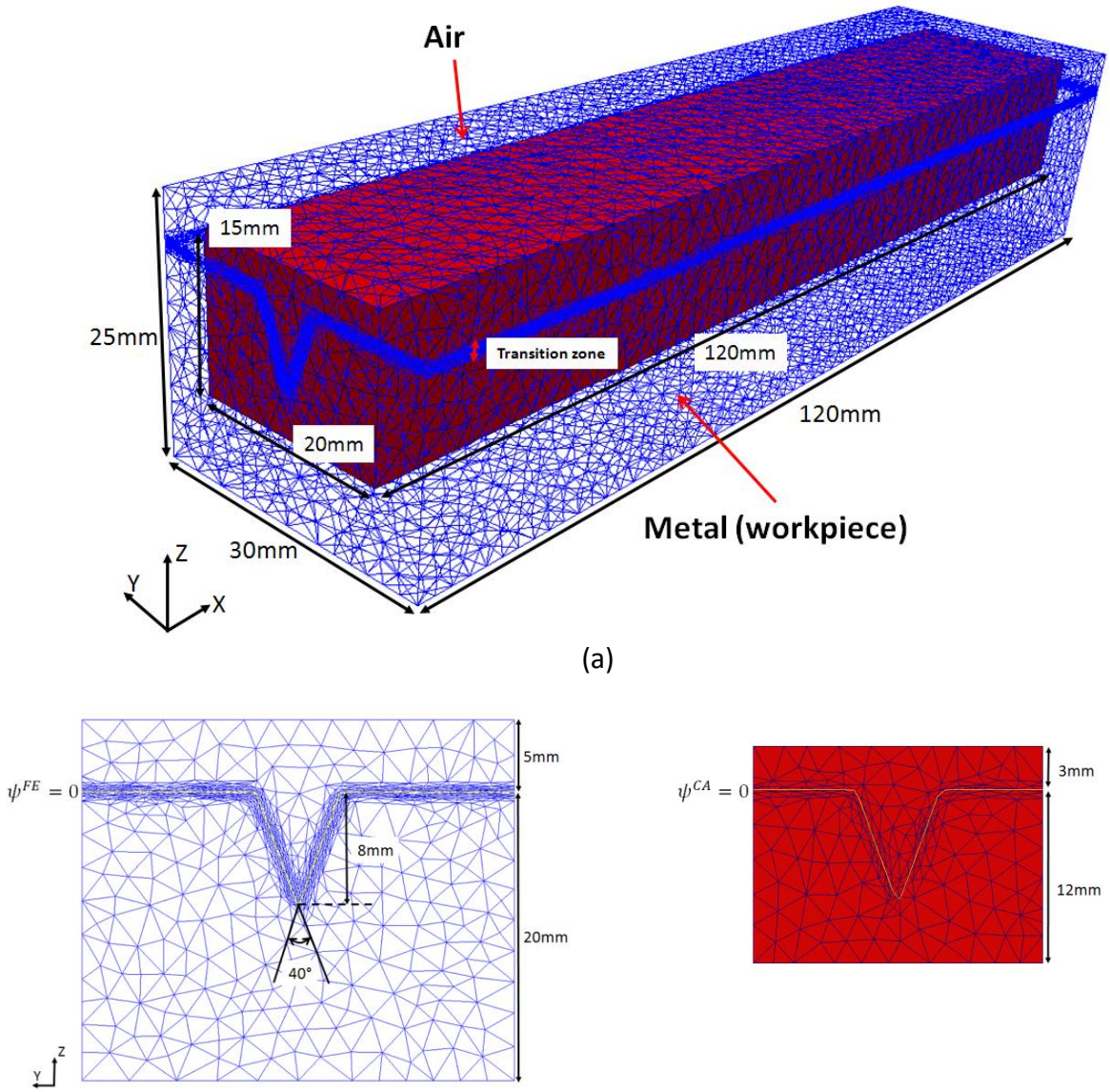

Fig. IV-30 Description of the CAFE model of GMAW process with V-shaped chamfer (a): the FE and the CA mesh in 3D, (b): the FE mesh in transverse cross section of X = 0, and (c): the CA mesh in transverse cross section of X = 0. The FE mesh (blue) and CA mesh (red) are divided into two parts, *i.e.* metal (the workpiece) and air, respectively. The air is located above the metal. A transition zone with the thickness of 1 mm is defined in the FE mesh. The yellow curve in (b) represents the metal/air interface with $\psi^{FE} = 0$. The yellow curve in (c) represents the metal/air interface with $\psi^{CA} = 0$. Note that ψ^{CA} is projected from ψ^{FE}.

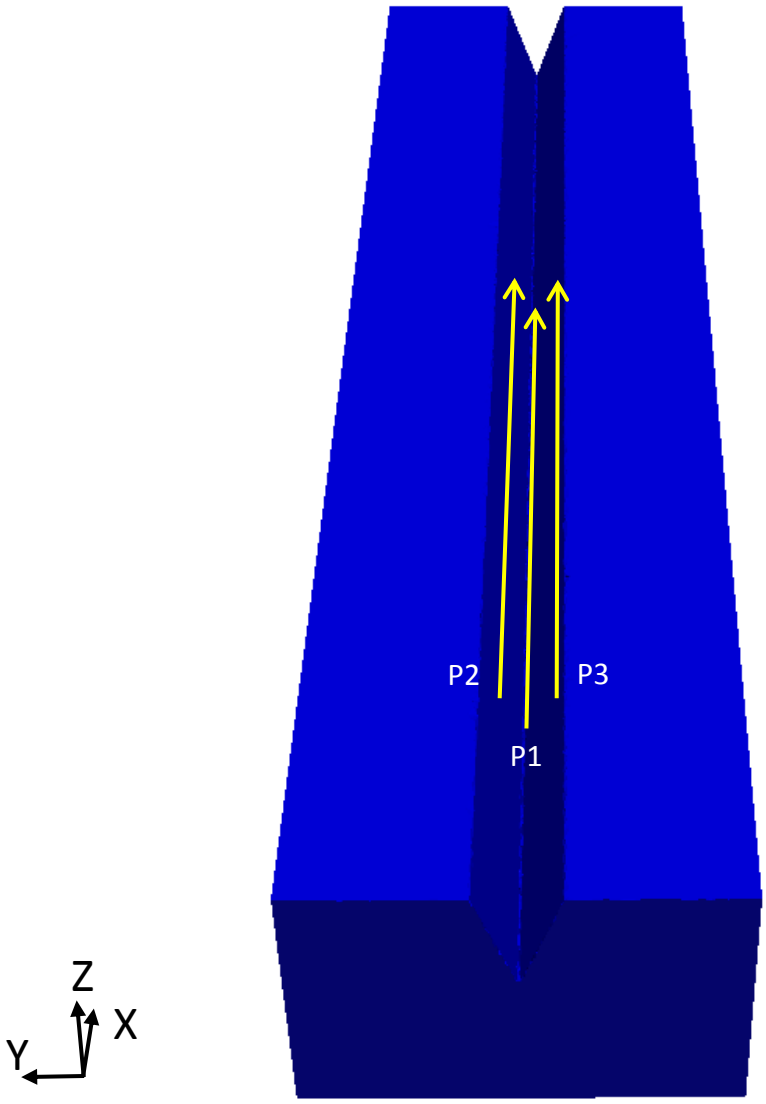

Fig. IV-31 Representation of the trajectories of heat source P1, P2, and P3

Tab. IV-12 Numerical parameters for the single linear pass upon GMAW process with V-shaped chamfer (The dendrite tip kinetic law (L2) is presented in **Tab. IV-3**)

Parameter	Symbol	Value	Unit
FE domain	Ω_{FE}	120×30×25	mm^3
Metal domain in FE mesh	Ω_{FE}^{Metal}	see **Fig. IV-30**	mm^3
Air domain in FE mesh	Ω_{FE}^{Air}	see **Fig. IV-30**	mm^3
Half thickness of transition zone	ϵ	0.8	mm
CA domain	Ω_{CA}	120×20×15	mm^3
Metal domain in CA mesh	Ω_{CA}^{Metal}	see **Fig. IV-30**	mm^3
Air domain in CA mesh	Ω_{CA}^{Air}	see **Fig. IV-30**	mm^3
CA element size (fixed)	l_{CA}	0.25~3	mm
Cell size	l_{cell}	80	μm
Time step	Δt	0.005	s
Number of processors	N_{pro}	40 (Cluster Intel)	-
Initial temperature	T_0	20	°C
Environmental temperature	T_{ext}	20	°C
Imposed temperature (Dirichlet)	T_{impose}	20	°C
Heat transfer coefficient	h_T	5	$W\ m^{-2}\ K^{-1}$
Emissivity	ε_r	0.25	-
Initial grain density	N_0	10^{11}	m^{-3}
Dendrite tip kinetic law	L	L2	-
Velocity of welding	v^H	10	$mm\ s^{-1}$
Input power of plasma torch	$\dot{Q}_{input}$	8000	W
The power for plasma	$\dot{Q}_{plasma}$	4700	W
The power for droplets	$\dot{Q}_{droplet}$	3300	W
Velocity of filling metal (electrode)	v_w	80	$mm\ s^{-1}$
Radius of filling metal (electrode)	R_w	0.6	mm
Temperature of droplets	T_d	2227	°C
Starting point of heat source (P1)	X_S, Y_S, Z_S	20, 15, 18	mm
Ending point of heat source (P1)	X_E, Y_E, Z_E	90, 15, 18	mm
Starting point of heat source (P2)	X_S, Y_S, Z_S	22, 17, 24	mm
Ending point of heat source (P2)	X_E, Y_E, Z_E	88, 17, 24	mm
Starting point of heat source (P3)	X_S, Y_S, Z_S	22, 13, 24	mm
Ending point of heat source (P3)	X_E, Y_E, Z_E	88, 13, 24	mm

Fig. IV-32 (FE) gives the FE result at 6 s of the first pass. The whole domain of the FE mesh is represented by the outline with black color, but only half of the metal domain (workpiece) is represented in order to visualize the formation of weld bead in the V-shaped chamfer. The metal/air interface is changed. However, it is clear that the adding metal does not fill the chamfer, so the newly formed metal/air interface is curved. The hot temperature spot at the surface of the weld bead indicates the position of the heat source (the plasma torch

precisely). The corresponding CA result is given by **Fig. IV-32** (CA). The whole domain of the CA mesh is represented by the outline with red color but only half of the metal domain is shown. In order to compare the different sizes of the FE and CA domains, the FE outline is also superimposed in this figure. It is noticed that the size of CA domain is smaller than that of FE domain. However, the CA domain is large enough to encompass the chamfer. The values of temperature, T, and the Level Set function, ψ, in CA mesh are projected from the FE mesh. The CA mesh is also heterogeneous in order to reflect the chamfer. Consequently, the V-shaped chamfer in **Fig. IV-32** (CA) is well retrieved by the Level Set function with the value of 0, and its surface is flat. Indeed, it could be more improved by refining the CA mesh. **Fig. IV-32** (Grains) gives the corresponding grain structure but also in half volume of the CA domain. The liquid and air are unvisualized. It is shown that the solidified weld bead is composed by the columnar grains due to the epitaxial growth and grain competition. The weld pool is located at the head of the weld bead, corresponding to the position of the plasma torch.

Fig. IV-33 gives the initial and final grain structures after each pass, with the same view as in **Fig. IV-32** but also in a transverse cross section of YZ plane. In **Fig. IV-33** (3D-Initial) and (3D-P1), half volume of the grain structure of the CA domain is presented in order to show the structure in the chamfer. The initial grain structure can reflect the flat surface of the V-shaped chamfer which is represented by the FE model due to the heterogeneous CA mesh. It is seen that a weld bead consisting columnar grains is formed after P1, shown in **Fig. IV-33** (3D-P1). Because the adding metal does not fill the V-shaped chamfer, the final weld bead is located in the bottom of the chamfer, as previously shown in **Fig. IV-32**. **Fig. IV-33** (cut-P1) shows that the columnar grains grow from the base metal, and occupy the whole weld bead. Note that the columnar grain structure domain implies that the heat source melts the metal in a domain larger than the V-shaped chamfer. The whole grain structure of the metal domain is shown for P2 and P3 in **Fig. IV-33** (3D-P2) and **Fig. IV-33** (3D-P3), respectively. Because the heat sources provided by the electrode in P2 and P3 are shifted +2 mm and -2 mm with respect to P1 respectively, the new weld beads are also shifted. It is seen that columnar grains grow from the base metal and the previous pass, even with axial grains. Finally, the chamfer is filled by columnar grain structures after P2 and P3, which is shown in **Fig. IV-33** (cut-P2) and (cut-P3).

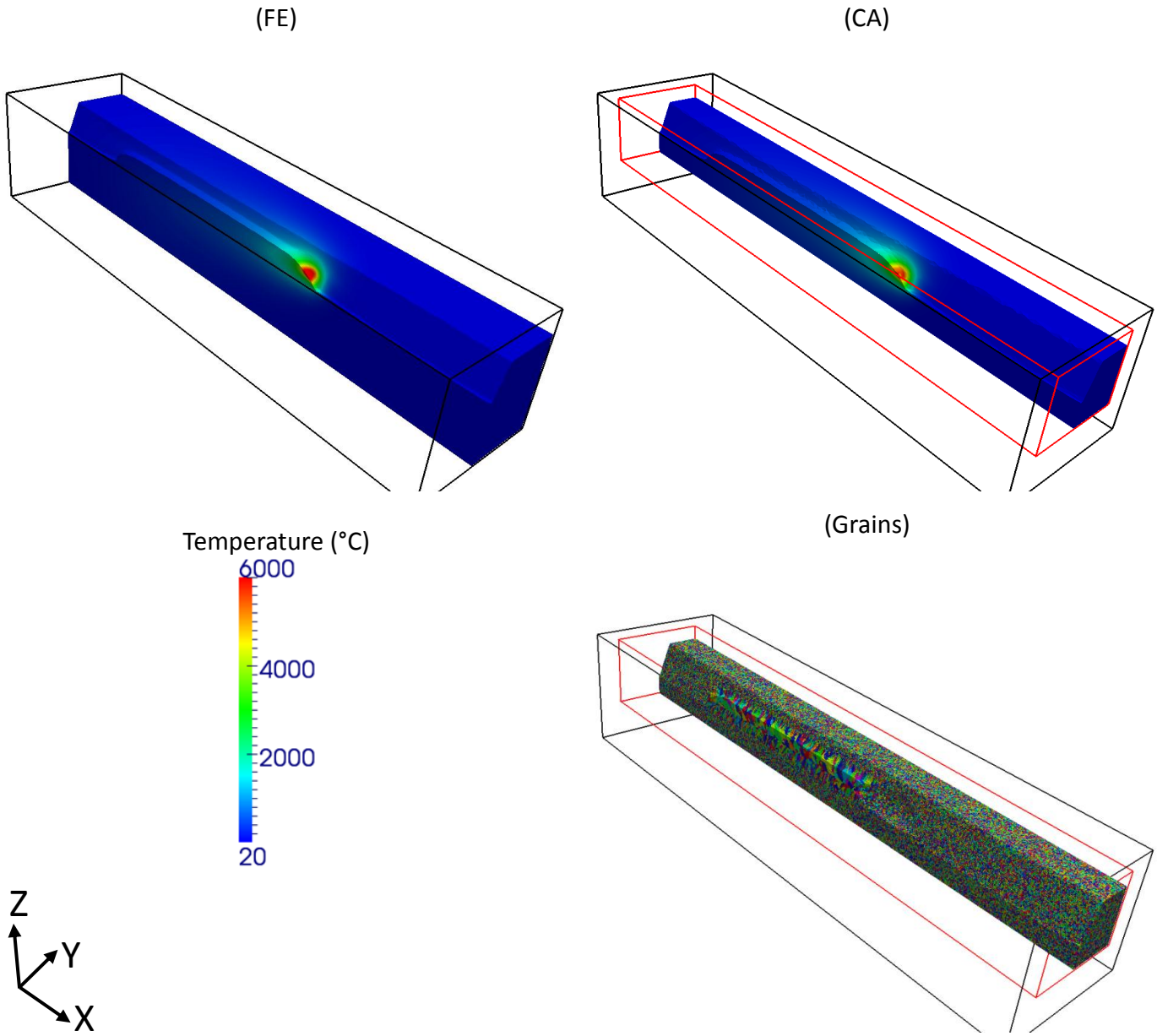

Fig. IV-32 Snapshot of the 3D CAFE grain structure simulation for the multiple linear passes GMAW with V-shaped fillet joint at 6 s of P1. (FE): half of the metal domain of the FE mesh, (CA): half of the metal domain of the CA mesh, and (Grains): the half volume of the grain structure computed based on the dendrite tip kinetic law (L2). The whole domains of the FE mesh and CA mesh are represented by the outlines with black color and red color, respectively. The air domain is not shown. In addition, in (Grains), the liquid structure is not shown, and only the solid as well as the mushy zone – liquid boundary is visualized.

(3D) (cut)

(Initial)

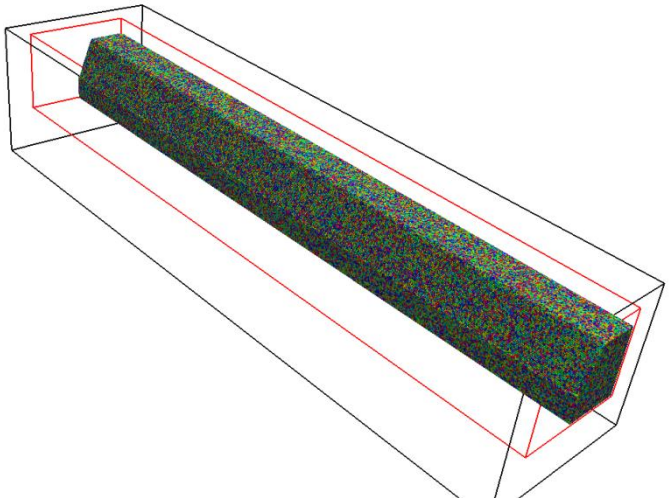

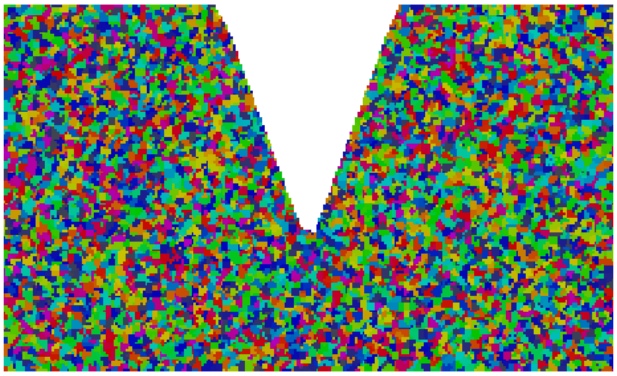

(P1)

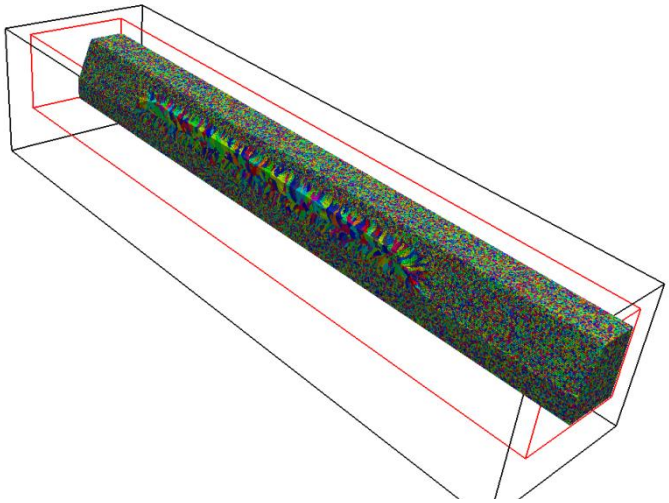

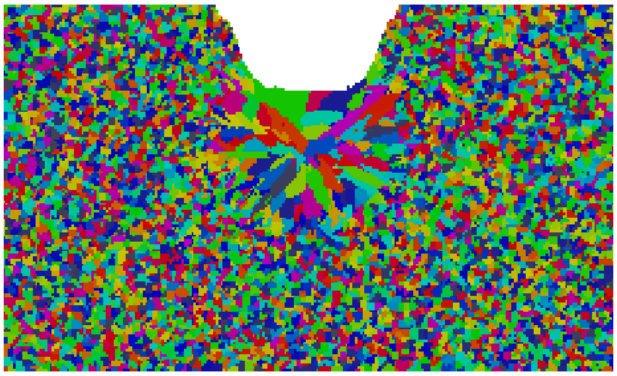

(P2)

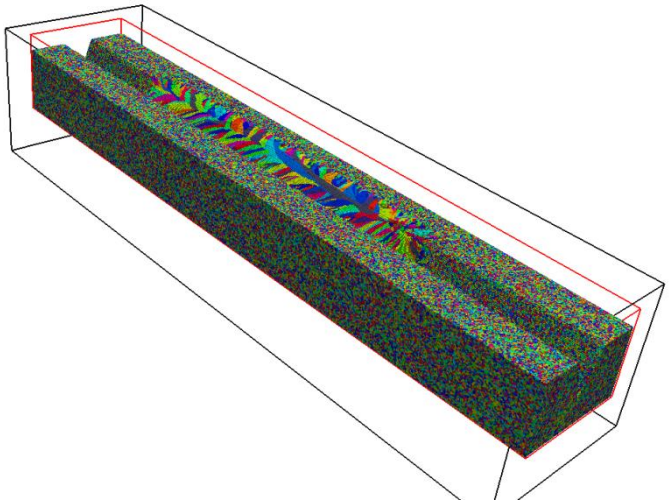

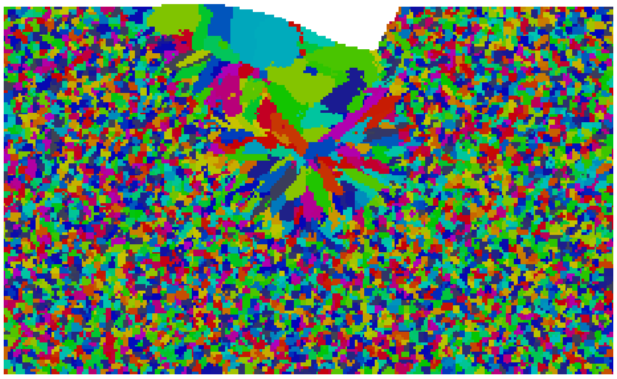

(P3)

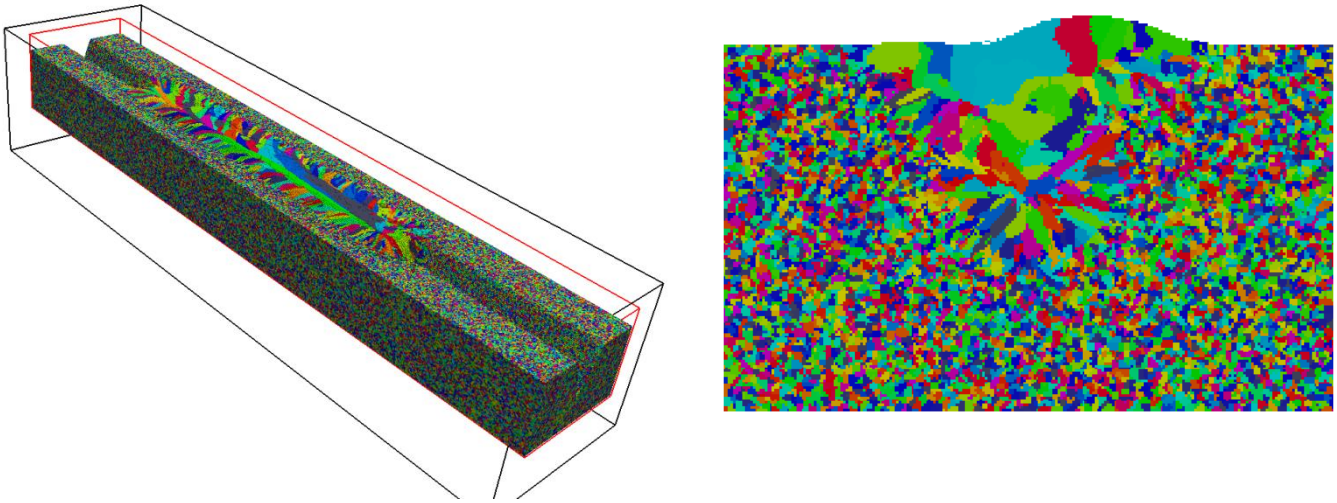

Fig. IV-33 3D CAFE grain structures of the multiple linear passes GMAW simulation with V-shaped chamfer. (3D): the 3D metal domain, and (cut): in a transverse cross section at coordinate X = 56 mm. (Initial), (P1), (P2), and (P3) represent the initial and final grain structure after P1, P2, and P3, respectively. Note that the air cells are not shown. (3D-Initial) and (3D-P1) only show half volume of the metal domain in order to visualize the structure in the V-shaped chamfer.

4.3. Conclusion

The present 3D CAFE model is applied to simulate the grain structure evolution for Gas Tungsten Arc Welding and for Gas Metal Arc Welding processes.

The results of the single linear pass GTAW show that the numerical parameters (*e.g.* the cell size) and the process parameters (*e.g.* the input power and velocity of the heat source) significantly affect the final grain structure. In addition, the dendrite tip kinetic law which is related to the material property is also an essential factor for the grain structure. For the multiple linear passes and multiple passes with overlapping depths GTAW, the results show that the final grain structures are dependent on the multiple passes definitions. The results of the GMAW process show that the present 3D CAFE model is able to simulate the welding process with metal addition. The final grain structures are simulated directly.

4.4. French summary

Le **chapitre IV** présente l'application du modèle 3D CAFE, précédemment détaillé, à la formation des structures de grains au cours du soudage. Il permet de prédire avec succès la structure formée lors d'un soudage TIG sans métal d'apport dans une configuration mono-passe ou multi-passe. L'influence des paramètres procédés sur l'évolution des orientations

des grains est similaire à celle observées expérimentalement. Durant l'ensemble de la solidification dans le bain de fusion, la croissance épitaxiale et la compétition de croissance entre grains sont correctement simulées. Le développement de larges structures de grains en soudage multipasses est retrouvé. L'influence de divers paramètres tels que la taille de cellule, l'énergie d'entrée ou encore la vitesse de la source de chaleur, est étudiée. De plus, le modèle permet également de s'intéresser à taille finale de grain pour un soudage MIG avec apport de métal aussi bien pour une configuration mono-passe ou multi-passe. Dans cette situation, l'approche Level Set permet de modéliser le développement du cordon, et l'apport de métal. L'approche présentée permet enfin d'étudier le développement des structures dans le cas de géométrie de pièces plus complexes liées à l'existence d'un chanfrein. Dans cette dernière situation, de même que dans les précédentes, un processus de croissance épitaxiale est bien simulé, conduisant à une dimension des densités de grains, et à la formation de grains larges. Une discussion est développée autour des résultats présentés.

Conclusion and perspectives

The 3D coupled Cellular Automaton – Finite Element (CAFE) model, initially proposed by Rappaz and Gandin [Rap93, Gan94] and later developed by Guillemot and Carozzani [Gui04, Car12] is now further extended to simulate the grain structure formation during solidification in welding process. The initial structure of the weld workpiece before welding being a fully solid state is considered. One of the advantages is to be able to handle millions of grains with a direct graphic representation. Such description is believed to be crucial in future for prediction of grain structure related defects.

A two meshes strategy with dynamic activation/deactivation of CA elements and allocation/deallocation of CA cells is developed for modeling the grain structure formed during welding processing with this 3D CAFE model. The management of these allocation/deallocation steps has been developed in order to focus the computation onto the 'domain of interest'. This domain of interest corresponds to the active elements in which cells develop. It allows to restrict the computation on a narrow domain in which the grain capture is modeled. Only the cells associated to the growing front are allocated and considered in the CA resolutions. They are deallocated and stored onto the hard disk when the structure is fully developed. The cells data is stored by a set of files corresponding to the related CA elements. This strategy enables to save computation time and has a large influence on memory cost. Four cell states are used, corresponding to liquid, growing, fully mushy, and air structures in order to model grain evolution during the welding process. Transition rules for these states are defined for the welding process (*i.e.* melting/remelting, addition of metals, *etc.*).

The implementations of the CAFE model are shown to successfully predict the grain structure upon single linear pass and multiple linear passes GTAW with no metal addition. The epitaxial grain growth and growth competition during the solidification of the weld pool is well reflected in these applications. The influences of many parameters (*e.g.* cell size, heat source velocity and input power) are tested.

The implementations of the CAFE model are also shown to predict the grain structure upon single linear pass and multiple linear passes GMAW with metal addition. The formation of the weld bead on the workpiece results in a change of the interface between the metal domain and the air domain. By changing the cells from air state to liquid state, the added metal is reflected in the CA model. Applications for GMAW with metal addition show that the epitaxial grain growth and growth competition take place in the base metal as well as in the newly formed weld bead.

We emphasize that the cell size is an essential numerical parameter to affect the results of the grain structure during welding process simulated by CAFE model. This is demonstrated in **Chapter IV**. Because the temperature gradient on the workpiece is significantly great during the welding process, the cell size with small value is required (~ 80 µm) in order to obtain the proper values of temperature for the growing cells by interpolation. Therefore, on the numerical simulation aspect, the influence of the cell size is highly related to the temperature gradient, particularly in welding cases. The higher the temperature gradient is, the smaller the cell size is needed. This management of the cell size has to be done in order to develop the computation with the correct estimation of maximum dendrite tip growth velocity in the large temperature gradient domains. This is a main difference between casting and welding simulation with CAFE model.

The dendrite tip kinetic law (related to the material property) is also an important factor to influence the final grain structure. If the dendrite tip velocity is more sensitive to the undercooling, the smaller cell size is required in order to model the cell capture steps in the CAFE approach.

Finally, the process parameters (*e.g.* heat source velocity and input power) largely modify the grain structure as a result of its influence on the temperature field.For the first time direct simulation of 3D grain structures in large domains are presented for the welding processes. The simulations can be conducted to predict the grain structures formed upon single pass or multiple passes during GTAW and GMAW. However, some perspectives can be addressed as follows:

All the simulations of the GMAW process as well as the multiple passes with overlapping depths upon GTAW process adopt the dendrite tip kinetic law L2 (approached law), but not

L1 (physical law). The direct reason is that the micro time step, δt, computed based on L1 is significantly small (in the order of 10^{-6} s), and it is impossible to finish the whole simulation before the date of PhD defense. Considering these simulations, the temperature gradient is very great. Therefore, the interpolated temperatures of the growing cells depart from the solid/liquid interface temperature due to the finite cell size. As the dendrite tip velocity computed by L1 is much sensitive to the undercooling, a small increase of the undercooling due to the interpolation induces a huge increase of the dendrite tip velocity computed by L1. Finally, the micro time step is thus too small to complete the simulation in a finite period. This numerical difficulty comes from the simulated high temperature gradient, which may limit the use of the expected kinetic law (*e.g.* L1). A numerical solution is to decrease the cell size to get the proper interpolated temperature for the growing cells at the weld pool boundary. Another effort should be done latter by introducing the modeling of fluid flow may lead to a decrease of the temperature gradient and largely improve the computation of cells capture.

In the present CAFE model in Level Set approach, there is temperature distribution problem in the zone where the value of the Heaviside function changes with time and space (see **Section 3.2.4**). This problem is due to the simplifications in the temperature solver (detailed in **Section 3.2.3**), *i.e.* the assumption of **Eq. (III-44)** and the explicit known of the right hand terms in **Eq. (III-45)**. Therefore, it is necessary to improve the FE results by developing the temperature solver without these simplifications.

In the present CAFE model, the Level Set function evolution solved by **Eq. (III-25)** and then reinitialized by **Eq. (III-26)** is not sufficient stable. The simulations of GMAW process is still limited in small adding metal rate (the limited value depends on the velocity of the plasma). The use of larger value of the adding metal rate may be prevented in the present case. So the reinitialization step (*i.e.* computation of the distance field in LS approach) should be improved in order to apply this CAFE model in welding simulation with large number of passes (*e.g.* narrow chamfer on large thickness pieces).

The present CAFE model can be used to predict the final grain structure after various welding processes. However, the validation of this model needs to be developed in the future. The simulated results should be compared to corresponding experimental results on

metallic alloys. A first validation could be done on GTAW process by comparing the evolution of predicted grain structure orientation with metallographic observation. Moreover this present CAFE model is only limited on the prediction of the structure evolution in the fusion zone due to the remelting and resolidification. However this grain structure evolves largely in HAZ during the cooling process due to grain boundaries mobility as experimentally observed [Elm01, Elm03]. A large set of models are proposed in the literature to model this evolution in welding process (*e.g.* Potts model [Yan00]). The grain structure evolution in the heat affected zone could also be the subject of investigations with the CAFE model. Another relevant extension in the welding modeling is the coupling with thermomechanical deformations. Thus, this CAFE model could be coupled with the theory of defect formation, such as the hot cracking prediction during welding process [Bor14].

Appendix A

The numerical and process parameters of the 2D GTAW and GMAW cases in **Section 3.5.2** are listed in **Tab. A-GTAW** and **Tab. A-GMAW**, respectively. The two cases are implemented in order to illustrate the strategy of dynamic allocation/deallocation of cells.

Tab. A-GTAW Parameters for the 2D GTAW process (The dendrite tip kinetic law (L2) is presented in **Tab. IV-3**)

Parameter	Symbol	Value	Unit
		GTAW	
FE domain	Ω_{FE}	350×190	mm^2
Initial FE element size	l_{FE}	20	mm
CA domain	Ω_{CA}	350×150	mm^2
CA element size (fixed)	l_{CA}	20	mm
Cell size	l_{cell}	3000	μm
Time step	Δt	0.5	s
Number of processors	N_{pro}	3	-
Initial temperature	T_0	20	°C
Environmental temperature	T_{ext}	20	°C
Heat transfer coefficient	h_T	1000	$W\ m^{-2}\ K^{-1}$
Emissivity	ε_r	0.91	-
Initial grain density	N_0	5×10^4	m^{-2}
Dendrite tip kinetic law	L	L2	-
Velocity of heat source	v^H	1.5	$mm\ s^{-1}$
Input power of heat source	$\dot{Q}_{input}$	1200	W
Semi-axes in y direction	a	50	mm
Semi-axes in x direction	c	8	mm
Starting point of heat source	X_S, Y_S	40, 95	mm
Ending point of heat source	X_E, Y_E	310,95	mm

Tab. A-GMAW Parameters for the 2D GMAW process (The dendrite tip kinetic law (L2) is presented in **Tab. IV-3**)

Parameter	Symbol	Value	Unit
FE domain	Ω_{FE}	175×90	mm^2
Metal domain in FE mesh	Ω_{FE}^{Metal}	175×45	mm^2
Air domain in FE mesh	Ω_{FE}^{Air}	175×45	mm^2
Half thickness of transition zone	ϵ	0.8	mm
CA domain	Ω_{CA}	175×70	mm^2
Metal domain in CA mesh	Ω_{CA}^{Metal}	175×35	mm^2
Air domain in CA mesh	Ω_{CA}^{Air}	175×35	mm^2
CA element size (fixed)	l_{CA}	8	mm
Cell size	l_{cell}	3000	μm
Time step	Δt	0.005	s
Number of processors	N_{pro}	3	-
Initial temperature	T_0	20	°C
Environmental temperature	T_{ext}	20	°C
Imposed temperature (Dirichlet)	T_{impose}	20	°C
Heat transfer coefficient	h_T	5	$W\ m^{-2}\ K^{-1}$
Emissivity	ε_r	0.25	-
Initial grain density	N_0	5×10^4	m^{-2}
Dendrite tip kinetic law	L	L2	-
Velocity of heat source	v^H	13.3	$mm\ s^{-1}$
Input power of heat source	$\dot{Q}_{input}$	5700	W
The power for plasma	$\dot{Q}_{plasma}$	4050	W
The power for droplets	$\dot{Q}_{droplet}$	1650	W
Velocity of filling metal (electrode)	v_w	100	$mm\ s^{-1}$
Radius of filling metal (electrode)	R_w	0.6	mm
Temperature of droplets	T_d	2227	°C
Starting point of heat source	X_S, Y_S	30, 45	mm
Ending point of heat source	X_E, Y_E	140, 45	mm

Appendix B

The values of the thermal conductivity of URANUS 2202 steel [Arc10] with respect to the temperature are shown in **Fig. B-1**. The black points represent the values from [Arc10]. The curve represents the tabulated value. The tabulated values at high temperature are extrapolated linearly from the values in literature. The thermal conductivity of liquid is supposed to be constant.

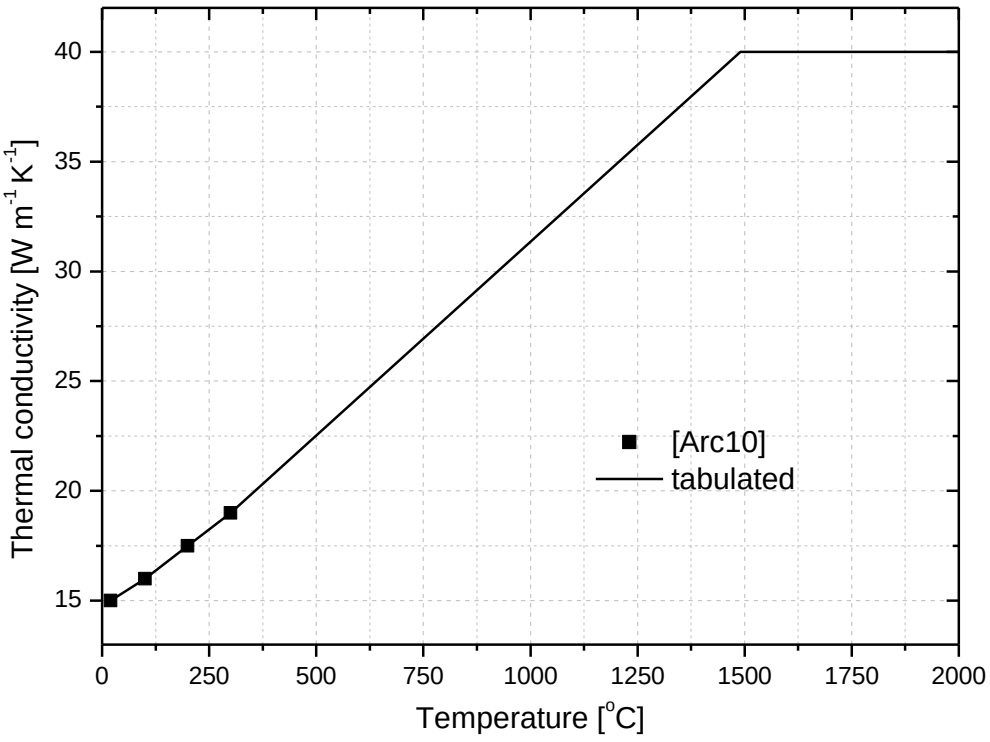

Fig. B-1 Thermal conductivity with respect to the temperature for URANUS 2202 steel

References

[Al-R02] N. Al-Rawahi and G. Tryggvason. Numerical simulation of dendritic solidification with convection: two-dimensional geometry. J. Comput. Phys., 180, 471-96, 2002.

[Al-R04] N. Al-Rawahi and G. Tryggvason. Numerical simulation of dendritic solidification with convection: three-dimensional flow. J. Comput. Phys., 194, 677-96, 2004.

[All11] L. E. Allgood. Gas Tungsten Arc Welding. Welding Fundamentas and Processes, ASM Handbook, 6A, 344-54, 2011.

[Ara73] Y. Arata, F. Matsuda, S. Mukae and M. Katoh. Effect of weld solidification mode on tensile properties of aluminum weld metal, Transaction of JWRI, 2, 184-90, 1973.

[Arc10] ArcelorMittal. URANUS 2202 Rev. 7: http://www.industeel.info/datasheets/pdf/ur2202.pdf, 2010.

[Bas06] O. Basset. Simulation numérique d'écoulements multi fluids sur grille de calcul. PhD thesis, Mines ParisTech, 2006.

[Bec96] C. Beckermann and C. Y. Wang. Equiaxed dendritic solidification with convection: part III. comparisons with NH_4Cl-H_2O experiments. Metall. Meter. Trans. A, 27A, 2784-95, 1996.

[Bec99] C. Beckermann, H.-J. Diepers, I. Steinbach, A. Karma and X. Tong. Modeling melt convection in phase-field simulations of solidification. J. Comput. Phys., 154, 468-96, 1999.

[Bel13] M. Bellet and M. Hamide. Direct modeling of material deposit and identification of energy transfer in Gas Metal Arc Welding. Int. J. Num. Meth. Heat Fluid Flow, 23, 1340-55, 2013.

[Bob88] M. Bobadilla, J. Lacaze and G. Lesoult. Influence des conditions de solidification sur le déroulement de la solidification des aciers inoxydables austénitiques. J. Cryst. Growth, 89, 531-44, 1988.

[Boe00] W. J. Boettinger, S. R. Coriell, A. L. Greer, A. Karma, W. Kurz, M. Rappaz and R. Trivedi. Solidification microstructures: recent developments, future directions. Acta Mater., 48, 43-70, 2000.

[Boe02] W. J. Boettinger, J. A. Warren, C. Beckermann and A. Karma. Phase-Field simulation of solidification. Annu. Rev. Mater. Res., 32, 163-94, 2002.

[Bor14] C. Bordreuil, and A. Niel. Modeling of hot cracking in welding with a cellular automaton combined with an intergranular fluid flow model. Comp. Mater. Sci., 82, 442-50, 2014.

[Bra92] J. U. Brackbill, D. B. Kothe and C. Zemach. A continuum method for modeling surface tension. J. Comput. Phys., 100, 335-54, 1992.

[Bri12] C. Brito, C. A. Siqueira, J. E. Spinelli and A. Garcia. Cellular growth during the transient directional solidification of Zn-rich Zn-Cu monophasic and peritectic alloys. J. Phys. Chem. Solids, 73, 1173-81, 2012.

[Bro04] D. J. Browne and J. D. Hunt. A fixed grid front-tracking model of the growth of a columnar front and an equiaxed grain during solidification of an alloy. Numer. Heat Tr. B, 45, 395-419, 2004.

[Cag86] G. Caginalp. An analysis of a phase field model of a free boundary. Arch. Ration. Mech. An., 92, 205-45, 1986.

[Cag89] G. Caginalp and E. A. Socolovsky. Efficient computation of a sharp interfaces by spreading via phase field methods. Appl. Math. Lett., 2, 117-20, 1989.

[Car12] T. Carozzani, H. Digonnet and Ch.-A. Gandin. 3D CAFE modeling of grain structures: application to primary dendritic and secondary eutectic solidification. Modelling. Simul. Mater. Sci. Eng., 20, 015010, 2012.

[Car12b] T. Carozzani. Développement d'un modèle 3D Automate Cellulaire-Éléments Finis (CAFE) parallèle pour la prédiction de structures de grains lors de la solidification d'alliage métalliques. Doctorat ParisTech THÈSE, 2012.

[Car14] T. Carozzani, Ch.-A. Gandin and H. Digonnet. Optimized parallel computing for cellular automaton-finite element modeling of solidification grain structures. Modelling. Simul. Mater. Sci. Eng., 22, 015012, 2014.

[Cha10] C. Chattopadhyay, S. Sangal and K. Mondal. A relook at the preferred growth direction of the solid-liquid interface during solidification of pure metals. Acta Mater., 58, 5342-53, 2010.

[Che02] L.-Q. Chen. Phase-field models for microstructure evolution. Annu. Rev. Mater. Res., 32, 113-40, 2002.

[Cic05] E. Cicala, G. Duffet, H. Andrzejewski, D. Grevey, and S. Ignat. Hot cracking in Al-Mg-Si alloy laser welding – operating parameters and their effects. Mat. Sci. Eng. A, 395, 1-9, 2005.

[Cwu12] A. Cwudzinski, J. Jowsa. Mathematical modeling of nickel behavior in the liquid steel flowed through the one strand tundish. Arch. Mater. Sci. Eng., 57, 63-8, 2012.

[Dan09] J. A. Dantzig and M. Rappaz. Solidification. EPFL Press, 2009.

[Dav75] G. J. Davies and J. G. Garland. Solidification structures and properties of fusion welds. Int. Mater. Rev., 20, 83-106, 1975.

[Dav92] S. A. David and T. DebRoy. Current issues and problems in welding science. Science, 257, 497-502, 1992.

[Dav03] S. A. David, S. S. Babu and J. M. Vitek. Welding: Solidification and microstructure. JOM-J. Min. Met. Mat. S., 55, 14-20, 2003.

[Deb95] T. DebRoy and S. A. David. Physical processes in fusion welding. Rev. Mod. Phys., 67, 85-112, 1995.

[Del10] P. Delaleau, C. Beckermann, R. H. Mathiesen, and L. Arnberg. Mesoscopic simulation of dendritic growth observed in X-ray video microscopy during directional solidification of Al-Cu alloys. ISIJ Int., 50, 1886-94, 2010.

[Des13] O. Desmaison. Modélisation numérique d'un procédé de soudage hybride arc / laser en approche Level Set : application au soudage multi-passes de tôles d'acier de forte épaisseur. Doctorat ParisTech THÈSE, 2013.

[Dil97] U. Dilthey, V. Pavlyk, and T. Reichel. Mathematical modeling of weld phenomena. London: The Institute of Materials, vol 3, 85-105, 1997.

[Dil98] U. Dilthey and V. Pavlyk. Modeling of casting, welding and advanced solidification processes. Warrendale: TMS, vol VIII, 589-96, 1998.

[Eik06] J. Eiken, B. Böttger and I. Steinbach. Multiphase-field approach for multicomponent alloys with extrapolation scheme for numerical application. Phys. Rev. E, 73, 066122, 2006.

[Elm01] J. W. Elmer, J. Wong and T. Ressler. Spatially resolved X-Ray Diffraction Mapping of phase transformation in the Heat-Affected zone of Carbon-Manganese steel arc welds. Metall. Mater. Trans. A, 32, 1175-87, 2001.

[Elm03] J. W. Elmer, T. A. Palmer, W. Zhang, B. Wood and T. DebRoy. Kinetic modeling of phase transformations occurring in the HAZ of C-Mn steel welds based on direct observations. Acta Mater., 51, 3333-49, 2003.

[Esa85] H. Esaka and W. Kurz. Columnar dendrite growth: experiments on tip growth. J. Cryst. Growth, 72, 578-84, 1985.

[Esk04] D. G. Eskin, Suyitno, and L. Katgerman. Mechanical properties in the semi-solid state and hot tearing of aluminium alloys. Progr. Mater. Sci., 49, 629-711, 2004.

[Fle74] M. C. Flemings. Solidification processing. Metall. Trans., 5, 2121-34, 1974.

[Gan94] Ch.-A. Gandin and M. Rappaz. A coupled Finite Element-Cellular Automaton model for the prediction of dendritic grain structure in solidification processes. Acta Metall. Mater., 42, 2233-46, 1994.

[Gan95] Ch.-A. Gandin, M. Rappaz, D. West and B. L. Adams. Grain texture evolution during the columnar growth of dendritic alloys. Metall. Mater. Trans. A, 26A, 1543-1550, 1995.

[Gan96] Ch.-A. Gandin, R. J. Schaefer and M. Rappaz. Analytical and numerical predictions of dendritic grain envelopes. Acta Mater., 44, 3339-47, 1996.

[Gan97] Ch.-A. Gandin and M. Rappaz. A 3D cellular automaton algorithm for the prediction of dendritic grain growth. Acta Mater., 45, 2187-95, 1997.

[Gan99] Ch.-A. Gandin, J.-L. Desbiolles, M. Rappaz and Ph. Thévoz. A three-dimensional Cellular Automaton-Finite Element model for the prediction of solidification grain structure. Metall. Mater. Trans. A, 30A, 3153-65, 1999.

[Gan03] Ch.-A. Gandin, G. Guillemot, B. Appolaire and N. T. Niane. Boundary layer correlation for dendrite tip growth with fluid flow. Mater. Sci. Eng., A 342, 44-50, 2003.

[Gao11] Y. M. Gao, Y. Jiang and S. Huang. Reduction of Molybdenum Oxide from Steelmaking Slags by Pure Liquid Iron. J. Min. Metall. Sect. B-Metall., 48, 25-36, 2012.

[Gli84] M. E. Glicksman. Free dendritic growth. Mat. Sci. Engrg., 65, 45-55, 1984.

[Gol74] D. Goldberg and G. R. Belton. The Diffusion of Carbon in Iron-Carbon Alloy at 1560°C. Metall. Trans., 5, 1643-48, 1974.

[Gol84] J. Goldak, A. Chakravarti and M. Bibby. A new finite element model for the welding heat sources. Metall. Trans. B, 15B, 299-305, 1984.

[Gra04] L. Granasy, T. Pusztai and J. A. Warren. Modeling polycrystalline solidification using phase field theory. J. Phys.: Condens. Matter, 16, R1205-35, 2004.

[Gro94] Ø. Grong. Metallurgical Modelling of Welding. Institute of Materials, Minerals and Mining, London, 1994.

[Gui04] G. Guillemot, Ch.-A. Gandin, H. Combeau and R. Heringer. A new Cellular Automaton-Finite Element coupling scheme for alloy solidification. Modelling. Simul. Mater. Sci. Eng., 12, 545-56, 2004.

[Gui06] G. Guillemot, Ch.-A. Gandin and H. Combeau. Modeling of macrosegregation and solidification grain structures with a coupled Cellular Automaton-Finite Element model. ISIJ Int., 46, 880-95, 2006.

[Gui07] G. Guillemot, Ch.-A. Gandin and M. Bellet. Interaction between single grain solidification and macrosegregation: Application of a Cellular Automaton-Finite Element model. J. Cryst. Growth, 303, 58-68, 2007.

[Gul13] G. H. Gulliver. The quantitative effect of rapid cooling upon the constitution of binary alloys. J. Inst. Metals., 9, 120-57, 1913.

[Hei86] G. N. Heintze and R. McPherson, Weld. J., 65, 71s, 1986.

[Hes91] H. W. Hesselbarth and I. R. Göbel. Simulation of recrystallization by cellular automata. Acta Metall. Mater., 39, 2135-43, 1991.

[Hus96] H. M. Hussain, P. K. Ghosh, P. C. Gupta and N. B. Potluri. Properties of pulsed current multipass GMA-Welded Al-Zn-Mg alloy. Weld. J. 75, 209s-15s, 1996.

[Hor61] G. Horvay and J. W. Cahn. Dendritic and spheroidal growth. Acta. Metall., 9, 695-705, 1961.

[Iva47] G. P. Ivantsov. Temperature field around a spheroidal, cylindrical and acicular crystal growing in supercooled melt. Dokl. Akad. Nauk SSSR, 58, 567-73, 1947.

[Kar00] A. Karma, Y. H. Lee, and M. Plapp. Three-dimensional dendrite tip morphology at low undercooling. Phys. Rev. E, 61, 3996-4008, 2000.

[Kha07] Md. Ibrahim Khan. Welding science and technology. New Age International publishers, 2007.

[Kim03] C. –H. Kim, W. Zhang and T. DebRoy. Modeling of temperature field and solidified surface profile during gas–metal arc fillet welding. J. Appl. Phys., 94, 2667-79, 2003.

[Kos14] T. Koshikawa, Ch.-A. Gandin, M. Bellet, H. Yamamura, and M. Bobadilla. ISIJ int., 54, 2014.

[Kou85a] S. Kou and Y. Le. Grain structure and solidification cracking in oscillated arc welds of 5052 aluminum alloy. Metall. Trans. A, 16A, 1345-52, 1985.

[Kou85b] S. Kou and Y. Le. Alternating grain orientation and weld solidification cracking. Metall. Trans. A, 16A, 1887-96, 1985.

[Kou02] S. Kou. Welding metallurgy. Wiley-Interscience, 2002.

[Kra09] M. J. M. Krane, D. R. Johnson and S. Raghavan. The development of Cellular Automaton-Finite Volume model for dendritic growth. Appl. Math. Model., 33, 2234-47, 2009.

[Kub75] P. Kubicek. Heterodiffusion of Chromium and Cobalt in Liquid Iron. Czech. J. Phys., B25, 535-41, 1975.

[Kum94] S. Kumar and S. C. Bhaduri. Three-Dimensional Finite Element modeling of Gas Metal-Arc welding. Metall. Trans. B, 25B, 435-41, 1994.

[Kur86] W. Kurz, B. Giovanola and R. Trivedi. Theory of microstructural development during rapid solidification. Acta Metall., 34, 823-30, 1986.

[Kur98] W. Kurz and D. J. Fisher. Fundamentals of solidification. Trans. Tech. Publications Ltd, Switzerland, 1998.

[Lan78] J. S. Langer and H. Müller-Krumbhaar. Theory of dendritic growth – I. elements and stability analysis. Acta Metall. Mater., 26, 1681-88, 1978.

[Lee00] Y. C. Lee, A. K. Dahle and D. H. StJohn. The role of solute in grain refinement of Magnesium. Metall. Mater. Trans. A, 31A, 2895-906, 2000.

[Lee13] J. Lee and K. Asim. Laser welds in lap-shear specimens. 03-12-2013 visited. http://sitemaker.umich.edu/jwo/laser_weld.

[Les86] G. Lesoult. Solidification – Cristallisation et microstructures. Techniques de l'ingénieur, M58, 1-28, 1986.

[Lin01] Q. Lin, X. Li and S. W. Simpson. Metal transfer measurements in gas metal arc welding. J. Phys. D: Appl. Phys., 34, 2001, doi:10.1088/0022-3727/34/3/317.

[Lin13] Lincoln Electric, GMAW Welding Guide. 05-12-2013 visited. http://www.lincolnelectric.com/assets/en_US/Products/literature/C4200.pdf

[Liu95] L. X. Liu and J. S. Kirkaldy. Thin film forced velocity cells and cellular dendrites – I. Experiments. Acta Matall. Mater., 43, 2891-904, 1995.

[Lu05] Y. Lu, C. Beckermann, and J. C. Ramirez. Three-dimensional phase-field simulations of the effect of convection on free dendritic growth. J. Cryst. Growth, 280, 320-34, 2005.

[McF09] S. McFadden and D. J. Browne. A front-tracking model to predict solidification macrostructures and columnar to equiaxed transitions in alloy castings. Appl. Math. Model., 33, 1397-416, 2009.

[Mit98] M. Mitchell. Computation in Cellular Automata: A selected review. Nonstandard Computation, 95-140, 1998.

[Mor78] K. Morgan, R. W. Lewis, and O. C. Zienkiewicz. An improved algorithm for heat conduction problems with phase change. Int. J. Numer. Meth. Eng., 12, 1191-5, 1978.

[Moy03] J. Moysan, A. Apfel, G. Corneloup and B. Chassignole. Modeling the grain orientation of austenitic stainless steel multipass welds to improve ultrasonic assessment of structural integrity. Int. J. Pres. Ves. Pip., 80, 77-85, 2003.

[Nas97] L. Nastac and D. M. Stefanescu. Stochastic modeling of microstructure formation in solidification processes. Modelling. Simul. Mater. Sci. Eng., 5, 391, 1997.

[Nas99] L. Nastac. Numerical modeling of solidification morphologies and segregation patterns in cast dendritic alloy. Acta Mater., 47, 4253-62, 1999.

[Old66] W. Oldfield. A quantitative approach to casting solidification: freezing of cast iron. Trans. Am. Soc. Metals, 59, 945, 1966.

[Pav04] V. Pavlyk and U. Dilthey. Simulation of weld solidification microstructure and its coupling to the macroscopic heat and fluid flow modeling. Modelling. Simul. Mater. Sci. Eng., 12, S33-45, 2004.

[Pet73] W. A. Petersen. Fine grained weld structures. Weld. J., 53, 74s-79s, 1973.

[Por92] D. A. Porter and K. E. Easterling. Phase transformations in metals and alloys. Chapman & Hall, London, 1992.

[Rap93] M. Rappaz and Ch.-A. Gandin. Probabilistic modeling of microstructure formation in solidification processes. Acta Metall. Mater., 41, 345-60, 1993.

[Rap96] M. Rappaz, Ch.-A. Gandin, J.-L. Desbiolles and Ph. Thévoz. Prediction of grain structures in various solidification processes. Metall. Mater. Trans. A, 27A, 695-705, 1996.

[Rap99] M. Rappaz and W. J. Boettinger. On dendritic solidification of multicomponent alloys with unequal liquid diffusion coefficients. Acta Mater., 47, 3205-19, 1999.

[Rap99b] M. Rappaz, J.-M. Drezet, and M. Gremaud. A new hot-tearing criterion. Metall. Mater. Trans. A, 30A, 449-55, 1999.

[Rap03] M. Rappaz, M. Bellet, M. Deville. Numerical modeling in material science and engineering, Springer, 2003.

[Rap03b] M. Rappaz, A. Jacot, and W. J. Boettinger. Last-stage solidification of alloy: theoretical model of dendrite-arm and grain coalescence. Metall. Mater. Trans. A, 34A, 467-479, 2003.

[Rut53] J. W. Rutter and B. Chalmers. A prismatic substructure formed during solidification of metals. Can. J. Phys., 31, 15-39, 1953.

[Ruv07] D. Ruvalcaba, R. H. Mathiesen, D. G. Eskin, L. Arnberg and L. Katgerman. In situ observations of dendritic fragmentation due to local solute-enrichment during directional solidification of an aluminum alloy. Acta Mater., 55,4287-92, 2007.

[Saa14] A.Saad, M.Bellet, and Ch-A. Gandin. A temperature-based approach for nonlinear phase transformations in solidification: application to macrosegregation. Model. Simul. Mater. Sc., (submitted) 2014.

[Sai58] T. Saito and K. Maruya. Diffusion of Silicon and Manganese in Liquid Iron. I Diffusion in Liquid Iron Saturated with Carbon. The Research Institute of Mineral Dressing and Metallurgy. 259-68, 1958.

[Sal12] R. S. Saluja, R. G. Narayanan and S. Das. Cellular automata finite element (CAFE) model to predict the forming of friction stir welded blanks. Comp. Mater. Sci., 58, 87-100, 2012.

[Sch42] E. Scheil. Bemerkungen zur schichtkristallbildung. Zeitschrift für Metallkunde, 34, 70-2, 1942.

[Shi08] P. Shi. TCS steels/Fe-alloy database V6.0 Thermo-Calc software AB (Stockholm, SE), 2008.

[Smi70] E. Smith, M. D. Coward and R. L. Apps. Weld heat-affected zone structure and properties of two mild steels. Weld. Metal Fabr., 38, 242-51, 1970.

[Smi99] L. Smith, M. Gittos and P. Threadgill. High quality and productivity joining processes and procedures for titanium risers and flowlines. Titanium Risers and Flowlines Seminar, Norway, Sintef Editor, 1999.

[Ste96] I. Steinbach, F. Pezzolla, B. Nestler, M. SeeBelberg, R. Prieler and G. J. Schmitz. A phase field concept for multiphase systems. Physica D, 94, 135-147, 1996.

[Ste99] I. Steinbach, C. Beckermann, B. Kauerauf, Q. Li, and J. Guo. Three-dimensional modeling of equiaxed dendritic growth on a mesoscopic scale. Acta Mater., 47, 971-82, 1999.

[Ste05] I. Steinbach, H. –J. Diepers, and C. Beckermann. Transient growth and interaction of equiaxed dendrites. J. Cryst. Growth, 275, 624-38, 2005.

[Sve90] L-E. Svensson and B. Gretoft. Microstructure and impact toughness of C-Mn weld metals. Weld. J., 69, 454s-61s, 1990.

[Tan12] W. Tan, N. S. Bailey and Y. C. Shin. Numerical modeling of transport phenomena and dendritic growth in Laser Spot Conduction Welding of 304 stainless steel. J. Manuf. Sci. E-T. ASME., 134, 2012, DOI 10.1115/1.4007101.

[The13] Thermo-Calc TCCS manuals Thermo-Calc software AB (Stockholm, SE), 2013.

[Til53] W. A. Tiller, K. A. Jackson, J. W. Rutter and B. Chalmers. The redistribution of solute atoms during the solidification of metals. Acta Metall., 1, 428-37, 1953.

[USA93] US Army, Operator's Circular, Welding Theory and Application. Training Circular, TC 9-237, 1993.

[Vil76] E. A. Villegas. The Diffusion of Nitrogen in Liquid Iron Alloys at 1600°C. Dissertation. 1976.

[Wan96a] C. Y. Wang and C. Beckermann. Equiaxed dendritic solidification with convection: part I. multiscale/multiphase modeling. Metall. Meter. Trans. A, 27A, 2754-64, 1996.

[Wan96b] C. Y. Wang and C. Beckermann. Equiaxed dendritic solidification with convection: part II. Numerical simulations for an Al-4 wt% Cu alloy. Metall. Meter. Trans. A, 27A, 2765-83, 1996.

[Wan03] W. Wang, P. D. Lee and M. McLean. A model of solidification microstructure in nickel-based superalloy: predicting primary dendrite spacing selection. Acta Mater., 51, 2971-87, 2003.

[Wan04] N. Wang, S. Mokadem, M. Rappaz, and W. Kurz. Solidification cracking of superalloy single- and bi-crystals. Acta mater., 52, 3173-3182, 2004.

[War95] J. A. Warren and W. J. Boettinger. Prediction of dendritic growth and microsegregation patterns in a binary alloy using the phase-field method. Acta Metall. Mater., 43, 689-703, 1995.

[Whe93] A. A. Wheeler, B. T. Murray and R. J. Schaefer. Computation of dendrites using a phase field model. Physica D. 66, 243-62, 1993.

[Yan00] Z. Yang, S. Sista, J. W. Elmer, and T. Debroy. Three dimensional Monte Carlo simulation of grain growth during GTA welding of Titanium. Acta Mater., 48, 4813-25, 2000.

[Yin11] H. Yin, S. D. Felicelli and L. Wang. Simulation of a dendritic microstructure with the lattice Boltzmann and Cellular Automaton methods. Acta Mater., 59, 3124-36, 2011.

[Zal10a] M. Zaloznik and H. Combeau. An operator splitting scheme for coupling macroscopic transport and grain growth in a two-phase multiscale solidification model: part I – model and solution scheme. Comp. Mater. Sci., 48, 1-10, 2010.

[Zal10b] M. Zaloznik, A. Kumar and H. Combeau. An operator splitting scheme for coupling macroscopic transport and grain growth in a two-phase multiscale solidification model: part II – application of the model. Comp. Mater. Sci., 48, 11-21, 2010.

[Zha08] X. H. Zhan, Z. B. Dong, Y. H. Wei and Y. L. Xu. Dendritic grain growth simulation in weld molten pool based on CA-FD model. Cryst. Res. Technol., 43, 253-9, 2008.

[Zha09] X. H. Zhan, Z. B. Dong, Y. H. Wei and R. Ma. Simulation of grain morphologies and competitive growth in weld pool of Ni-Cr alloy. J. Cryst. Growth, 311, 4778-83, 2009.

[Zha13] H. Zhang, K. Nakajima, Ch.-A. Gandin, and J. He. Prediction of carbide precipitation using partial equilibrium approximation in Fe-C-V-W-Cr-Mo high speed steels. ISIJ Int., 53, 493-501, 2013.

[Zhu01a] M. F. Zhu and C. P. Hong. A modified Cellular Automaton model for the simulation of dendritic growth in solidification of alloys. ISIJ Int., 41, 436-45, 2001.

[Zhu01b] M. F. Zhu, J. M. Kim and C. P. Hong. Modeling of globular and dendritic structure evolution in solidification of an Al-7mass%Si alloy. ISIJ Int., 41, 992-8, 2001.

[Zhu02] M. F. Zhu and C. P. Hong. A three dimensional modified Cellular Automaton model for the prediction of solidification microstructure. ISIJ Int., 42, 520-6, 2002.

[Zhu07] M. F. Zhu, C. P. Hong, D. M. Stefanescu and Y. A. Chang. Computational modeling of microstructure evolution in solidification of Aluminum alloys. Metall. Mater. Trans. B, 38B, 517-24, 2007.

Modélisation tridimensionnelle Automate Cellulaire - Éléments Finis (CAFE) pour la simulation du développement des structures de grains dans les procédés de soudage GTAW / GMAW

RESUME : Le développement des structures de grains se formant durant les procédés de soudage par fusion a un large impact sur les propriétés et la résistance mécaniques des assemblages. Des défauts, tels que la fissuration à chaud, sont aussi liés à la texturation de grains propre à l'étape de solidification. La simulation directe du développement tri-dimensionnelle (3D) des structures de grains dans ces procédés, à l'échelle industrielle, est rarement proposée. Dans ce travail, une modélisation couplée 3D Automate Cellulaire (CA) – Eléments Finis (FE) est proposée pour prédire la formation des structures de grains dans les procédés de soudage multipasses GTAW (Gas Metal Arc Welding) et GMAW (Gas Metal Arc Welding). A l'échelle macroscopique, la modélisation FE permet la résolution des équations de conservation de la masse, de l'énergie et de la quantité de mouvement pour l'ensemble du domaine en s'appuyant sur un maillage adaptatif. Pour le procédé GMAW avec apport de matière, le modèle FE est enrichi et développé dans une approche level set (LS) afin de modéliser l'évolution de l'interface métal / air due au développement du cordon de soudure. Le domaine FE contient ainsi la pièce étudiée et l'air environnant dans lequel le cordon se développe. Les calculs FE sont couplés avec l'approche CA utilisée pour modéliser le développement de la structure de grains. Un maillage fixe ('maillage CA') est superposé au maillage adaptatif FE ('maillage FE'). Les champs macroscopiques propres au maillage FE sont ainsi interpolés entre le maillage adaptatif FE et le maillage fixe CA. Une nouvelle stratégie d'allocation / désallocation de la grille de cellules CA est ensuite utilisée basée sur l'allocation / désallocation des éléments du maillage CA. La grille CA est constituée d'un ensemble régulier de cellules cubiques superposées au domaine soudée. A l'échelle micro-, la grille est utilisée afin de simuler les étapes de fusion et solidification, à la frontière entre le domaine pâteux et le bain liquide, durant le processus de soudage. Les évolutions de températures des cellules sont définies par interpolation du maillage CA. Un couplage du modèle avec les chemins de solidification et les évolutions enthalpiques tabulés est aussi implémenté, permettant de suivre la thermique et les évolutions de fractions de phase propre à l'évolution du procédé. Avec de réduire les temps de calcul et la quantité de mémoire informatique nécessaire à ces simulations, une optimisation des maillages FE/CA et des tailles de cellules CA est proposée pour les deux approches FE et CA. La modélisation 3D proposée est appliquée à la simulation de la formation des structures de solidification formées durant le soudage GTAW et GMAW multipasses de pièces d'acier inoxydables de nuances UR 2202. Dans le procédé GTAW, l'influence de l'évolution des structures de grains selon les paramètres procédés est étudiée. L'orientation normale des grains avec l'augmentation de la vitesse de soudage est montrée. Dans le procédé GMAW, la modélisation permet de simuler la refusion et la croissance des grains des couches successives. De manière générale, les structures de grains prédites montrent qualitativement les évolutions attendues présentées dans la littérature.

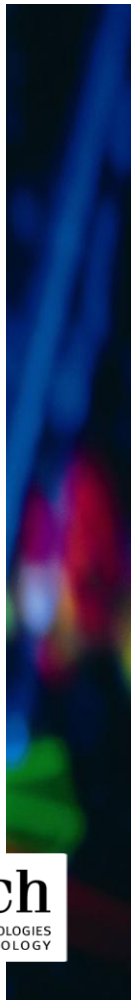

Mots clés : soudage, modélisation 3D CAFE, croissance épitaxiale, structure de grains, solidification, GTAW / GMAW

MINES ParisTech

ParisTech
INSTITUT DES SCIENCES ET TECHNOLOGIES
PARIS INSTITUTE OF TECHNOLOGY

Three dimensional Cellular Automaton – Finite Element (CAFE) modeling for the grain structures development in Gas Tungsten / Metal Arc Welding processes

ABSTRACT : Grain structure formation during fusion welding processes has a significant impact on the mechanical strength of the joint. Defects such as hot cracking are also linked to the crystallographic texture formed during the solidification step. Direct simulation of three-dimensional (3D) grain structure at industrial scale for welding processes is rarely modeled. In this work, a 3D coupled Cellular Automaton (CA) – Finite Element (FE) model is proposed to predict the grain structure formation during multiple passes Gas Tungsten Arc Welding (GTAW) and Gas Metal Arc Welding (GMAW). At the macroscopic scale, the FE model solves the mass, energy and momentum conservation equations for the whole system based on an adaptive mesh. For GMAW with metal addition, the FE model is enriched and established in a level set (LS) approach in order to model the evolution of the metal/air interface due to the weld bead development. The FE domain then contains the workpiece and the surrounding air where the weld bead forms. FE computations are coupled with the CA approach used to model the grain structure evolution. A fixed mesh, referred to as CA mesh, is superimposed to the adaptive FE mesh. FE fields are interpolated between the adaptive FE mesh and the fixed CA mesh. A new dynamic allocation/deallocation strategy of a CA grid of cells is then used based on the dynamic activation/deactivation of the elements of the CA mesh. The CA grid is made of a regular lattice of cubic cells superimposed onto the welded domain. At the micro scale, this grid is used in order to simulate the melting and solidification steps at the boundaries between the mushy domain and the liquid pool during the welding process. The temperature evolutions of the cells are computed by interpolation from the CA mesh. Coupling with tabulated transformation paths and phase enthalpy is also implemented, which permits to track the phase amount and latent heat release during the process. In order to master the resolution time and memory cost of the simulations, a management of the FE/CA mesh dimensions and CA cell size is considered for both FE and CA models. The 3D CAFE model is applied to simulate the formation of solidification structures during multiple passes GTAW and GMAW processes on a duplex stainless steel UR 2202. In GTAW, the evolution of the grain structures with respect to the welding process parameters is considered. The normal orientation of the grains with the increase of the heat source velocity is shown. In GMAW, the model is shown to compute the remelting and growth of successively deposited layers. Overall, the predicted structures qualitatively reveal the expected evolutions presented in the literature.

Keywords : welding, 3D CAFE modeling, epitaxial growth, grain structures, solidification, GTAW / GMAW

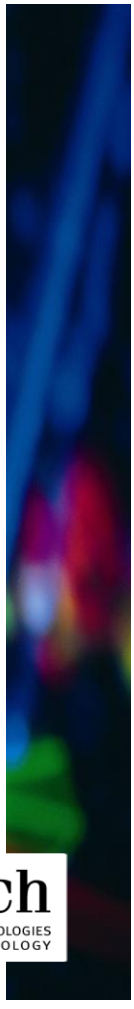

MINES ParisTech

ParisTech
INSTITUT DES SCIENCES ET TECHNOLOGIES
PARIS INSTITUTE OF TECHNOLOGY